Blade Health Monitoring Solution for Shrouded Impellers using Clearance Measurements



Siripong Cheanklin

St Anne's College

A thesis submitted in partial fulfilment of the requirements for the degree of

Doctor of Philosophy

Department of Engineering Science

University of Oxford

Michaelmas Term 2023

Abstract

This thesis proposes a novel blade health monitoring solution for shrouded impellers, presenting a significant achievement in the field. The proposed solution establishes a correlation between the blade condition and the deflection of the impeller shroud. The blade condition can be determined by measuring the clearance between the shroud and an eddy current sensor installed through the static casing. This clearance measurement approach is a unique and unexplored method for monitoring the blade condition of shrouded impellers, as indicated by an extensive literature review.

A comprehensive investigation was conducted to evaluate the feasibility of the eddy current-based clearance measurement to monitor blade condition, incorporating experimental, numerical (FEA and CFD), and theoretical studies.

The experimental studies were performed with scaled impellers in healthy and cracked blade conditions. The experimental results confirmed the feasibility of the clearance measurement to detect blade crack propagation. The linear relationship between the crack length and the shroud deflection was also established.

Numerical studies were conducted to investigate the effect of impeller design parameters on the shroud deflection. The findings of the parametric analysis suggested that blade thickness and shroud thickness had the most significant impact on the change in the shroud deflection. The parametric studies unveiled the relationship between the maximum inlet shroud deflection and the impeller material in terms of the ratio of density to the modulus of elasticity. This relationship was explained by a simplified model for a blade disk system in the theoretical studies.

The inlet shroud deflection of the full-scaled impeller in various blade conditions was also determined using the FEA simulation models. The objective was to demonstrate that the proposed clearance measurement system can be implemented on industrial equipment. The study results lead to the proposed guidelines for designing a blade crack detection system for a full-scaled shrouded impeller.

Besides the academic impact, these studies also affect industrial communities. The results from the feasibility studies should lead to the development of an industrial blade health monitoring system for shrouded impellers, which primarily benefits production planning. In addition, OEMs could benefit from understanding blade failure mechanisms, which could ultimately inform impeller design.

To my deepest love and affection, Amornrat,

and our wonderful daughter, Varinphon.

Acknowledgement

I would like to express my appreciation to Professor Kam Chana, my research supervisor, for his patient guidance and constructive suggestions and for spending his valuable time on weekly meetings. Without these assistances, developing a novel blade health monitoring system for a shrouded impeller would have never been accomplished.

I would also like to thank Professor Li He for his advice on CFD simulations. Although we rarely had the opportunity for discussion, you consistently made time for me.

I am indebted to the academic and support staff, technicians, and fellow researchers at the Osney Lab for their help and support. Dr Vikram Shidar, Sunny Chana, and Jamie Dean, in particular, assisted me with the assembly and operation of the high-speed spinning rig.

In addition, I would like to express my gratitude to SCG Chemicals Co., Ltd. for the full scholarship that make this education journey possible. Mr Sophon Arayasathaporn and Dr Jirut Wattoom deserve special recognition for providing me with the opportunity and firm support.

Most importantly, none of this could have happened without my family. Without your love, encouragement, and belief in me, I would not be able to accomplish this.

Contents

Abstract i

List of Figures ix

List of Tables xxvi

Nomenclature xxvii

1 Introduction 1

1.1 Background 1

1.2 Motivation 7

1.3 Research Aims and Objectives 10

1.4 Thesis Outline 12

2 Literature Review 14

2.1 Introduction 14

2.2 Centrifugal gas compressors with shrouded impellers 15

2.2.1 Dynamic similarity of centrifugal compressors 15

2.2.2 Shrouded impellers 20

2.3 Blade crack studies 22

2.3.1 Blade crack studies 23

2.3.2 Cracked blade modelling 24

2.4 Typical blade health monitoring methods 27

2.4.1 Strain gauge 27

2.4.2 Blade Tip Timing 29

2.4.3 Blade tip clearance 34

2.4.4 Applications of blade tip timing and blade tip clearance 37
2.4.5 Types of sensors for non-intrusive blade health monitoring 40
2.5 Eddy current sensor and associated electronic system 44
2.5.1 Principle of an eddy current sensor 44
2.5.2 Eddy current sensor models 47
2.5.3 Associated electronic system 54
2.6 Chapter conclusion 55

3 Experimental Setup 56
3.1 Introduction 56
3.2 High-speed spinning facility 56
3.3 Scaled impeller 59
3.3.1 Design and manufacturing 60
3.3.2 Runout measurements 65
3.3.3 Residual unbalance measurement 70
3.3.4 Blade resonance frequencies 74
3.4 Instrumentation 79
3.5 Signal processing 85
3.6 Eddy current sensor calibration for clearance measurement 87
3.6.1 Calibration for clearance measurement 87
3.6.2 Uncertainty analysis of the clearance measurement system 94
3.8 Chapter conclusion 98

4 Computational Electromagnetic Simulations 100
4.1 Introduction 100

4.2 Low-frequency electromagnetic simulation model 101
4.3 Software validation 102
4.4 Simulation model 104
4.5 Mesh sizing 108
4.6 Simulation results and discussion 109
4.7 Conclusion 113

5 Experimental Studies of Blade Crack Detection 114
5.1 Introduction 114
5.2 Impeller with healthy blades 115
5.3 Impeller with a cracked blade – the preliminary experiment 126
5.3.1 Crack detection experiment 127
5.3.2 Stuck blade fragment incident 137
5.3.3 Discussion for the preliminary experiment in crack detection 138
5.4 Impeller with a cracked blade – the main experiment 139
5.5 Chapter conclusion 149

6 Numerical Studies of Blade Crack Detection 151
6.1 Introduction 151
6.2 Static structural analysis 151
6.3 Simulation models 152
6.3.1 Simulation models and boundary conditions 152
6.3.2 Mesh sizing 155
6.4 FEA of the scaled impeller 157
6.4.1 FEA of the scaled impeller with healthy blades 156

6.4.2 FEA of the scaled impeller with a cracked blade.....166
6.5 Effect of impeller design parameters on the inlet shroud deflection.....170
6.5.1 Effect of the fillet radius on the inlet shroud deflection.....171
6.5.2 Effect of the blade thickness on the inlet shroud deflection.....173
6.5.3 Effect of the shroud thickness on the inlet shroud deflection.....176
6.5.4 Effect of the back-end wall thickness on the inlet shroud deflection...180
6.5.5 Effect of the number of blades on the inlet shroud deflection.....182
6.5.6 Effect of the impeller size on the inlet shroud deflection.....185
6.5.7 Effect of the impeller material on the inlet shroud deflection.....187
6.6 Chapter conclusion.....192

7 Proposed Blade Crack Detection System..... 194
7.1 Introduction.....194
7.2 Passing fluid interaction.....194
7.2.1 CFD Simulation model.....196
7.2.2 Model validation.....200
7.2.3 Mesh sizing.....202
7.2.4 CFD simulation results.....203
7.3 Static structural analysis of the full-scaled impeller.....207
7.3.1 Simulation models.....207
7.3.2 Mesh sizing.....210
7.4 FEA of the actual impeller.....211
7.4.1 Effect of the passing fluid.....211
7.4.2 Effect of a dry gas seal.....213
7.4.3 FEA of the impeller with healthy blades.....215

7.4.4 FEA of the impeller with a cracked blade 219
7.5 The proposed blade crack detection system 227
7.6 Chapter conclusion 231

8 Conclusion 232
8.1 Overall conclusions 232
8.2 Recommendations for future works 236

Appendix: Dimensional analysis 238
References 242

List of Figures

1. 1 A train of compressors driven by a steam turbine in a petrochemical plant 2

1. 2 A rotor with four shrouded impellers in tandem arrangement inside the opened horizontal split casing 3

1. 3 The cross-sectional schematic diagram of the impeller and casing showing a gas flow path 3

1. 4 A shrouded impeller with damaged blades (a) the location of the damaged blade; (b) a cracked impeller blade; (c) the size of the damaged blade 4

1. 5 The trend of the radial shaft vibrations and speed of a compressor during the blade damaged incident 5

1. 6 Finite element model of the impeller (a) the location of the cracked blade; (b) the crack path; (c) the deflection of the inlet shroud of the healthy impeller; (d) the deflection of the inlet shroud of the impeller with a cracked blade 9

1. 7 Comparison between the deflection of the healthy impeller and the impeller with the cracked blade number 5 10

1. 8 The investigation research schematic 11

2. 1 Application areas of the various types of industrial compressors in terms of the relation between the head coefficient and the flow coefficient [45] 16

2. 2 Comparison of efficiency and losses to flow coefficient, as affected by the impeller design [71] 18

2. 3 Typical cross-sectional diagram of a shrouded impeller (adapted from Zhou et al. (2020) [41]) 20

2. 4 Shrouded impeller blade damage a) cracked blade at leading edge b) an impeller with broken blades [56] 22

2. 5 A simplified lumped-parameter model of an impeller with a cracked blade [49] 25

2. 6 The strain gauge configured in the Wheatstone bridge circuit [39] 28

2. 7 Attached stain gauges on the impeller [34] 29

2. 8 Blade tip timing installation [35] 30

2. 9 Schematic diagram of optical blade tip timing [9] 30

2. 10 Non-vibrating blade (a) compared with vibrating blades (b and c) and the measured Time of Arrival (TOA) [36] 31

2. 11 Number of sensors and the obtained results [4] 33

2. 12 The configuration of an optical blade tip timing sensor and reflective tape on a shrouded blade disk [81] 34

2. 13 Blade tip clearance measurement techniques (a) tip clearance of an axial gas turbine [59]; (b) shematic of blade tip clearance sensor installation [6] 35

2. 14 A blade tip sensor permits the monitoring of blade tip clearance and the time of arrival [6] 36

2. 15 The installation of eddy current and optical sensors [93] 38

2. 16 The average and instantaneous blade deflections when a foreign object was stuck in blade 9 [93] 39

2. 17 Blade condition as determined by variations in the blade lengths [106] 39

2. 18 A closed loop active clearance control [107] 40

2. 19 Isentropic Light Piston Facility (ILPF) used in testing (a) the schematic diagram; and (b) a magnified image of the turbine section [6] 42

2. 20 The sensor installation (a) the arrangement of sensors in Perspex block; and (b) the test cassette [6] 42

2. 21 The blade passing signals from different sensors compared with the rotor speed signal (a) optical sensor: (b) capacitance sensor; (c) eddy current sensor; and (d) pressure transducer [6] 43

2. 22 The schematic diagram of the eddy current sensor and the target 45

2. 23 The decrease of induced eddy current in target material [80] 46

2. 24 The standard depth of penetration versus excitation frequency of various non-ferromagnetic materials including titanium, Inconel 625, stainless steel, and aluminium 47

2. 25 The schematic diagram of solenoid coil above the plane surface of an electrically conductive target [86] 49

2. 26 The predicted and measured impedance of a coil with varying normalised lift-offs (k) from the aluminium alloy and mild steel samples at various normalised frequencies (f_0) [85] 50

2. 27 The air-core transformer model for explaining the interaction between an eddy current sensor and a target [29] 51

2. 28 Short multiple-layer coil in solenoidal form, adapted from Terman (1943) [31] 53

3. 1 The testing facility (a) CAD model of the shrouded impeller inside the containment; and (b) the testing facility with the top lid opened (air motor configuration)..... 57

3. 2 The high-velocity impact simulation (a) simulation model; and (b) simulation results..... 58

3. 3 CAD models (a) the actual size impeller; and (b) the scaled impeller..... 61

3. 4 Comparison between the deflection of the healthy scaled impeller and the scaled impeller with a cracked blade number 10..... 62

3. 5 The scaled 3D-printed plastic impeller with conductive painted surfaces..... 64

3. 6 The setup of runout measurements in three locations (a) inlet shroud location; (b) outlet shroud location; and (c) back-end-wall location..... 67

3. 7 Runout profile at the inlet shroud location..... 67

3. 8 Polar plot of the inlet shroud runout profile..... 68

3. 9 Runout profile at the outlet shroud location..... 68

3. 10 Outlet shroud profile shows the downward distortion between two adjacent blades..... 69

3. 11 Runout profile at the back-end-wall location..... 69

3. 12 The setup of the four-run balancing method showing the signal channel accelerometer and an attached trial weight..... 72

3. 13 The four-run balancing diagram..... 72

3. 14 Comparison of the FFT spectrum of the impeller before and after adding a correction weight..... 73

3. 15 A setup of blade natural frequencies measurement, the red arrow shows the point was impacted during the test 76

3. 16 Unwindowed and windowed response signals from impact testing..... 76

3. 17 An example of the FFT response of blade number 1, showing the distinctive peaks at 814 Hz or 1,127 Hz 77

3. 18 The predicted blade modal deformations (a) the 1st mode at 865 Hz; and b) the 2nd mode at 1,205 Hz..... 77

3. 19 Comparison between the whole impeller vibration modes and blade vibration modes, red arrows indicate the movement direction (a) the impeller twist mode at 260 Hz; (b) the impeller one-nodal diameter mode at 444 Hz; (c) the 1st blade mode at 865 Hz; and (d) the 2nd blade mode at 1,205 Hz..... 78

3. 20 Comparison of the windowed blade response signals of individual blades .. 79

3. 21 Sensor mounting locations (a) 1/rev (speed) sensor; (b) BTT sensor at the inlet blades; (c) BTT sensor at the outlet blades; (d) clearance sensor at the inlet shroud; (e) clearance sensor at the outlet shroud; (f) clearance sensor at the back-end wall; (e) accelerometer on the bearing support; and (h) accelerometer on the sensor holder ring..... 82

3. 22 The schematic diagram of the sensors (a) sensor locations; and (b) the direction of blade order is opposite to that of the rotor rotation (CW)..... 83

3. 23 Signal processing diagram of 1/rev (speed), Blade Tip Timing, and clearance signals..... 86

3. 24 The synchronised blade passing and clearance signals compared to the speed signal. 86

3. 25 The setup of sensor calibration at the speed of 100 RPM (a) and (b) at the inlet shroud location; (c) at the outlet shroud location; and (d) at the back-end wall location 90

3. 26 The range of eddy current sensor calibration 91

3. 27 Inlet shroud signals at different sensor clearances as compared to the impeller runout 91

3. 28 The relation between the sensor output signal and the sensor clearance in reference to blade number 11, only 13 positions shown..... 92

3. 29 The quadratic relation between the sensor clearance and the output signal. 92

3. 30 The relation between the sensor output signal and the absolute clearance, only 13 positions shown..... 93

3. 31 Outlet shroud signals at different sensor clearances as compared to the impeller runout 93

3. 32 Back-end wall signals at different sensor clearances as compared to the impeller runout 94

3. 33 The overlaid 50 data sets of the inlet shroud clearance signals at 2-mm clearance (referring to blade #11) 96

3. 34 The uncertainty of the clearance signals at 2-mm clearance (referring to blade #11)..... 97

3. 35 The uncertainty of the clearance signals versus the absolute clearances, only 13 measurements shown 97

3. 36 The uncertainty of the clearance measurement system, all 52 measurement positions 98

4. 1 The current path of the coil simulation model is defined by the circular edge of the coil with arrows 102

4. 2 The alternating magnetic field (the red arrows) of the induction coil..... 103

4. 3 Equivalent circuit for eddy current measurement 106

4. 4 Electromagnetic simulation model (a) a rectangular coil of an eddy current sensor; (b) a cross-sectional model of the rectangular coil; (c) a 3D simulation model showing inductive coil and target; (d) surface of the target material; (e) a side view of the simulation model; and (f) mesh distribution of coil and target..... 107

4. 5 The coil inductances and the coil output voltage against the number of elements 109

4. 6 Comparison of eddy current sensor frequency responses between measurement and simulation results 110

4. 7 The induced eddy currents in the target with different coil standoffs (a) at 1 mm or 0.10 z/L; (b) at 2 mm or 0.19 z/L; (c) at 4 mm or 0.39 z/L; and (d) at 6 mm or 0.58 z/L 112

4. 8 The alternating magnetic field (white arrow) of the rectangular coil over a conductive target at a 2-mm standoff (a) a narrow section view; and (b) a longitudinal section view 112

4. 9 The predicted relationship between the sensor output signal and the absolute clearance corresponding to the measured results..... 113

5. 1 The rotor speeds in the healthy blade condition testing..... 119

5. 2 Inlet shroud clearance signals in voltage of the healthy impeller at different speeds..... 120

5. 3 Polar plot of the absolute inlet shroud clearance of the healthy impeller at different speeds.....120

5. 4 The change of inlet shroud clearance of the healthy impeller at different speeds 121

5. 5 Outlet shroud signals in voltage of the healthy impeller at different speeds 121

5. 6 Polar plot of the absolute outlet shroud clearance of the healthy impeller at different speeds.....122

5. 7 The change of outlet clearance of the healthy impeller at different speeds ..122

5. 8 Back-end wall clearance signals in voltage of the healthy impeller at different speeds.....123

5. 9 Polar plot of the absolute back-end wall clearance of the healthy impeller at different speeds.....123

5. 10 The change of back-end wall clearance of the healthy impeller at different speeds.....124

5. 11 Impeller movement diagram as the rotor speed increases.....124

5. 12 Inlet blade tip timing signal of the impeller with healthy blades, measured from the inlet blade sensor at a rotor speed of 3,500 RPM.....125

5. 13 Outlet blade tip timing signal of the impeller with healthy blades, measured from the outlet blade sensor at a rotor speed of 3,500 RPM 125

5. 14 The frequency spectra of the impeller with healthy blades system at 3,500 RPM (a) vibration of the bottom bearing; and (b) vibration of the sensor holder ring 126

5. 15 The scaled impeller with sensor installation in the preliminary experiment (a) a shrouded impeller in the containment; (b) a 1/rev (speed) sensor; (c) a clearance sensor on the inlet shroud; and (d) a BTT sensor on the inlet blades.....128

5. 16 Blade conditions (a) a healthy blade; (b) an initial 11-mm crack on blade number 10; (c) the broken blade number 10; and (d) a piece of the blade fragment stuck on blade number 7 129

5. 17 The rotor speed during the five runs.....130

5. 18 Inlet shroud clearance signal of the impeller with the initial 11-mm crack on blade number 10 during the 1st run.....132

5. 19 Inlet shroud clearance signal of the impeller with the initial 11-mm crack on blade number 10 during the 2nd run. 133

5. 20 Inlet shroud clearance signal of the impeller with the initial 11-mm crack on blade number 10 during the 3rd run 133

5. 21 Inlet shroud clearance signal of the impeller with the initial 11-mm crack on blade number 10 during the 4th run 134

5. 22 Inlet shroud clearance signal of the impeller with the initial 11-mm crack on blade number 10 during the 5th run 134

5. 23 Comparison of the inlet shroud clearance signals of the impeller with the initial 11-mm crack on blade number 10 between the five runs at the same speed of 3,000 RPM 135

5. 24 Tip timing before and at the blade-off incident from the 5th run.....135

5. 25 Tip timing before and at the blade-off incident from the 5th run (magnified) 136

5. 26 Blade passing signals before and after the blade-off incident from the 5th run 136

5. 27 The damaged impeller (a) the location of the broken blade and the stuck blade fragment; and (b) the sawtooth pattern on the broken-off blade 137

5. 28 Inlet shroud clearance signal during the impact at blade number 7.....138

5. 29 Impeller blade conditions (a) a healthy blade; (b) a 4-mm cracked blade; (c) a 7-mm cracked blade; (d) a 10-mm cracked blade; (e) a 15-mm cracked blade; and (f) a 20-mm cracked blade 144

5. 30 Inlet shroud clearance signals of the healthy impeller compared with the impeller with a cracked blade at a rotor speed of 3,500 RPM.....145

5. 31 The differences in clearance signals with reference to the signal of the impeller with healthy blades at a rotor speed of 3,500 RPM 145

5. 32 The change of the inlet shroud clearance at different impeller blade conditions at 3,500 RPM with reference to the impeller with healthy blade condition at 200 RPM 146

5. 33 The polar plot of the change of the inlet shroud clearance at different impeller blade conditions with reference to the impeller with healthy blade condition at the same speed of 3,500 RPM.....146

5. 34 The relation between the crack length and the change in shroud deflection at the inlet shroud position at 3,500 RPM.....147

5. 35 Comparison of blade arrival times among the different blade conditions, including a healthy blade, a 10-mm cracked blade, and a 20-mm cracked blade at a rotor speed of 3,500 RPM.....147

5. 36 Comparison of the delayed arrival times among the different blade conditions, including a healthy blade, a 10-mm cracked blade, and a 20-mm cracked blade with reference to blade number 1 at a rotor speed of 3,500 RPM 148

5. 37 Comparison of the frequency spectra impeller with a 20-mm cracked blade system at 3,500 RPM (a) vibrational spectra of the bottom bearing; and (b) vibrational spectra of the sensor holder ring 148

6. 1 Finite element simulation model (a) the scaled impeller with a cracked blade; (b) mesh of the simulation model; (c) the applied boundary conditions; and (d) the crack path 154

6. 2 The maximum and minimum inlet shroud deflection against the number of elements 156

6. 3 Simulation results of the healthy impeller at the rotating speed of 3,500 RPM (a) total deflection at the front view; (b) total deflection at the back view; (c) blade total deflection; and (d) blade stress distribution 160

6. 4 The predicted relationship between the maximum stress and the impeller speed 161

6. 5 The predicted deflections (a) inlet shroud, radial; (b) back-end wall, axial; (c) Outlet shroud, radial; and(d) Outlet shroud, axial 161

6. 6 Comparison of the radial inlet shroud deflections of the healthy impeller between the experimental and the simulation results in a polar plot.....162

6. 7 The relationship between the radial inlet shroud deflection and the rotating speed of the impeller.....162

6. 8 The relationship between the axial shroud deflection and the speed of the impeller 163

6. 9 The relationship between the shroud twist angle (CCW) and the speed of the impeller 163

6. 10 Comparison of the axial back-end wall deflections of the healthy impeller between the experimental results and the simulation results 164

6. 11 The relationship between the axial back-end wall deflection and the speed of the impeller 164

6. 12 Comparison of the axial outlet shroud deflections of the healthy impeller between the experimental results and the simulation results 165

6. 13 The relationship between the outlet shroud deflections and the speed of the impeller 165

6. 14 Comparison of the axial outlet shroud deflections of the healthy impeller between the experimental results and the simulation results after accounting for the effect of radial deflection 166

6. 15 Deflections of a cracked blade of the scaled impeller (a) 4-mm crack; (b) 7-mm crack; (c) 10-mm crack; and (d) 20-mm crack 168

6. 16 Comparison of the radial deflections of the impeller with a cracked blade between the experimental results and the simulation results at 3,500 RPM 169

6. 17 The predicted relationship between the crack length and the change in the inlet shroud deflection at 3,500 RPM, compared with the experimental results 169

6. 18 CAD model of impellers with different fillet sizes (a) 2-mm fillet radius (baseline case); (b) 4-mm fillet radius 172

6. 19 The inlet shroud deflections of the healthy impellers at different fillet sizes 172

6. 20 The inlet shroud deflections of an impeller with a 20-mm cracked blade at different fillet sizes 173

6. 21 CAD model of impellers with different blade thicknesses (a) 1-mm blade thickness (baseline case); and (b) 2.5-mm blade thickness.....174

6. 22 The inlet shroud deflections of the healthy impellers at different blade thicknesses.....175

6. 23 The relationship between the change of the shroud deflection and the blade thickness of the healthy impeller.....175

6. 24 Comparison of the change in the inlet shroud deflection of an impeller with a 20-mm cracked blade at different blade thicknesses.....176

6. 25 CAD model of impellers with different shroud thicknesses (a) 4.46-mm shroud thickness (baseline case); and (b) 17.83-mm shroud thickness 178

6. 26 The inlet shroud deflections of the healthy impeller at different shroud thicknesses.....178

6. 27 Comparison of the changes of the inlet shroud deflection of an impeller with a 20-mm cracked blade at different shroud thicknesses.....179

6. 28 The relationship between the change of the maximum shroud deflection and the shroud thickness at two different blade conditions.....179

6. 29 CAD model of impellers with different back-end wall thickness (a) 2-mm shroud thickness (baseline case); and (b) 5-mm shroud thickness.....180

6. 30 The inlet shroud deflections of the healthy impellers at different back-end wall thicknesses.....181

6. 31 Comparison of the changes of the inlet shroud deflection of an impeller with a 20-mm cracked blade at different back-end wall thicknesses.....181

6. 32 CAD model of impellers with different numbers of blades (a) 13-blade impeller (baseline case); and (b) 17-blade impeller.....183

6. 33 The relationship between the change of the shroud deflection and the number of blades for the healthy blade condition.....183

6. 34 The inlet shroud deflections of impellers with different numbers of blades in three blade conditions including healthy blade, 10-mm cracked blade, and 20-mm cracked blade.....184

6. 35 Comparison of the changes of the inlet shroud deflection of an impeller with a 20-mm cracked blade for different numbers of blades 185

6. 36 The relationship between the change of the shroud deflection and the size of the healthy impeller.....186

6. 37 Comparison of the changes in the inlet shroud deflection of an impeller with a 20-mm cracked blade at different impeller sizes 186

6. 38 The inlet shroud deflections of the healthy impellers at different materials 190

6. 39 The relationship between the shroud deflection of a healthy impeller and the ratio of density to the modulus of elasticity of the impeller material 190

6. 40 The inlet shroud deflections of an impeller with a 20-mm cracked blade for different impeller materials 191

6. 41 The relationship between the change of the maximum shroud deflection and a ratio of density to the modulus of elasticity at two different blade conditions .191

7. 1 Simulation diagram 195

7. 2 CFD simulation model (a) computational domains in CFD studies; (b) simulation model, including a rotating region attached to the impeller and static region attached to the stationary parts; (c) mesh of the fluid domain; and (d) applied boundary conditions 199

7. 3 Comparison between the predicted polytropic head and the machine data .201

7. 4 Averaged mass flow rate and the averaged discharge temperature against the number of elements 202

7. 5 Contours of pressure and Mach number at a 50% span (a) the pressure distribution; and (b) the Mach number distribution 204

7. 6 Pressure distribution contours (a) at the pressure side of a blade; (b) at the suction side of a blade; (c) at the inside surface of the shroud; and (d) at the inside surface of the hub.....205

7. 7 The pressure distributions on the pressure side and suction side along the streamwise direction at various spans.....206

7. 8 The pressure difference acting on the blade between the pressure side and the suction side.....206

7. 9 A shrouded impeller with damaged blades (a) the location of a damaged blade; (b) a cracked impeller blade; and (c) the size of the damaged blade of a 50 mm radius, the blue arrow indicates the crack path.....208

7. 10 Finite element simulation model (a) the scaled impeller with a cracked blade; (b) mesh of the simulation model, the green arrow indicates the inlet shroud location (clearance measurement location); (c) the applied boundary conditions; and (d) the crack path 209

7. 11 The maximum and minimum inlet shroud deflection against the number of elements 210

7. 12 The effect of the passing fluid pressure boundary condition on the inlet shroud deflections 212

7. 13 The effect of the passing fluid pressure on the change of the inlet shroud deflection between healthy and 50% cracked blade conditions 212

7. 14 The effect of the seal pressure boundary condition on the inlet shroud deflections 214

7. 15 Comparison between the whole impeller vibration modes and blade vibration modes, red arrows indicate the movement direction (a) the impeller one-nodal diameter mode at 553 Hz; (b) the impeller twist mode at 582 Hz; (c) the 1st blade mode at 2,443 Hz; and (d) the 2nd blade mode at 5,172 Hz..... 216

7. 16 Effect of applying fluid pressure boundary conditions, including passing fluid pressure distribution and seal pressure, on the natural frequencies of the actual impeller 217

7. 17 Simulation results of the healthy impeller (a) total deflection at the front view; (b) total deflection at the back view; (c) blade total deflection; and (d) blade stress distribution 218

7. 18 Deflections of the actual impeller with healthy blades 219

7. 19 Deflections of a cracked blade of the full-scaled impeller (a) 12.5% crack; (b) 25% crack; (c) 50% crack; and (d) 75% crack 223

7. 20 The inlet shroud deflection of the full-scaled impeller in various conditions (healthy to 37.5% crack) 224

7. 21 Polar plot of the change of the inlet shroud deflection in the first region: 6.25% crack to 37.5% crack 224

7. 22 The inlet shroud deflection of the full-scaled impeller in various conditions (37.5% crack to part loss) 225

7. 23 The predicted relation between the crack length (%) and the change in the peak of the inlet shroud deflection 225

7. 24 Polar plot of the predicted relation between the crack length (%) and the change in the peak of the inlet shroud deflection, the red arrow shows the direction of rotation.....226

7. 25 The back-end wall axial deflections at different blade conditions.....226

7. 26 The proposed locations for clearance sensor installations and the inlet shroud, and the back-end wall locations.....230

List of Tables

2. 1 Comparison of blade tip timing results from four different types of sensors [6] 44

3. 1 Comparison between the actual size impeller and the scaled impeller..... 62

3. 2 Balancing record of the four-run method 73

3. 3 Sensors and locations 84

4. 1 The coil inductance from the empirical formula and the simulation 103

4. 2 Electromagnetic properties of the materials used in simulations 106

4. 3 The rectangular coil inductance and resistance..... 109

6. 1 Mechanical properties of the material used in simulations..... 154

6. 2 The list of parameters in the parametric studies..... 171

6. 3 The mechanical properties of materials used in the parametric studies 189

7. 1 Thermodynamic properties of a cracked gas..... 198

7. 2 The composition of a cracked gas 198

7. 3 Compressor operating data 201

7. 4 Mechanical properties of the actual impeller 208

Nomenclature

Roman

A	Amplitude; Magnetic vector potential; Area
B	Magnetic field
c_o	Speed of light
C	Capacitor, Capacitance
C_p	Specific heat at constant pressure
CR	Compression ratio
C_v	Specific heat at constant volume
D	Impeller diameter; Constant offset
E	Electric field; Modulus of elasticity
EO	Engine order
f	Driving frequency; Frequency
F	Centrifugal force
$\{F\}$	Force matrix
h	Lift-off distance
H1	Primary magnetic field
H2	Secondary magnetic field
H_p	Polytropic head of a compressor
i_0	alternating current of amplitude
I	Current
J	Current density
k	Normalised lift-off; Stiffness; Ratio of specific heat
$[K]$	Stiffness matric
L	Inductor; Effective Coil Inductance; Length
m	Number of vibration mode
$\dot{m}$	Mass flow rate
M	Mutual inductance; Mach number
MW	Molecular weight

n	Number of measurements; Polytropic exponential index
N	Number of sensors; Rotational speed
N_s	Specific speed
P	Pressure
Q	Quality factor
r	Radius
R	Blade mean radius; Resistor; Resistance; Molar gas constant
S	Standard deviation
t	Time
t_{n-1}	Value of the Student's t-distribution with population n
T	Temperature
U	Uncertainty
V	Volume
W	Stored energy in a magnetic field
W_c	Mass of a correction weight
W_t	Mass of a trial weight
x	Blade deflection; Displacement; Standoff distance
Z	Coil impedance; Compressibility factor

Greek

γ	Specific heat ratio
δ	Standard depth of penetration
Δ	Different
ΔP	Ratio of the head
Δt	Time difference
ε_0	Absolute permittivity
η_p	Compressor polytropic efficiency
η_c	Adiabatic efficiency
θ	Angle
λ	Free space wavelength
μ_r	Relative magnetic permeability

μ_0	Absolute magnetic permeability
Π	Dimensionless group
ρ	Density
σ	Electrical conductivity
φ	Flow coefficient; Phase
ψ	Head coefficient
ω	Frequency, Angular velocity
Ω	Rotational speed

Subscripts

0	Normalised; Absolute
1	Inlet; First
2	Outlet; Second
a	Location a
b	Location b
avg	Averaged
eff	Effective

Abbreviation

1X	Speed frequency
13X	Blade pass frequency (13 blades)
2PP	Two-Parameter Plot method
3D	Three-dimensional
AC	Alternating current
API	American Petroleum Institute
BTC	Blade Tip Clearance
BTT	Blade Tip Timing
CAD	Computer-aided design
CCW	Counter-clockwise
CFD	Computational Fluid Dynamics
CW	Clockwise

DAQ	Data acquisition
DC	Direct current
FEA	Finite Element Analysis
FFT	Fast Fourier transform
FOD	Foreign Object Damage
FSI	Fluid-structural interaction
FSO	Full-scale output
IGV	Inlet Guide Vane
ILPF	Isentropic Light Piston Facility
MMS	Machine Monitoring System
ND	Nodal Diameter
OEM	Original Equipment Manufacturer
RLC	Electrical circuit consists of resistor, inductor, and capacitor
RPM	Revolution Per Minute
SLS	Selective Laser Sintering
SST	Shear Stress Transport turbulence model
TOA	Time of Arrival
VSD	Variable Speed Drive

Chapter 1

Introduction

1.1 Background

Centrifugal compressors with shrouded impellers are the critical machine which get wide uses in refineries, gas separation and processing, and petrochemicals plants. In petrochemical plants, their primary function is to pressurise processed hydrocarbon gas drawn from cracking furnaces for the separation sequences in fractionation towers. This type of compressor is selected for the broad operating range [19], high efficiency [20], long-term reliability (a typical shutdown schedule is every five to seven years) [15, 26], robustness to foreign object damage, and minor performance degradation caused by fouling [1]. However, due to the high investment and operating costs, general hydrocarbon processing plants usually have no redundant main compressors. Therefore, an unforeseen breakdown problem, which can occur, often leads to an immediate total plant shutdown, resulting in production loss, lost business opportunities, and high maintenance costs. The unplanned shutdown interrupts the downstream polymer plants that use the plant's production as raw material [21].

Figure 1.1 shows A train of cracked gas compressors driven by a 52 MW steam turbine at 5,800 RPM to pressurise gas from 1.5 to 42 bar with a 5.5 ton/min mass flow. This compressor train has three compressor units divided by increasing pressure: low pressure, medium pressure, and high pressure.



Figure 1. 1 A train of compressors driven by a steam turbine in a petrochemical plant

In each compressor unit, the multistage shrouded impellers with curved rotating blades transfer kinetic energy to the passing process gas. Figure 1.2 shows the rotor of a centrifugal compressor with four shrouded impellers stacked in tandem inside the opened horizontal split casing. This casing has two compression stages, each of which includes two impellers connected by return channels. Figure 1.3 shows a schematic diagram of the impeller, shaft, and casing as well as the gas flow path. The flow directed by the inlet guide vanes at the centre of the impeller in the axial direction. The impeller accelerates the flow while it is passing through the rotating

blade passages. The flow exits the impeller at the outlet in the tangential direction through the return passage and enters the next stage. The pressure is increased when the flow velocity reduces in the volute connected to the last impeller stage. In the case of a medium-pressure compressor unit, for example, the pressure rises from 2.5 bar to 12.2 bar with a two-stage shrouded impeller.

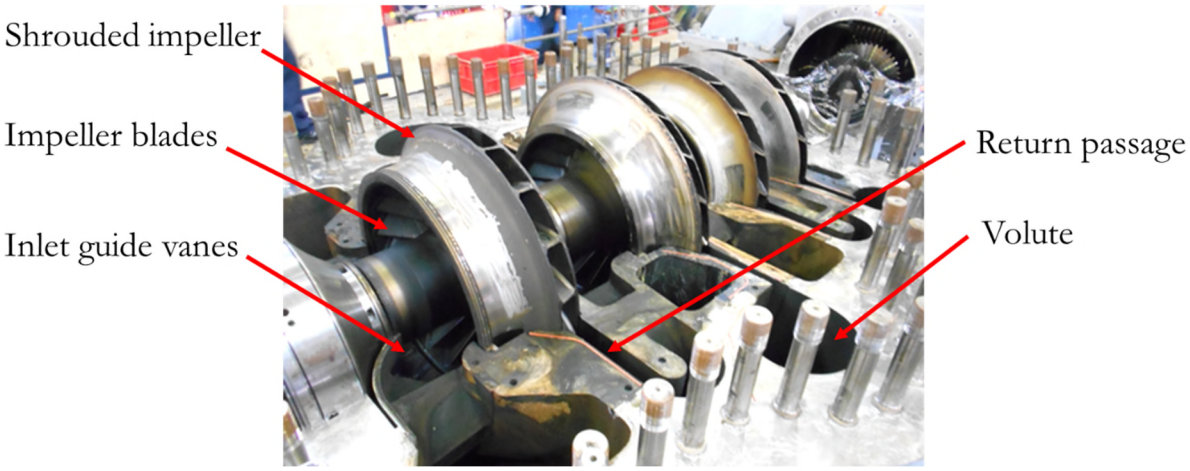


Figure 1. 2 A rotor with four shrouded impellers in tandem arrangement inside the opened horizontal split casing

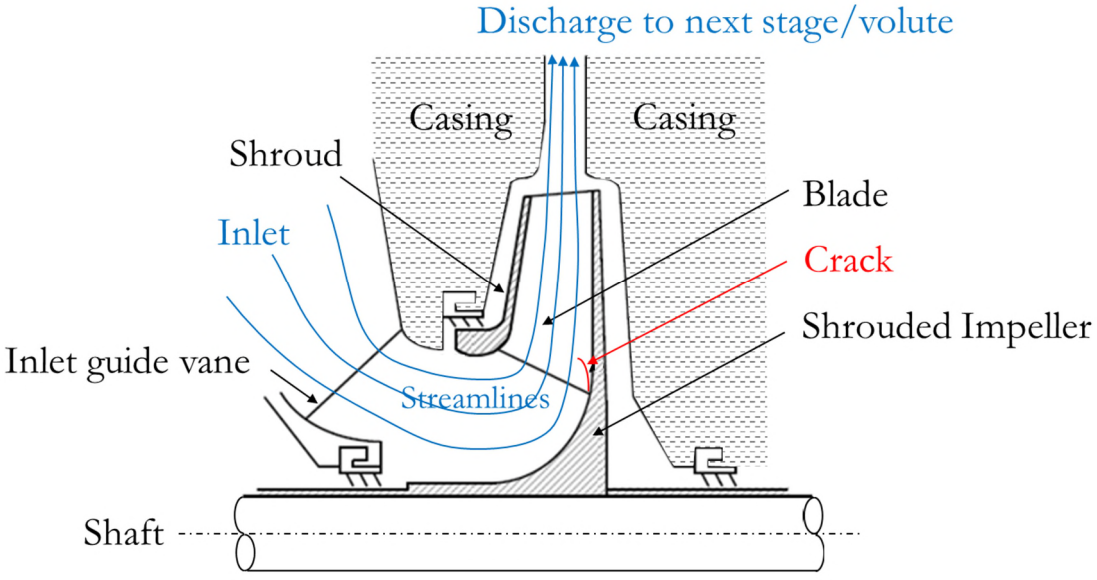
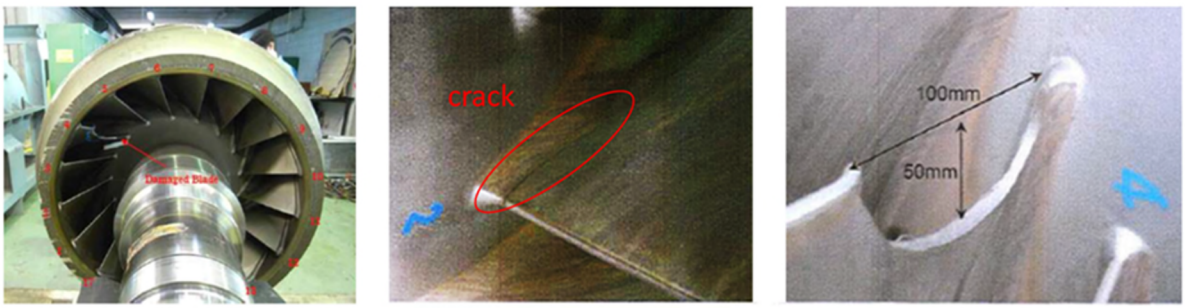


Figure 1. 3 The cross-sectional schematic diagram of the impeller and casing showing a gas flow path

One of the severest compressor breakdowns is associated with an impeller blade crack. Statistical investigation indicates that the blade failure relates to 65 percent of centrifugal compressor malfunctions [10]. High-cycle fatigue has been indicated as the major root cause of blade crack damage [11, 12, 13, 14].

In 2009, for example, a blade damaged incident at a petrochemicals plant in Thailand led to an unplanned total plant shutdown. The combined production loss and maintenance cost was over £2.5 million. An example of a rotor with a damaged blade is shown in Figure 1.4 (a). A visual inspection indicated that the crack started at a blade root near the rotor hub side and propagated through the blade aerofoil, as shown in Figure 1.4 (b). Figure 1.4 (c) shows that the broken blade that caused the radial shaft vibration was over the vibration control limit. The past maintenance record shows that this failure frequently occurred at the first stage of the medium-pressure compressor. From the industrial standard rotor shaft vibration trend shown in Figure 1.5, it can be seen that the overall vibration increased suddenly at the blade-off incident with no previous detection as the crack propagated.



(a) (b) (c)

Figure 1. 4 A shrouded impeller with damaged blades (a) the location of the damaged blade; (b) a cracked impeller blade; (c) the size of the damaged blade

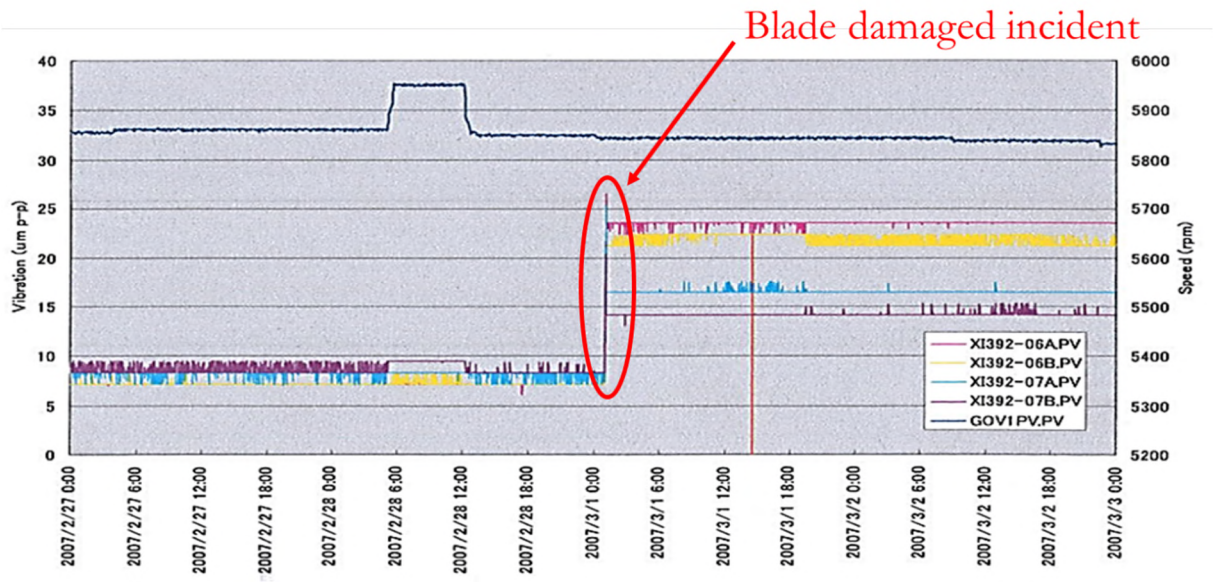


Figure 1. 5 The trend of the radial shaft vibrations and speed of a compressor during the blade damaged incident

As outlined in the previous paragraph, the industrial standard machine protection system does not provide enough advance notice to prevent a blade damage incident. The machine protection system operates by using eddy current sensors to measure the radial shaft vibration monitoring changes in the rotor unbalance force [16]. In the case of an impeller with an early-stage cracked blade, the rotor unbalance force barely changes because the residual unbalance of the impeller does not alter significantly [12]. Thus, the existing system is limited in detecting blade crack failures.

Thus, if there had been a measurement system to determine the blade condition in advance, machine operators could limit the operational loss by smoothly shutting down the machine. In other words, reducing the operational loss would be the main benefit of that system.

Several measurement techniques have been applied to monitor the blade health condition of a centrifugal compressor with a shrouded impeller. The original technique is the dynamic strain measurement using strain gauges attached to blade surfaces [18, 23, 24, 25]. In this technique, measurement systems require a slip ring or wireless data transfer system to transmit signals from a rotating component to a stationary receiver. However, it is impractical to install these complex, vulnerable, short life and costly systems on every blade in both the research/development stage or in-service [3]. Moreover, the aerodynamics and mechanical properties of the blade are disturbed by the strain gauge installation [2].

In addition, conventional blade tip timing systems are not practical because of the structure of the shrouded impellers. From Figure 1.3, it can be seen that the blades' leading edges are located inward, far from the casings. Thus, installing a blade tip timing sensor will interrupt the gas flow path. Besides, sensor performance is another concerning issue, especially the optical blade tip timing sensor which performs poorly in a contaminated environment [4]. These limitations have motivated the present research to focus on developing the blade health monitoring system for shrouded impellers.

1.2 Motivation

A proposed novel method involves linking the blade health condition with the deflection of the rotor shroud, which can be determined through shroud/casing clearance measurement. The idea behind this method was underpinned by the Finite Element Analysis (FEA) studies of the actual size impeller with and without a cracked blade.

These studies were conducted with a perfectly balanced rotor with no fluid interaction assumptions using the Static Structural Analysis module in ANSYS®. Figure 1.6 shows the created simulation models and results. The actual crack path in Figure 1.4 (c) was used for reference. The crack on the cracked blade model was set halfway through the actual crack path (90-degree crack).

The simulation results predict that the impeller shroud deflection relates to the blade's condition, as shown in Figures 1.6 (c) and (d). In particular, the highest deflection of the shroud occurs near the area connected to the cracked blade. Figure 1.7 shows the distinction of the radial shroud deflection between the healthy impeller and the impeller with the cracked blade number 9. The deflection range is around 0.6 mm to 0.65 mm, with the most significant difference around 0.03 mm at the area connected with the cracked blade. The deflection is directly related to the change in the clearance between the outer shroud surface and the compressor casing.

An eddy current sensor mounted to the compressor casing could be used to identify this change in deflection by measuring clearance between the sensor and impeller shroud [3, 6]. Unlike the capacitance sensors, which are susceptible to the effects of ionised particles within the flow field such as oil, dust and rub particles [5], eddy current sensors are considered more appropriate for this application due to the high immunity to non-metallic contamination and the ability to measure clearance to micron accuracy [6]. Ionised particles entering the field of the probe may cause fluctuations in the clearance signal, which may in turn affect the health monitoring system.

The intensive literature review in Chapter 2 indicates that using shroud/casing clearance measurement to monitor the blade condition of the shrouded impellers is a novel method. Previously, this type of approach has not been patented, commercially developed, or presented in the open literature.

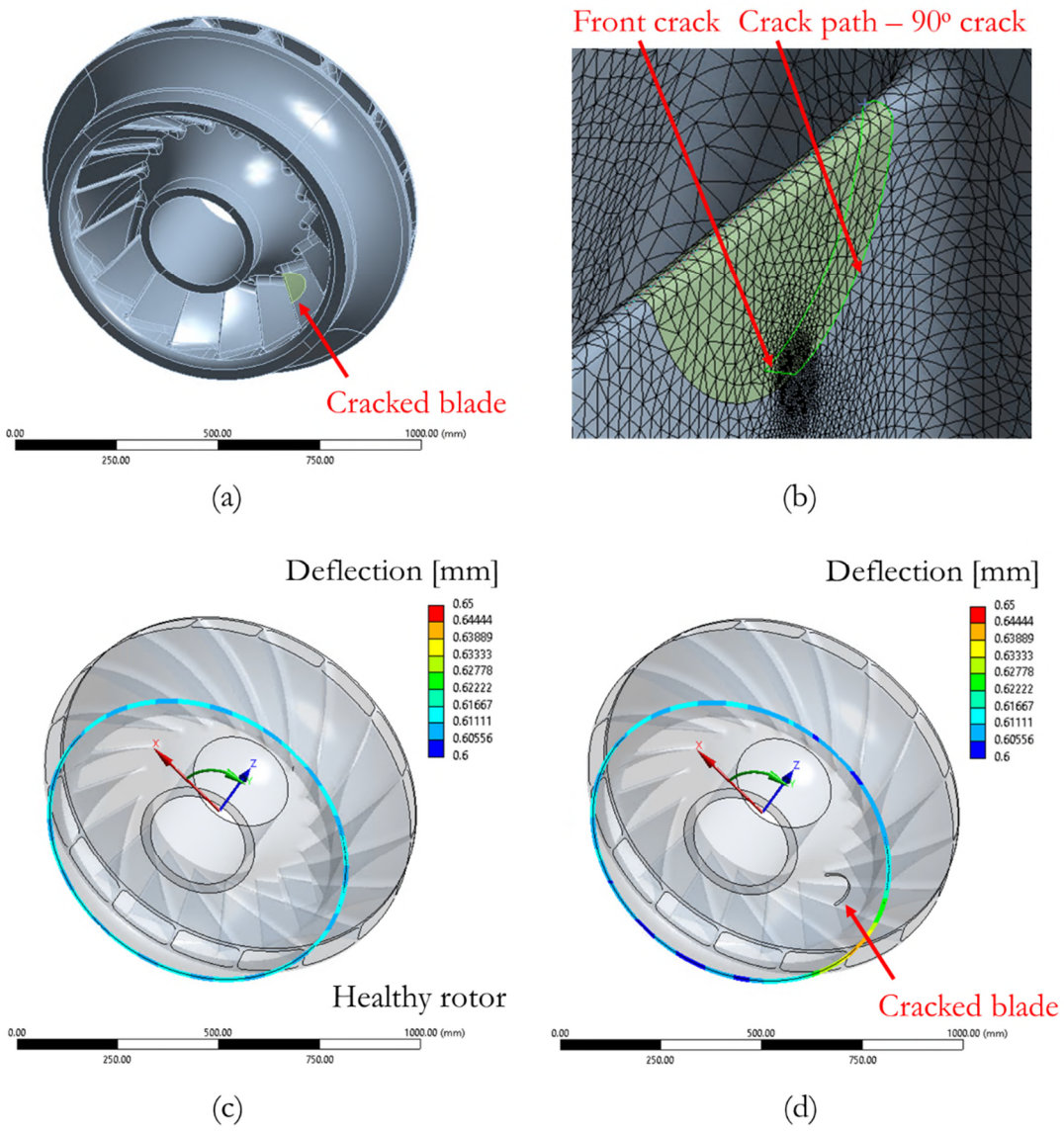


Figure 1. 6 Finite element model of the impeller (a) the location of the cracked blade; (b) the crack path; (c) the deflection of the inlet shroud of the healthy impeller; (d) the deflection of the inlet shroud of the impeller with a cracked blade

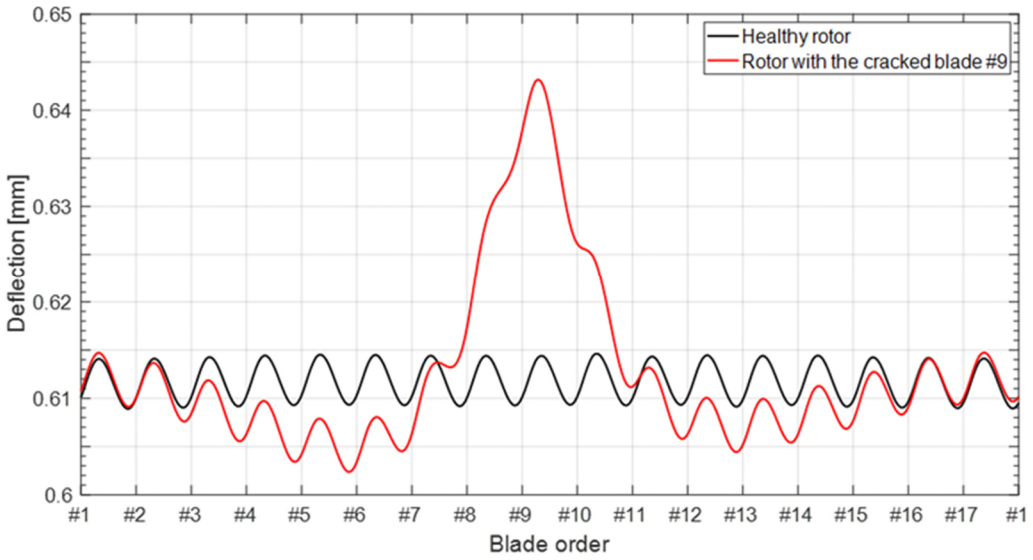


Figure 1. 7 Comparison between the deflection of the healthy impeller and the impeller with the cracked blade number 9

1.3 Research Aims and Objectives

This research aims to examine the relationship between the blade health condition and the deflection of the impeller outer shroud, which can be determined through the change of shroud/casing clearance. The influence of various impeller designs and blade conditions was investigated by combining experimental, computational (FEA and CFD), and theoretical studies. A research schematic is shown in Figure 1.8.

The following objectives were established to achieve the research aim:

- Qualify the use of shroud/casing clearance measurement to determine the condition of impeller blades
- Determine the relationship between the blade crack growth rate and the shroud/casing clearance

- Evaluate the limitation of the proposed system in terms of detection capability – for example, the minimum crack size that can be detected or the effect of various impeller designs
- Determine the optimisation criteria for sensor design for monitoring the blade condition of a shrouded impeller, i.e., size, shape, and driving frequency
- Propose an optimised blade health monitoring system for an actual-sized impeller in terms of the number of sensors and positions.

The knowledge obtained from achieving these objectives was expected to facilitate the development of a blade health monitoring system for shrouded impellers on an industrial scale. In addition, this research is expected to pave the way for future investigations of the behaviour of operating shrouded impellers, for which studies are limited.

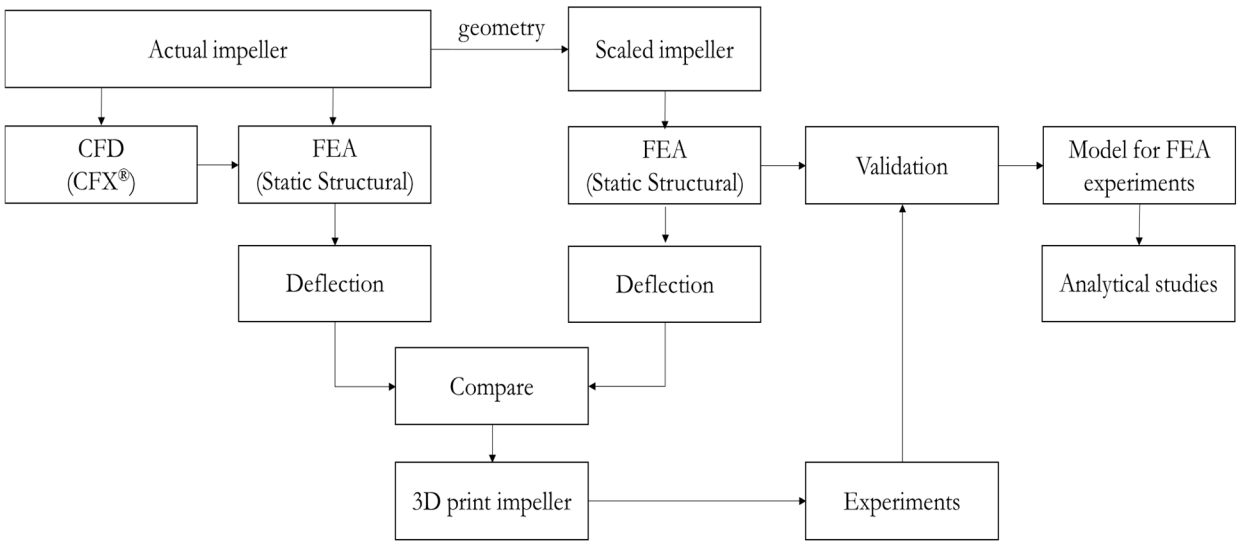


Figure 1. 8 The investigation research schematic

1.4 Thesis Outline

The thesis is organised into the following chapters:

Chapter 2 provides an overview of published literature related to this research. The literature review is categorised into four aspects, including 1) centrifugal compressors with shrouded impellers, 2) causes of impeller blade cracks, 3) the typical blade health monitoring methods, and 4) the principle of eddy current sensor and its application in clearance measurement.

Chapter 3 details testing facilities and instrumentations used in the experimental studies. The sensor calibration and signal processing are also explained.

Chapter 4 performs the computational electromagnetic simulation to investigate the response and range of a rectangular-shaped magnetic flux eddy current sensor used in the experimental studies.

Chapter 5 presents experimental results from the preliminary experiment. The experimental results validated the feasibility of crack detection using the shroud/casing clearance measurement.

Chapter 6 presents experimental results from the main experiment. The relationship between the condition of the blades and the rotor shroud deflection was determined. The experimental results indicate the limitations of crack detection using the proposed system.

Chapter 7 presents the numerical studies of the scaled impeller. The parametric studies were carried out to investigate the influence of different impeller design parameters on the shroud deflection.

Chapter 8 presents numerical studies of a full-scaled impeller with various blade conditions to predict the changes to the shroud deflection. The Computational Fluid Dynamics (CFD) analysis was conducted to determine the effect of passing fluid.

Chapter 9 provides a conclusion and recommendations for future work.

Chapter 2

Literature Review

2.1 Introduction

The objective of this chapter is to contextualise the current study by reviewing the principal concept and relevant research in the published literature. This review is divided into four sections. Section 2.2 covers the principle of centrifugal compressors with shrouded impellers, including design, operating range, and applications. Section 2.3 addresses the cause of blade crack damage, the mechanism of crack, and the currently proposed crack detection methods. In section 2.4, typical blade monitoring methods are addressed, discussing the principles of a strain gauge, blade tip timing, and blade tip clearance and their applications. In addition, the advantages and disadvantages of various types of sensors for non-intrusive blade health monitoring are presented. Finally, section 2.5 discusses the principles of eddy current sensors and associated electronics systems as well as their application in clearance measurement.

2.2 Centrifugal gas compressors with shrouded impellers

Centrifugal compressors or radial compressors are rotating machines that transfer kinetic energy to process gas using impellers. The centrifugal compressors have a broad range of applications, depending on the type of process gas, flow rate, inlet pressure, and target build-up pressure. These variations lead to impeller sizes, rotational speed, number of stages, and power consumption. The impeller size, which depends on the suction flow rate, can vary from 200 mm to 1800 mm [46]. For petrochemical processes, the typical size of centrifugal compressors for this gas transmission application is around 3.7 MW to 15 MW, with the operating speed range between 8,000 RPM to 14,000 RPM [43].

2.2.1 Dynamic similarity of centrifugal compressors

In order to compare the performance of centrifugal compressors with different designs, the non-dimensional parameters are proposed based on dimensional analysis. The often cited definitions of non-dimensional parameters, in the centrifugal compressor field, are given below:

Head coefficient

Head coefficient (ψ) represents the increasing of the compression work to the specific kinetic energy of the gas. The head coefficient is commonly defined as the ratio of the head (ΔP) to the inlet density, rotational speed, and impeller diameter,

$$\psi = \Delta P/(\rho_1 N^2 D^2). \quad (2.1)$$

Unlike axial flow compressors or turbines that the flow coefficient is the ratio of axial flow velocity to the blade rotating speed, for centrifugal compressor the flow coefficient (φ) is defined differently as

$$\varphi = \dot{m}/(\rho_1 N {D_2}^3) \tag{2.2}$$

with $\dot{m}$ being the mass flow rate, ρ_1 the typical gas inlet density, N impeller rotational speed and D_2 impeller outlet diameter. In general, centrifugal compressors with radial impellers are designed to operate within a certain range of flow coefficient between 0.01 to 0.16 [45], as shown in Figure 2.1.

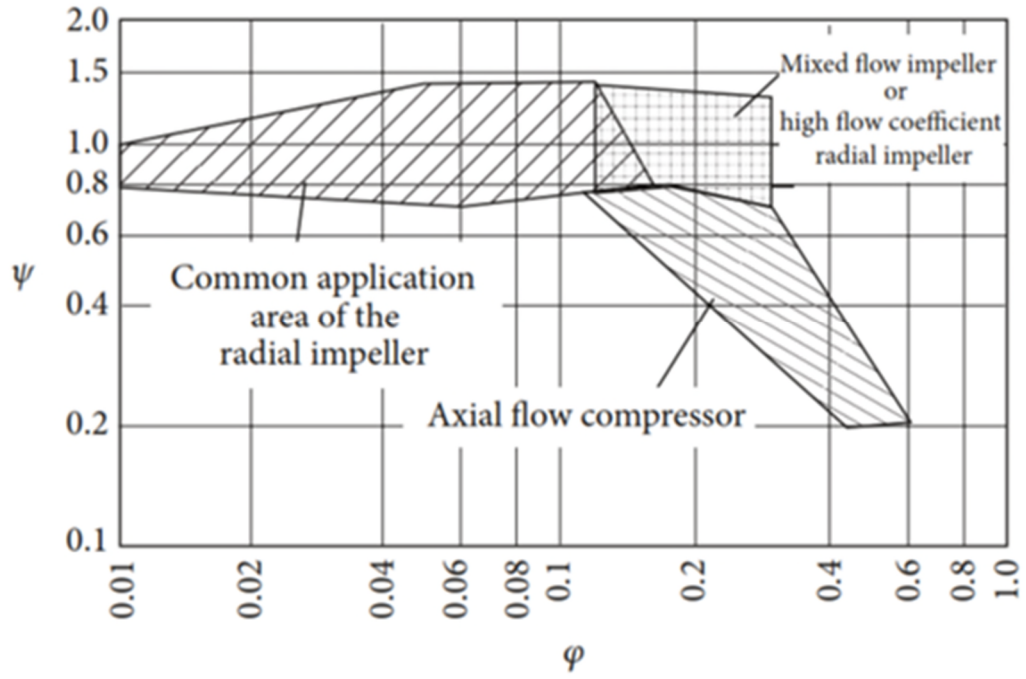


Figure 2. 1 Application areas of the various types of industrial compressors in terms of the relation between the head coefficient and the flow coefficient [45]

Specific speed

Specific speed (N_s) is defined as the ratio of head coefficient to flow coefficient,

$$N_s = \frac{\varphi^{1/2}}{\psi^{3/4}} = \frac{\dot{m}^{1/2}\rho^{1/4}N}{\Delta P^{3/4}}. \quad (2.3)$$

For single-stage centrifugal compressors, the specific speed has a definite limit between 0.3 and 2. It is impractical to design a radial compressor under or over this range [60].

Compression ratio

Compression ratio (CR) or pressure ratio is defined as the absolute discharge pressure to the absolute suction pressure,

$$CR = \frac{P_2}{P_1}. \quad (2.4)$$

Single-stage centrifugal compressors have a relatively low compression ratio, typically less than 2. For each compressor, the compression ratio depends not only on the design but also on the specific gravity of the process gas. For example, a single-stage centrifugal compressor designed to be operated with natural gas has a pressure ratio of 1.4. If this compressor was operated with air (lower specific gravity), it would provide a pressure ratio of around 1.6 [62].

Isentropic efficiency

Efficiency of a centrifugal compressor can be variously defined depending on topics of interest or applications [42]. One of the most commonly used definition is based on the adiabatic efficiency (also known as isentropic efficiency), which is defined as the ratio of actual compression work to the compression work used in the ideal isentropic compression process with no heat transfer. When considering the

process gas as a perfect gas, the adiabatic efficiency can be defined in terms of total pressure and temperature as

$$\eta_c = \frac{(P_2/P_1)^{(\gamma-1)/\gamma}-1}{(T_2/T_1)-1}. \quad (2.5)$$

where γ is the specific heat ratio ($\gamma = C_p/C_v$).

In general, a centrifugal compressor has an efficiency of between 60 – 80%, which is lower than that of an axial compressor operating at the same pressure ratio and mass flow rate [1]. Figure 2.2 shows the comparison of efficiency and losses to flow coefficient, as affected by the impeller design. A compressor with a low flow coefficient tends to have low efficiency because its impeller has narrow flow channels. Consequently, the internal friction losses are increased. This requires the amount of work input to overcome the friction losses [63].

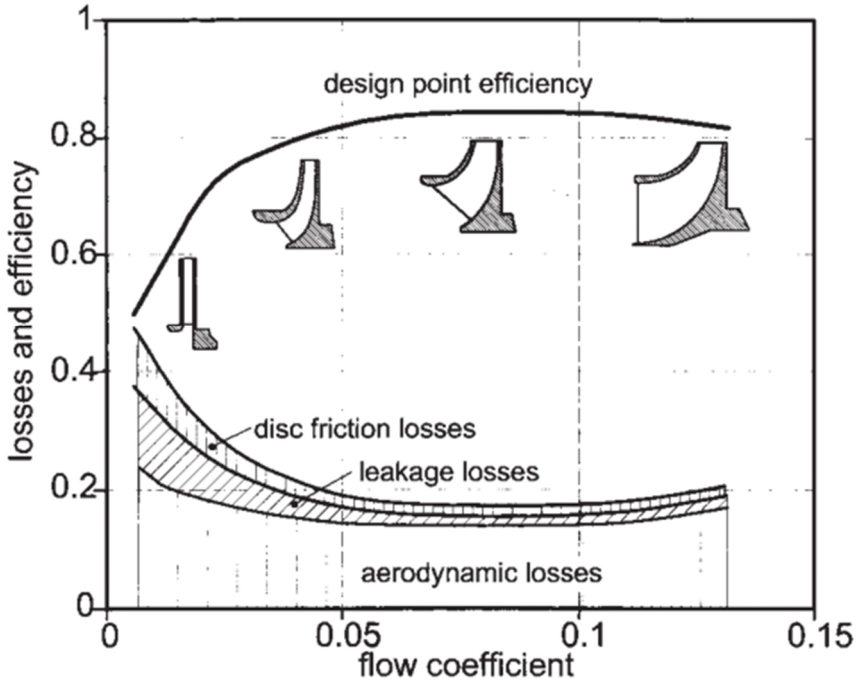


Figure 2. 2 Comparison of efficiency and losses to flow coefficient, as affected by the impeller design [71]

Polytropic efficiency

The polytropic efficiency (η_p) is the ratio of the actual work done during the polytropic process to work done along a polytropic path in the reversible adiabatic process (isentropic process) [60]. For an actual compressor, the polytropic efficiency can be determined from pressure and temperature measurements with the following equation,

$$\eta_p = \frac{k-1}{k}\frac{\ln(P_2/P_1)}{\ln(T_2/T_1)}. \quad (2.6)$$

Notably, the value of polytropic efficiency of a compressor used in Chapter 7 Proposed Blade Crack Detection System was referred to a datasheet given by machine OEM.

Polytropic head

The polytropic head of a centrifugal compressor represents the amount of energy added to the fluid as it flows through the compressor. It represents the work done to increase the fluid's pressure and temperature. The polytropic head is an essential criterion for evaluating the performance of centrifugal compressors [60]. The polytropic head of a compressor is defined as

$$H_p = \frac{Z_{avg}RT_1}{MW}\left(\frac{n}{n-1}\right)\left[\left(\frac{P_2}{P_1}\right)^{\frac{n-1}{n}} - 1\right] \quad (2.7)$$

where P_2/P_1 are discharge to suction pressure ratio. The inlet and outlet pressures were measured by pressure transducers installed at the inlet and the discharge channel, respectively. The polytropic exponent index, n, represents the relationship between the gas pressure and volume during gas expansion or compression in a

polytropic process ($pV^n = constant$). The polytropic exponent index n can be calculated with the following equation,

$$n = \frac{k\,\eta_p}{k\,\eta_p - (k-1)} \tag{2.8}$$

where k and η_p are the ratios of specific heats and the compressor polytropic efficiency, respectively.

2.2.2 Shrouded impellers

The shrouded or closed impellers are classified as a subcategory of radial impellers. This impeller design has a curved disk or "shroud" covering blades along the camber line. Thus, the blades are located between the shroud and the back-end wall. Figure 2.3 shows a cross-sectional diagram of a shrouded impeller with its terminology.

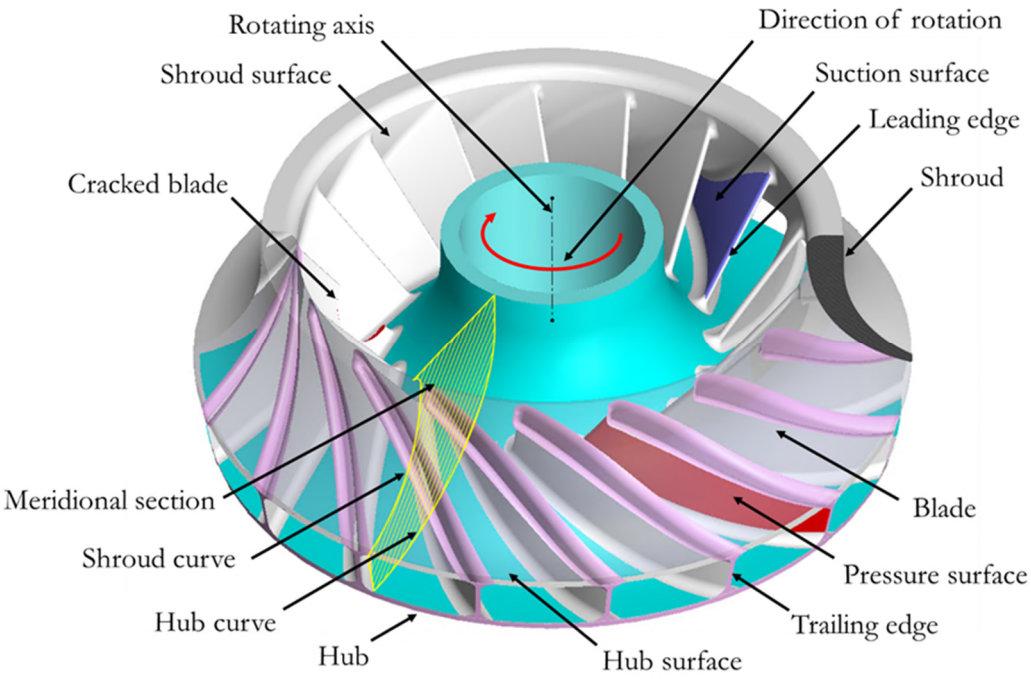


Figure 2. 3 Typical cross-sectional diagram of a shrouded impeller (adapted from Zhou et al. (2020) [41])

This shrouded impeller design is typically used in multi-stage centrifugal compressors, in which axial movement is significant due to the internal assembly tolerance, and a long distance between impellers and a thrust bearing [61]. Therefore, the connecting shroud maintains the compressor's performance during changing axial movement. On the contrary, since the performance of an unshrouded impeller relies on the blade tip clearance, potential losses in performance caused by tip leakage flow are more likely [15, 42].

In addition, the added mass of a shroud increases the impeller stress, which is related proportionally to peripheral speed. Thus, the peripheral speed of a shrouded impeller is usually lower than that of an unshrouded impeller. For example, an unshrouded steel impeller can be operated at a maximum tip speed of 430 m/s, while the tip speed of a shrouded steel impeller is limited to around 360 m/s [42]. Therefore, the shrouded impellers are suitable for low impeller stress applications such as in low-pressure ratio stages of process gas compressors.

The main drawback of shrouded impellers is their complicated design and manufacturing. Two manufacturing methods are widely used to construct high-performance shrouded impellers employed in process gas industries. The first, and perhaps most typical method, is welding or blazing, where the pre-fabricated curve blades are welded to the shroud and hub. The structural integrity of the welded joints is crucial during the design and manufacturing processes. The disadvantage

of this construction method is that the welds in the passages might affect the flow. [1]. The second method uses a five-axis milling machine to fabricate a one-piece shrouded impeller from a billet. The high flow coefficient impellers are preferable because the large flow path allows for tool accessibility [73]. However, to produce a machinable design that can achieve a target performance, this milling method is considered costly and time-consuming [70].

2.3 Blade crack studies

Impeller blade damage is among the most severe breakdowns in industrial centrifugal compressors. Li et al. (2013) [10] reported that based on statistical data blade-related failures statistically account for 65 percent of compressor malfunctions. Surprisingly, few studies have been published on the subject of blade crack, or shrouded impeller blade cracks. Figure 2.4 shows an example of an impeller with a blade crack failure.



Figure 2. 4 Shrouded impeller blade damage a) cracked blade at leading edge b) an impeller with broken blades [56]

2.3.1 Blade crack studies

Several studies have similarly concluded that fluid-induced (or wake-induced) fatigue is the primary source of shrouded impeller blade crack damage [11]. This high cycle fatigue causes blade cack propagation, which thus leads to blade fracture [58].

Higashio et al. (2010) [25] reported that the impeller resonance could be stimulated by the wakes generated from inlet guide vanes (IGV). In their study, the unsteady CFD analysis was performed to calculate the unsteady excitation force in term of pressure fluctuation that causes the vibrational stress on the blades of a shrouded impeller. The simulation result indicated that the source of pressure fluctuation is the wakes of the upstream inlet guide vanes. The significant stress fluctuation occurred when the impeller resonance was found, in which the harmonics of pressure fluctuation match or are close to the natural frequencies of the impeller. In this case, the harmonics of pressure fluctuation are equal to the number of inlet guide vanes or the number of inlet guide vane minus one.

Similarly, White et al. (2011) [56] conducted a Root Cause Failure Analysis (RCFA) on repeated impeller blade crack failures in a five-stage propane compressor. Based on the design information, operating evidence, and analysis results, the researchers indicated that the main root cause was the vane wake excitation that induced the high cycle fatigue on the impeller blades. This vane wake excitation might be

intensified by the deposit carry over and off-design operation. The redesigned vane was proposed to shift the vane excitation harmonics from the blade resonant frequencies. However, it was not possible to eliminate the vane excitation harmonics. A polymer build-up over operating time increased the mass of blades, resulting in changing blade resonant frequencies. Thus, the blade modal excitation can still be present.

Kowshik et al. (2012) [78] conducted experiments and CFD analysis to investigate the cause of the rotating instability in a centrifugal blower with a shrouded impeller operating close to the instability limit (surge condition). According to the study, the instability is governed by the interaction between the discharge flow and the unsteady vortices travelling along the impeller's perimeter. However, the paper did not address the instability effect on the blade structural integrity.

The characteristic of the internal flow field of a radial impeller with crack damage was determined in a numerical study by Liang et al. (2021) [51]. The study results show that the occurrence of cracks disturbs the internal flow inside the impeller passage, reducing the internal flow performance. The maximum stress which appeared in the middle section and at the trailing edge of the crack can lead to further crack propagation.

2.3.2 Cracked blade modelling

Compared to a number of studies on the effects of a crack on a radial aerofoil blade widely used in axial compressors and gas turbines (e.g., Witoś (2013) [74], Madhavan et al. (2014) [75], and Zeng et al. (2019) [76]), studies on the dynamic response of a

shrouded impeller with a cracked blade is limited. Most comparable is the study about the dynamic response of a bladed disk, which has a shroud connecting adjacent blades.

In order to understand the effect of a cracked blade on the dynamic response of a bladed disk system, a simplified lumped-parameter model was widely used [48, 49, 50, 52, 53]. In this model, the dynamic of each blade is represented by a single-degree-of-freedom with equivalent mass connected with equivalent stiffness and damping. Between two adjacent blades, the equivalent coupling stiffness is added between two masses to represent blade-disk stiffness. Figure 2.5 shows the impeller model with a cracked blade.

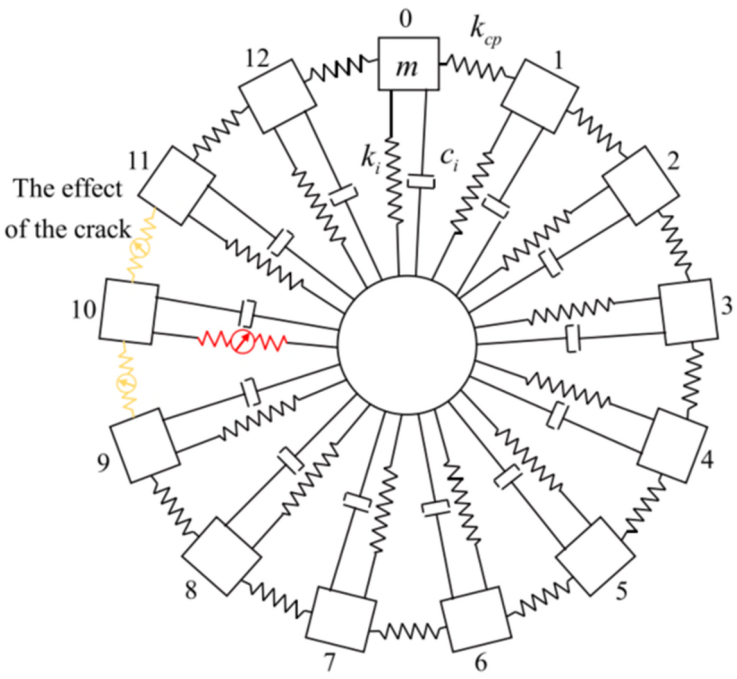


Figure 2. 5 A simplified lumped-parameter model of an impeller with a cracked blade [49]

According to the study by Hou in 2006 [47], the mechanisms of crack-induced mistuning in a blade-disk system was determined using a lumped-mass model. A cracked blade was modelled as a beam with a crack at the blade root. The characteristics of the bladed disk were examined by varying the crack depths and the ratio of blade stiffness to blade-disk coupling stiffness (coupling ratio). The results confirmed the expectation that the crack reduced local blade stiffness, reducing the blade natural frequency. Nonetheless, the decrease in frequency can be observed once the crack reaches a certain size, which is around 25% of blade width in the case of weak and moderate coupling systems. This detectable crack size increases to 75% of blade width in the case of a strong coupling system. Hence, Hou suggested that the blade crack detection system that monitors blade frequencies may not be adequate for early crack detection.

Wang and Sui (2015) [54] proposed a simplified two-dimensional model based on fracture mechanics for predicting the fatigue crack propagation life on a centrifugal compressor with a shrouded impeller. The stress intensity factor mode I (tensile mode) and mode II (in-plan shear) were calculated as a function of crack length.

In an article by Jinlong et al. (2020) [13], the fatigue life prediction model of a cracked blade of a shrouded impeller was proposed. This prediction model was developed from the fatigue theory by combining the non-linear correlation between the mean stress and the fatigue crack from FEA results with the fatigue limit from the fatigue test.

2.4 Typical blade health monitoring methods

Various techniques were proposed for monitoring blade conditions to detect blade damage in an early stage, including rubbing, crack, or foreign object damage (FOD). Most of the techniques focus on monitoring open or semi-open impellers such as axial compressors and turbines or unshrouded centrifugal compressors with reachable blade tips. Some of these promising techniques have been discussed below.

2.4.1 Strain gauge

Strain gauge measurement is an original method for measuring blade stress. Strain gauges operate on the basis that the electrical conductance of material varies in proportion to the change in geometry [39]. Thus, when the strain gauge is deformed (change in stain) by an applied stress, the resistance of the gauge changes. The Wheatstone Bridge circuit is commonly used to convert the small change in gauge resistance into the output voltage. Through this method, the force, pressure, or vibration at the surface of a test specimen can be measured by attaching a strain gauge. Figure 2.6 shows the working diagram of the strain gauge configured in the Wheatstone bridge circuit.

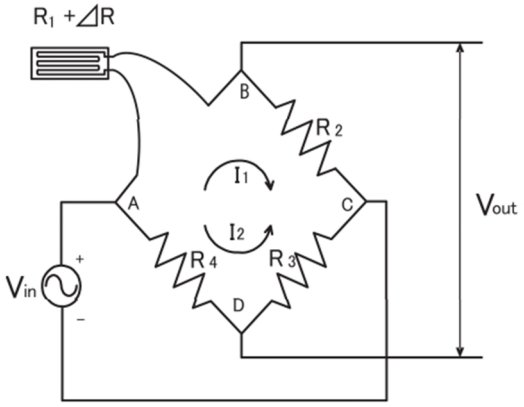


Figure 2. 6 The strain gauge configured in the Wheatstone bridge circuit [39]

Applying strain gauges to measure the dynamic stress of an operating machine is not convenient. This measurement technique requires a slip ring or wireless data transfer system, such as a telemetry system, to transmit the strain signal to a data acquisition module in the stationary component. For this reason, these complex, vulnerable, short-life, and costly systems cannot practically be installed on every blade in both the research/development stage and in-service [6]. Moreover, the aerodynamics and mechanical properties of the blade are disturbed by the strain gauge installation [7]. These have led to the development of non-intrusive monitoring techniques.

In an article by Itawa et al. in 2017 [34], strain gauges were used to measure the blade dynamic stress of a compressor during operation. The dynamic blade stress results were used to validate the proposed dynamic blade stress estimation method, which combined blade vibration measurement and finite element modal analysis. The blade vibration data were obtained by using optical blade tip timing sensors. The results of both methods were consistent. However, the researchers mentioned

that blade tip timing was less difficult to implement than strain gauges. Figure 2.7 shows the affixed strain gauges on a semi-open impeller's blade suction surfaces.

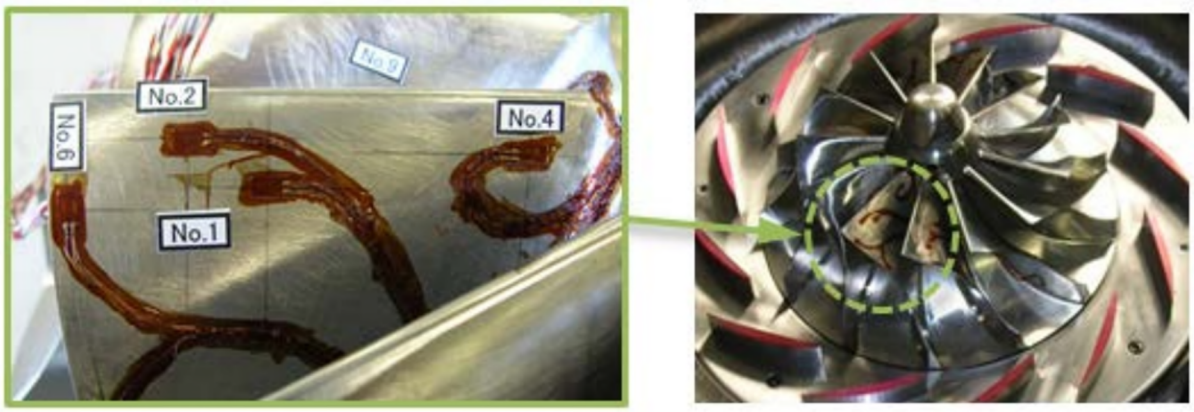


Figure 2. 7 Attached stain gauges on the impeller [34]

2.4.2 Blade Tip Timing

One of the promising non-intrusive monitoring techniques is blade tip-timing (BTT), where non-contact blade tip sensors (e.g., optical, microwave, inductive, capacitive or eddy current sensors) are attached circumferentially in the casing to measure the blade tip deflection, as shown in Figure 2.8 [35]. Through this configuration, all blades can be measured in real time by using one to six sensors. The common principle of blade tip-timing measurement is to use the response of the sensor to detect the appearance or absence of a passing blade. As for optical sensors, the response is the back-scatter light of the laser beam which focuses on the passing blade tip. Figure 2.9 shows the schematic diagram of the optical blade tip-timing system [9]. The term "Time of Arrival" (TOA) is defined as the time difference between each blade passing the sensor. The time of arrival of each blade depends on the rotational speed and blade deflection, as shown in Figure 2.10 [36]. The deflection of the blade is caused by the amplitudes and frequencies of the

vibration. The non-vibrating blade is used as a reference in the expected TOA calculation, equal to the number of blades divided by the shaft speed. The vibration of the blade causes a change in blade tip position. Thus, the tip of the blade passes a sensor before or after the reference. The blade deflection (x) is calculated by the difference between the measured TOA and the expected TOA (Δt) as:

$$x = \Delta t \Omega R \tag{2.9}$$

where R is the blade mean radius and Ω is the rotational speed of the rotor.

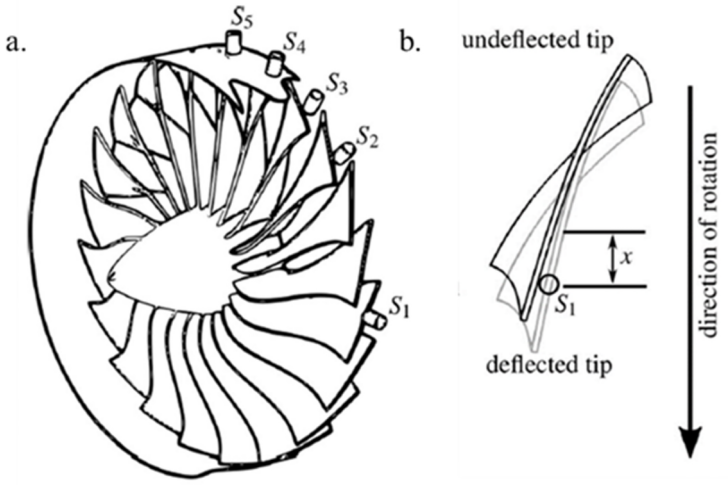


Figure 2. 8 Blade tip timing installation [35]

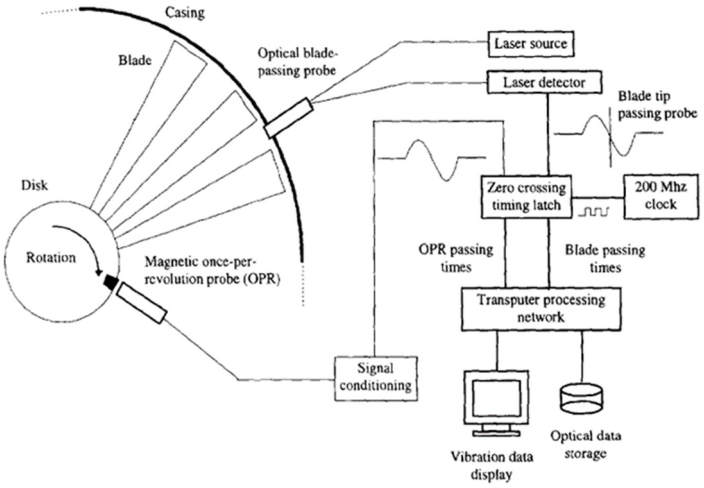


Figure 2. 9 Schematic diagram of optical blade tip timing [9]

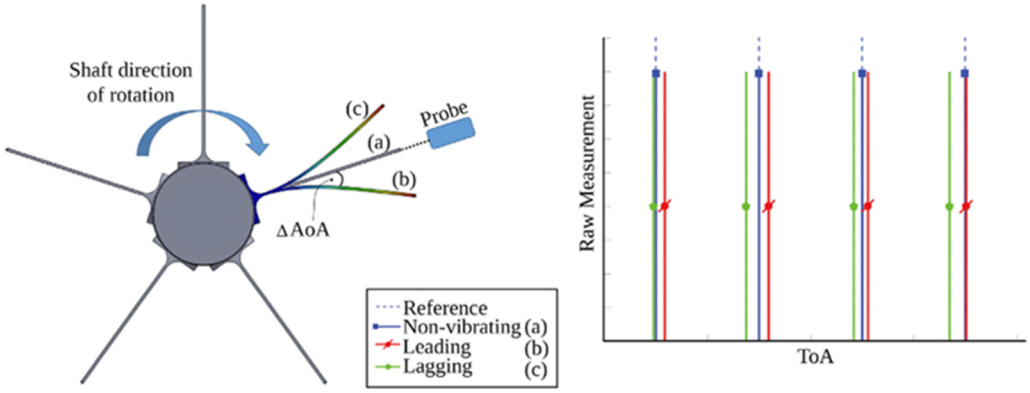


Figure 2. 10 Non-vibrating blade (a) compared with vibrating blades (b and c) and the measured Time of Arrival (TOA) [36]

The health of the blade and rotor can be evaluated by analysing the pattern of the time of arrival. Pattern differences can be used to distinguish characteristics that influence the blade vibration due to thermal expansion, synchronisation with the rotational shaft speed (e.g., rotor imbalance), or presence in a non-synchronous signal (e.g., crack growth or blade vibration) [6].

Blade tip-timing data analysis can be carried out via indirect and direct methods [40]. Indirect methods involve using only one or two sensors to collect blade tip-timing data during the transient conditions (acceleration or deceleration). During that period, the change in the running speed excites the resonances of rotor components, especially the rotor and blades, which results in the amplitude and frequency of blade resonance. This standard method is referred to as the "Single Parameter method" which was proposed by Zablotsky and Korostelev in 1970 [57]. Another indirect method for obtaining synchronous vibration proposed by Heath and Imregun in 1998 is called "Two-Parameter Plot method" or 2PP [55]. This method uses two sensors mounted with different angles, θ_a and θ_b, in the same

axial position on the casing. By assuming that the blade vibrates in harmonic motion with a single degree of freedom for a given engine order, the amplitude $A(\omega)$ and phase $\varphi(\omega)$of blade vibration derived from two blade tip displacement signals (x_a and x_b) are presented as:

$$x_a = A(\omega)\sin\big(EO\theta_a + \varphi(\omega)\big) + D \tag{2.10}$$

$$x_b = A(\omega)\sin(EO\theta_a + \varphi(\omega) + EO(\theta_b - \theta_a)) + D \tag{2.11}$$

where EO is the engine order, D is the constant offset.

Direct methods, on the other hand, typically use at least six sensors to collect data during steady speed conditions. The displacement vibration of blades at a specific engine order is computed by using a least-square sine fit of the data [64]. The amplitude and phase at each rotational speed is thus obtained. The number of sensors (N) relates to the number of vibration modes that can be measured simultaneously as:

$$N = 2m + 2 \tag{2.12}$$

where m is the number of vibration modes of the blade [72]. Figure 2.11 shows the signals of one passing blade measured by four sensors installed at different positions. The signals represent the blade vibration waveform (original amplitude).

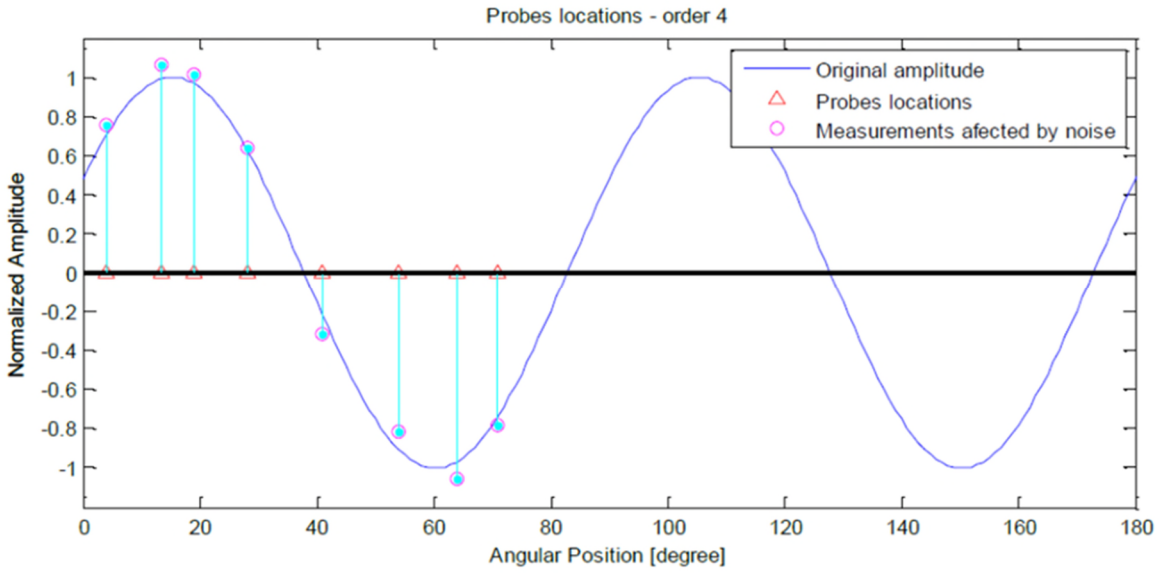


Figure 2. 11 Number of sensors and the obtained results [4]

In an article by Battiato et al. (2017) [81], the beam shutter blade tip timing system was configured with a shrouded blade disk to measure the blade dynamical behaviour – vibration. This system used a sender/receiver embedded laser sensor with a reflective tape attached onto the stationary surface underneath the rotating disk, as shown in Figure 2.12. During the disk spinning, the passing blade functions as a shutter, obstructing the returning beam through the sensor. The delayed times of the absent signal were converted to the Time of Arrival (TOA) and blade vibration, respectively.

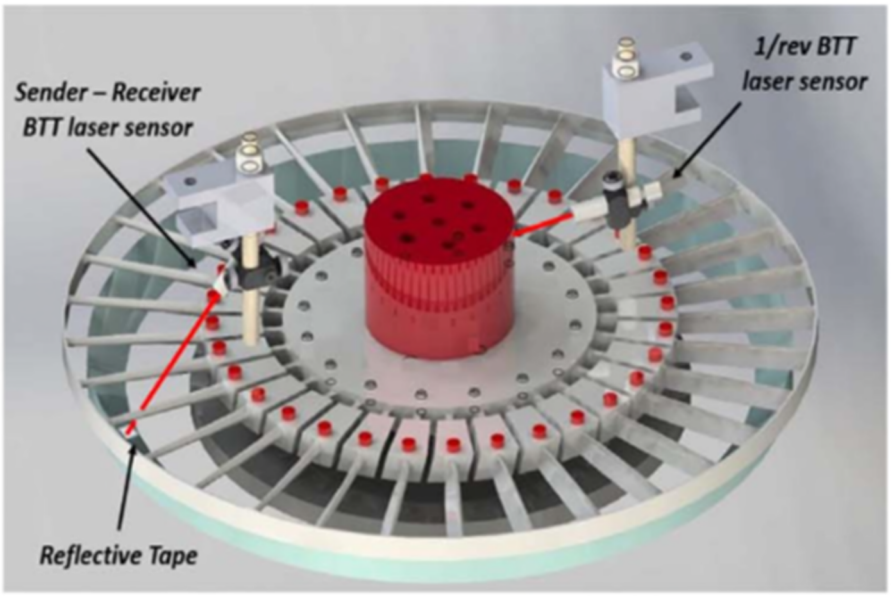


Figure 2. 12 The configuration of an optical blade tip timing sensor and reflective tape on a shrouded blade disk [81]

However, the proposed blade tip timing system with beam shutter technique is impractical to deploy in centrifugal compressors with shrouded impellers. Due to the design of the shrouded impeller with curved blades located inward between the shroud and the back-end-wall, there is no place to attach the reflective tape. Besides, the contaminated environment decreases the efficiency of the optical sensor.

2.4.3 Blade tip clearance

Like blade tip timing, blade tip clearance (BTC) is also a non-intrusive monitoring technique. It provides data on blade health monitoring and performance optimisation as part of an active clearance control system [66, 67, 68]. Instead of measuring blade tip arrival time, blade tip clearance measures the relative clearance between the tip of a rotating blade and a stationary casing, as shown in Figure 2.13 (a). In gas turbine engines, this clearance is called "Tip clearance". The tip clearance

of the vibrating blade is dependent on amplitude and frequency of the vibration in addition to the rotational speed. A schematic of the sensor installation is shown in Figure 2.13 (b).

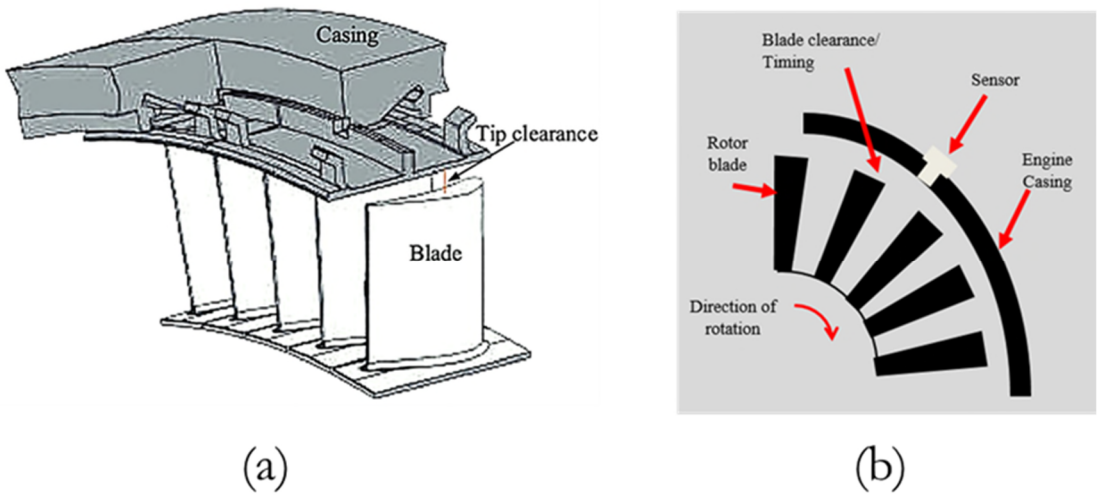


Figure 2. 13 Blade tip clearance measurement techniques (a) tip clearance of an axial gas turbine [59]; (b) shematic of blade tip clearance sensor installation [6]

Eddy current and capacitance sensors are examples of sensors that can be utilised for both blade tip clearance and blade tip timing measurements because both parameters are contained in the measured signal, as shown in Figure 2.14. However, both parameters require different data processing techniques. While blade tip timing measures the time of arrival between the peaks of the signals, blade tip timing measures the changing of the peak amplitude which relates to the tip clearance.

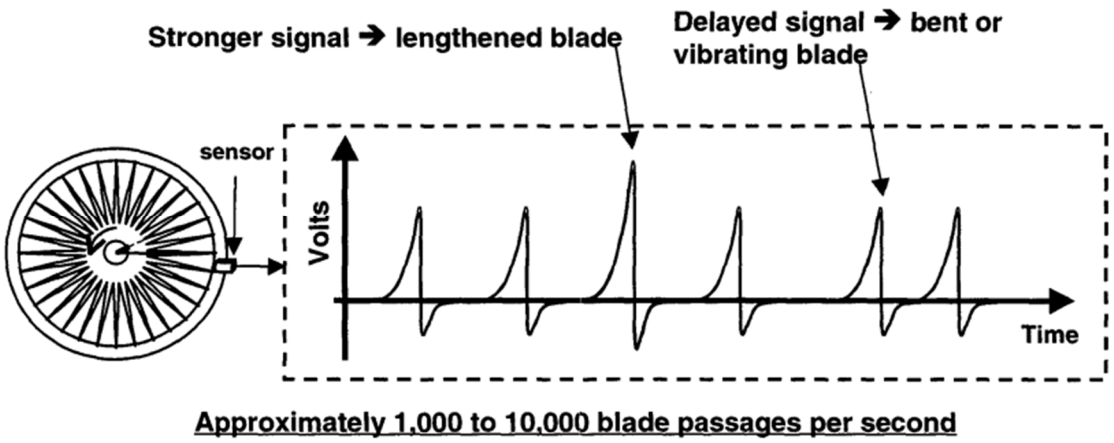


Figure 2. 14 A blade tip sensor permits the monitoring of blade tip clearance and the time of arrival [6]

The work of Sheard (2011) [5] shows that a frequency-modulated capacitance tip clearance measurement system is capable of making precise blade by blade tip clearance measurement. The measurement accuracy was inversely proportional to the distance between the blade tip and the sensor. The accuracy of 10 μm is achievable when the target is in the 1 mm sensor range.

In 2017, Sridhar and Chana [7] demonstrates the performance of their modified high temperature eddy current sensors in an extreme environment. The test was performed in the actual gas turbine engine with the speed up to 68,000 RPM. The tip clearance results indicated that the high temperature sensors were able to function accurately at 1400 ^{o}C without the requirement of a cooling system.

Although, the blade tip clearance measurement is a proven technique for blade monitoring of compressors and gas turbines. This technique is not suitable to implement in shrouded impellers due to the limitation by impeller design, similar to blade tip timing measurement (as previous discussed). However, it is possible to

adapt this method to evaluate blade condition by measuring the deflection of the outer shroud surface in terms of the changing clearance between the outer shroud surface and the sensor. This adapted method is based on the principle that the shroud and hub are connected by blades. Consequently, the deflection of the shroud is altered by a change in the blade's structural integrity.

2.4.4 Applications of blade tip timing and blade tip clearance

A number of applications have been reported for the blade tip timing and blade tip clearance in blade health monitoring and performance optimisation. Some of these reports have been discussed below.

First, the online detection of foreign object damage (FOD) is made possible via the blade tip timing monitoring system. In an article by Cardwell et al. (2010) [17], blade passing data in terms of time of arrival is obtained by installing eddy current sensors and optical sensors through a casing of a Spey RB168-101 engine, as shown in Figure 2.15. The blade reference position and speed are determined by a once-per-revolution signal from the engine speed sensor. Various objects such as stones were used as the foreign objects. Figure 2.16 shows the average and instantaneous blade deflections when a foreign object was stuck in blade 9; the green and the red circles refer to instantaneous and 1,000 revaluations averaged, respectively. A clear outlier on blade number 9 was presented when a foreign object was introduced to the inlet duct of the engine.

Blade tip timing and blade tip clearance signals can also be used to detect a crack in the rotor blade. The two-stage signal processing technique was proposed by

Hanachi et al. (2012) [44]. In the first stage, a physical model is used to first eliminate the known noise (e.g., a bending effect from centrifugal force) before the crack initiation can be specified by the sinusoidal effects from the rotor imbalance. In a healthy assembly, blades stretch out and react when the rotor accelerates and decelerates, respectively. When the initiated crack appears, however, the blade does not react due to the plastic deformation of the rotor blade caused by crack propagation. This results in the blade length increasing in the operating cycle, as shown in Figure 2.17. The second stage involves identifying the crack location by detecting the autocorrelations in noise and non-stationary time series.

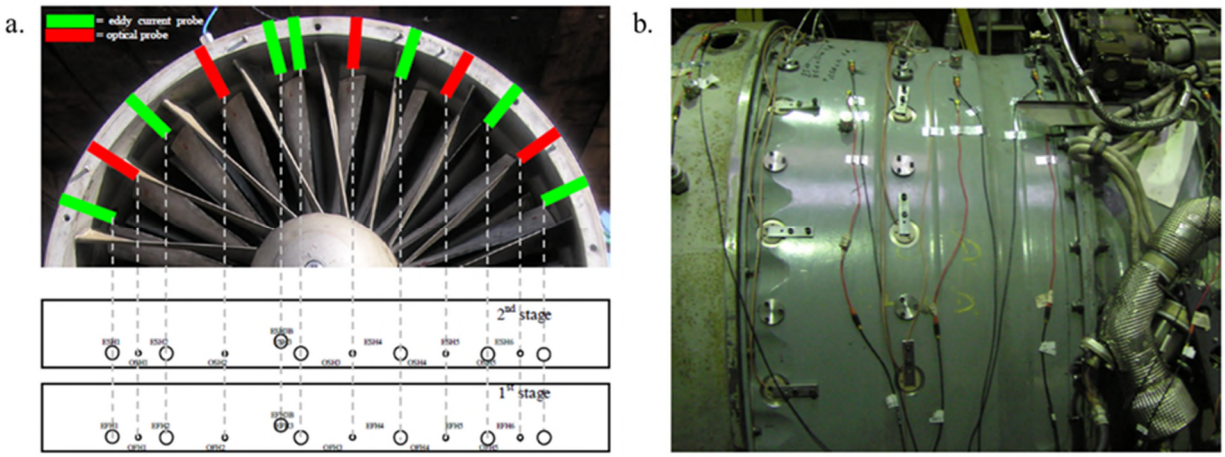


Figure 2. 15 The installation of eddy current and optical sensors [93]

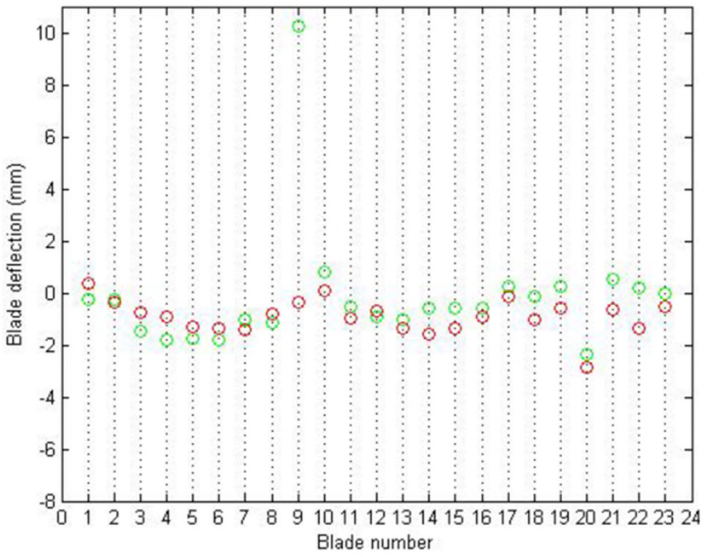


Figure 2. 16 The average and instantaneous blade deflections when a foreign object was stuck in blade 9 [93]

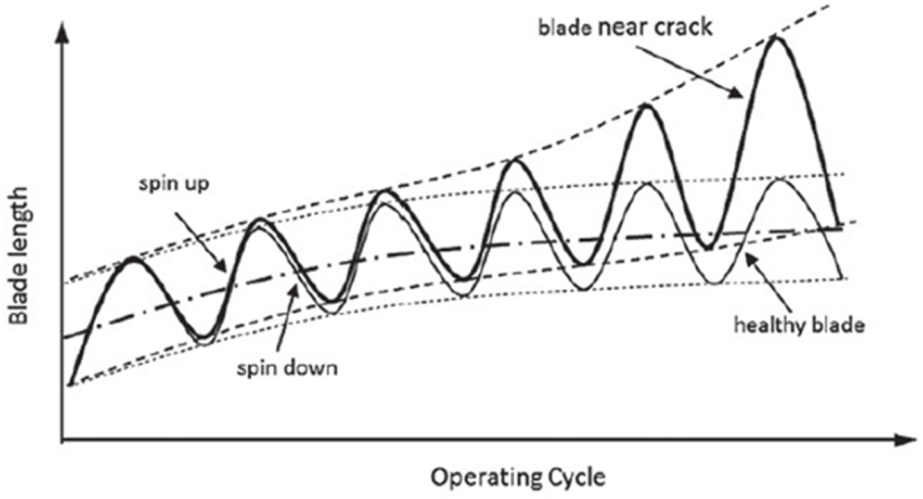


Figure 2. 17 Blade condition as determined by variations in the blade lengths [106]

In the case of jet engines, various active clearance control methods have been proposed to increase the efficiency of turbine engines by autonomously optimising the clearance between a blade tip and a casing [107, 108, 109]. Blade tip clearance

sensor is one of the most critical components of the closed loop control system, as shown in Figure 2.18. The controller uses the signals from the blade tip clearance sensors to control actuators which adjust the tip clearance to suit the different working conditions such as taking off, cruising, landing, and long-term deterioration. To obtain precise and responsive response data, blade tip clearance sensors should be installed to the high-pressure section of a turbine. Thus, robust, and reliable sensors are required for this harsh environment.

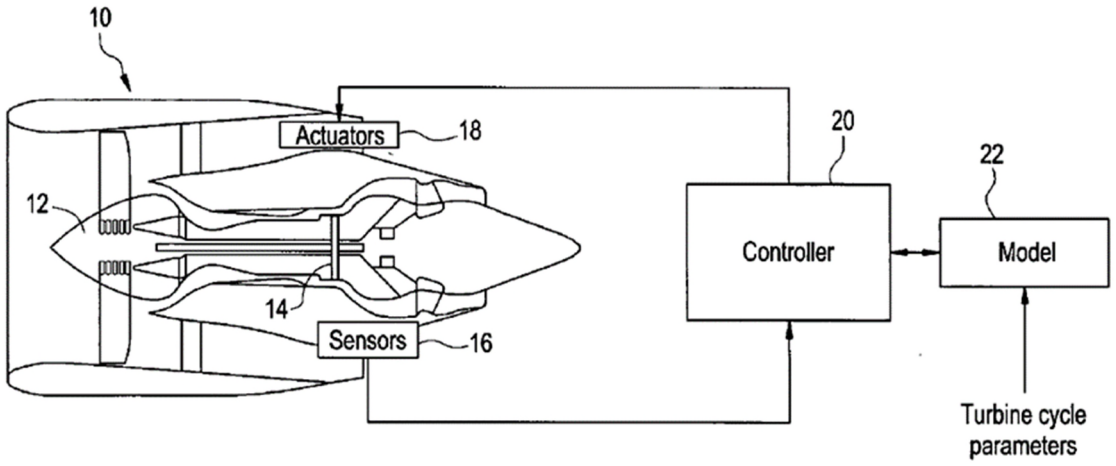


Figure 2. 18 A closed loop active clearance control [107]

2.4.5 Types of sensors for non-intrusive blade health monitoring

At present, a variety of sensors have been adapted for applications in blade health monitoring, especially in blade tip timing and blade tip clearance measurements. While the most widely used sensors are optical sensors [4, 9], they are not suitable for contaminated environments where light can be refracted by passing particles. Therefore, capacitive [5], eddy current [93], or microwave [79] sensors have been developed to address these problems.

The performances of various sensors for blade tip detection were compared and reported by Chana (2007) [6]. The four sensors, including a 6 mm diameter eddy current sensor, a 10 mm diameter capacitive sensor, and two 1.6 mm diameter pressure transducers, were selected to compare with a commercial optical sensor system normally used in an engine development process for tip timing.

Testing was conducted in the Isentropic Light Piston Facility (ILPF), which is a short duration wind tunnel for testing full-sized high-pressure turbine stages, as shown in Figure 2.19. This facility was designed for the matching of the non-dimensional turbine fluid mechanics and heat transfer parameters of a modern gas turbine engine. It comprises four sections: 1) a light-weight piston, 2) a fast-acting plug valve, 3) a turbine stage as a working area, and 4) a turbo-brake. The sensors were installed in a Perspex block fitted in the testing cassette of the turbine stage as shown in Figure 2.20. During the testing, the rotor tip clearance is equal to around 0.5 mm (1% of the blade span) at the speed of 9,500 RPM. During the 500 milliseconds of the testing time, the sensor signals were recorded at the sampling rate of 800 kHz together with the speed signals from a 1-line and 60-line disk mounted on the shaft.

The raw data from different sensors against the rotor-passing period is presented in Figure 2.21. The optical sensor, the capacitance and eddy current sensors provided sufficient signal quality for blade tip detection. In contrast to the pressure transducers that provided a less promising signal, particularly in terms of signal scatter and peak definition. Moreover, the capacitance and eddy current sensor

have an additional feature in blade tip clearance measurement as a result of the change in signal amplitude during blade passing. Table 2.1 shows the comparison of the sensors in terms of blade arrival times. The capacitance sensor gives the closest blade passing time with only 0.32 percent of deviation from the optical sensor. However, in practical use it is prone to contamination, e.g., dust, dirt, water, and oil. Therefore, an eddy current sensor was recommended for blade health monitoring in harsh environments like the gas turbine engine.

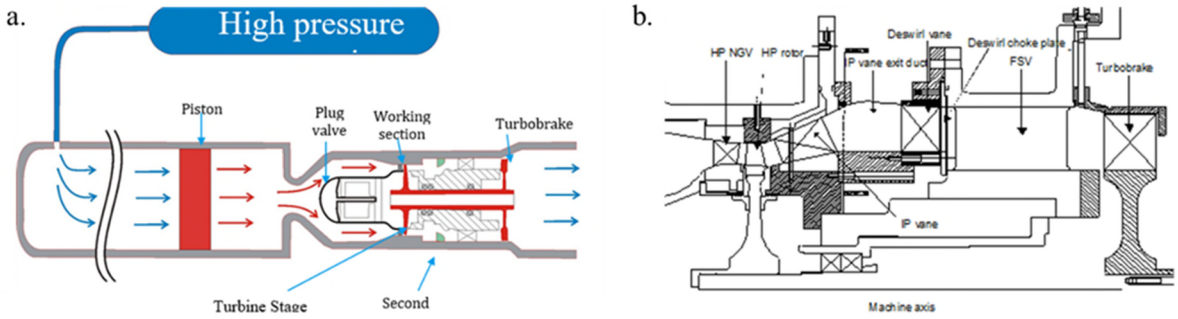


Figure 2. 19 Isentropic Light Piston Facility (ILPF) used in testing (a) the schematic diagram; and (b) a magnified image of the turbine section [6]

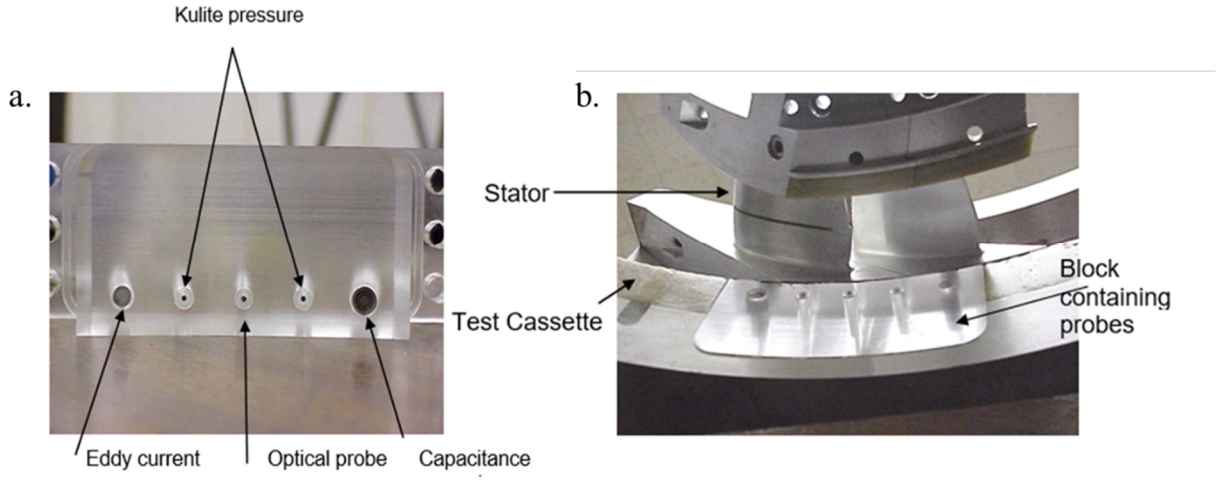


Figure 2. 20 The sensor installation (a) the arrangement of sensors in Perspex block; and (b) the test cassette [6]

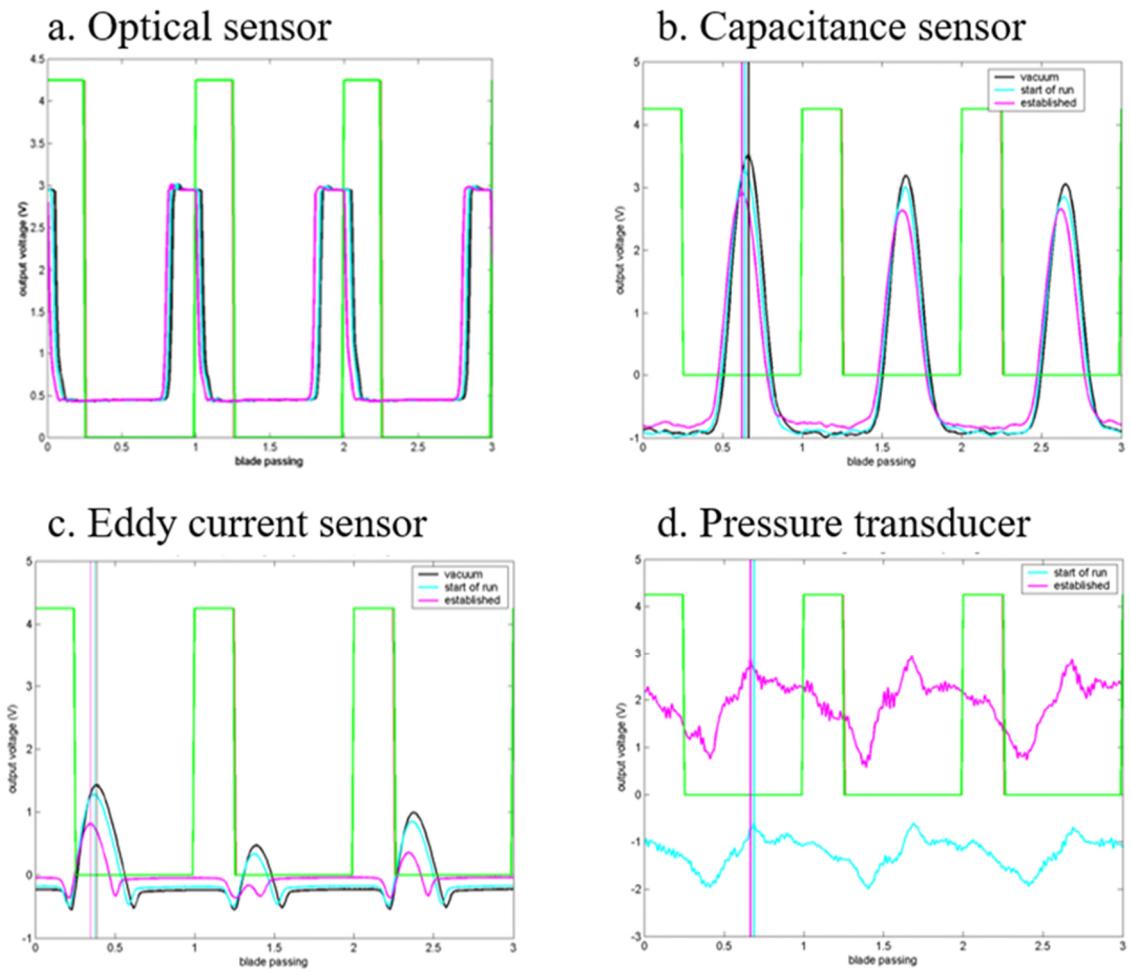


Figure 2. 21 The blade passing signals from different sensors compared with the rotor speed signal (a) optical sensor: (b) capacitance sensor; (c) eddy current sensor; and (d) pressure transducer [6]

Table 2. 1 Comparison of blade tip timing results from four different types of sensors [6]

Sensor	Blade passing time [s]	Blade pitch width [mm]	Deviation from optical [%]
Optical	1.0462×10^{-4}	30.70	-
Eddy current	1.0605×10^{-4}	31.12	1.37
Capacitive	1.0428×10^{-4}	30.60	0.32
Pressure transducer #1	1.0246×10^{-4}	30.07	2.06
Pressure transducer #2	1.0733×10^{-4}	31.50	2.59

2.5 Eddy current sensor and associated electronic system

Having been introduced in the early 1950s by Dr Friedrich Foerster, practical eddy current testing instruments are widely used in various applications such as position, alignment, material surface crack detection, and vibration measurements [69]. While all these applications are based on the precise position measurement acquired from the relative distance between the sensor and a target, they differ in terms of data processing and interpretation.

2.5.1 Principle of an eddy current sensor

An eddy current sensor uses an electronic driving system to generate a high-frequency current through a sensor coil, which results in a fluctuating magnetic field (henceforth referred to as 'a primary field'). When the sensor is brought close to a conductive target, the primary field induces eddy currents in the target material according to Faraday's law of induction. Eddy currents are small closed loops in a

perpendicular plane of the primary magnetic field. These currents in turn generate an opposite secondary magnetic field according to Lenz's law. The interaction of these fields depends on the strength of the primary magnetic field in terms of distance, driving frequencies, and the target's electromagnetic properties. This interaction is detected by the associated electronic system and converted into a voltage output proportional to the distance between the sensor and the target. In general, the effective range of an eddy current sensor is equal to half of the outer diameter of a coil [6]. The schematic diagram of the interaction between an eddy current sensor and a target is shown in Figure 2.22.

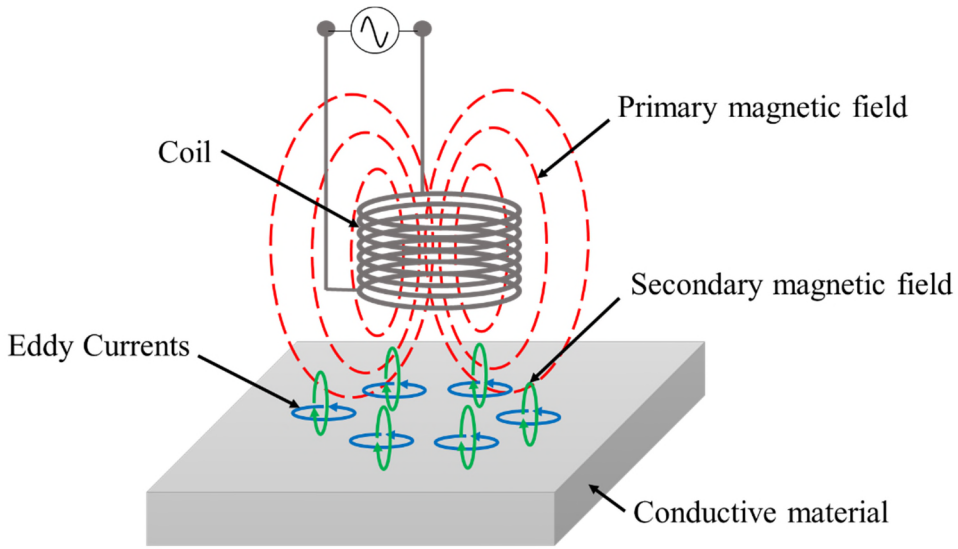


Figure 2. 22 The schematic diagram of the eddy current sensor and the target

The target material plays a major role in the usage of eddy current sensors. The quantity of eddy currents depends on the magnetic permeability and electrical conductivity of the target. The induced eddy currents have the highest density at the surface of a non-magnetic but conductive target adjacent to an eddy current sensor, as shown in Figure 2.23. This density reduces exponentially with depth, phenomenon referred to as the 'Skin effect'. The skin effect of a particular target material varies by the excitation frequency of the sensor. The term 'standard depth

of penetration' (δ) is defined as the depth at which the eddy current density reduces to 1/e, or around 37% of the surface density [1]. Notably, the standard depth of penetration (or skin depth) is a function of the driving frequency (f), electrical conductivity (σ), and relative magnetic permeability (μ_r) of the target material, as given by

$$\delta = \frac{1}{\sqrt{\pi f \mu_r \mu_0 \sigma}} \tag{2.13}$$

where μ_0 is the absolute magnetic permeability (1.26×10^{-6} H/m). Figure 2.24 shows a decrease in the standard depth of penetration with the increase of the excitation frequency of various materials. Materials with lower electrical conductivity have a deeper penetration of eddy currents. The thickness of the target material is recommended to be at least double the skin depth thickness to eliminate the effect of the target thickness in the measurement [82]. In addition, the driving frequency of the coil can also be adjusted to suit the target material.

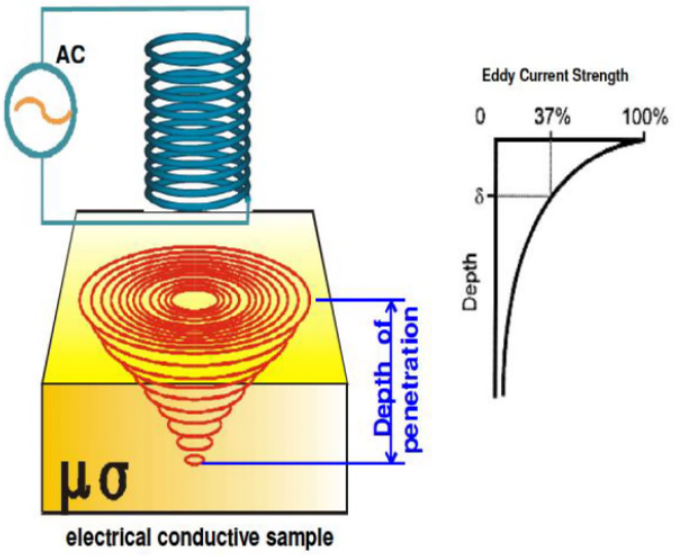


Figure 2. 23 The decrease of induced eddy current in target material [80]

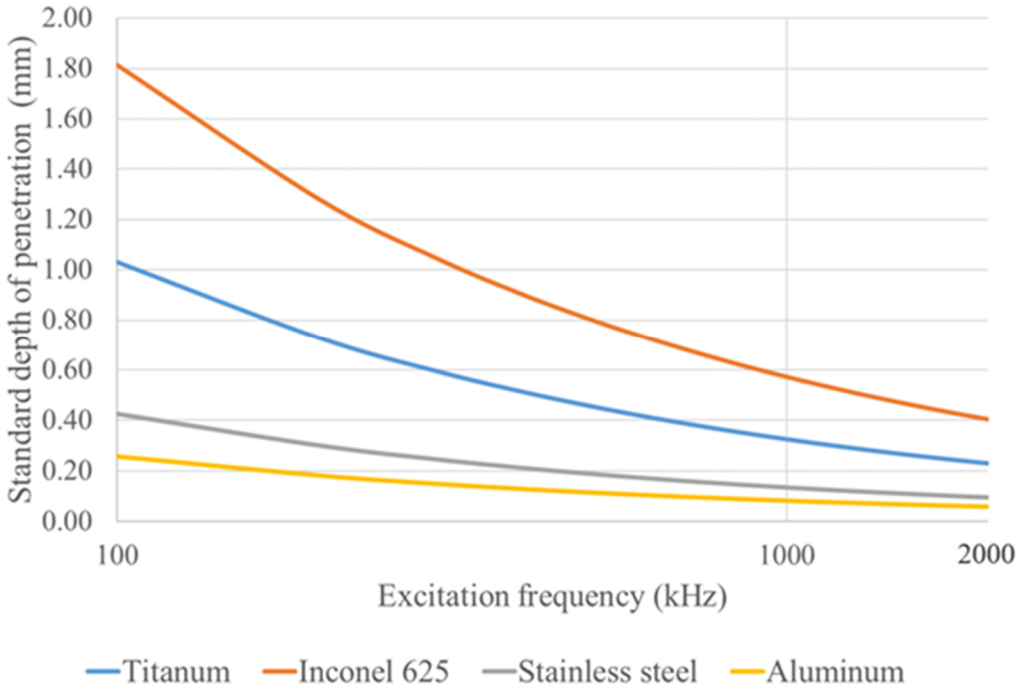


Figure 2. 24 The standard depth of penetration versus excitation frequency of various non-ferromagnetic materials including titanium, Inconel 625, stainless steel, and aluminium

As for a ferromagnetic target which has a higher relative magnetic permeability (e.g., nickel or iron), the lower driving frequency is recommended to obtain sufficient eddy current flow [27]. Therefore, the eddy current sensors are prescribed to be used with the non-magnetic but conductive target for obtaining high accuracy in the measurement [28].

2.5.2 Eddy current sensor models

The analytical solution of a single-turn coil over the plane surface of a non-ferromagnetic but electrically conductive target is given in the work of Dodd and Deeds in 1968 [83]. Hajian and Blitz (1986) [84] extended the method to develop formulas for the components of the normalised impedance of a coil over a non-

ferromagnetic target. Further work by Oaten and Blitz in 1992 [85] presented the general solution of both ferromagnetic and non-ferromagnetic targets. Figure 2.25 shows the schematic diagram of an air-cored coil above the plan surface of an electrically conductive target used to derive the analytical solution. In their analysis, an alternating current of amplitude i_0 produces the magnetic vector potential A, which can be expressed in cylindrical coordinates as

$$\frac{\partial^2 A}{\partial r^2} + \left(\frac{1}{r}\right)\frac{\partial A}{\partial r} + \frac{\partial^2 A}{\partial z^2} - \frac{A}{r^2} = -\mu J + j\omega\mu_0\sigma A \qquad (2.14)$$

where J is the current density in a single-turn delta function. By solving this equation, the effect of eddy current can be calculated.

By solving equation 2.14, the changes in coil inductive reactance and resistance for non-ferromagnetic material are given by

$$\frac{\omega L}{\omega L_0} = 1 + ({k_0}^2/8P)(\frac{Q}{\sqrt{2}BP} - 1) \qquad (2.15a)$$

$$\frac{R}{\omega L_0} = {k_0}^2 Q/[8PS(\sqrt{2}\beta P - 1)] \qquad (2.15b)$$

where

$$P = k(k + k_0)(2k + k_0)$$

$$Q = {k_0}^2 + 6k^2 + 6kk_0$$

$$S = k_0 - \frac{8}{3\pi} + \frac{1}{2k_0}$$

$$\beta = (\omega\mu_0\sigma{r_0}^2)^{1/2} = {f_0}^{1/2}$$

Notably, the equations 2.15a and 2.15b are only valid when the normalised lift-off ($k = h/r_0$) and the normalised coil length ($k_0 = l_0/r_0$) are larger than 0.7 and 1.5, respectively.

The work of Oaten and Blitz in 1992 [85] illustrated the lift-off curves of a coil with varying lift-offs from aluminium alloy (non-ferromagnetic) and mild steel (ferromagnetic) samples at various normalised frequencies (f_0). As illustrated in Figure 2.26, for a non-ferromagnetic sample, the effective coil inductance (L) decreases as the sample approaches the coil (decreases k). On the other hand, for a ferromagnetic sample, when the lift-off between the coil and the sample is reduced, the coil's effective inductance increases.

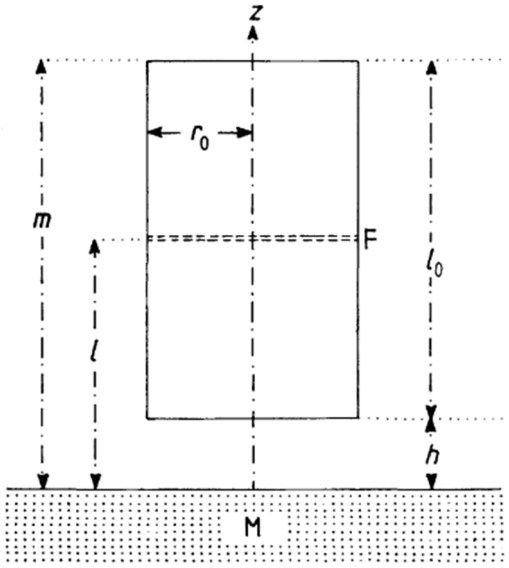


Figure 2. 25 The schematic diagram of solenoid coil above the plane surface of an electrically conductive target [86]

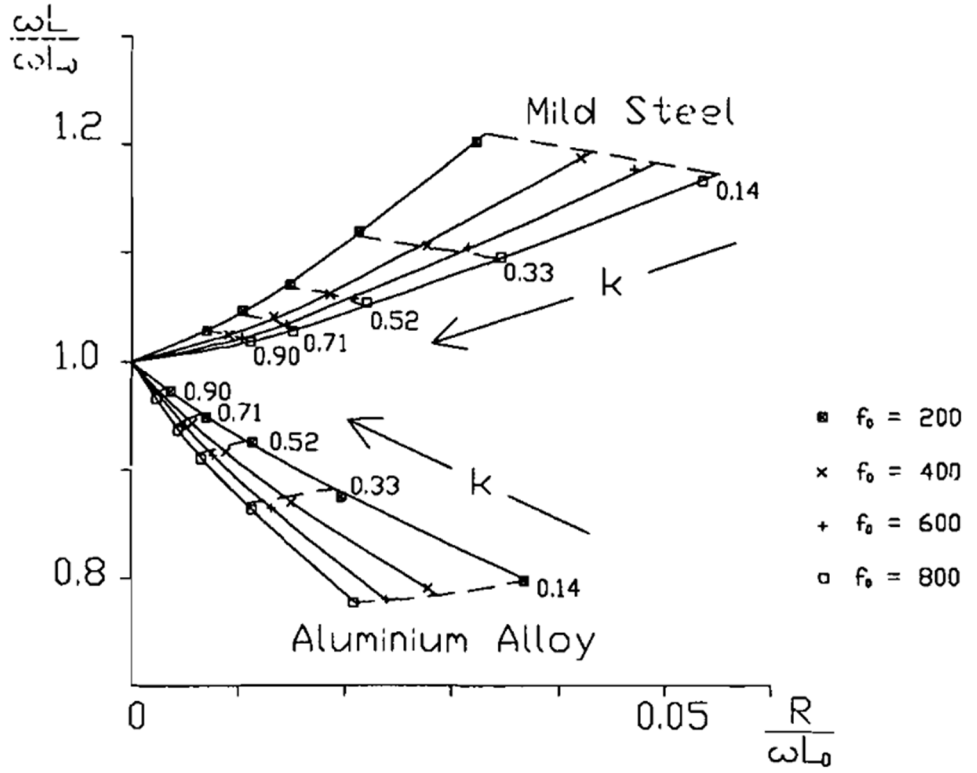


Figure 2. 26 The predicted and measured impedance of a coil with varying normalised lift-offs (k) from the aluminium alloy and mild steel samples at various normalised frequencies (f_0) [85]

In an article by Tian et al. (1998) [29], the interaction between an eddy current sensor and a target is modelled as the air-core transformer, as shown in Figure 2.27. In this model, the primary magnetic field (H1) and the secondary magnetic field (H2) created by the eddy current are represented in loop 1 and loop 2, respectively. The mutual inductance (M) represents the interaction between the two adjacent magnetic fields. This mutual inductance is dependent on the standoff (x), which is the distance between the sensor coil and the target.

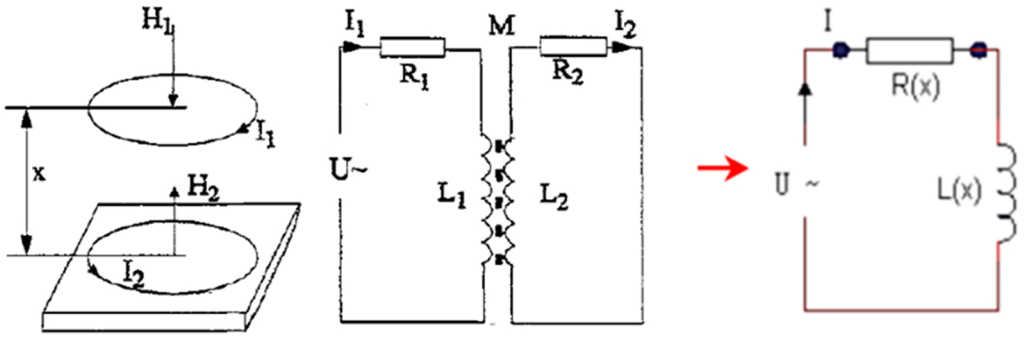


Figure 2. 27 The air-core transformer model for explaining the interaction between an eddy current sensor and a target [29]

This air-coil transformer model can be simplified to an equivalent circuit as a series of LR by applying Kirchhoff's law:

loop1:

$$R_1 I_1 + j\omega L_1 I_1 - j\omega M I_2 = U \qquad (2.16)$$

loop2:

$$-j\omega M I_1 + R_2 I_2 + j\omega L_2 I_2 = 0 \qquad (2.17)$$

Therefore, the effective coil impedance (Z_{eff}) of the equivalent impedance is

$$Z = R + j\omega L = R_1 + \frac{\omega^2 M^2 R_2}{{R_2}^2 + \omega^2 {L_2}^2} + j\omega\left(L_1 - \frac{\omega^2 M^2 L_2}{{R_2}^2 + \omega^2 {L_2}^2}\right) \qquad (2.18)$$

Thus, the effective resistance R and inductance L of the sensor coil are derived as

$$R_{eff} = R_1 + \frac{\omega^2 M^2 R_2}{{R_2}^2 + \omega^2 {L_2}^2} \qquad (2.19)$$

$$L_{eff} = L_1 - \frac{\omega^2 M^2 L_2}{{R_2}^2 + \omega^2 {L_2}^2} \qquad (2.20)$$

Obviously, both effective parameters vary by the stand-off (x). Therefore, the distance between the sensor coil and the target can be measured by changing those parameters using associated electronic systems. As for a non-ferromagnetic target,

the target moves closer to the coil, which results in the decreasing of the effective inductance and the increasing of the effective resistance.

In addition, the performance of the sensor is specified by the quality factor, Q, defined as

$$Q = Q(x) = \frac{\omega L(x)}{R(x)} \tag{2.21}$$

where ω is the operating frequency of the sensor (rad/s). Quality factor is used to indicate the linear range of the sensor. The quality factor describes the ratio of the stored energy to the dissipated energy of the coil. The high accuracy and stability of the sensor is obtained by the high value of the quality factor, with a preferable value of larger than 15 at unloaded condition [30].

According to the effective inductance equation (2.20) and the quality factor equation (2.21), it is apparent that the performance of the sensor depends mainly on the inductance of the coil, L_1. The term inductance is defined as the property of a component that opposes the change of current flowing through it by creating an opposed magnetic field [31]. Inductance is also related to the stored energy in the magnetic field, W, as given by

$$L = 2\frac{W}{I^2} \tag{2.22}$$

The inductance of the coil depends on its geometrical configurations For a short multi-layer coil, the inductance, L_0, can be estimated by using the empirical formula proposed by Wheeler (1928) [32], as given by

$$L_0 = \frac{0.8a^2n^2}{6a+9b+10c}\ (\mu H) \tag{2.23}$$

where a, b, and c are the dimensions of the coil in inches, as shown in Figure 2.28, and n is the number of turns. Notably, the accuracy of this formula is within one percent when compared with the analytical formula in Radio Engineer's Handbook by Terman (1943) [31].

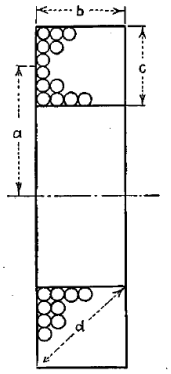


FIG. 27.—Short multiple-layer coil of solenoidal form.

Figure 2. 28 Short multiple-layer coil in solenoidal form, adapted from Terman (1943) [31]

Over the past decades, the method of modelling the response of an eddy current sensor with a target has been shifted from solving the Maxwell's equations analytically to computational simulation. Because the commercial finite element software provides a reliable solution for sensor design and optimisation [37], development time and costs are reduced.

The work of Jamia et al. (2019) [38] presents the finite element simulation model of an eddy current sensor and rotating blades for blade tip timing measurement. The simulation model addressed the effect of tip clearance, blade geometry, and blade velocity on the output of the eddy current sensor. In addition, the experimental data was used to validate the model. The study results indicated that the tip

clearance and rotational speed influence the precision of the blade tip timing measurement.

2.5.3 Associated electronic system

In addition to generating a high frequency current for driving a sensor coil, several associated electronic systems are also involved in converting the change of the impedance to the output voltage that represents the change of measuring displacement.

Typically, the amplitude of the response of the sensor to an applied voltage is monitored. Since the amplitude of the response depends on the induced eddy currents in the target, the change of amplitude is thus converted to the distance between the sensor and the target [30, 31].

Another alternative method for measuring the reactance was introduced by Oxford University Innovation Ltd., as Published Number 2007/12571 A1 [33]. Instead of amplitude measurement, the small change in the reactance is obtained by the phase measurement. This method is claimed to be suitable for turbo-machine assemblies in which high sensitivities are required to eliminate the signal interference.

2.6 Chapter conclusion

In this chapter, the principle of centrifugal compressors with shrouded impellers was briefly explained in terms of design, characteristics, typical operating conditions, and manufacturing. The literature review shows that shrouded impellers are prone to blade crack damage where the wakes generated by the upstream inlet guide vanes often cause high cycle fatigue damage on the impeller blades.

Based on a thorough review of several typical blade health monitoring methods, it was found that most, if not all, of the existing methods were impractical to apply to shrouded impellers given their geometrical limitations.

Hence, my research aims to develop a new approach to crack detection for shrouded impellers using shroud/casing measurement.

In addition, sensor types typically utilised in blade health monitoring are examined. Previous work indicated that eddy current sensors are preferable for clearance measurement application in crack gas compressors due to their micron level accuracy and ability to operate in contaminated environments. Finally, the principle of eddy current sensor and associated electronic systems were also discussed.

Chapter 3

Experimental Setup

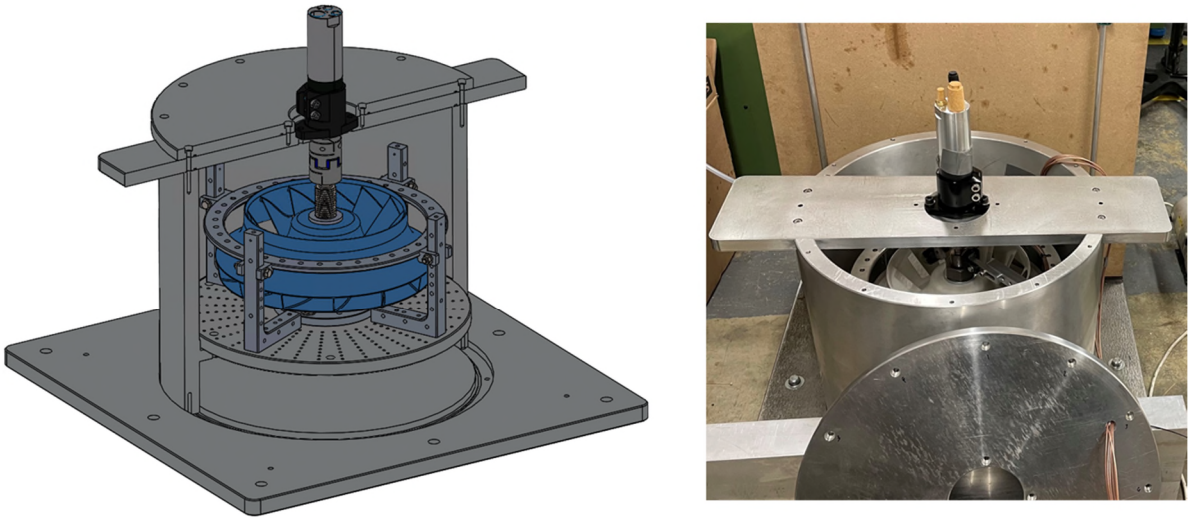
3.1 Introduction

This chapter describes the experimental facilities and instrumentation used to test the hypothesis of using the deflection of the outer shroud for blade crack detection. Section 3.2 overviews the design of the high-speed spinning rig with a driving system. In section 3.3, a scaled impeller design, manufacturing, and testing are explained. Section 3.4 addresses the instrumentation which were used in these experiments. Signal processing and sensor calibration for clearance measurement are described in sections 3.5 and 3.6, respectively.

3.2 High-speed spinning facility

In these experimental studies, I designed a new high-speed spinning rig under the advice of Professor Kam Chana. The rig installation and commissioning were completed with the help of Dr Vikram Sridhar and laboratory technicians. Figure 3.1 shows the newly fabricated spinning rig with the air motor configuration. The

high-speed spinning rig consists of 3 main components, including 1) the aluminium containment, 2) the driving system, and 3) the rotor inside the containment.



(a) (b)

Figure 3. 1 The testing facility (a) CAD model of the shrouded impeller inside the containment; and (b) the testing facility with the top lid opened (air motor configuration)

For safety reasons, the aluminium containment was designed to absorb impact and stop penetration of debris in the case of an impeller breaks off during operation. The high-velocity impact simulations were conducted in the design process with the explicit module of ANSYS® software. In the simulation, a broken piece of a scaled rotor was modelled as a spherical ball with a speed of 200 m/s. This speed was equivalent to the tangential speed of a 400 mm impeller at 9,550 RPM. The mass of the ball, 8 kg, was one-third of the mass of a stainless-steel impeller. The simulation results showed that the 30-mm aluminium wall thickness is able to absorb the

impact without breaking through with the safety factor of 10. Figure 3.2 shows the simulation model and results.

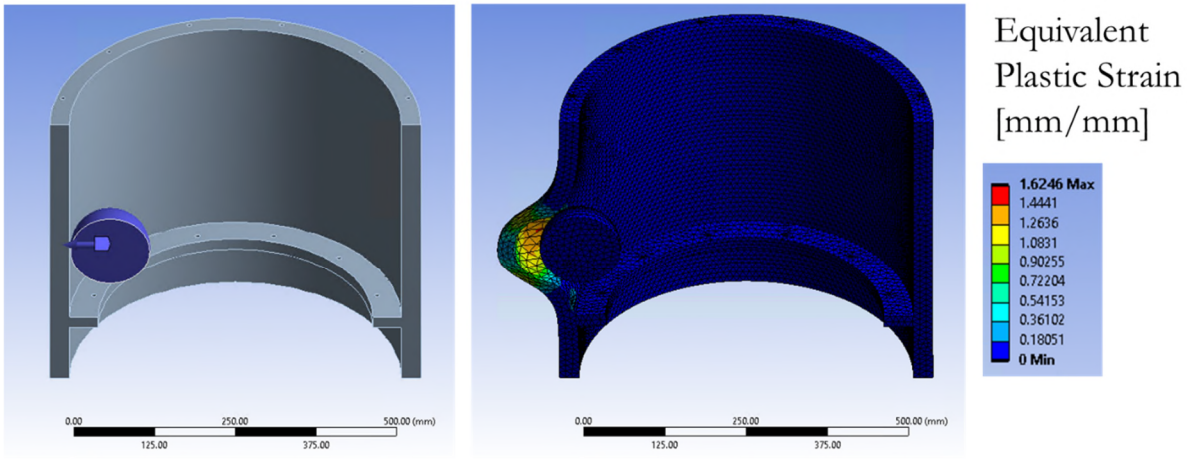


Figure 3. 2 The high-velocity impact simulation (a) simulation model; and (b) simulation results

Thus, the aluminium containment has an internal diameter of 514 mm and a height of 480 mm with a 30-mm wall thickness. It was built from a single piece of aluminium billet by a five-axis milling machine. Inside the containment, the middle hole-plate, up-rising columns, and circular ring inside are used for sensor mounting. The aluminium top lid can be opened to access the rotor and sensors. The crossbar supports a driving system: an air motor or a pulley in the case of driving with an electrical motor. The flexible coupling was used to connect the driving system and the rotor. The containment was sealed with nitrile rubber O-rings at the top lid and the base plate to create a vacuum condition.

The driving system of the spinning rig can be switched between an air motor and an electric motor depending on the required speed. The speed limits of the air motor

and the electric motor are 3,500 RPM and 5,000 RPM, respectively. However, the 15-kW electric motor was preferred due to its speed stability and ease of operation. When driving with the electrical motor, the desired operating speed can be controlled by adjusting the motor driving frequency via a Variable Speed Drive (VSD) which connects to the motor.

The rotor was assembled vertically inside the containment. The rotor consists of a scaled plastic impeller and a stainless-steel shaft. The impeller hub was mounted with a stainless-steel shaft with a key to limit relative radial movement. In addition, the impeller and the shaft were locked together with a left-hand nut and two set screws (placed perpendicular to each other). The nut was tightened in the opposite direction of rotor rotation (clockwise) to prevent loosening during operation. The rotor shaft connected with the pulley with a flexible coupling, whereas another end of the rotor shaft was supported with a bearing. The design, manufacturing and testing of the scaled impeller are explained in section 3.3.

3.3 Scaled impeller

The scaled impeller plays a vital role in these blade crack detection studies. It has to be designed to represent not only the shape of the actual impeller but also its behaviours, especially the shroud deflection when a blade crack occurs. In other words, the amplitude of the shroud deflection of the scaled impeller is similar to the predicted amplitude of the actual impeller, although the propellers are made of different materials.

3.3.1 Design and manufacturing

In this research, geometric scaling was used as the scaling method for designing a shrouded impeller for experimental testing. The objective of the scaling, as stated in the introductory paragraph, was to obtain a scaled impeller for experimental testing with a magnitude of shroud deflection equivalent to the actual-sized impeller. Therefore, the experimental results in blade health monitoring will be comparable to the actual-sized impeller.

To achieve the objective, various impeller models were built and analysed with the Static Structural Analysis module in ANSYS® software to obtain a proper impeller design. The shape of the scaled impeller, including curved blades, shroud, and back-end wall, was modelled after the shape of the actual impeller rotor. However, the number of blades, the thickness of each impeller component, and the impeller building material varied in these trial simulations.

After comparing the different impeller designs, the final impeller design had a shroud diameter of 380 mm, which was 39.4% the diameter of the actual rotor. Notably, the outer diameter of the impeller was limited to the internal diameter of the containment. The number of blades was reduced from 17 blades to 13 blades while maintaining the curvature of the blades. Other critical design parameters are shown in Table 3.1. Figure 3.3 shows the CAD models of the actual size rotor compared with the scaled impeller. The predicted deflections from FEA given in Figure 3.4 show a distinctive difference between the healthy impeller and the impeller with a cracked blade.

Two sets of 3D-printed impellers with the same design were used in these experimental studies. The first impeller was used in the feasibility study of shrouded impeller blade health monitoring using clearance measurement (preliminary experiment). The result, as the magnitude of the shroud deflection during crack propagation, was used for planning the subsequent primary experiment. The second impeller was used in the primary experiment to determine the healthy impeller's behaviour as a baseline case and investigate the relationship between the shroud deflection and crack length. The results of the experiments are described in Chapter 5. Notably, the first impeller was not inspected or tested for back-to-back comparison with the second impeller. Thus, these two impellers may not be completely identical.

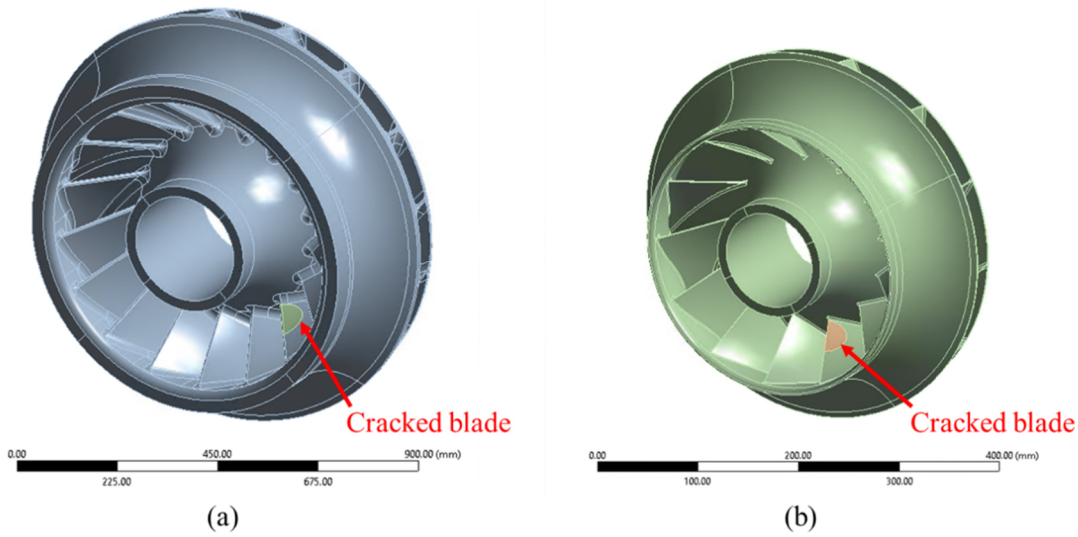


Figure 3. 3 CAD models (a) the actual size impeller; and (b) the scaled impeller

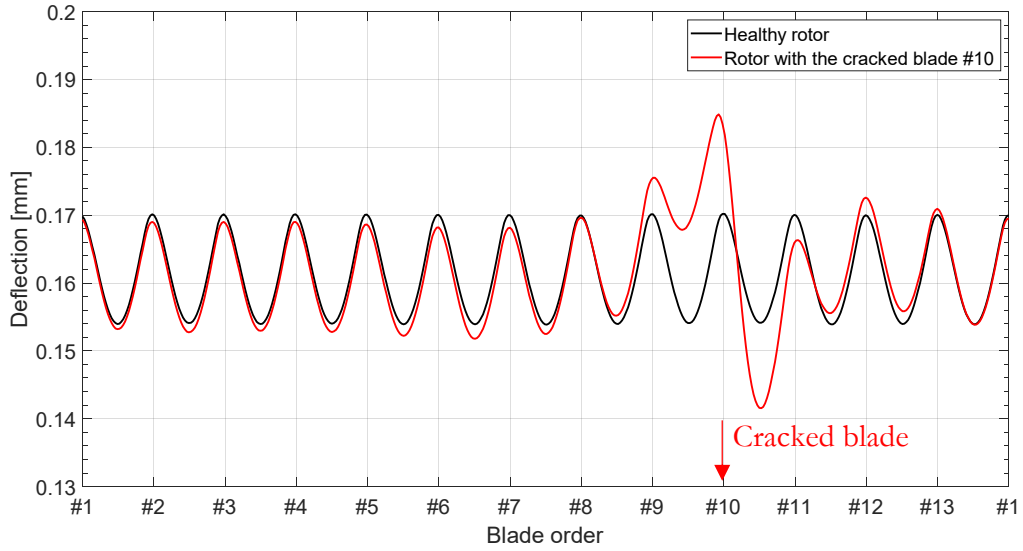


Figure 3. 4 Comparison between the deflection of the healthy scaled impeller and the scaled impeller with a cracked blade number 10

Table 3. 1 Comparison between the actual size impeller and the scaled impeller

Parameters	**Actual Impeller**	**Scaled Impeller**
Operating speed [RPM]	5,800	1,500 - 4,900
Maximum tip speed [m/s]	207.6	70.5
Maximum relative Mach number (blade tip)	0.61	0.21
Material	Alloy Steel	Fibre-reinforced polymer
Weight [kg]	454	3.6
Diameter [mm]	964	380
Axial length [mm]	311	117
Number of blades	17	13
Leading edge length [mm]	190.1	74.9
Blade thickness [mm]	9	1
Shroud thickness		
Maximum [mm]	47.5	5.4
Minimum [mm]	12.1	1.5

The scaled impellers were 3D-printed in the United Kingdom by 3D Systems Ltd. Using the Selective Laser Sintering (SLS) technique, one of the additive manufacturing processes. This technique uses a laser as the power source for sintering powdered material, in this case, a fibre-reinforced polymer. Thus, the impeller was printed layer-by-layer from the bottom up with each layer being 100 – 120 μm thick. The minimum wall thickness of a printing part is 1 mm. The surfaces of the 3D-printed impeller were intentionally left as original without post-machining. However, the surface finish was visually inspected to determine the quality of the printing.

Conductive paint (silver solvent) was applied to the impeller to create an electrically conductive surface for Blade Tip Timing (BTT) and clearance measurements by eddy current sensors. The conductive coating was painted by hand. Thus, the coating thickness may not be uniform. However, the conductive coating was repainted the output signal from the eddy current sensor operating at 485 kHz at the fixed stand-off was saturated. This implied that the thickness of the conductive coating was thicker than double the skin depth thickness at 0.18 mm. The calculation of the skin depth thickness is explained in section 2.5.1 Principle of eddy current sensor. The painted areas include blade leading edges, trailing edges, the inlet shroud, the outlet shroud, and the back-end wall, as shown in Figure 3.5.

To identify a cracked blade, markers were placed on the impeller blades to distinguish individual blades (#1 to #13). The first blade was specified as opposite

the shaft key, as shown in Figure 3.21 (b). The direction of the blade order was counter-clockwise, opposite to the direction of the rotor rotation.

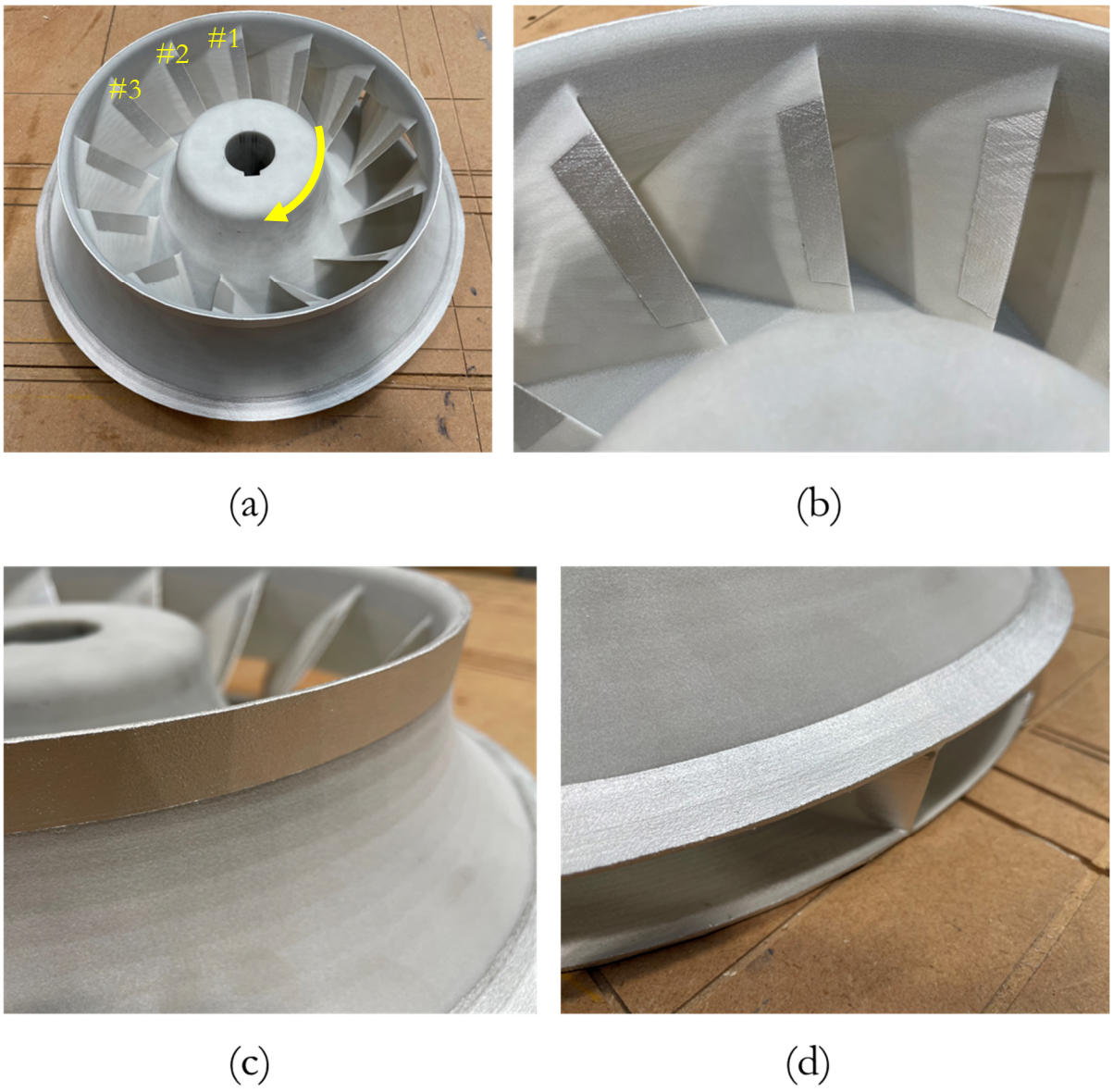


Figure 3. 5 The scaled 3D-printed plastic impeller with conductive painted surfaces

3.3.2 Runout measurements

The objective of the mechanical runout measurement was to obtain a baseline for the impeller's shape baseline for sensor calibration and clearance measurement. The runout of the impeller was caused by the imperfection of the impeller printing process. The term 'mechanical runout' means this measurement only focuses on the surface profile deviation relative to a reference location.

The runout measurements were performed using a digital dial gauge along three rotor locations where clearance sensor to be located, including the inlet shroud, the outlet shroud, and the back-end wall, as shown in Figure 3.6 a, b, and c, respectively. The runout was measured in 52 positions at equal distances in each location. A laser beam was projected on the impeller to precisely control the measurement position. The measurement process was repeated five times to ensure repeatability and reliable results.

Figure 3.7 shows the runout profile with uncertainty bars at the inlet shroud location with the first blade as a reference position. The range of runout in this position was 2.04 mm. Note that the uncertainty bars are depicted as horizontal lines on the graph because the uncertainty values were approximately 20 μm. These less uncertainty values also appear in the runout profiles at the outlet shroud and back-end-wall locations, as shown in Figure 3.9 and 3.11, respectively. The polar plot of the inlet shroud runout in Figure 3.8 shows that the two lobes of maximum runout were aligned along the fourth and eleventh blades.

The runout profile at the outlet shroud location is shown in Figure 3.9. It can be seen that the runout fluctuation occurred between each blade. This fluctuation was related to the shroud profile, which bent down between two adjacent blades, as shown in Figure 3.10. The range of the outlet shroud runout was 2.11 mm.

Finally, the runout profile at the back-end-wall location is presented in Figure 3.11. The runout fluctuation was also observed at this location. However, the range of runout (1.35 mm) was less compared to the outlet shroud location. This difference may be because the impeller was printed from the bottom up, layer by layer. Thus, the back-end-wall was supported by the printer platform during the manufacturing process.

In short, the mechanical runout at three locations was measured. The results show the surface profile variations caused by the impeller manufacturing process. These measurements were the baseline for sensor calibration in the following section.

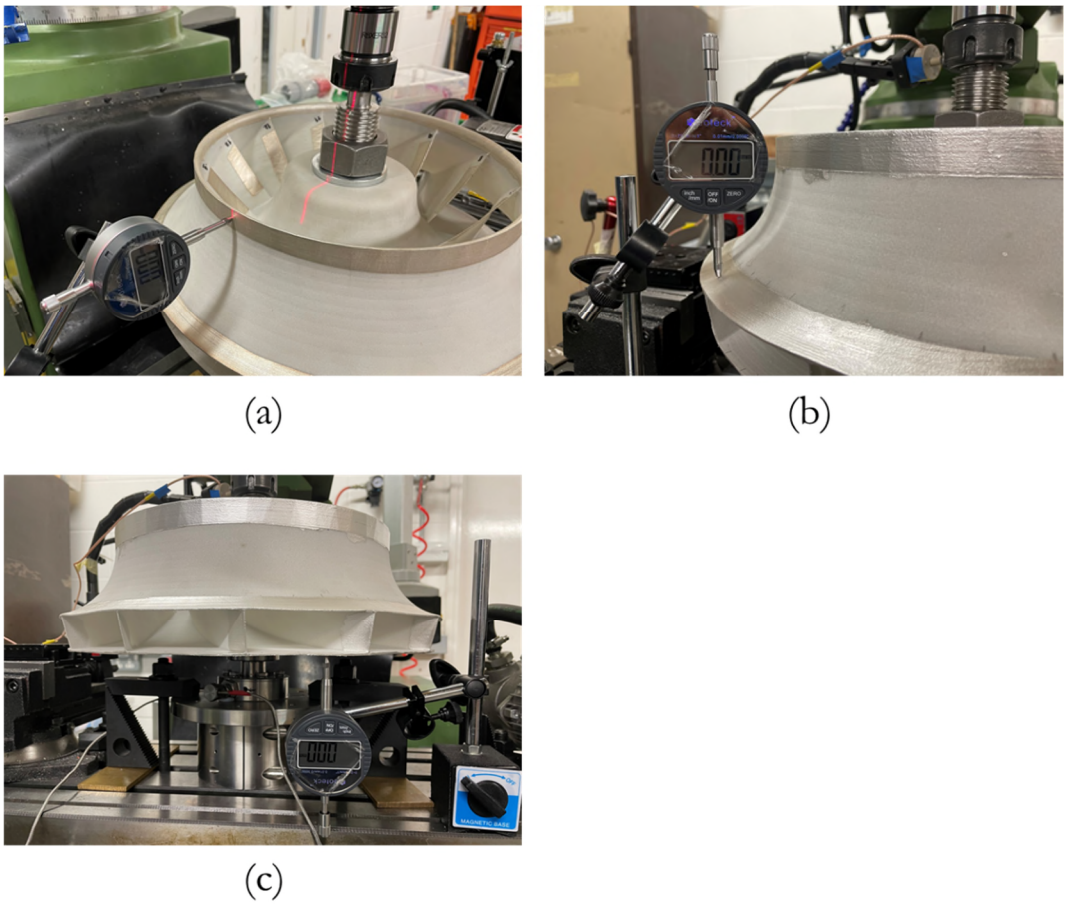


Figure 3. 6 The setup of runout measurements in three locations (a) inlet shroud location; (b) outlet shroud location; and (c) back-end-wall location

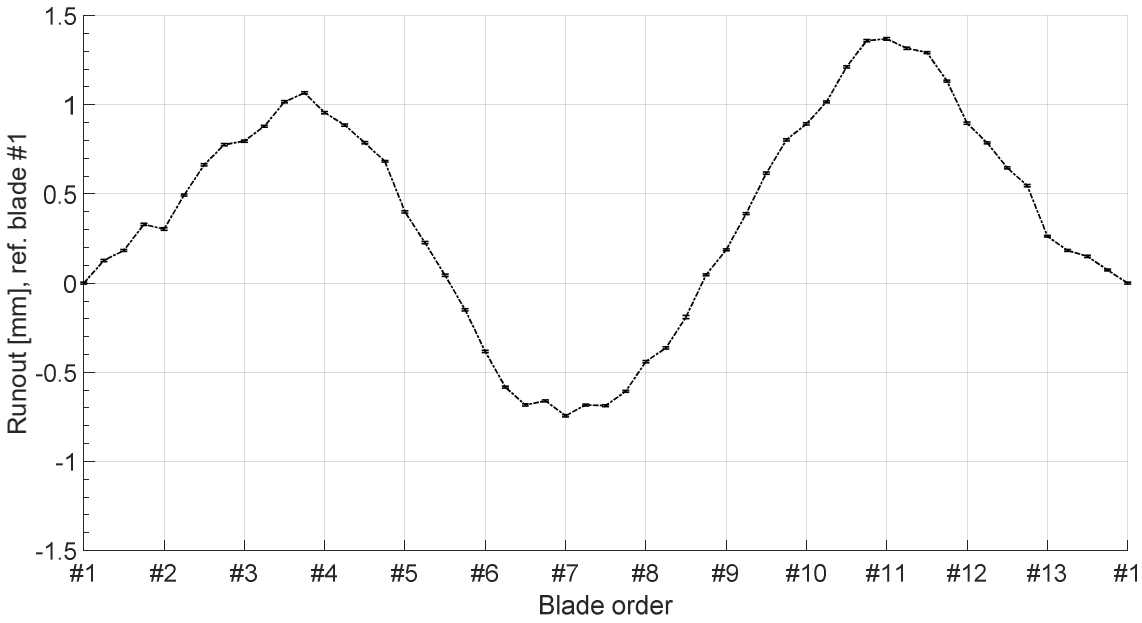


Figure 3. 7 Runout profile at the inlet shroud location

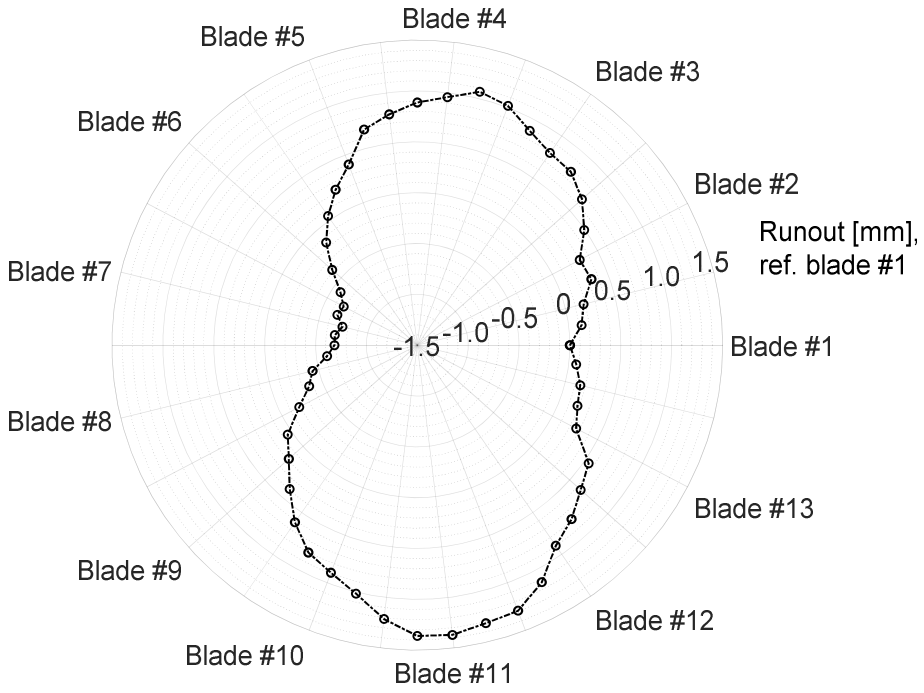


Figure 3. 8 Polar plot of the inlet shroud runout profile

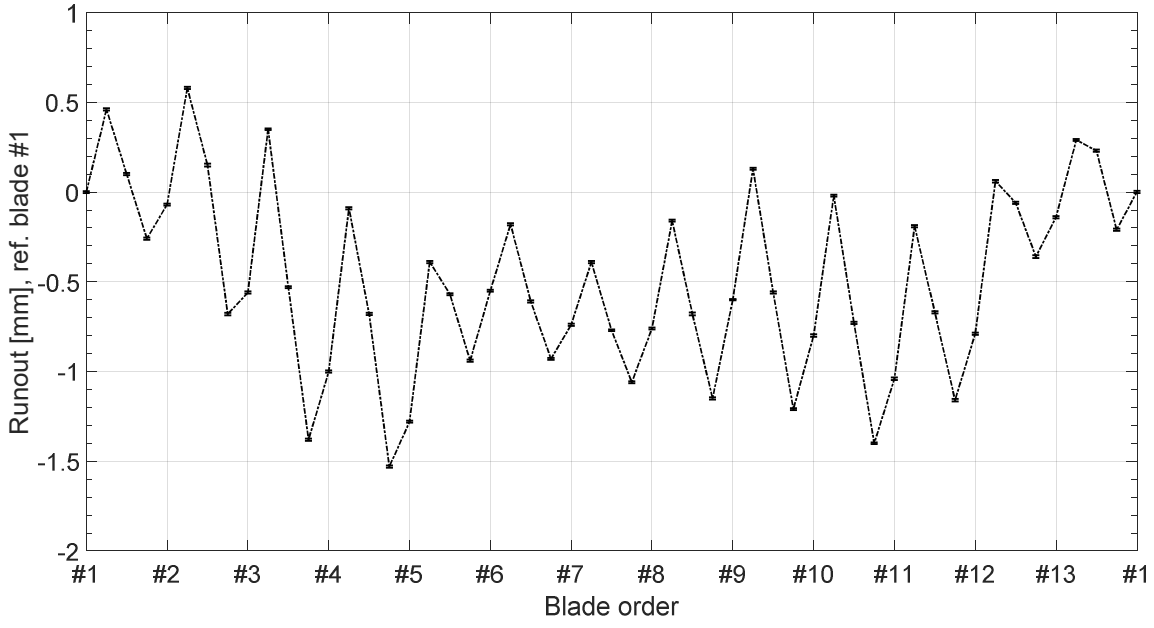


Figure 3. 9 Runout profile at the outlet shroud location

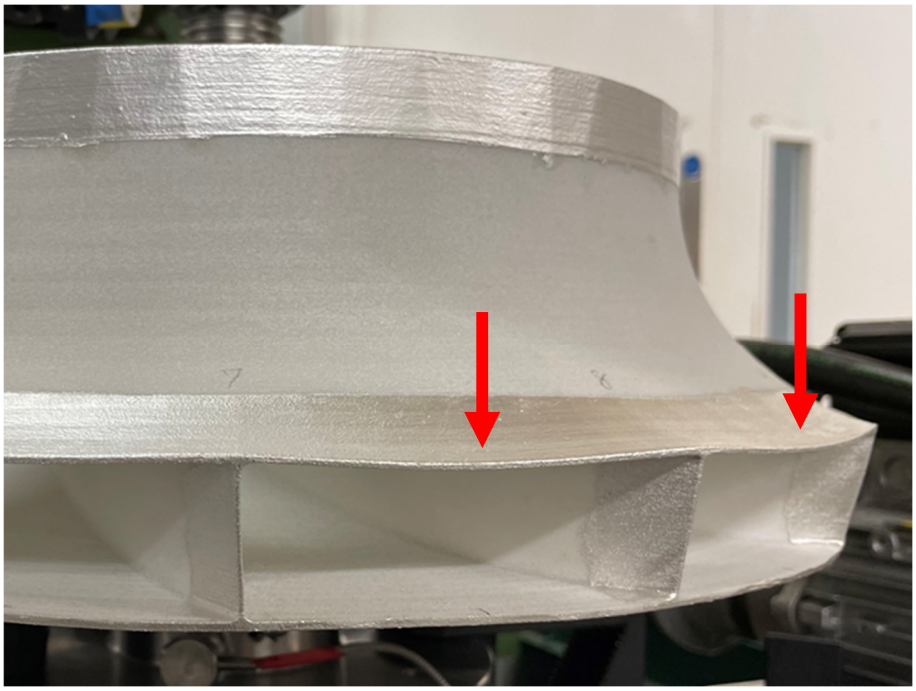


Figure 3. 10 Outlet shroud profile shows the downward distortion between two adjacent blades

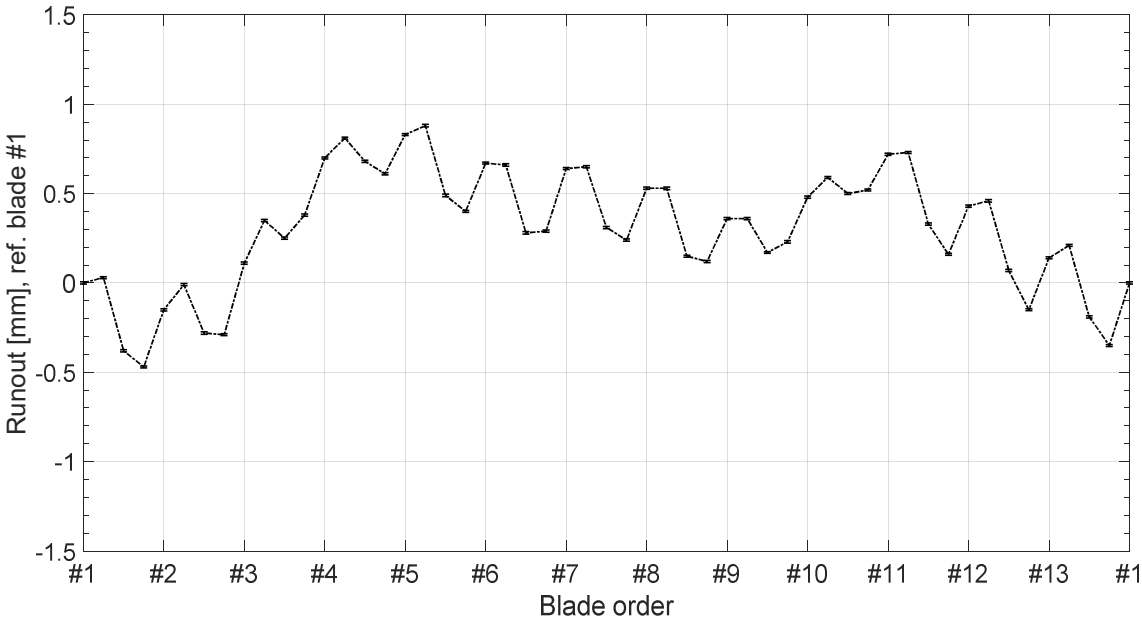


Figure 3. 11 Runout profile at the back-end-wall location

3.3.3 Residual unbalance measurement

The aim of the measurement was to obtain the baseline of the residual impeller unbalance for determining the effect of the unbalanced force on the impeller behaviour in terms of deflection.

The rotor unbalance measurement was performed using the four-run method. This method is commonly used in signal-plane balancing because only one accelerometer is required, eliminating the complexity of using an additional tachometer for phase measurement [89]. Figure 3.12 shows the setup of the four-run balancing method with an accelerometer at the rotor bearing support. A milling machine vertically drove the impeller at the speed of 792 RPM, given the speed frequency (1X) of 13.2 Hz. The 1X vibration amplitude, which is the product of the rotor unbalance at a specific running speed, is calculated from the vibration signals.

The first step of the four-run balancing method was to run the original impeller to measure the impeller vibration. A base circle was drawn using the amplitude of 1X vibration extracted from FFT as a radius $\overrightarrow{V_0}$.

Then the first trial weight of 8 grams was added to the impeller's back-end wall at the position corresponding to the trailing edge of blade number 5 (143°). The trial weight mass was calculated to generate 10 percent of the centrifugal force generated by the rotor weight. The vibration of the rotor with the trial weight was recorded in this second run. At blade number 9 on the base circle, a circle was drawn using the amplitude of the second run as a radius $\overrightarrow{V_1}$. After that, the trial weight was removed.

This process was repeated with the same trial weight at blade number 1 (32.3°) and blade number 9 (281.5°), respectively. The intersection of the three circles connecting with the centre point of the base circle indicated the mass and the position of the correction weight, as shown in Figure 3.13. The correction weight can be calculated using

$$W_c = \frac{|\overrightarrow{V_0}|W_t}{|\overrightarrow{V_t}|} \tag{3.1}$$

where W_t was the mass of the trial weight.

Finally, the correction weight of 11.2 grams was added between blade 9 and blade 10 (274°). The vibration spectrum in Figure 3.14 shows a decrease in 1X vibration amplitude from 0.54 mm/s RMS to 0.22 mm/s RMS. Thus, the residual unbalance at 11.2 grams was located at 94°. Table 3.2 shows the four-run balancing record.

Notably, because the effect of the residual unbalance on the rotor vibration was small, the rotor unbalance was left at the original condition. In addition, balancing the impeller by removing the materials may have affected the structural integrity of the printed impeller.



Figure 3. 12 The setup of the four-run balancing method showing the signal channel accelerometer and an attached trial weight

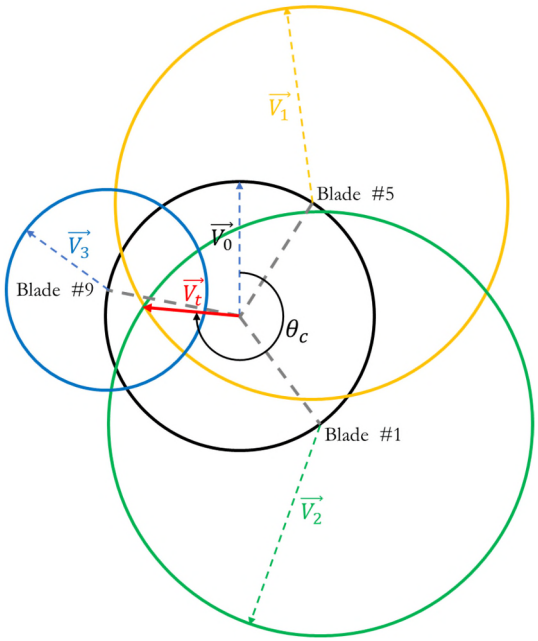


Figure 3. 13 The four-run balancing diagram

Table 3. 2 Balancing record of the four-run method

Run	Condition	Added weight (grams)	Position	Position (degree) ref to key phaser CW	1X vibration (mm/s RMS)
1	Original rotor	NA	NA	NA	0.54
2	Add trial weight #1	8	Blade #5 outlet	143	0.78
3	Add trial weight #2	8	Blade #3 outlet	32.3	0.83
4	Add trial weight #3	8	Blade #9 outlet	281.5	0.39
5	Add correction weight	11.2	Between blade #9 & blade #10	274	0.22

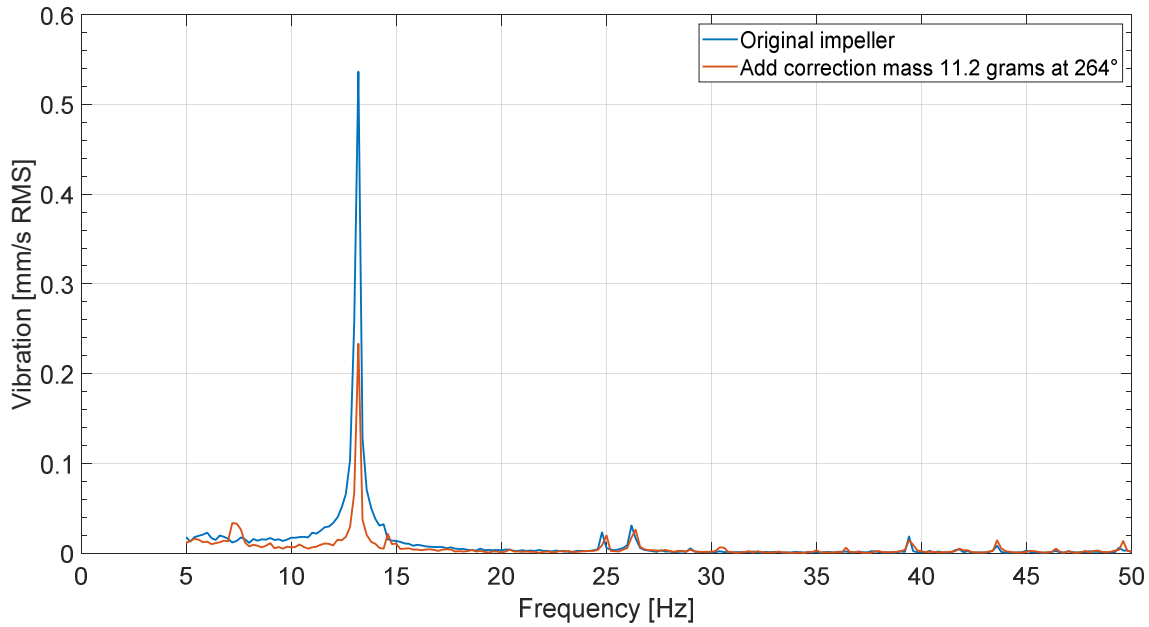


Figure 3. 14 Comparison of the FFT spectrum of the impeller before and after adding a correction weight

3.3.4 Blade resonance frequencies

The blade resonance frequency measurement aims to identify the resonance frequencies of individual blades of the printed impeller. This information was used to not only verify the printed impeller's quality in terms of mistuning, but also to plan the experiment, and validate the FEA model.

Blade resonance frequency measurement was performed using the impact testing method. In this method, the impeller blade was hit at the centre of the leading edge with a plastic hammer to cause it to vibrate at its natural frequency. Two measurement condenser microphones ECM8000 were placed on the top of the impeller, as shown in Figure 3.15. The sound pressure from a vibrating impeller blade was recorded using a National Instrument® DAQ system at a sampling rate of 100,000 Samples/s. The signal was captured for 0.5 seconds for a frequency resolution of 2 Hz. The capture period covered the period of vibration that died out (around 0.2 seconds). Figure 3.16 shows a blade response signal from impact testing.

Subsequently, the raw data was imported and performed signal processing on MATLAB®. The exponential window was applied to reduce the leakage effect and improve the signal-to-noise ratio, as recommended in an article by Fladung, W. A. (1997) [87].

Figure 3.17 shows an example of the FFT plot of the windowed blade response signal of blade number one. The distinctive peaks occurred at 814 Hz and 1,127 Hz. The predicted modal deformation from FEA in Figure 3.18 indicated that these two

frequencies might be the first and second blade vibration modes. These two blade modes were obtained in isolation from whole impeller vibration modes. Figure 3.19 shows the impeller twist and one-nodal diameter vibration modes compared to the first and second blade vibration modes. Obviously, the vibration modes of the whole impeller were lower than the blade vibration modes. This difference in vibration mode frequencies may relate to the design of the impeller with thin blades, in which the mass of each blade was a fraction of the total mass of the impeller.

When this impeller is rotated, these two blade modes could be excited by the harmonic of blade pass frequency (13X) at the impeller speed of 4,000 RPM and 5,200 RPM, respectively. Note that the error of the predicted first and second modes were 6.2 percent and 6.9 percent, respectively.

The comparison of the frequency response of individual blades is shown in Figure 3.20. It can be seen that each blade had two peak frequencies. However, the frequencies were slightly different, meaning that the printed impeller blades were not identical to the simulation model. Thus, the printed impellers in this study were mistuned. Notably, multiple impact tests were performed on each blade. Thus, the frequency response of blade number one appears to be different between Figure 3.17 and Figure 3.20.

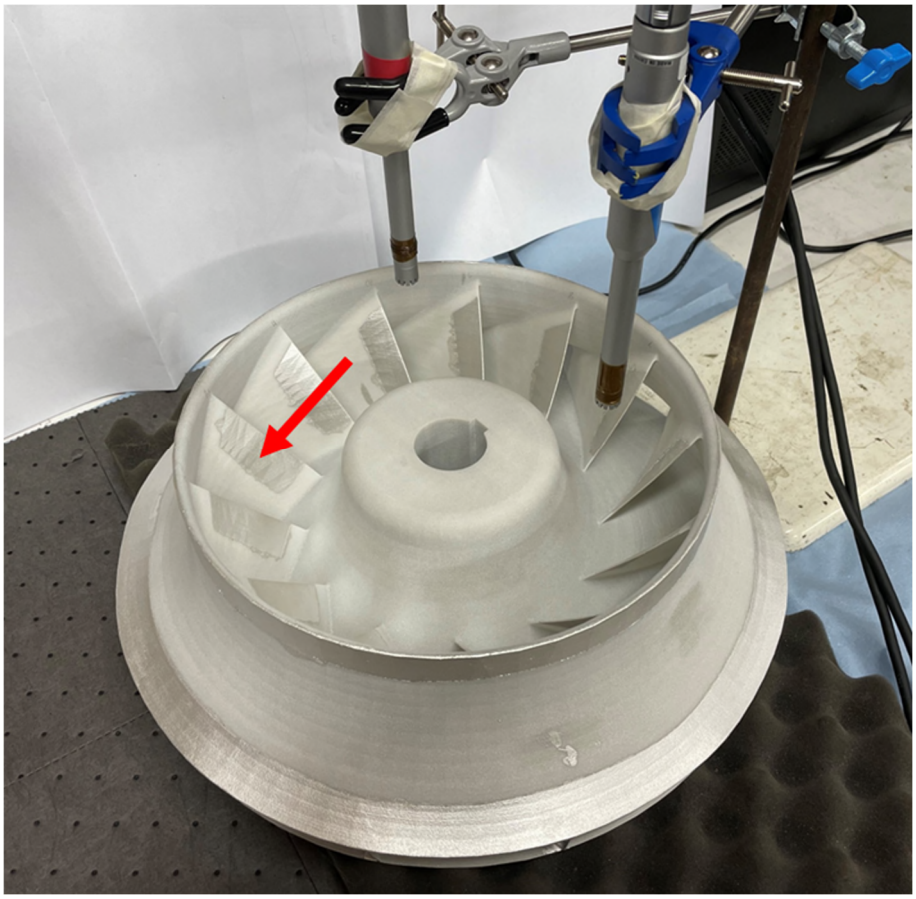


Figure 3. 15 A setup of blade natural frequencies measurement, the red arrow shows the point was impacted during the test

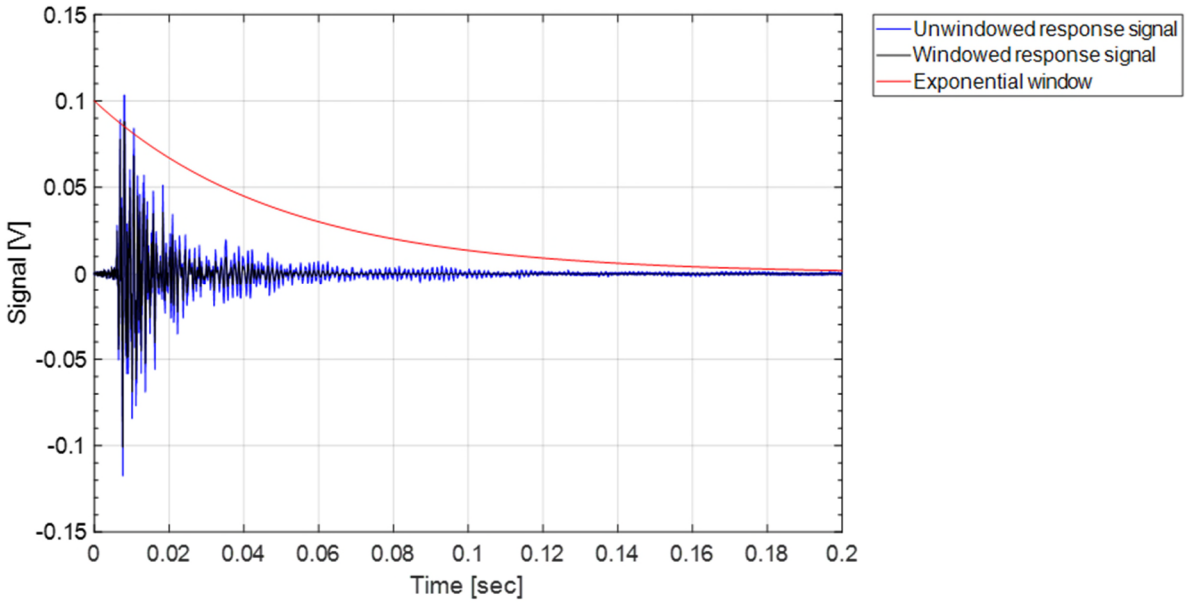


Figure 3. 16 Unwindowed and windowed response signals from impact testing

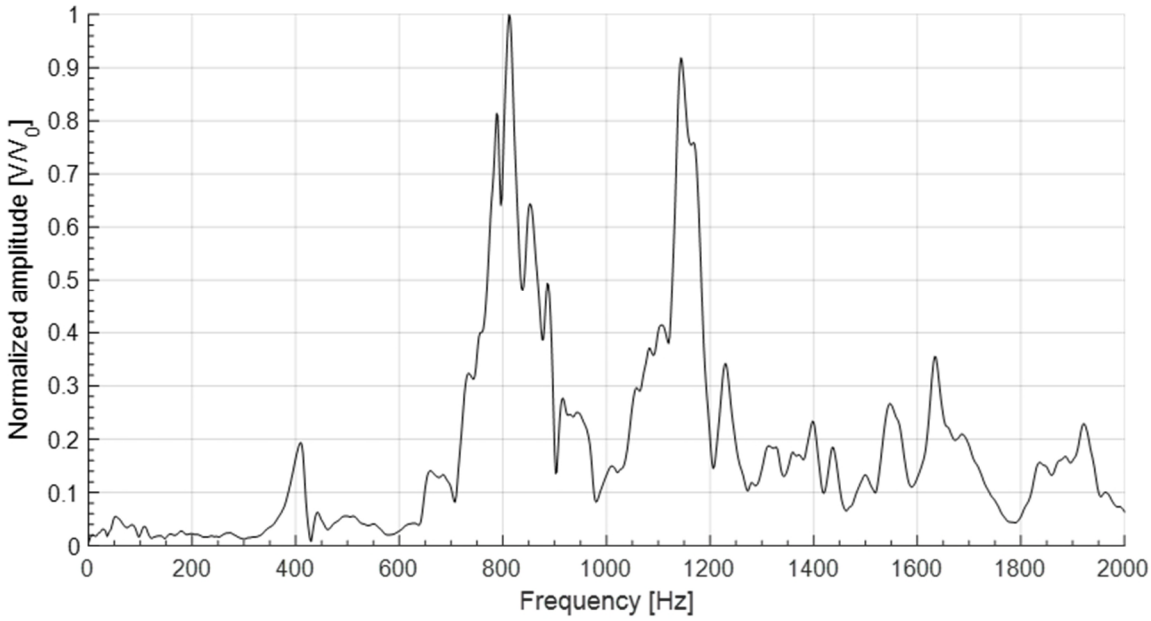
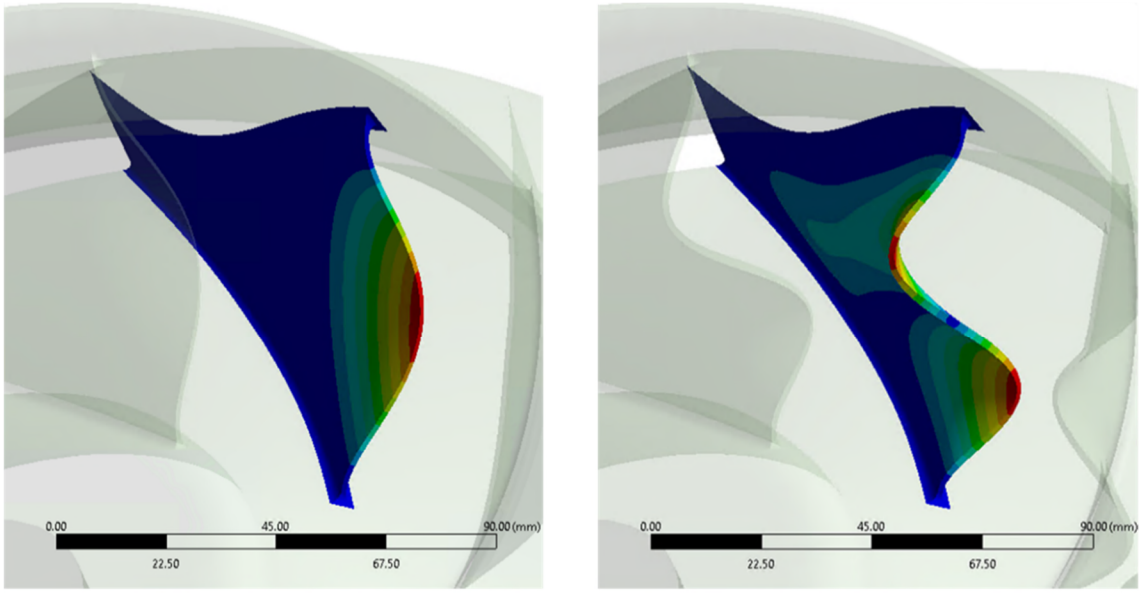


Figure 3. 17 An example of the FFT response of blade number 1, showing the distinctive peaks at 814 Hz or 1,127 Hz



(a) (b)

Figure 3. 18 The predicted blade modal deformations (a) the 1st mode at 865 Hz: and (b) the 2nd mode at 1,205 Hz

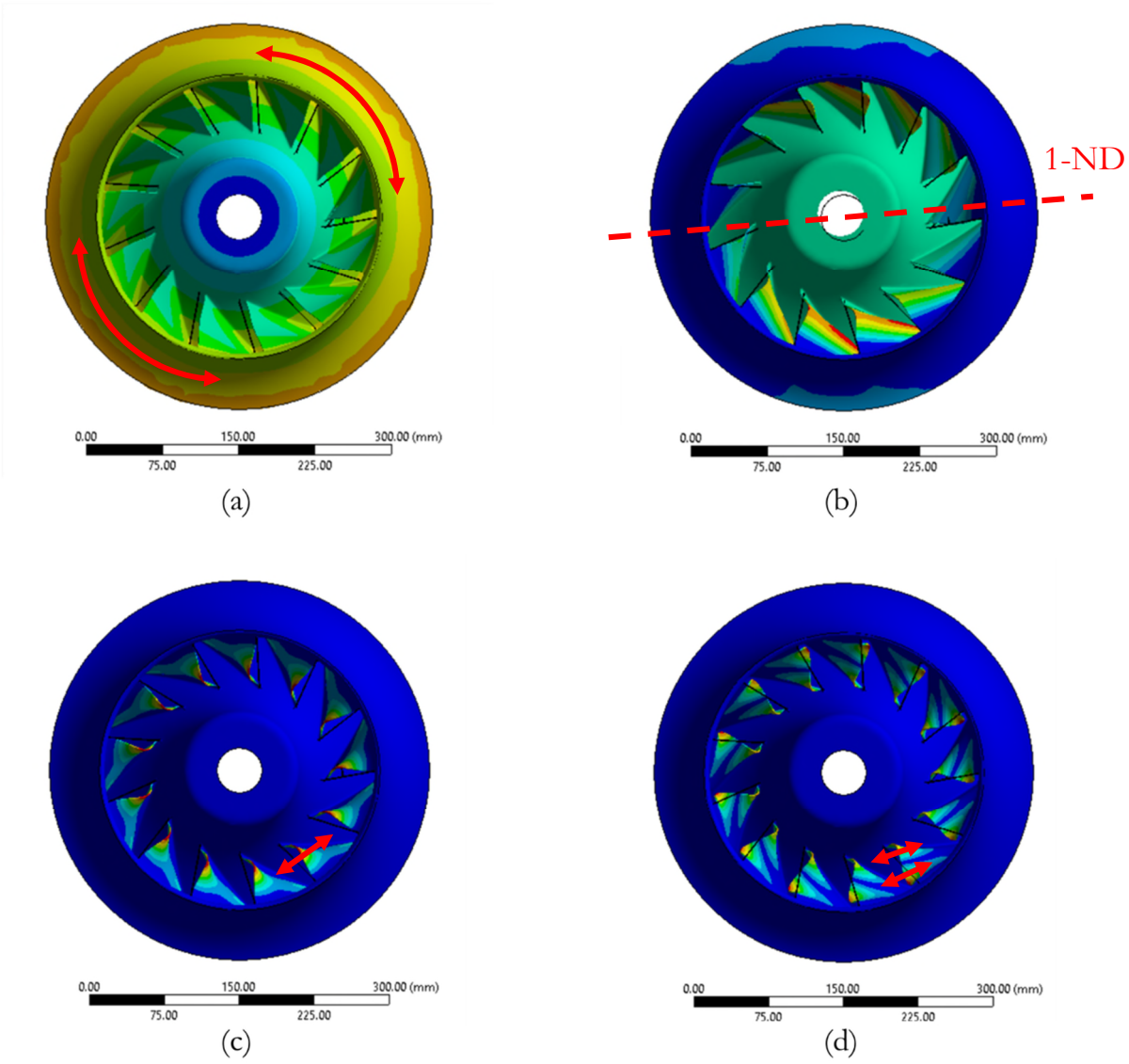


Figure 3. 19 Comparison between the whole impeller vibration modes and blade vibration modes, red arrows indicate the movement direction (a) the impeller twist mode at 260 Hz; (b) the impeller one-nodal diameter mode at 444 Hz; (c) the 1st blade mode at 865 Hz; and (d) the 2nd blade mode at 1,205 Hz

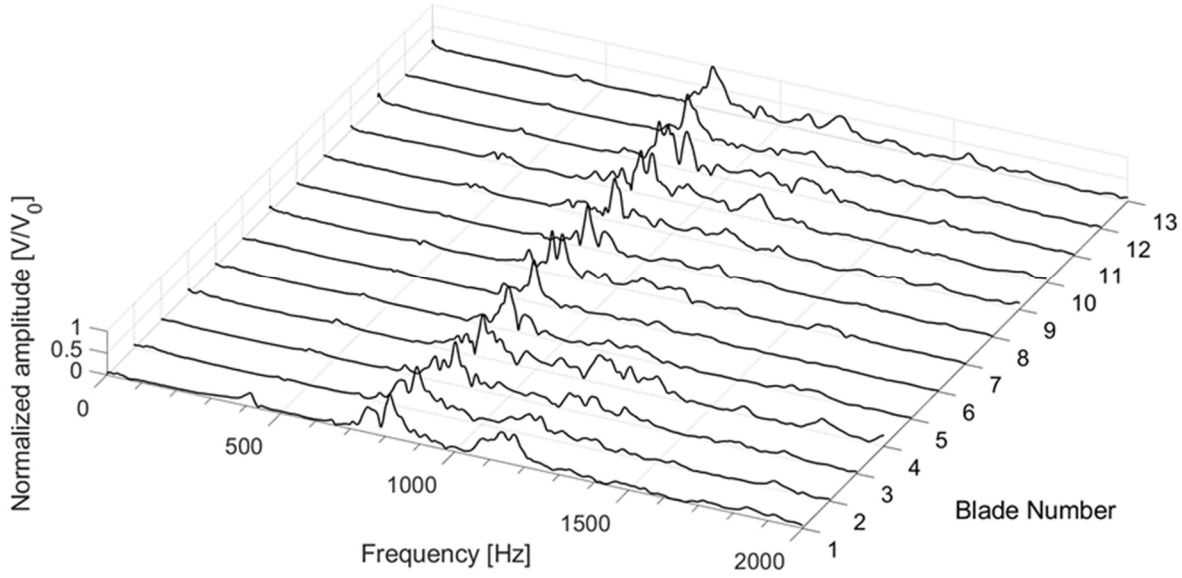


Figure 3. 20 Comparison of the windowed blade response signals of individual blades

3.4 Instrumentation

In these experimental studies, the deflections of a shrouded impeller were determined with the clearance measurements using in-house rectangular eddy current sensors developed at the University of Oxford [7]. These eddy current sensors have a rectangular coil design so that the coil is elongated on one side. The dimensions of the rectangular coil were 6.5 mm wide by 10.2 mm long by 6.25 mm high with a coil thickness of 1.5 mm. The outside diameter of the sensors, including the plastic cover, was 13 millimetres, so these sensors were referred to as 13-mm rectangular eddy current sensors.

The advantage of this sensor design is that it improves the sensor resolution when the object is aligned along the sensor's longitudinal section [88] and can be

customised to the shape of the target. On the other hand, installing the sensor is the disadvantage of this rectangular sensor design compared to commercial sensors with a circular coil design.

Thus, the eddy current sensor installation was the crucial step in the experiment setup. The sensors must be controlled to ensure each sensor is perpendicular to the target surface, except at the outlet shroud location. A digital dial gauge, a laser level and a linear sliding platform were used during sensor installation. An inclined sensor potentially affects measurement accuracy due to non-symmetric eddy current building up on the target surface. In addition, due to the distorted distance between the sensor and the target surface, the clearance conversion is inaccurate. However, this inaccurate clearance conversion may have less effect when considering the change of clearance (Δ clearance) because it could be considered a systematic error.

In this research, the eddy current sensors were placed in various locations to capture the impeller deflection, including the inlet shroud, the outlet shroud, and the back-end wall, as shown in Figure 3.21 (d) to (f), respectively. The electromagnetic simulation results from Chapter 4 were used to determine an area of detection and to ensure that there was no interference between the adjacent sensors.

Two 6-mm eddy current sensors were placed at the blade leading edges to capture the blade appearances for creating the Blade Tip Timing (BTT) signals. These small-sized sensors were chosen for detecting the leading edges with a thickness of 1 mm. In addition, another sensor was placed at the blade trailing edge as shown in Figure

3.21 (c). The outlet BTT signal in terms of the time of arrival (TOA) was determined from the output of this sensor.

Note that installing a sensor in these two locations is not practical with industrial impellers because it obstructs the gas flow path. However, they were included in these experiments so that the conventional and the proposed methods could be compared.

To create a 1/rev signal for rotor speed calculation, another 13-mm eddy current sensor was placed at the shaft key, as shown in Figure 3.21 (a). The 1/rev signal was also used to synchronise the BTT and the clearance signals for each revolution. The schematic diagram in Figure 3.22 (a) shows the circumferential locations of each sensor relative to the speed sensor. The list of sensors and their locations are shown in Table 3.3.

In addition, two accelerometers were mounted at the support bearing and the sensor holder ring to monitor the test rig's vibration during experiments, as shown in Figure 3.21 (e) and (f), respectively.

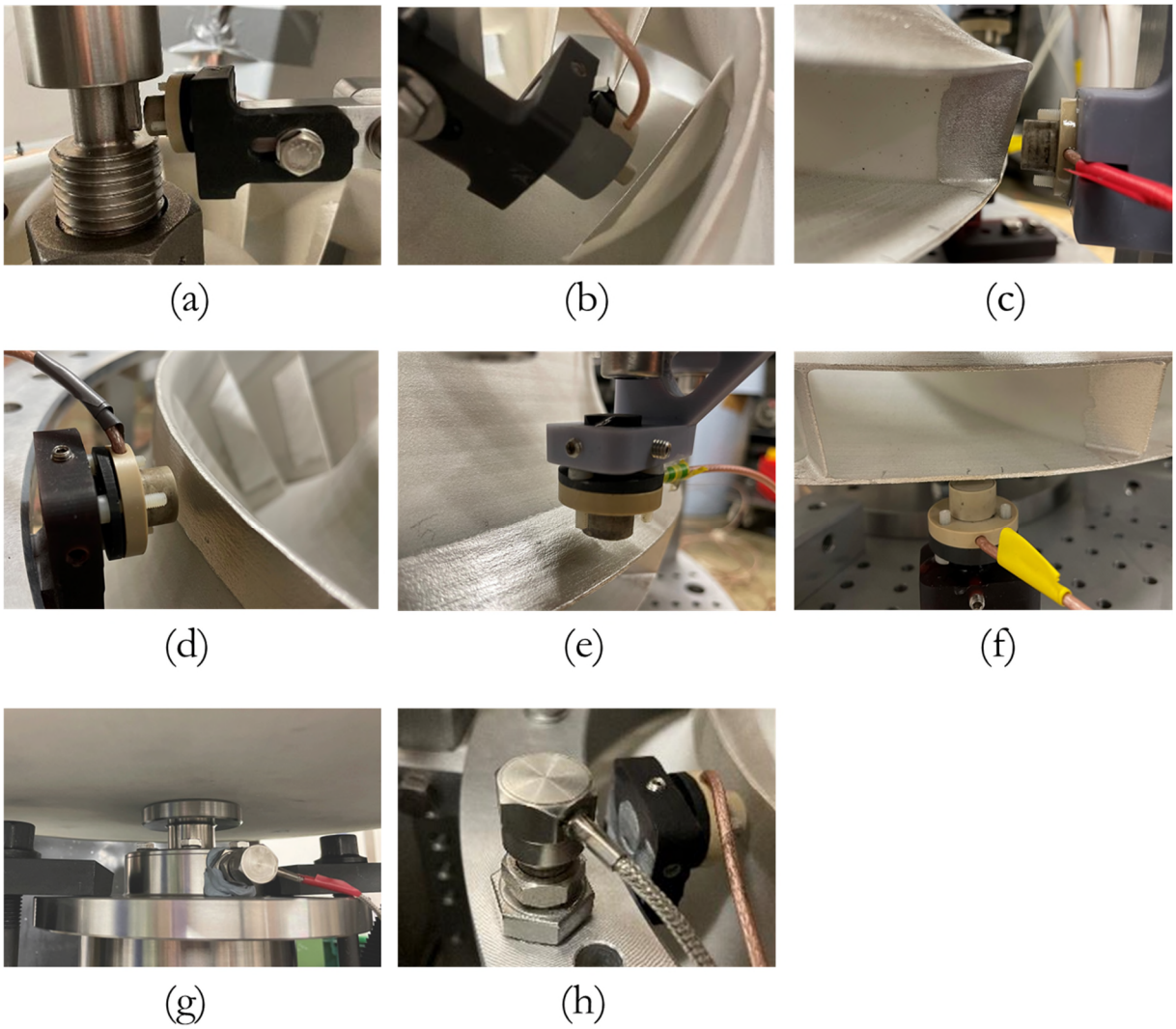


Figure 3. 21 Sensor mounting locations (a) 1/rev (speed) sensor; (b) BTT sensor at the inlet blades; (c) BTT sensor at the outlet blades; (d) clearance sensor at the inlet shroud; (e) clearance sensor at the outlet shroud; (f) clearance sensor at the back-end wall; (e) accelerometer on the bearing support; and (h) accelerometer on the sensor holder ring

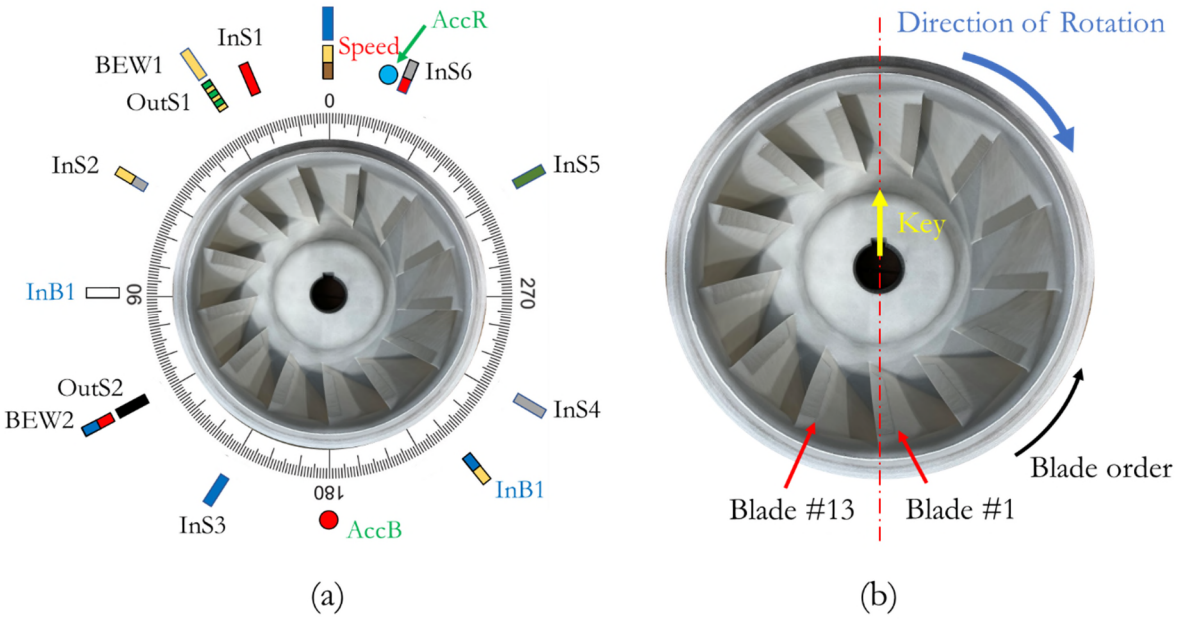


Figure 3. 22 The schematic diagram of the sensors (a) sensor locations; and (b) the direction of blade order is opposite to that of the rotor rotation (CW)

Table 3. 3 Sensors and locations

No.	Sensor tag	Measurement	Type	Location, ref to speed sensor (degree)
1	Speed	1 per rev	13-mm Eddy current sensor	0
2	InB1	BTT at inlet blades	6-mm Eddy current sensor	90
3	InB2	BTT at inlet blades	6-mm Eddy current sensor	220
4	OutB	BTT at outlet blades	13-mm Eddy current sensor	0
5	InS1	Inlet shroud clearance	13-mm Eddy current sensor	20
6	InS2	Inlet shroud clearance	13-mm Eddy current sensor	60
7	InS3	Inlet shroud clearance	13-mm Eddy current sensor	150
8	InS4	Inlet shroud clearance	13-mm Eddy current sensor	240
9	InS5	Inlet shroud clearance	13-mm Eddy current sensor	300
10	InS6	Inlet shroud clearance	13-mm Eddy current sensor	340
11	OutS1	Outlet shroud clearance	13-mm Eddy current sensor	30
12	OutS2	Inner-inlet shroud clearance	13-mm Eddy current sensor	120
13	BEW1	Back-end wall clearance	13-mm Eddy current sensor	30
14	BEW2	Back-end wall clearance	13-mm Eddy current sensor	120
15	AccB	Vibration of the bearing support	Accelerometer 100mV/g	180
16	AccR	Vibration of the sensor holder ring	Accelerometer 100mV/g	345

3.5 Signal processing

Signal processing is the crucial step to obtaining the deflection of the whole rotor. Figure 3.23 shows the signal processing diagram of the 1/rev, Blade Tip Timing, and clearance signals. After raw data was imported into MATLAB®, signals from each data acquisition (DAQ) card must be synchronised first because four DAQ cards were used to receive simultaneous signals from the 13 sensors in these experiments. Then, the FIR lowpass filter was applied for noise elimination.

Blade passing and clearance signals were divided into periods of rotor revolution using the peaks of the 1/rev signals. These peaks were located using the integral method proposed by Chana et al. (2016) [8]. A peak for each revolution is defined as a point when the area over a threshold reaches 50% of the total area. This can be calculated using the trapezoidal rule, as given by equation 3.2.

$$\int_a^b f(x)dx \approx \frac{b-a}{2N}\sum_{n=1}^{N}\left(f(x_n)+f(x_{n+1})\right) \qquad (3.2)$$

The time differences between the two successive peaks were used to measure the rotor speed. The integral method was also used to locate peaks of the blade passing signals to calculate the inter blade time of arrival. Figure 3.24 shows the comparison of the synchronised 1/rev, blade passing, and clearance signals.

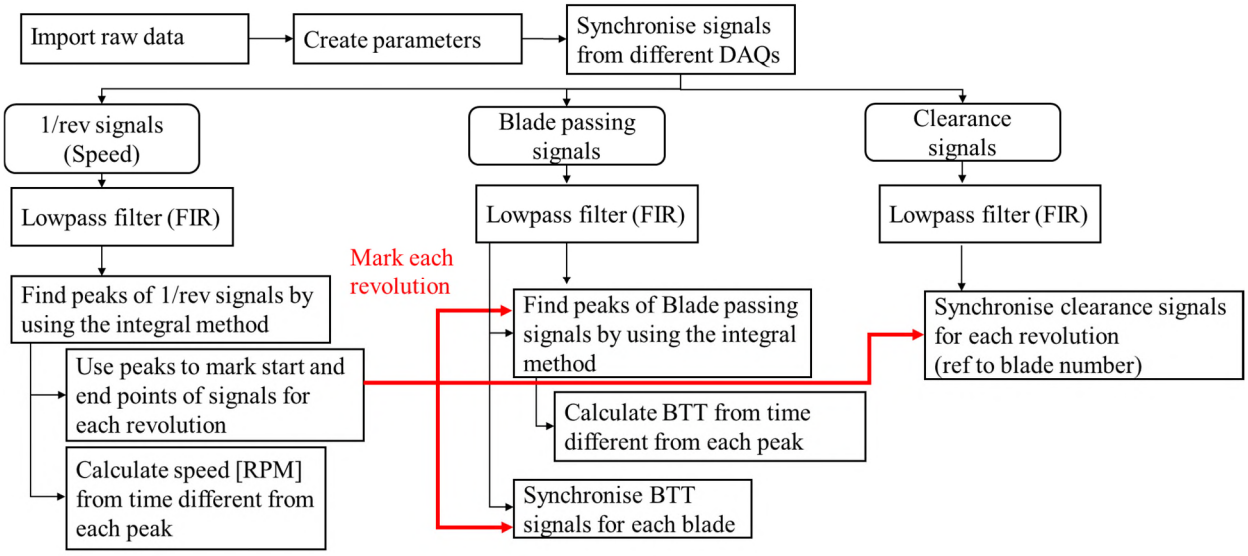


Figure 3. 23 Signal processing diagram of 1/rev (speed), Blade Tip Timing, and clearance signals

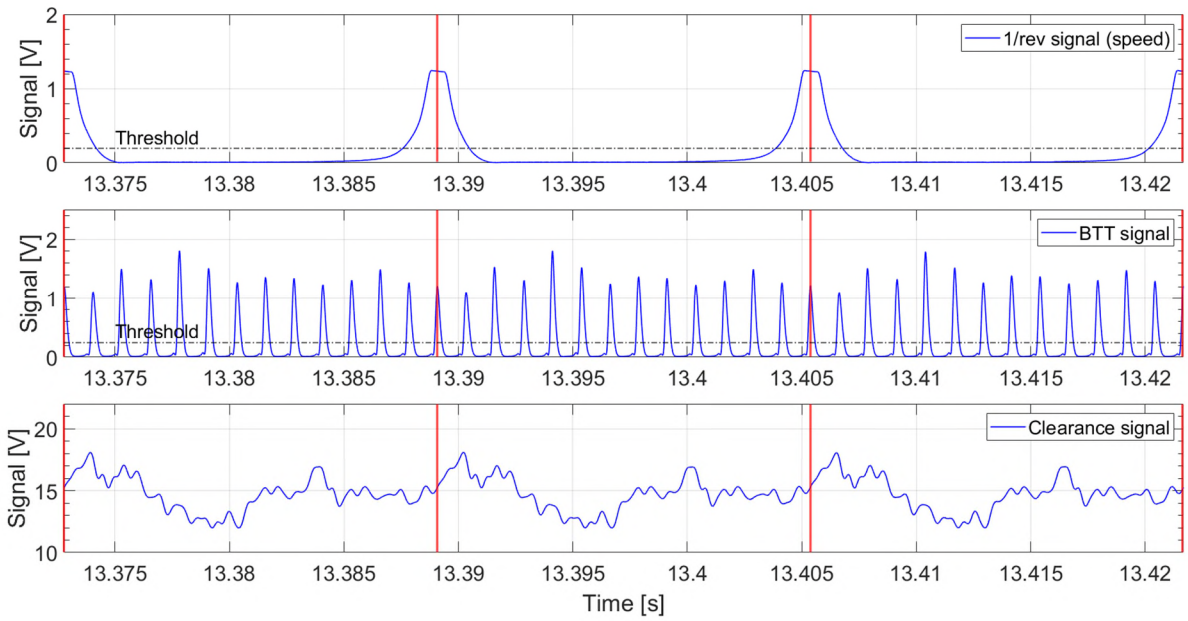


Figure 3. 24 The synchronised blade passing, and clearance signals compared to the speed signal

3.6 Eddy current sensor calibration for clearance measurement

The eddy sensor calibration of the clearance signals was performed to convert the measured signals to the absolute clearance, which links to the rotor deflection. The process of the calibration, results and measurement uncertainty are explained in the following sections.

3.6.1 Calibration for clearance measurement

In this calibration, the impeller was driven by the milling machine at the speed of 100 RPM. The sensor calibration was conducted in three locations: inlet shroud, outlet shroud and back-end wall, as shown in Figure 3.25. For each location, the 52 calibration positions were the same as where the impeller runout was measured in section 5.3.2. The known clearance was set up between a sensor tip and the maximum runout position at that location. The digital dial gauge, the laser level, and the linear sliding platform were used to determine the accuracy of the clearance.

Given that the sensor clearance for each position depends on the local impeller runout, the range of the sensor calibration was selected to cover the clearances of the maximum and minimum runout positions. However, this range was within the sensor's measurement range, as shown in Figure 3.26. At the inlet shroud location, for example, eddy current sensors were calibrated over a 0.4 to 3.5 mm range in the increments of 0.05 mm.

Figure 3.27 shows the inlet shroud signals at different sensor clearances compared with the impeller runout. The amplitude of the clearance signal was inversely

proportional to the increase of clearance between the sensor and the impeller's shroud. The fluctuation of the signals might be the effect of the non-uniform thickness of the electric paint applied on the impeller. To create calibration curves, the clearance signals were extracted at 52 positions corresponding to the measured runout positions.

The plot of the sensor output against the sensor clearance in reference to blade number 11 is shown in Figure 3.28. Notably, only data from 13 positions are presented in this Figure. It can be seen that the signal output depended on the sensor clearance and the inlet shroud position. The calibration curve in Figure 3.29 shows the quadratic equation relationship between the sensor clearance and the output signal. Therefore, the calibration curve for each position was fitted with the quadratic equation,

$$y = ax^2 + bx + c. \tag{3.3}$$

This quadratic equation relationship was consistent with the predicted results from the electromagnetic simulation in Chapter 4. Finally, the 52 calibration coefficient sets were separately applied to convert the signals to clearances for each measurement location. Notably, this calibration method was time-consuming and may not be suitable for the clearance sensor calibration of an actual industrial machine. The simplified calibration method for an industrial machine was proposed in Chapter 8.

As mentioned in the previous paragraph, since the sensor clearance for each position is related to the local impeller runout. The absolute clearance for each

position was thus the setup clearance plus the difference of the runout at that position to the reference location. The plot between the absolute clearance versus the signal output from the selected 13 locations is presented in Figure 3.30. These locations correspond with the blade and shroud connecting locations at the inlet side. The sensitivity of the eddy current sensor is high at the closer clearance, and vice versa. The fact that calibration curves from different positions were not perfectly aligned might be due to the effect of the conductive paint thickness on the intensity of the eddy current. Therefore, the calibration coefficients were calculated separately at each position.

This calibration process was repeated for eddy current sensors measured at the outlet shroud and the back-end wall positions. Figures 3.31 and 3.32 show the clearance signal from the clearance sensor at the outlet shroud and the back-end wall, respectively. Notably, the calibration of the clearance measurement system was performed through the same DAQ system used in the experiments.

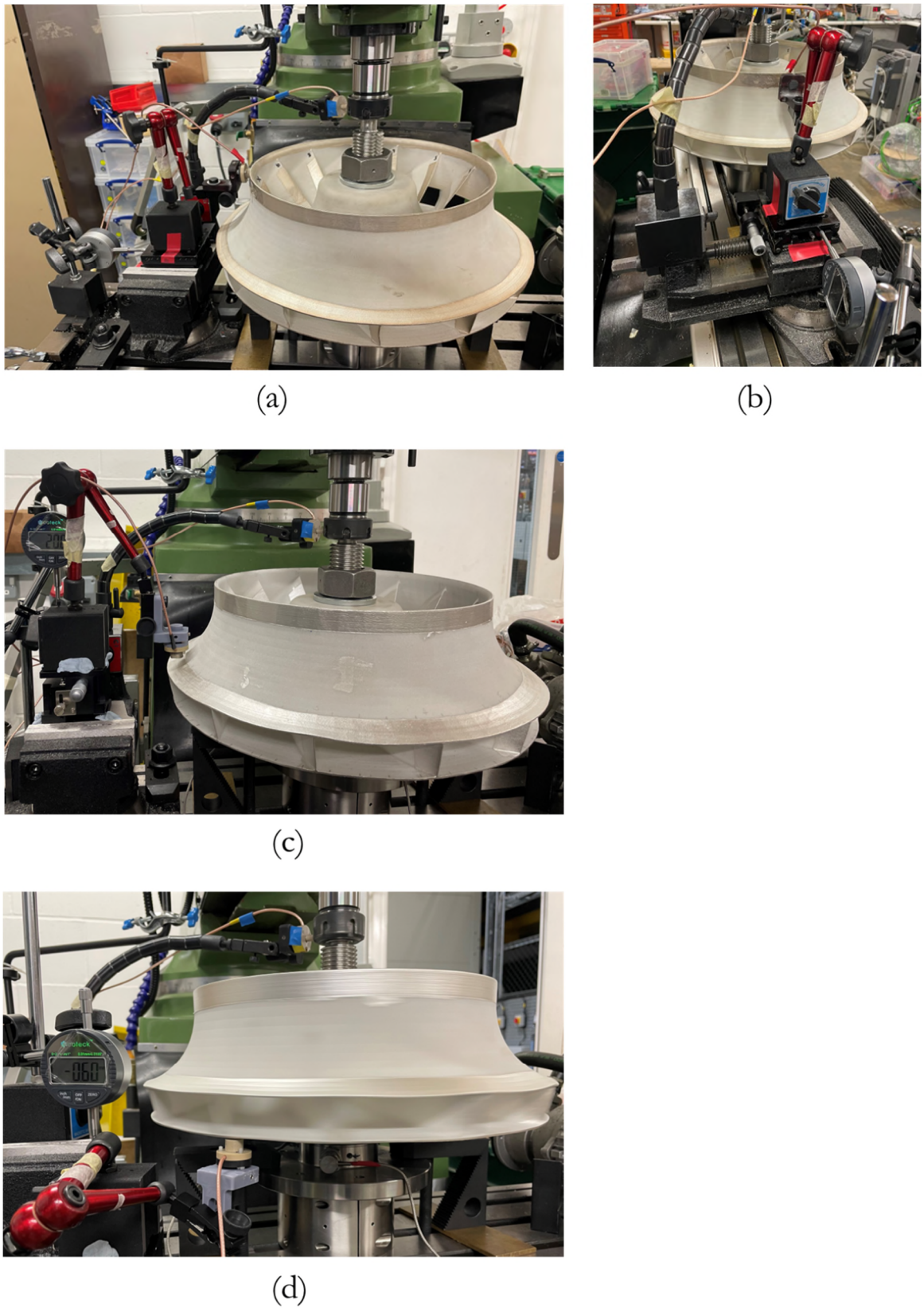


Figure 3. 25 The setup of sensor calibration at the speed of 100 RPM (a) and (b) at the inlet shroud location; (c) at the outlet shroud location; and (d) at the back-end wall location

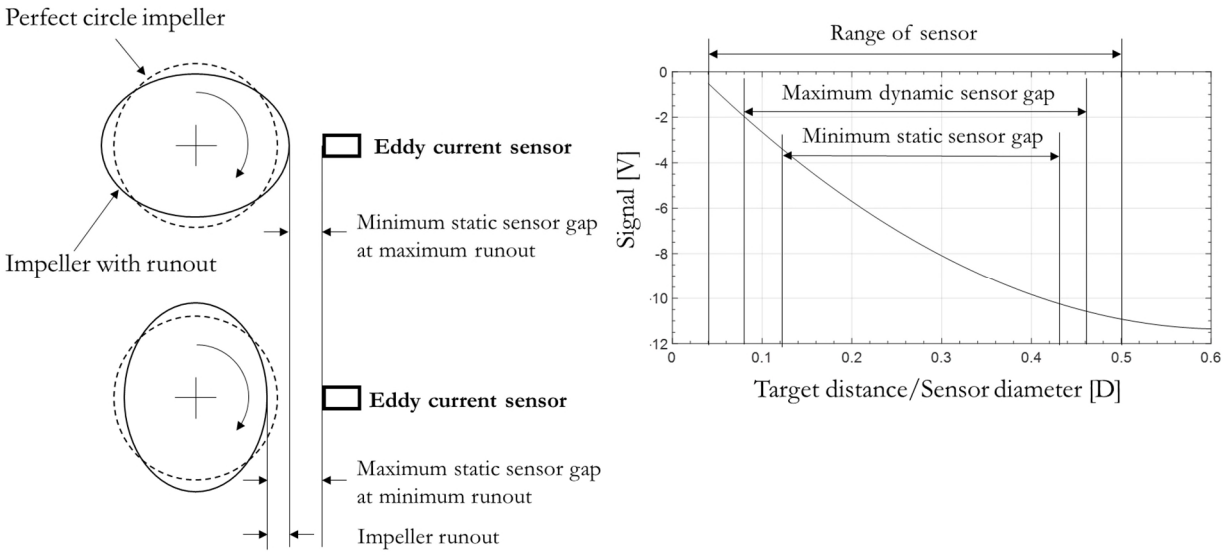


Figure 3. 26 The range of eddy current sensor calibration

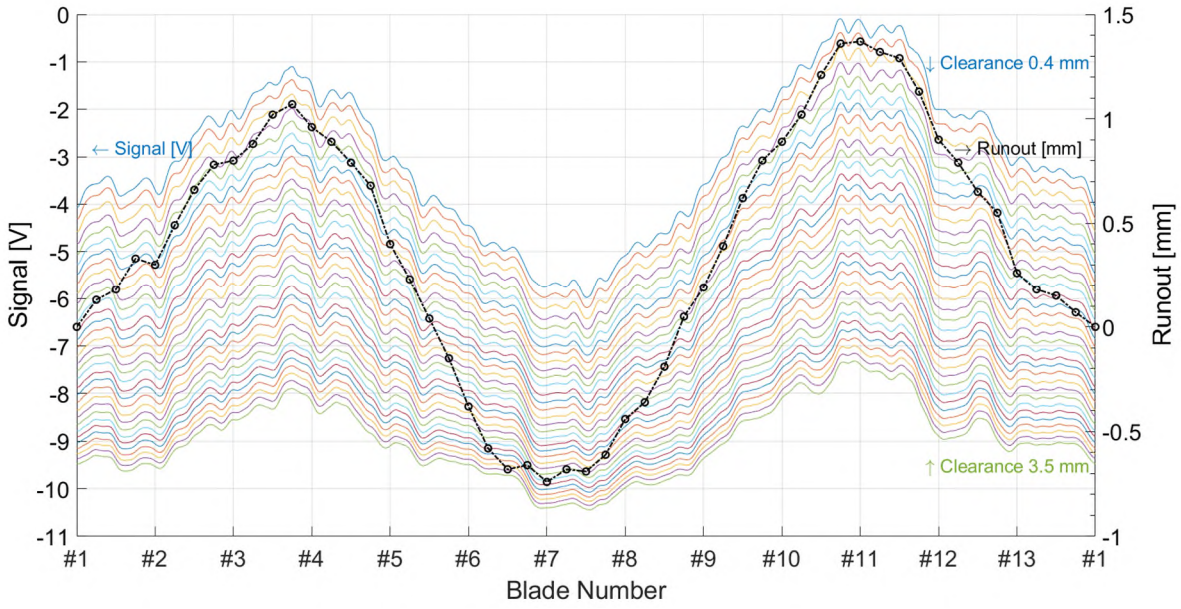


Figure 3. 27 Inlet shroud signals at different sensor clearances as compared to the impeller runout

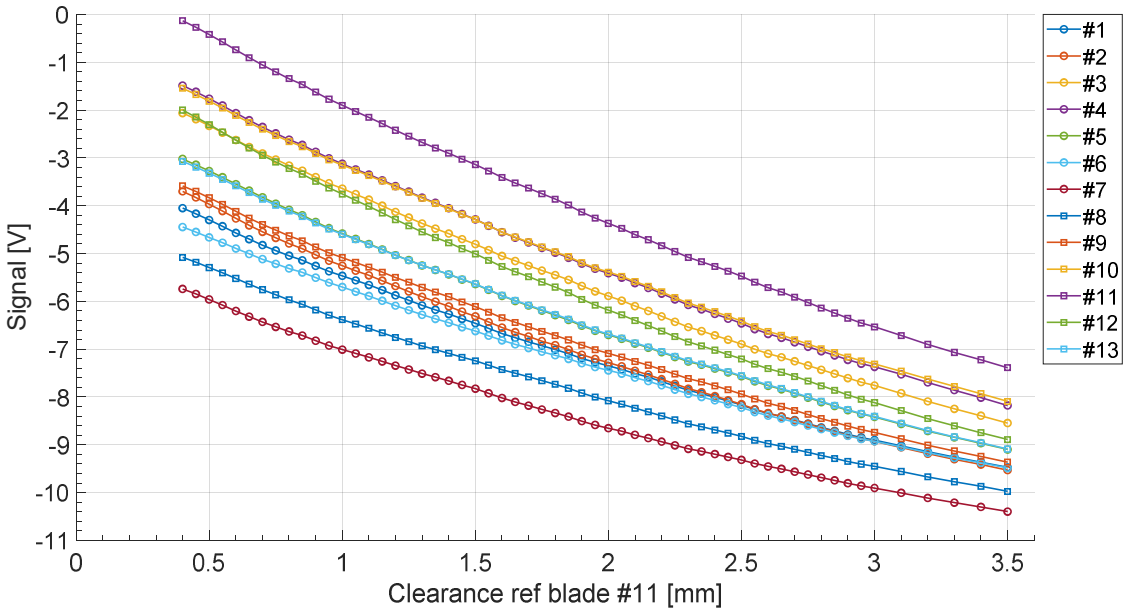


Figure 3. 28 The relation between the sensor output signal and the sensor clearance in reference to blade number 11, only 13 positions shown

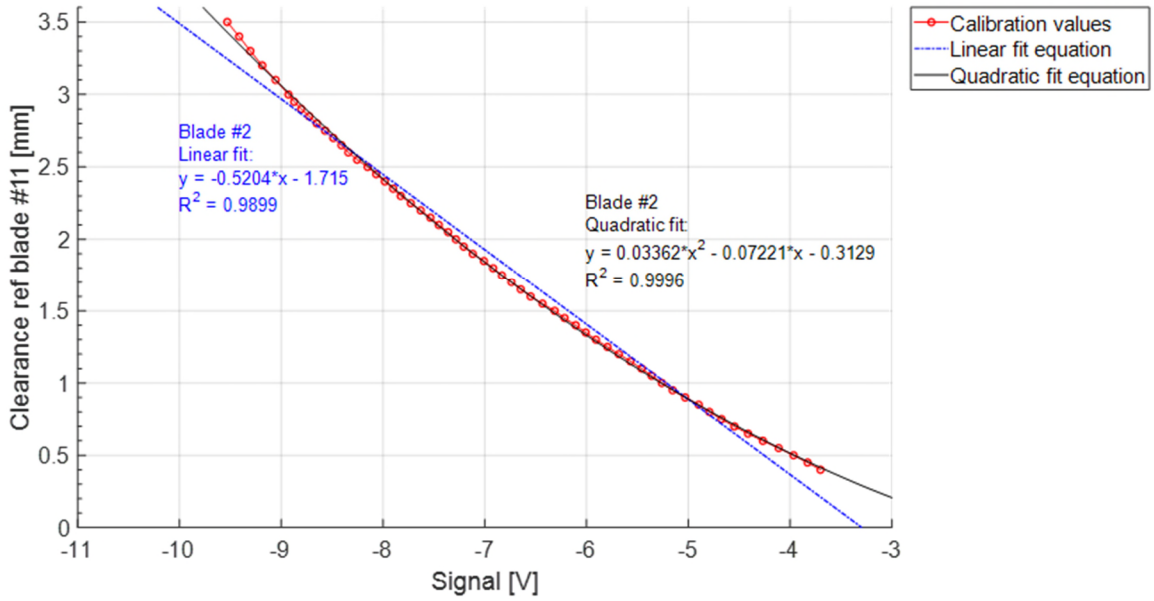


Figure 3. 29 The quadratic relation between the sensor clearance and the output signal

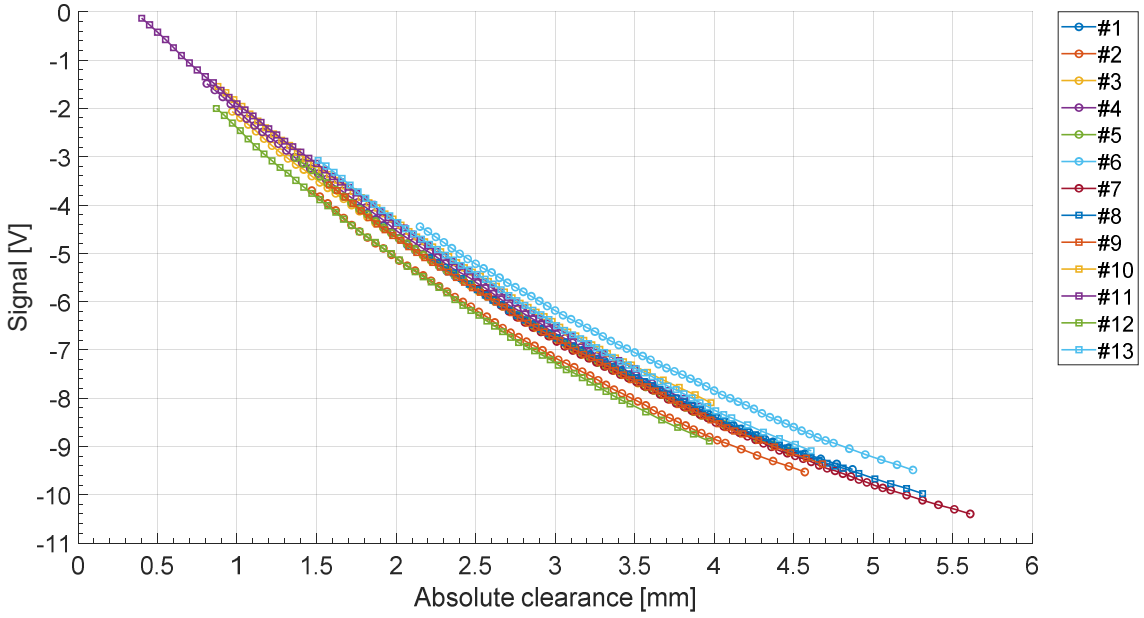


Figure 3. 30 The relation between the sensor output signal and the absolute clearance, only 13 positions shown

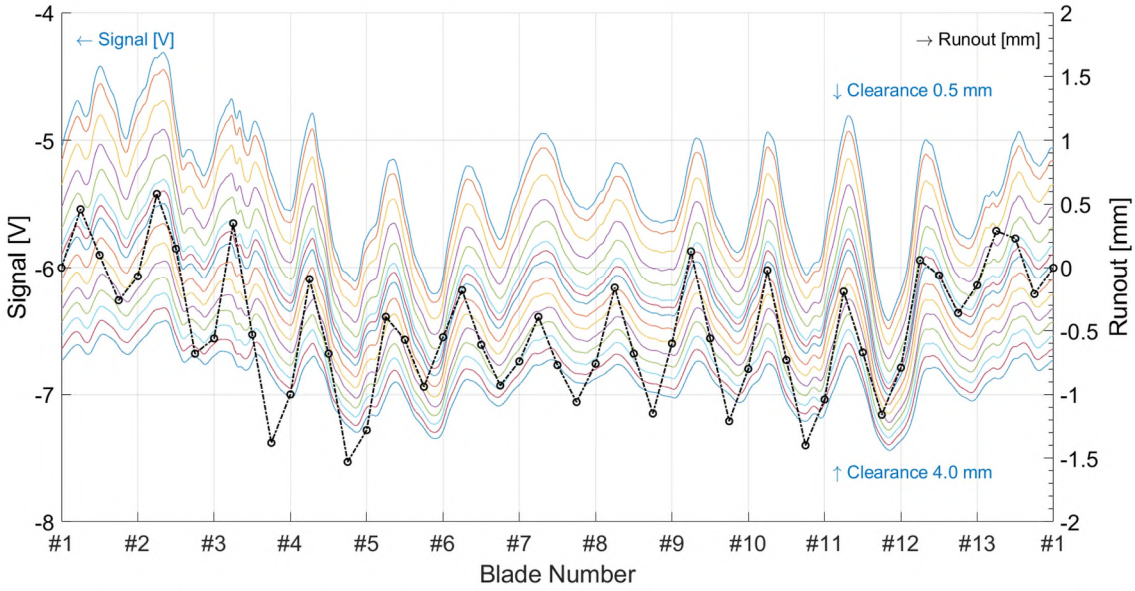


Figure 3. 31 Outlet shroud signals at different sensor clearances as compared to the impeller runout

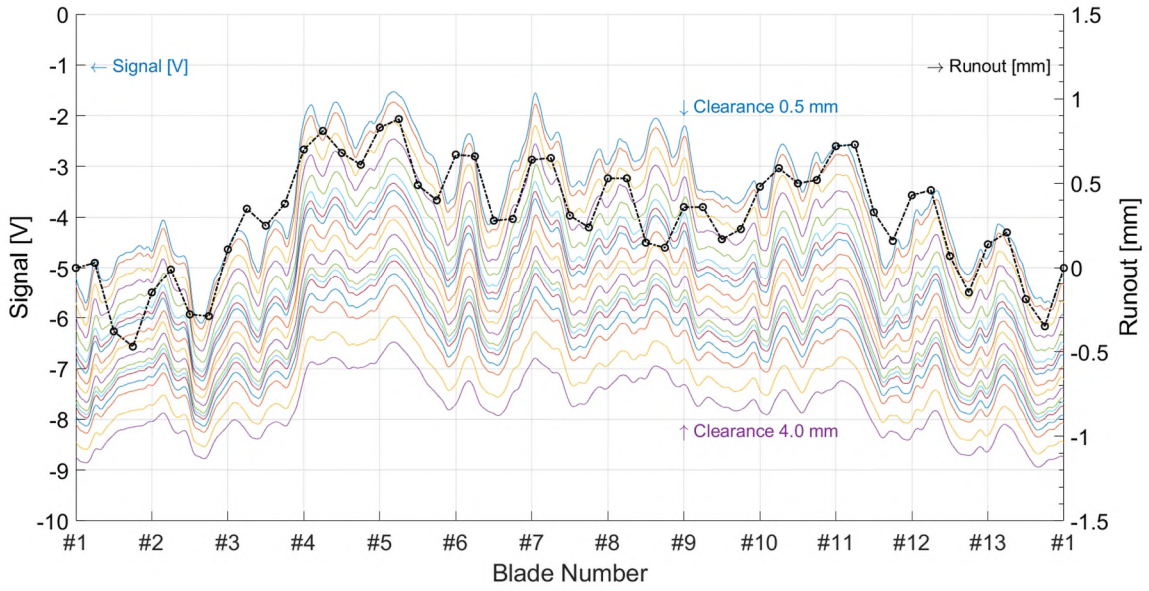


Figure 3. 32 Back-end wall signals at different sensor clearances as compared to the impeller runout

3.6.2 Uncertainty analysis of the clearance measurement system

The uncertainty analysis was performed in order to consider all error sources that contribute to the measurement uncertainty of the clearance measurement system. The sources of measurement errors consisted of the random measurement error and the systematic measurement error from instruments [112]. The results indicated the limitations of the clearance measurement in terms of the minimum clearance that can be detected. This uncertainty, in turn, was related to the minimum detectable crack size on an impeller's blade.

In the part of random error (u_r), the experimental uncertainty was calculated based on Student's t-distribution of 50 data sets with a 99% confidence interval. Each data set was acquired from one rotation of the impeller. Thus, 50 data sets meant 50 impeller revolutions. Figure 3.33 shows the overlaid diagram of the clearance

signals. The inlet shroud signals were measured at a 2-mm clearance in reference to the blade number 11 position. The experimental uncertainty (random error), u_r, is defined as

$$u_r = \pm \frac{t_{n-1}S}{\sqrt{n}}. \quad (3.4)$$

where S, and n are the standard deviation and the number of measurements. The uncertainty of the clearance signals in mV is shown in Figure 3.34. The experimental uncertainty fluctuated along the measurement positions. The uncertainty for each measurement position was extracted at 52 positions corresponding to the measured runout positions. Figure 3.34 shows the uncertainty in mV against the absolute clearance.

The experimental uncertainty in terms of μm was converted using the calibration equation acquired in the previous section. Thus, the random error of the clearance measurement system (total of 52 positions) was less than ±3.5 μm, as shown in Figure 3.36.

In the part of systematic error (u_t), due to the use of in-house sensors that lacked a manufacturer datasheet, the specification of the clearance measurement system from Monitran® [111] was used for estimating instead. Notably, in the experiments, the in-house eddy current sensors were modified from Monitran® MTN/EP340F sensors. These sensors were used together with Monitran® MTN/ECPD drivers.

According to the manufacturer's datasheet, the linearity of the clearance measurement system (combined sensor, cable, and driver) was 0.1% of full-scale

output (FSO). The system had a sensitivity of 2 mV/μm and FSO of 16 V. Therefore, the nonlinearity could result in a systematic error of ±16 mV, which corresponds to an uncertainty of ±8 μm.

The total measurement uncertainty was calculated by the following equation,

$$u_t = \sqrt{{u_r}^2 + {U_s}^2}. \tag{3.6}$$

or

$$u_t = \sqrt{7^2 + 16^2} = 17.5\ \mu m.$$

Therefore, the measurement uncertainty of the clearance system used in the experiments was less than ±9 μm.

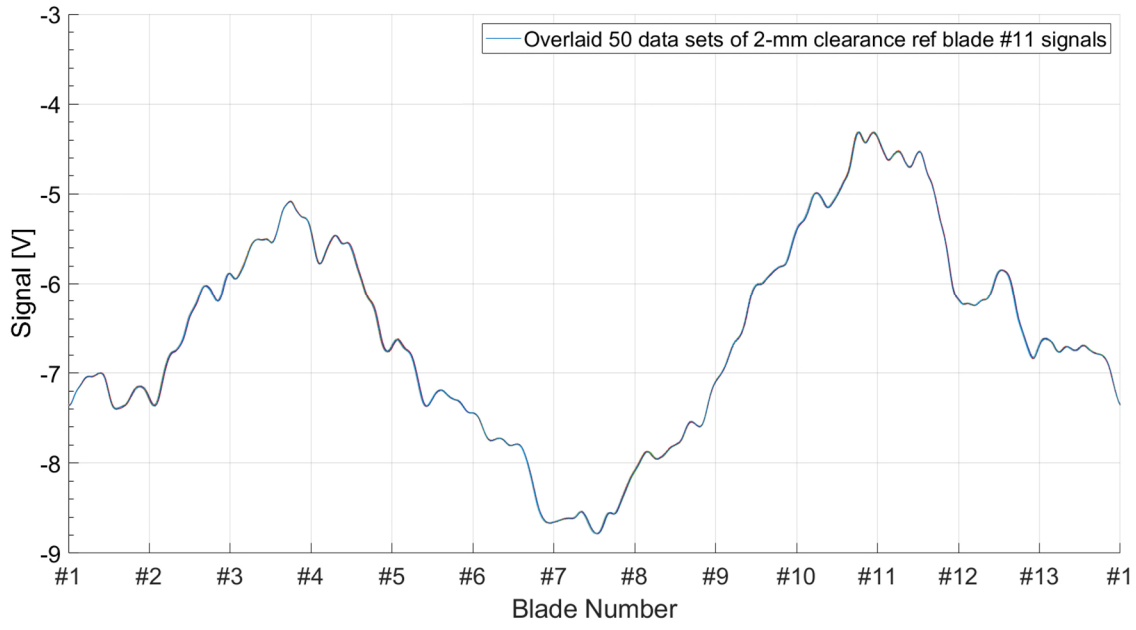


Figure 3. 33 The overlaid 50 data sets of the inlet shroud clearance signals at 2-mm clearance (referring to blade #11)

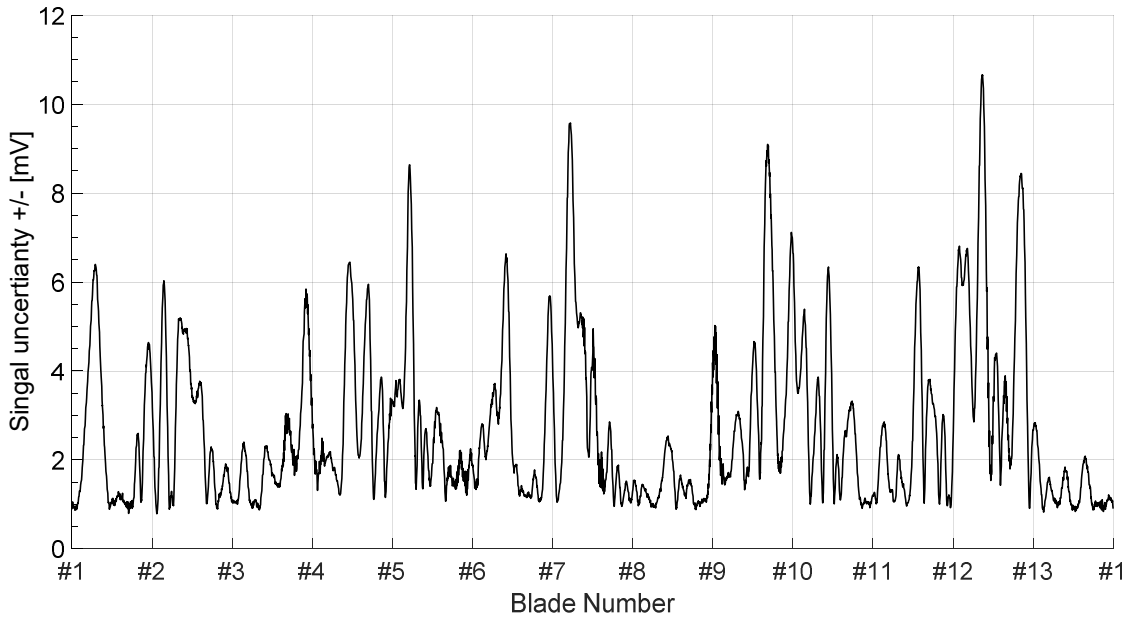


Figure 3. 34 The uncertainty of the clearance signals at 2-mm clearance (referring to blade #11)

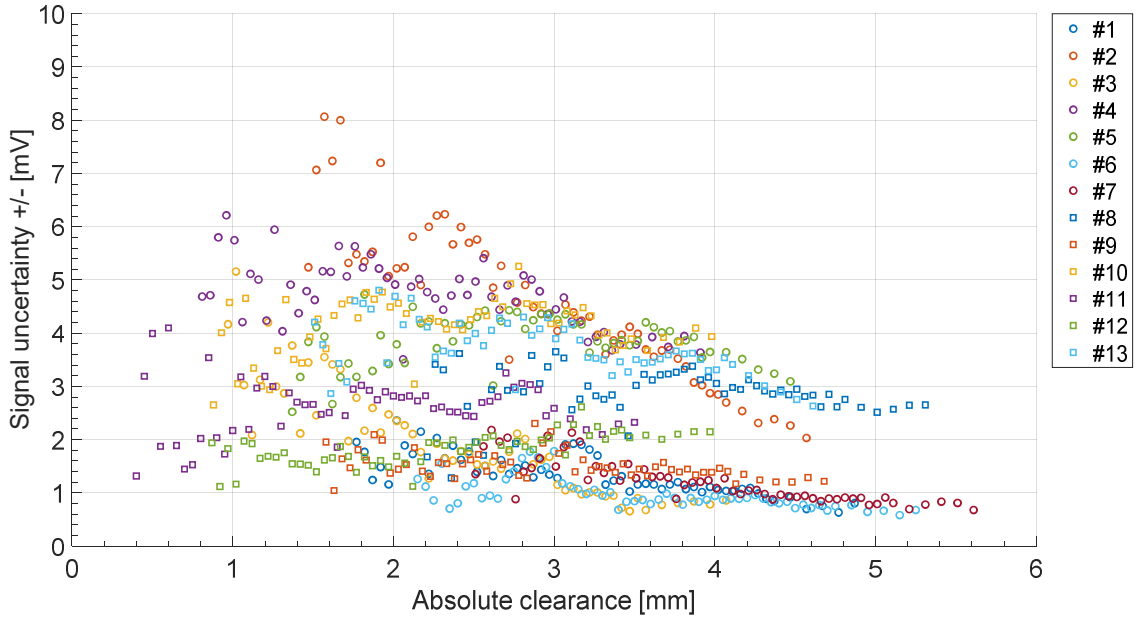


Figure 3. 35 The uncertainty of the clearance signals versus the absolute clearances, only 13 measurements shown

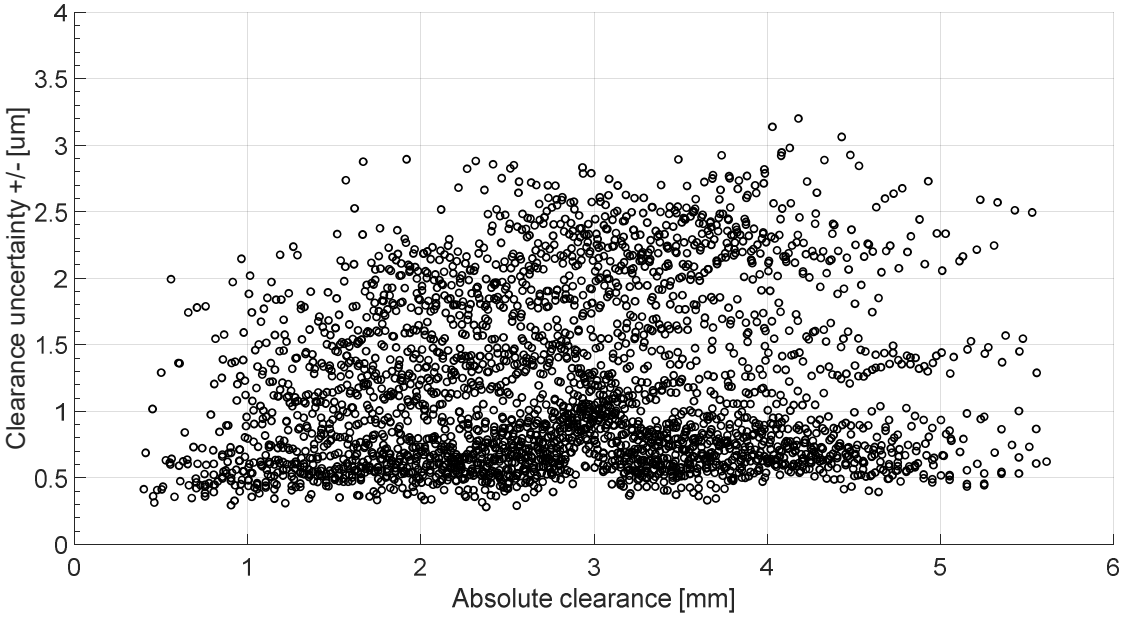


Figure 3. 36 The uncertainty of the clearance measurement system, all 52 measurement positions

3.7 Chapter conclusion

This chapter described the design, fabrication, and functionality of the high-speed spinning rig for the scaled impeller, which was the key component of this research. The scaled impeller with 1-mm-thick blades was 3D-printed using additive manufacturing. The shape of the scaled impeller was based on an actual compressor impeller. The characteristics of the scaled impeller, including the runout, the residual unbalance, and the blade resonant frequencies were measured for reference. Conductive paint was applied on the impeller at the target locations for the clearance measurements using eddy current sensors. The instrumentation section explains the sensor types, associated electronics, and their installation locations. The eddy sensor

calibration for clearance measurement was performed. The uncertainty analysis showed that the uncertainty of the clearance measurement was less than ±9 μm.

Chapter 4

Computational Electromagnetic Simulations

4.1 Introduction

The purpose of computational electromagnetic simulations is to determine the response of an eddy current sensor used in the experiments. The Finite Element Analysis (FEA) were performed by solving the Maxwell's equations together with the equation of continuity, both in the case of the sensor alone and with the interaction between the sensor and the target.

Maxwell's equations consist of

1) Gauss' law for electric fields: $\vec{\nabla}.\vec{E} = \frac{\rho}{\varepsilon_0}$, (4.1)
2) Gauss' law for magnetic fields: $\vec{\nabla}.\vec{B} = 0$, (4.2)
3) Faraday's law: $\vec{\nabla} \times \vec{E} = -\frac{\partial \vec{B}}{\partial t}$, (4.3)
4) Ampere-Maxwell's law: $\vec{\nabla} \times \vec{B} = \mu_0 \left(\vec{J} + \varepsilon_0 \frac{\partial \vec{E}}{\partial t}\right)$. (4.4)

In addition, the equation of continuity can be written as:

$$\vec{\nabla}.\vec{J} = -\frac{\partial \rho}{\partial t}. \quad (4.5)$$

The electromagnetic field in the frequency domain was modelled through the AC/DC module of COMSOL Multiphysics®, a commercial finite element software. These simulations comply with the characteristics of the eddy current sensor and the target, which is coupling between the alternating magnetic field and induced currents.

4.2 Low-frequency electromagnetic simulation model

The inductive coil of an eddy current sensor was simulated using the software's coil features. These features are suitable for creating a low-frequency electromagnetic model in which an electric current passing through a conductive material produces a magnetic field. The term low-frequency is defined as an instant when the maximum dimension of a modelling object, L_c, is less than one percent of the free space wavelength of the operating frequency, λ [92]. Notably, the free space wavelength is defined as

$$\lambda = \frac{c_o}{f} \tag{4.6}$$

where c_o is the speed of light in vacuum, and f is the operating frequency. In this simulation, the L_c is around 50 mm, which is less than one percent of the free space wavelength at around 6,000 mm (at 485 kHz).

4.3 Software validation

The software validation was conducted by comparing the inductance from the finite element simulation with the value obtained from the Wheeler's approximation in chapter 3.2. A commercial eddy current sensor with the inductance value of 100 μH, was selected for the comparison. The circular coil of the sensor is an 8-mm internal diameter consisting of 80 turns of a 0.1-mm diameter copper wire. The 80-turn coil was created by winding the wire 10 turns per layer for a total of 8 layers. Figure 4.1 shows the simulation model with the current path indicated by the arrow on the coil's circular edge.

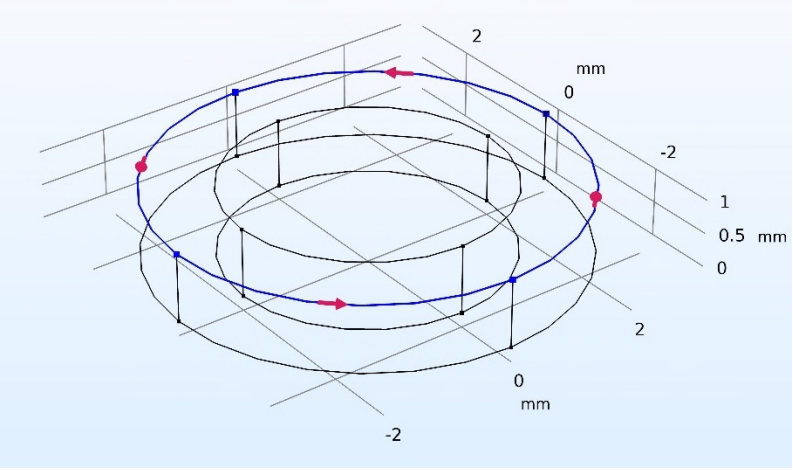


Figure 4. 1 The current path of the coil simulation model is defined by the circular edge of the coil with arrows

Figure 4.2 shows the cross-section of the alternating magnetic field of the circular inductive coil (indicated by the red arrows). The symmetry magnetic field can be clearly observed. In the axial direction, the magnetic field is intense within about half the coil diameter.

The comparison of the results is shown in Table 4.1. The simulation value of 95.4 μH is greater than the Wheeler's approximation of 89.9 μH. However, this simulation value was closer to the measurement and the sensor specification at 99.5 μH and 100 μH, respectively. Therefore, the software yields a reliable result and thus can be used for electromagnetic simulation.

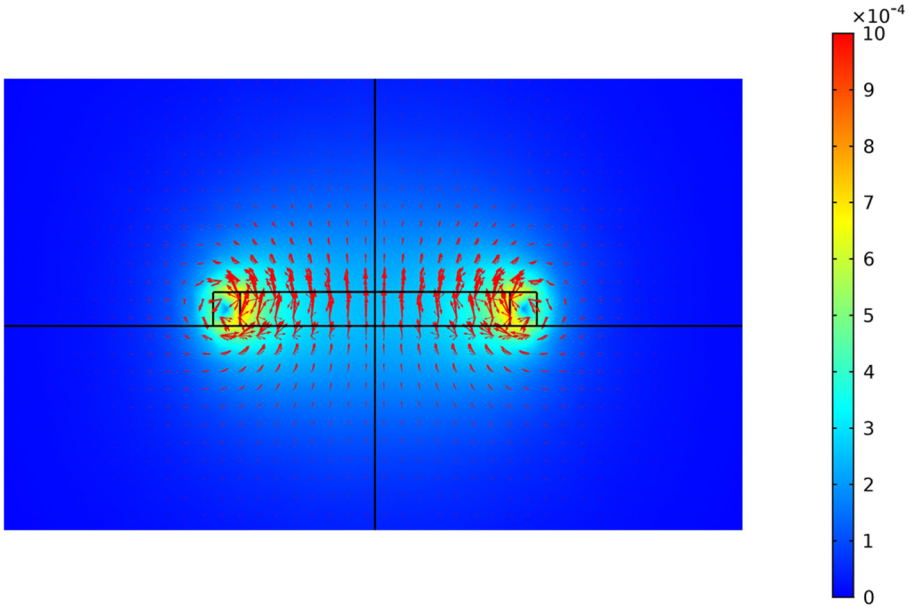


Figure 4. 2 The alternating magnetic field (the red arrows) of the induction coil

Table 4. 1 The coil inductance from the empirical formula and the simulation

Calculation methods	Coil's inductance [μH]
Sensor specification	100
Measurement	98.5
Wheeler's approximation	89.9
Simulation result	95.4

4.4 Simulation model

According to the predicted FEA results, the inlet shroud location in Figure 3.20 (d) is crucial for detecting blade cracks with clearance measurements. Nonetheless, the variation in shroud/sensor clearance caused by the impeller runout necessitates considering the sensor's response to changes in clearance. Thus, an electromagnetic simulation was performed to predict the response of a rectangular eddy current sensor at this measurement location. The 3D simulation model consists of a rectangular coil aligned along the sensor's longitudinal section over the conductive target, as shown in Figure 4.4 (c).

The sensor coil simulation model was based on the in-house rectangular coil of a 13-mm eddy current sensor used for clearance measurement in Chapter 3. Figure 4.4 (a) shows that the rectangular coil consists of 150 turns of 0.2-mm diameter copper wire. The coil-winding has 6 layers, with 25 turns per layer. The final result is a rectangular coil with a dimension of 6.5 mm wide by 10.2 mm long by 6.25 mm high with a coil thickness of 1.5 mm, as shown in Figure 4.4 (b). Notably, the advantage and disadvantage of this sensor design are explained in section 3.4 Intrumentation.

In, this simulation, the homogenised multi-turn option was selected in the coil features to simulate the coil created from tightly wound conductive wires with an insulation layer [91]. The shape of the coil, the number of turns and the coil cross-section area were required to define the current path and calculate the total length.

As the target of an eddy current sensor, a portion of the inlet shroud was simulated as a curved plate with the same radius, width, and thickness as the actual design. The transition boundary condition was assigned on the target's upper surface to represent the thin conductive layer of silver paint [90]. The skin depth of silver is about 0.09 mm at 485 kHz, and thus constitutes an appropriate boundary condition (see Section 2.5.1 for the definition of skin depth).

The outer domain of the simulation model was assigned as an infinite element domain. Through this assignment, simulations involving a magnetic field in free and open space can be resolved without defining an additional boundary condition [91]. The infinite element model assigned to the outer shell of the simulation model is shown in Figure 4.4 (c). The zero magnetic vector potential was also assigned as an initial condition in all domains.

The equivalent circuit was connected to the coil simulation model to determine the coil output voltage. The equivalent circuit consisted of resistances and capacitors with the alternating voltage excitation source of 20 mA, as shown in Figure 4.3. This equivalent circuit was a simplified circuit of newly developed electronic which the driving frequency of the connected eddy current sensor can be adjusted (see Chapter 3 for details). The materials' electromagnetic properties are shown in Table 4.2.

Table 4. 2 Electromagnetic properties of the materials used in simulations

Electromagnetic properties	Copper	Silver	Air
Electrical conductivity [S/m]	5.998×10^7	6.21×10^7	1.0×10^{-6}
Relative permeability	0.999994	0.99998	1.00000037
Relative permittivity	1	1	1

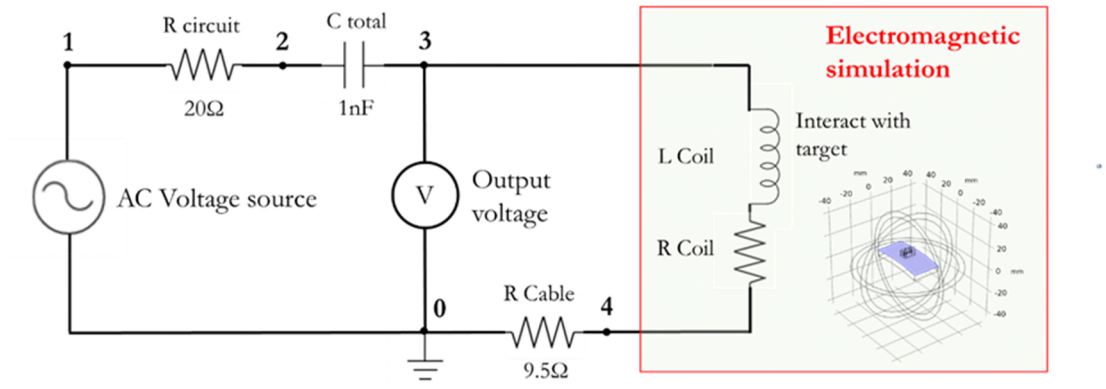


Figure 4. 3 Equivalent circuit for eddy current measurement

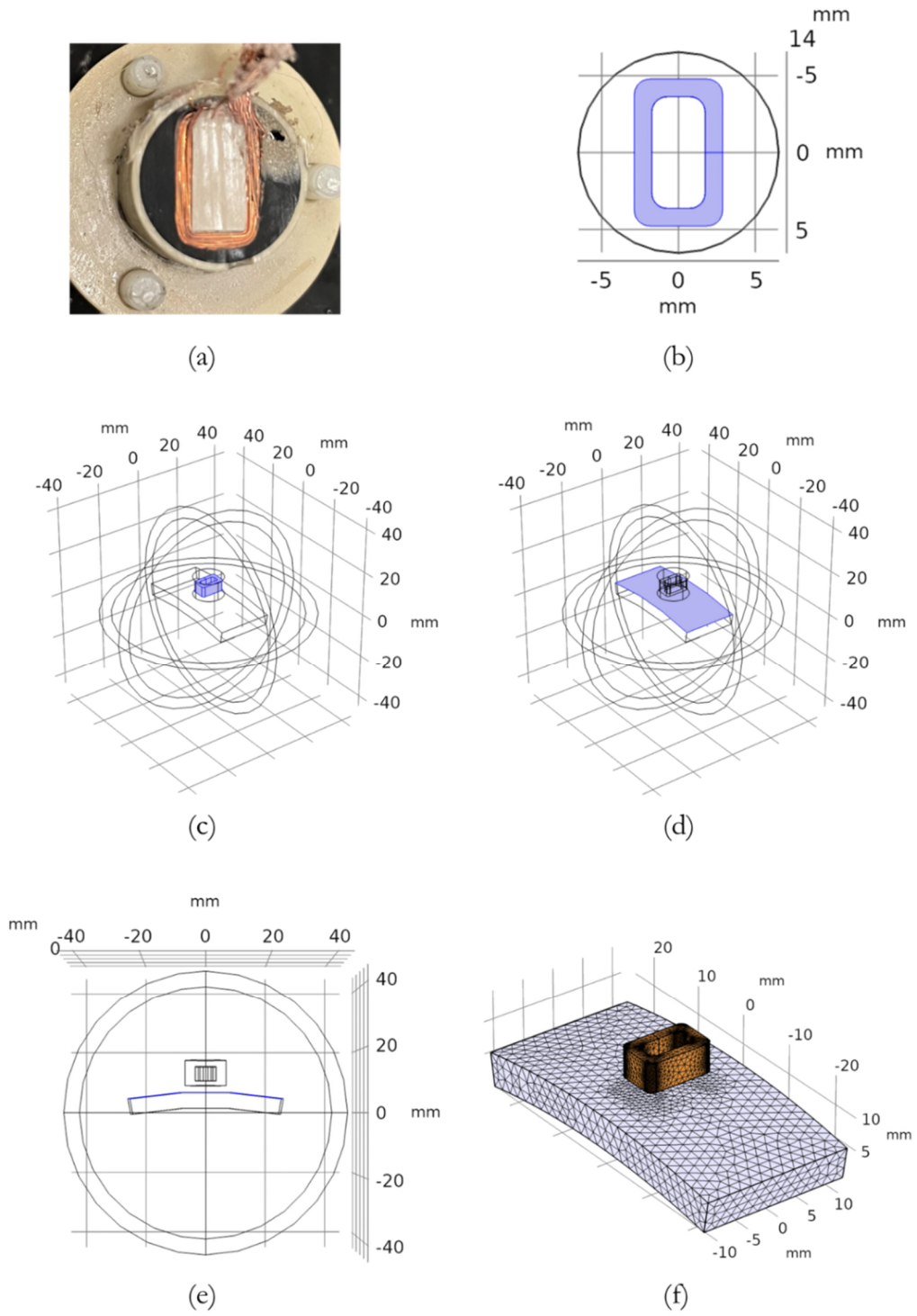


Figure 4. 4 Electromagnetic simulation model (a) a rectangular coil of an eddy current sensor; (b) a cross-sectional model of the rectangular coil; (c) a 3D simulation model showing inductive coil and target; (d) surface of the target material; (e) a side view of the simulation model; and (f) mesh distribution of coil and target

4.5 Mesh sizing

In finite element simulations, the solution is formulated by solving algebraic equations of the discretised elements. A trade-off between the accuracy of the simulation results and the calculation time is presented. Therefore, mesh sizing was conducted to reduce the computer calculation time without compromising the accuracy of the results.

The mesh sizing process used a rectangular coil with a 2-mm standoff from the conductive curved target, as shown in Figure 4.3 (f). The minimum element sizes of the tetrahedral elements varied from 0.1 to 2 mm. The finer the size of the element, the more the number of elements can be incorporated. At the minimum element size of 0.1 mm, the simulation model contained around 5.5×10^5 elements.

As Figure 4.5 indicates, the increase in the number of elements leads to the convergence of the simulation results in both coil inductance and coil output voltage. Thus, the minimum element size of 0.15 mm with 3.43×10^5 elements was specified due to the optimum between the results (0.4 percent different compared with the minimum element size of 0.1 mm) and the simulation time at around 30 minutes.

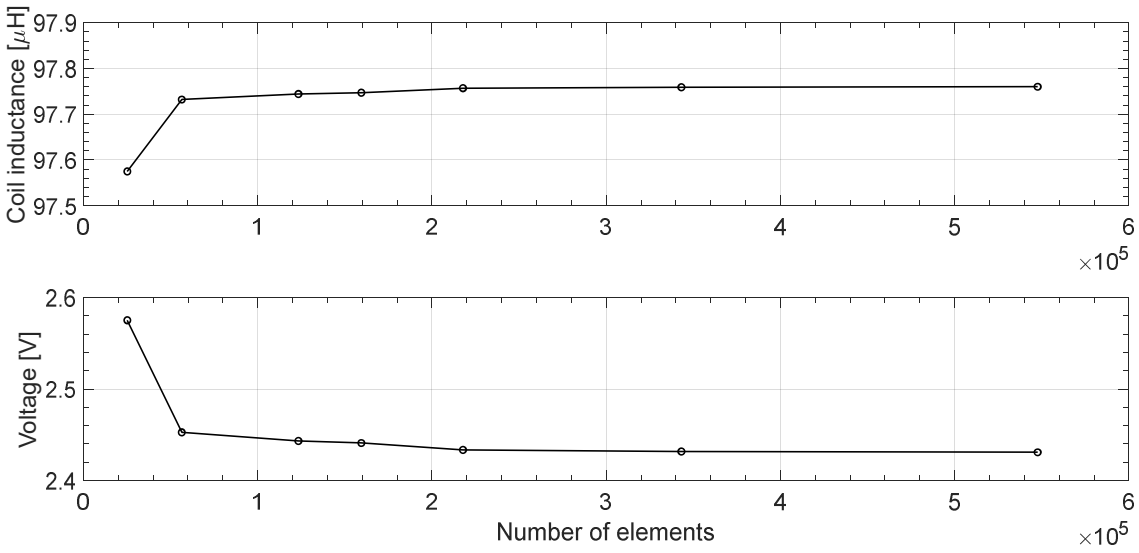


Figure 4. 5 The coil inductances and the coil output voltage against the number of elements

4.6 Simulation results and discussion

First, the simulation of the rectangular coil without a target was performed to predict the coil inductance and resistance. The comparison of the prediction and measurement in Table 4.3 confirms the validity of the coil model.

Table 4. 3 The rectangular coil inductance and resistance

Rectangular coil	Measurement	Simulation	Error [%]
Inductance [μH]	99.2 ±2.4	100.8	1.6
Resistance [Ohm]	2.2 ±0.17	2.02	6.9

The frequency response of the rectangular eddy current sensor without a target was simulated by varying the driving frequency from 300 kHz to 800 kHz. Figure 4.6 shows the correspondence between the simulation results and the measured frequency responses of the rectangular eddy current sensors used in the

experiments. The resonant frequency of this RLC system, which consists of a resistor (R), an inductor (L) and a capacitor (C), is about 500 kHz, close to the calculated resonant frequency of 505.4 kHz. Note that the resonant frequency (f_0) of an RLC system is given by

$$f_0 = \frac{1}{2\pi}\sqrt{\frac{1}{LC}}. \tag{4.7}$$

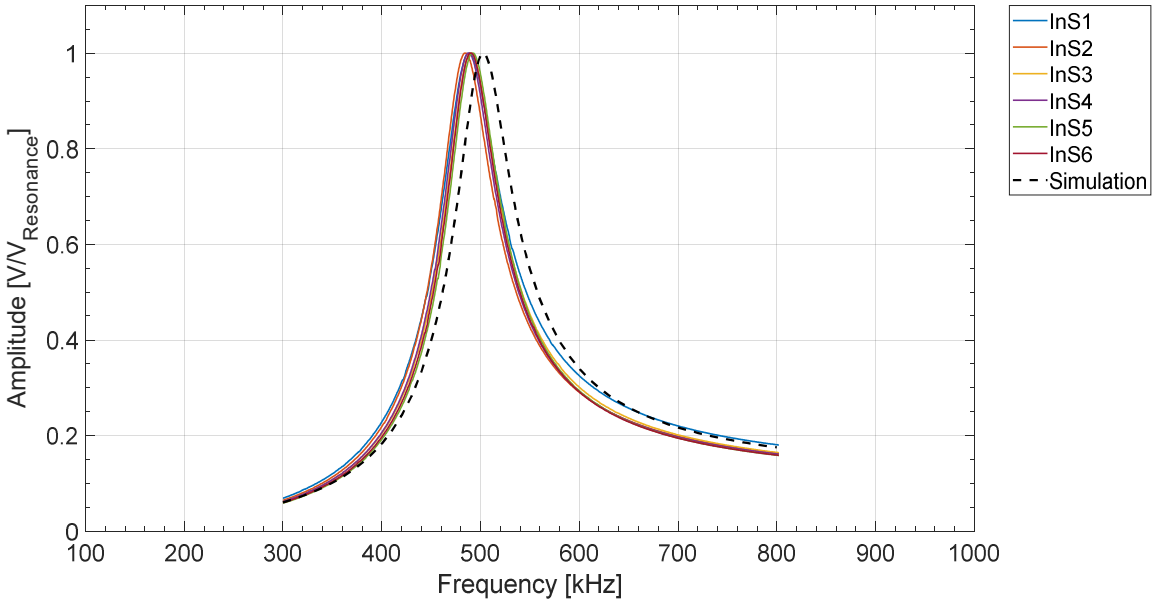


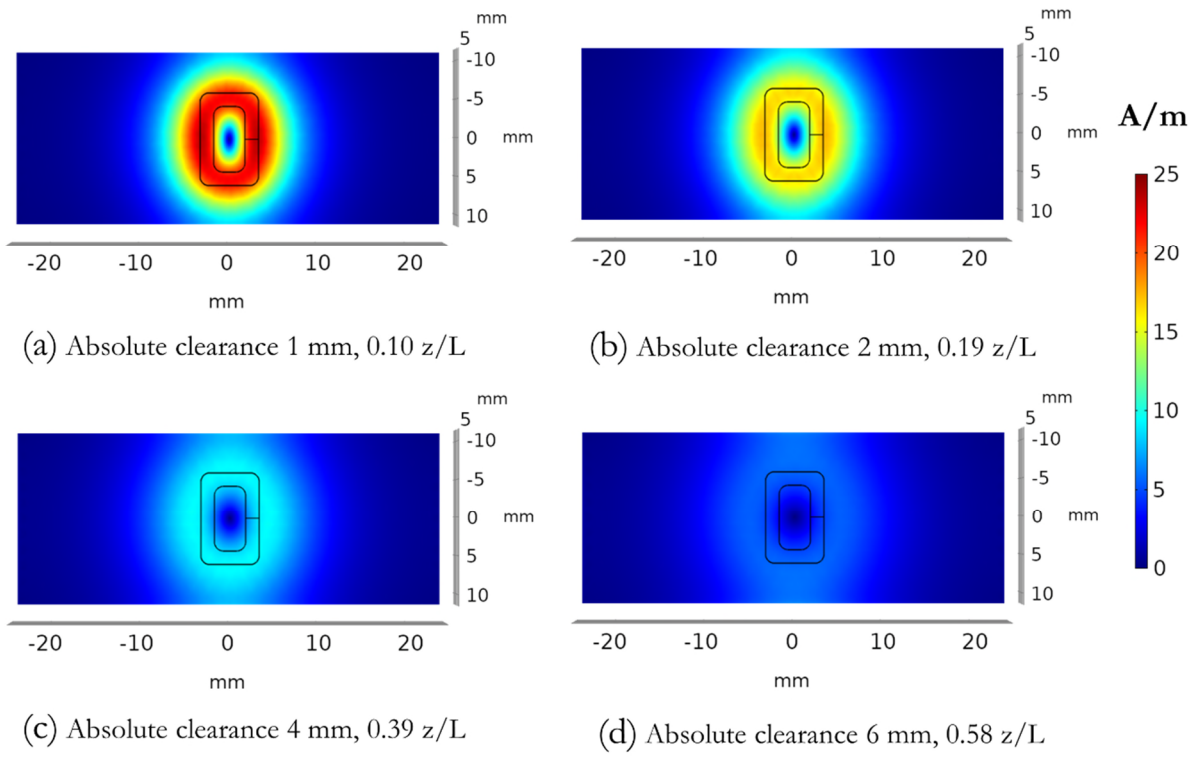
Figure 4. 6 Comparison of eddy current sensor frequency responses between measurement and simulation results

Finally, the response of the rectangular coil over the conductive curvature target at various standoffs was analysed using the simulation model in Figure 4.4. In this analysis, the simulation case is divided into sub-simulations at different standoffs ranging from 0.5 mm to 10 mm, with 0.5 mm intervals. The coil driving frequency in this simulation was set at 485 kHz, matching the driving frequency of the electronics used in the experiment.

Figure 4.7 shows the induced eddy currents in the target at various coil distances (standoff). In this plot, the nomenclature z and L represent the standoff and the long side of the rectangular induction coil (effective coil length), respectively. It can be observed that the intensity of the induced eddy current in the target depends on the standoff between the sensor coil and the target's outer surface. In other words, the intensity of the induced eddy current decreases as the standoff increases. This decrease in the induced eddy current intensity is a result of diminishing magnetic field strength with increasing distance, as shown in Figure 4.8.

In addition, the surface plot in Figure 4.7 (a) shows that the induced eddy current intensity has a range of approximately two times the length of a rectangular coil. Thus, this predicted result provides the minimum distance between two adjacent sensors as a guideline to avoid the sensor cross-effect.

The predicted relationship between the coil output voltage and the standoffs is presented in Figure 4.9. This relationship was consistent with the sensor calibration result in the previous chapter. It is clear that the eddy current sensor's sensitivity reduces as the clearance increases. Thus, the range of a 13-mm rectangular eddy current sensor for effective clearance measurement is around 5 mm or 0.5 times the length of the rectangular coil. This sensor range corresponds to the rule of thumb: an eddy current sensor loses sensitivity at 0.5 times the diameter of a circular coil.



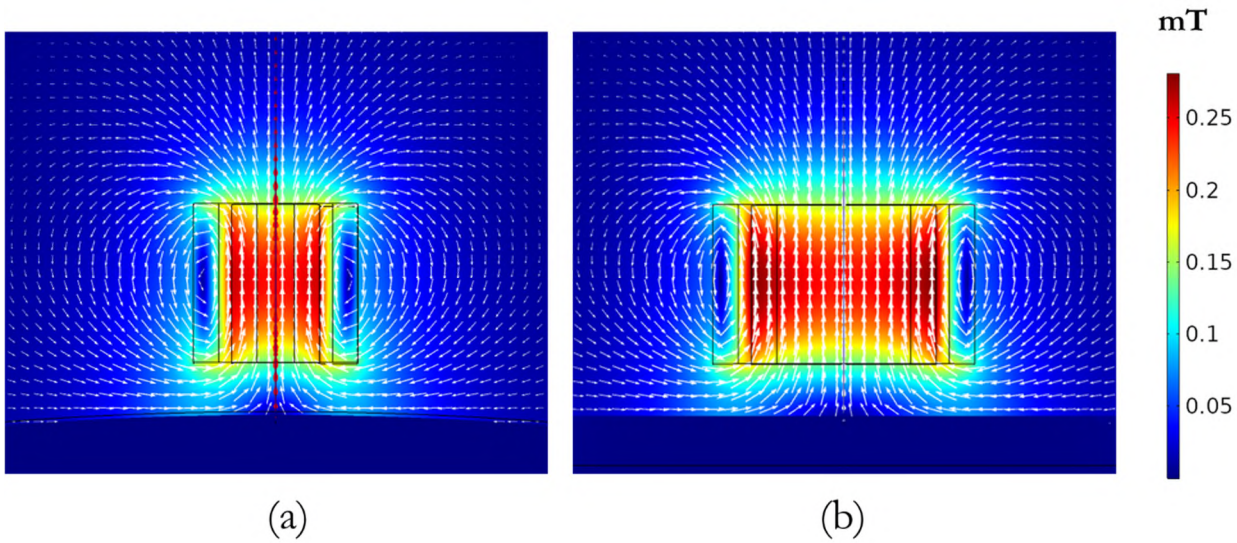
(a) Absolute clearance 1 mm, 0.10 z/L

(b) Absolute clearance 2 mm, 0.19 z/L

(c) Absolute clearance 4 mm, 0.39 z/L

(d) Absolute clearance 6 mm, 0.58 z/L

Figure 4. 7 The induced eddy currents in the target with different coil standoffs (a) at 1 mm or 0.10 z/L; (b) at 2 mm or 0.19 z/L; (c) at 4 mm or 0.39 z/L; and (d) at 6 mm or 0.58 z/L



(a) (b)

Figure 4. 8 The alternating magnetic field (white arrow) of the rectangular coil over a conductive target at a 2-mm standoff (a) a narrow section view; and (b) a longitudinal section view

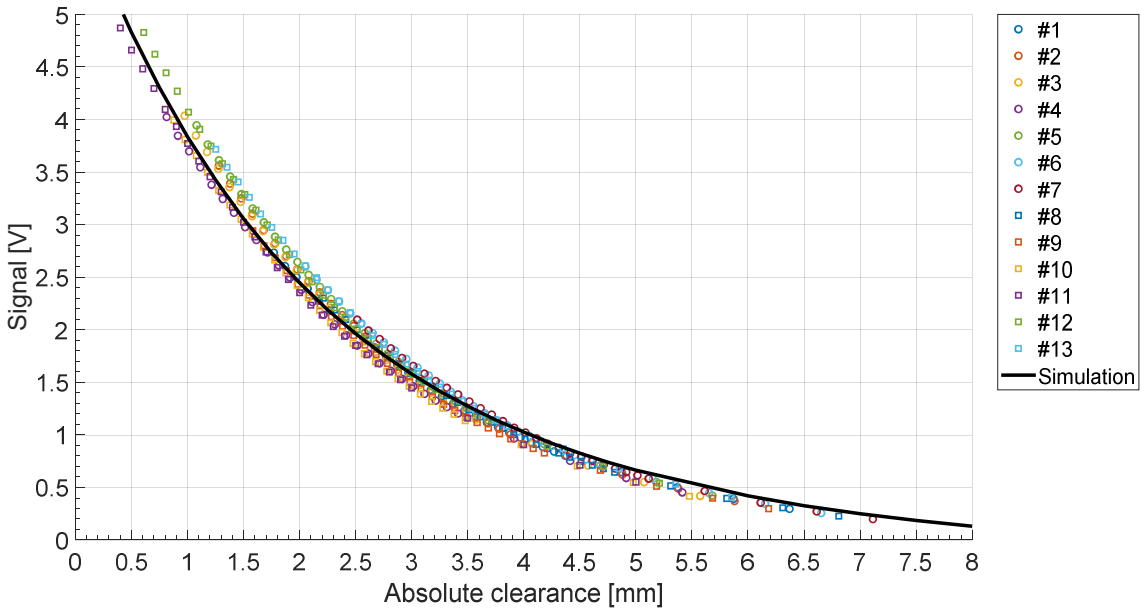


Figure 4. 9 The predicted relationship between the sensor output signal and the absolute clearance corresponding to the measured results

4.7 Conclusion

In short, the computational electromagnetic simulation of the eddy current sensor and the conductive target was performed. The simulation result shows the consistency between the predicted sensor responses and those obtained from the sensor calibration in section 3.6. The prediction of the induced eddy current on the target conductive surface was used to determine the sensor installation in both setup clearance and distance between two adjacent sensors.

In addition, this electromagnetic simulation model can be applied to the actual size impeller for eddy current sensor design, optimisation, and placement in blade crack detection.

Chapter 5

Experimental Studies of Blade Crack Detection

5.1 Introduction

In this chapter, the experimental studies were conducted using 3D-printed impellers and the testing facilities described in Chapter 3. The experiments consisted of the healthy impeller and cracked blade impeller conditions. The healthy impeller experiment was used as a baseline for comparing with the crack condition experiment and for validating the simulation model in Chapter 6.

On the other hand, blade crack detection experiments were conducted to achieve three objectives. The first objective was to evaluate the feasibility of using the shroud clearance measurement to detect a damaged blade on a shrouded impeller. The second objective was to establish the relationship between the crack size in length and the impeller shroud deflection characteristics. The third objective was to

determine the minimum crack size in terms of length that can be detected with the proposed measurement method.

Thus, this chapter was divided into three sections, starting with the impeller with a healthy blade condition, followed by the preliminary and main experiments of an impeller with a cracked blade condition. The crack length was varied in the main cracked blade experiment to investigate the shroud deflection characteristics.

Notably, two identical 3D-printed impellers were used in these experimental studies. The first impeller was used in the preliminary experiment for the feasibility study of using clearance measurement for blade crack detection – which was tested prior. This impeller was not inspected or tested for back-to-back comparison with the second impeller. Thus, the impeller runout measurement and eddy current sensor calibration were performed only on the second impeller. This second impeller was used in the impeller with healthy blade experiment and later in the impeller with a cracked blade experiment.

5.2 Impeller with healthy blades

The second impeller with healthy blades was tested as a baseline case in this series of experiments. The change of the clearance signals was used to determine the effect of the centrifugal force from the rotor unbalance on the rotor deflection. This experiment was conducted under partial vacuum conditions at an absolute pressure of 49.2 kPa. The electrical motor was used to drive the impeller at five different speeds, from 200 RPM to 3,500 RPM, as shown in Figure 5.1.

The clearance signals from the inlet shroud sensor in Figure 5.2 shows the increase of signal amplitude with increasing rotor speed. Referring to the calibration results in Chapter 3, this increasing signal amplitude means that the impeller shroud (as a target) was moved closer to the sensor while the rotor speed increased.

Figure 5.3 shows the polar plot of absolute clearance between the impeller inlet shroud and the sensor tip. This point-by-point clearance was calculated using calibration curves obtained from the eddy current sensor calibration in a total of 52 points, detailed in Chapter 3. The clearance reduction implies that the shroud was expanded as the rotor speed increased. This impeller shroud expansion was caused by the centrifugal force acting on the impeller, as predicted by the FEA result in Chapter 6.

The change of inlet shroud clearance with reference to the clearance at 200 RPM is shown in Figure 5.4. It can be seen that the change is proportional to the impeller speed. In addition, the non-uniform shroud expansion was observed at an increasing speed. This non-uniform expansion was expected since the rotor shape was not perfectly round, as mentioned in session 3.3.2. The magnitude of the shroud expansion was around 0.1 to 0.2 mm at 3,500 RPM, depending on the impeller circumference location.

In the same way, the outlet shroud signal also increased with speed, as shown in Figure 5.5. This increase in signal meant that the shroud/sensor clearance was reduced. Since the clearance sensor was fixed with the holder ring, the impeller outlet shroud was lifted in the axial direction when speed increased. Figures 5.6 and

5.7 present the absolute clearance and the change of clearance regarding the clearance at 200 RPM, respectively. Figure 5.7 shows that the outlet shroud distortion increased with rotational speed, especially at the middle span. This distortion may be caused by the low stiffness of the thin outlet shroud and the large span between the two adjacent blades. The same distortion can also be seen at the back-end wall measurement location in Figure 5.10.

However, this measured outlet shroud clearance was different compared to the FEA simulation results in Chapter 6. This is because the eddy current sensor was calibrated only in the axial position (detailed in session 3.6.1), whereas the shroud expanded in the radial direction from the effect of centrifugal force. Therefore, this outlet shroud location may not be suitable for clearance measurement as the outlet shroud deflected in two directions.

In contrast with the outlet shroud, the back-end wall clearance signal decreased with speed, as shown in Figure 5.8. The result was an increase in the back-end wall/sensor clearance. In other words, as rotor speed increased, the back-end wall moved up. The polar plots of the absolute clearance and the change of clearance are shown in Figures 5.9 and 5.10, respectively.

Figure 5.11 demonstrates the impeller movements from the centrifugal force as the rotor speed increases in three locations: the inlet shroud, the outlet shroud and the back-end wall. The experimental results indicated that the inlet shroud was the optimal location for the clearance sensor installation.

The blade arrival times with uncertainties from the inlet blade and outlet blade sensors at a rotor speed of 3,500 RPM are shown in Figures 5.12 and 5.13, respectively. While relatively constant, the arrival times for both measurement locations varied by each blade. Obviously, the tip timing data of the trailing edge was more uniform than the leading edge. The visual inspection confirmed the non-uniform space between each leading edge. This fluctuation in tip timing results indicated the discrepancy in the impeller manufacturing processes of 3D printing, particularly in the case of a thin blade profile of 1 mm thickness.

The support bearing and sensor holder ring vibrations were also measured as a baseline for comparison with the impeller with a cracked blade condition. The impeller speed (1X) was the main component of the vibrations at the frequency of 58 Hz, as shown in Figure 5.14. Surprisingly, the peak of the blade pass frequency (13X) at the frequency of 758 Hz did not appear on the plots. This might be due to the thin blades (less blade mass) or the absence of fluid passing interaction.

After the healthy impeller datum testing, a visual inspection was conducted to investigate the impeller condition, including crack, rubbing, and permanent deformation. No indication of damage was found at the rotor shroud, hub, blades, and back-end wall. The dimensions of the impeller were checked with the digital dial gauge before and after the testing at the inlet shroud, the outlet shroud and the back-end wall locations, which were the key clearance measurement locations. The inspection results confirmed that the impeller deformation was not permanent. The impeller's temporary deformation at high speed may be related to the stress on the

impeller not exceeding the yield strength of the fibre-reinforced polymer (impeller's building material).

In short, the impeller with the healthy blade datum testing shows temporary deformations of the rotor, which is detectable by the clearance measurement. The experimental results were used as the baseline case for the subsequent cracked blade experiments and the FEA simulation model validation.

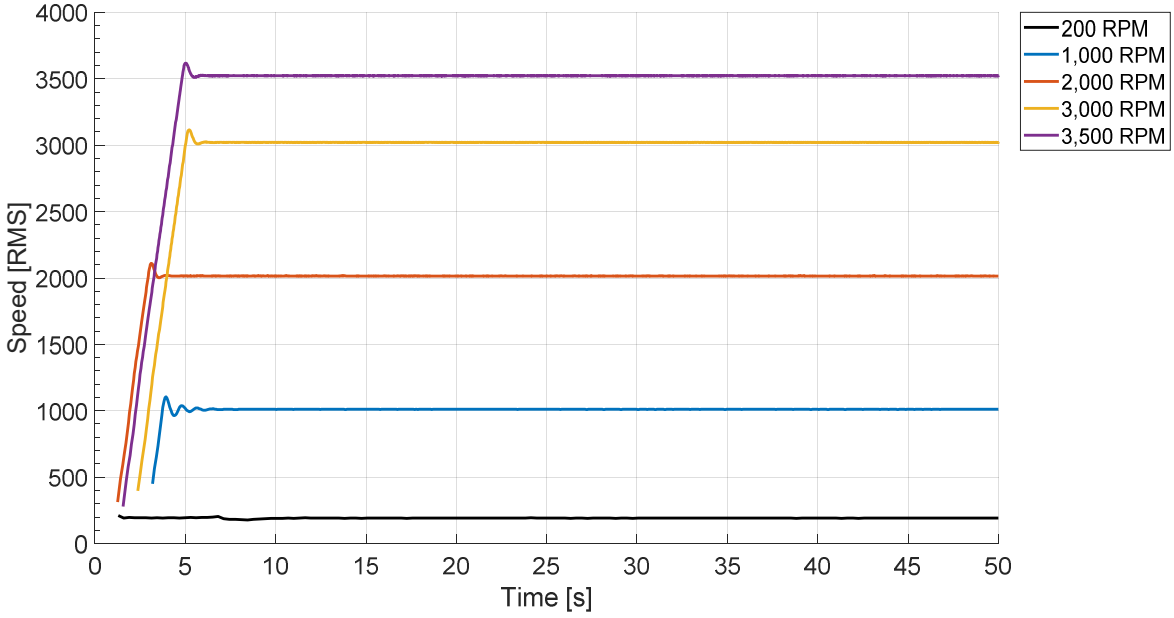


Figure 5. 1 The rotor speeds in the healthy blade condition testing

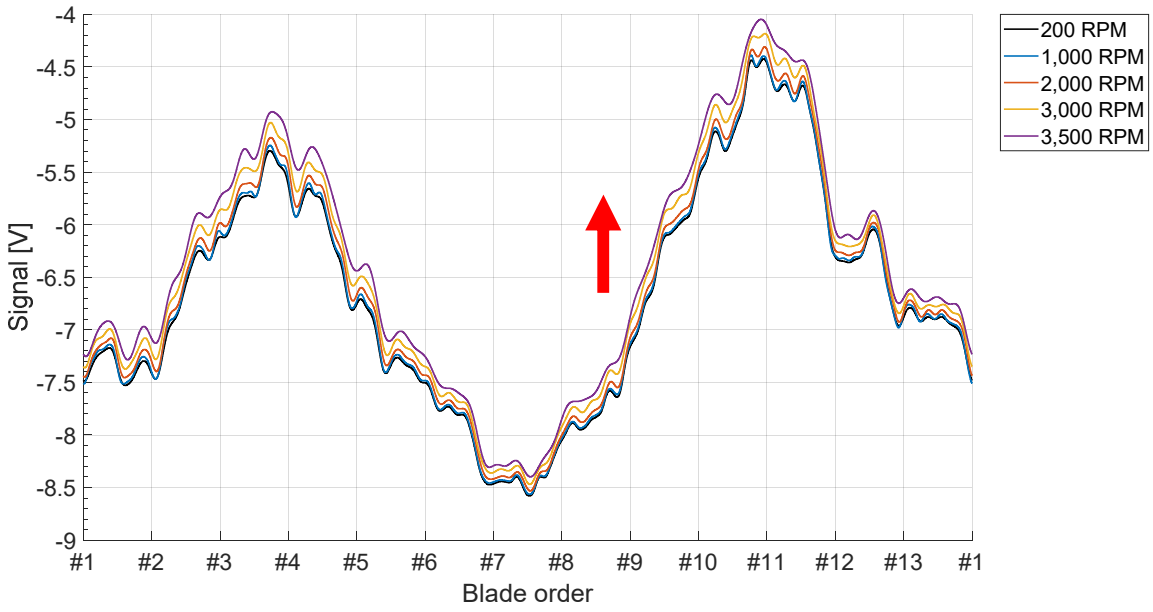


Figure 5. 2 Inlet shroud clearance signals in voltage of the healthy impeller at different speeds

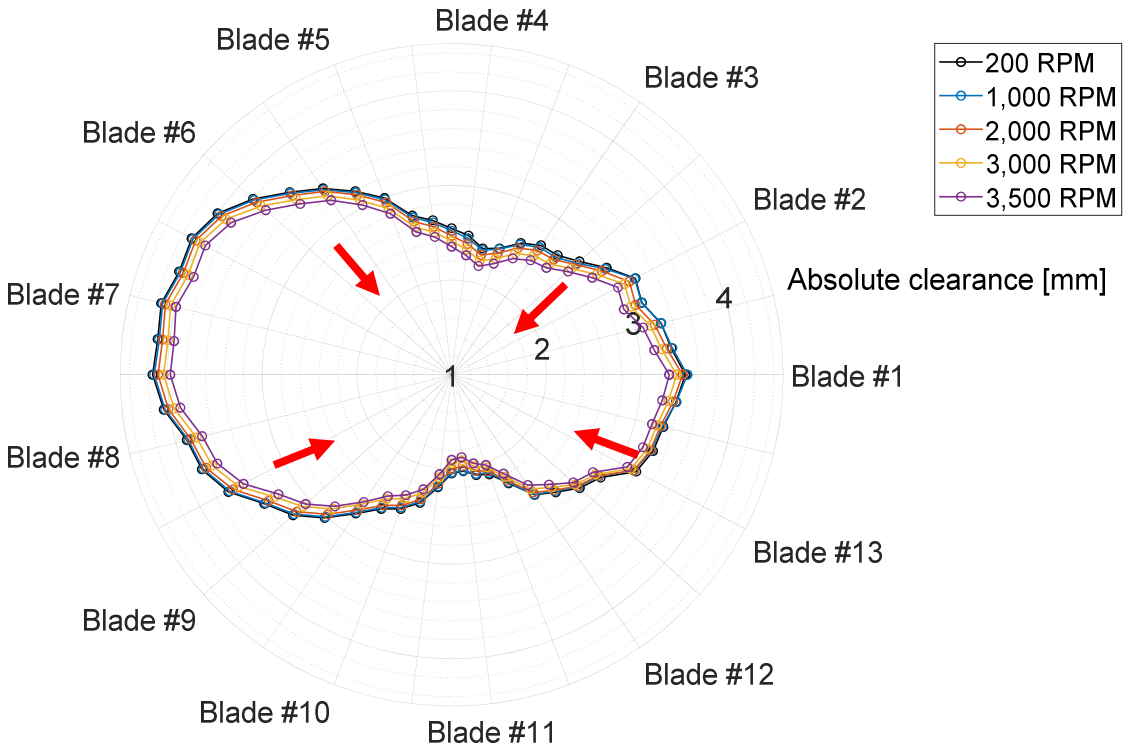


Figure 5. 3 Polar plot of the absolute inlet shroud clearance of the healthy impeller at different speeds

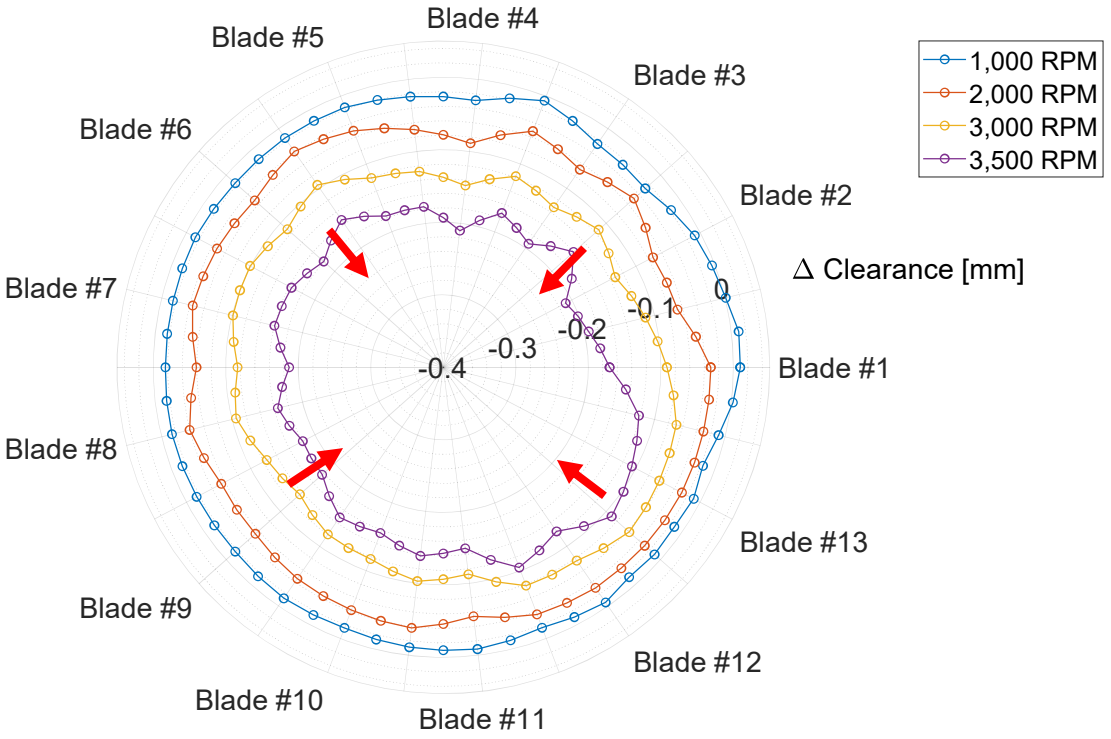


Figure 5. 4 The change of inlet shroud clearance of the healthy impeller at different speeds

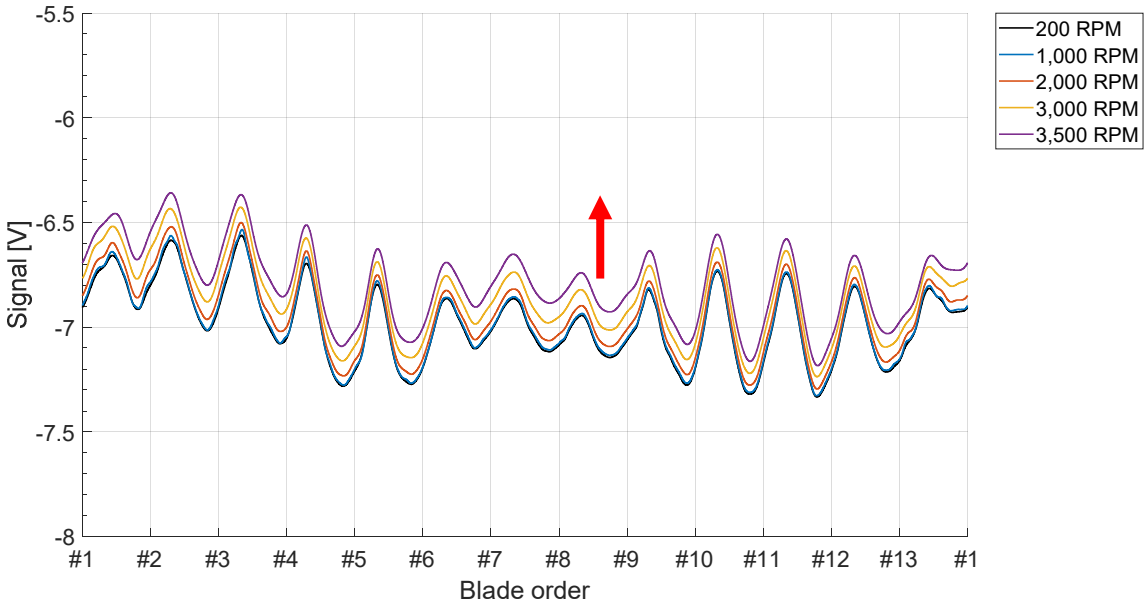


Figure 5. 5 Outlet shroud clearance signals in voltage of the healthy impeller at different speeds

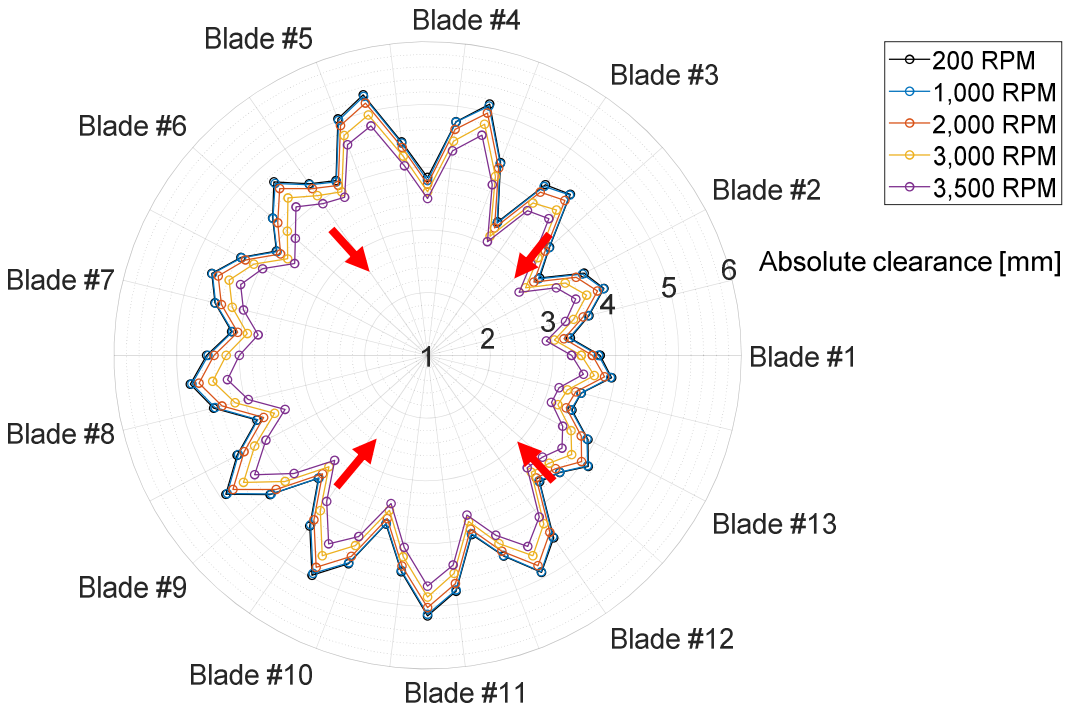


Figure 5. 6 Polar plot of the absolute outlet shroud clearance of the healthy impeller at different speeds

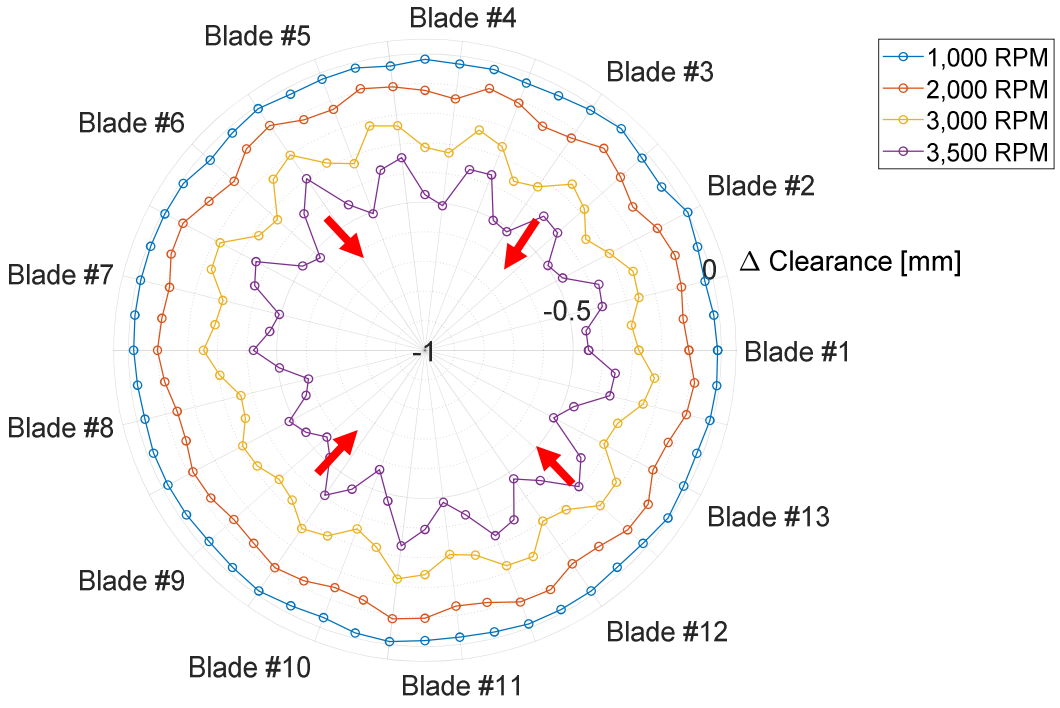


Figure 5. 7 The change of outlet clearance of the healthy impeller at different speeds

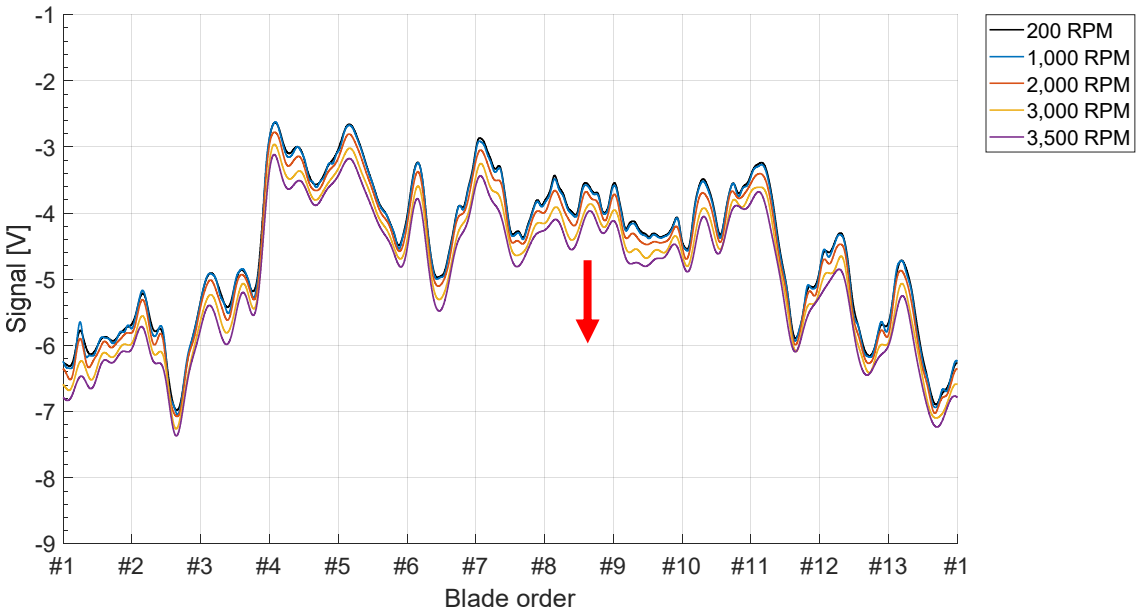


Figure 5. 8 Back-end wall clearance signals in voltage of the healthy impeller at different speeds

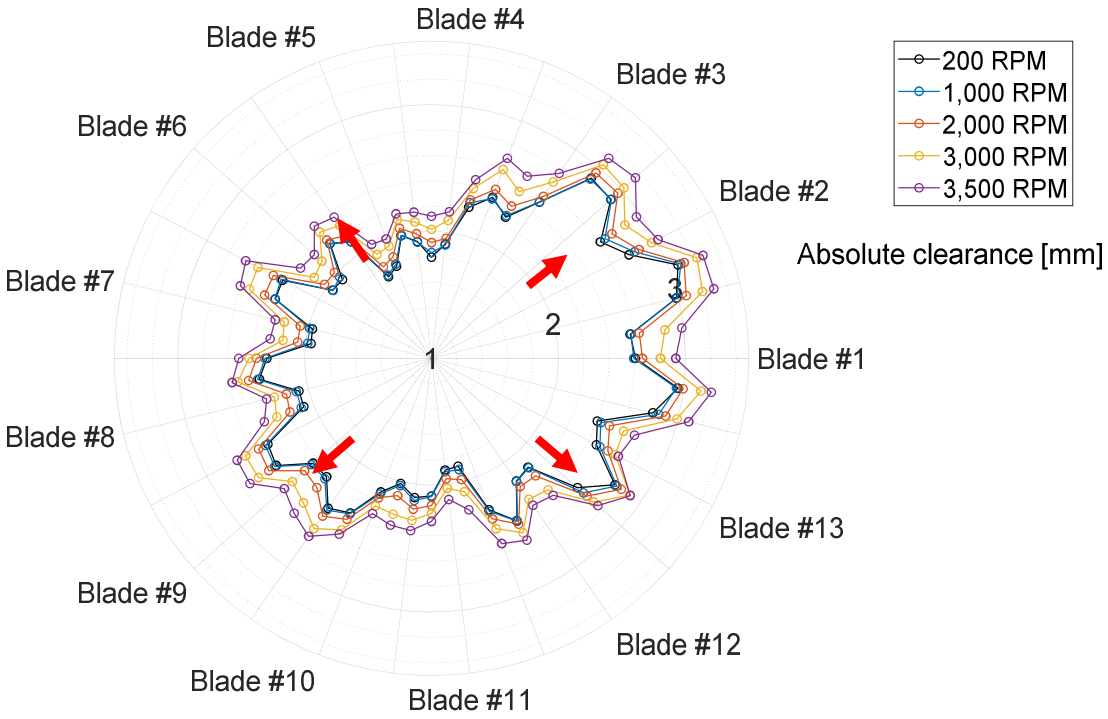


Figure 5. 9 Polar plot of the absolute back-end wall clearance of the healthy impeller at different speeds

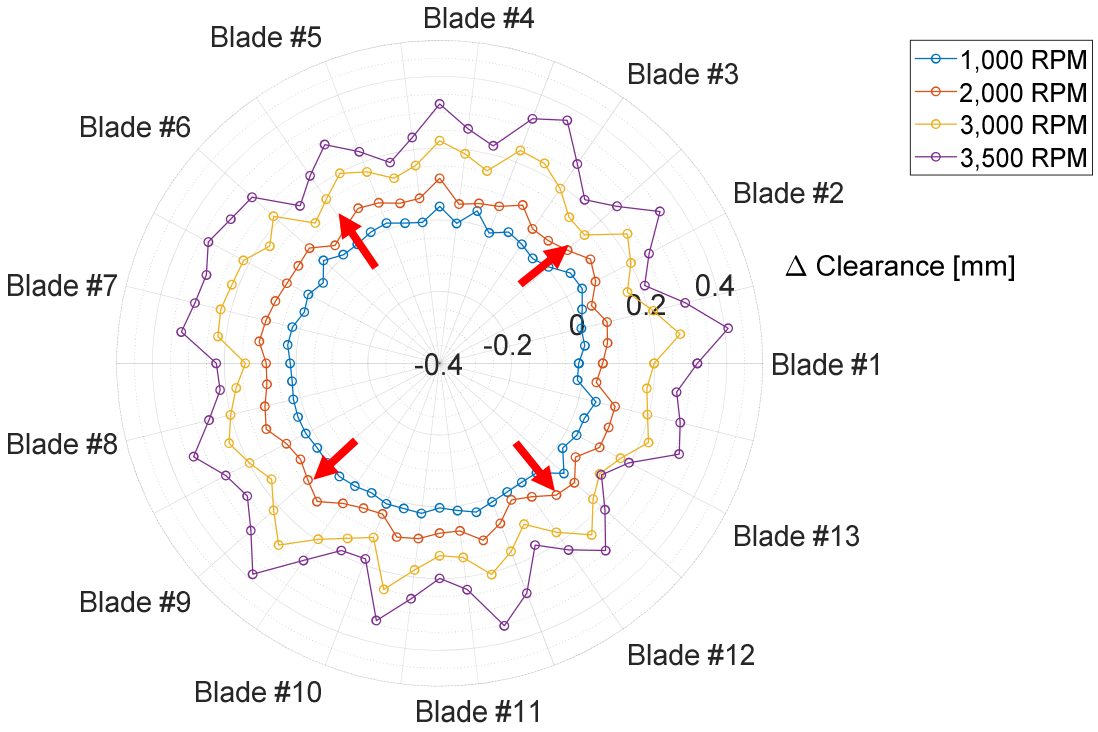


Figure 5. 10 The change of back-end wall clearance of the healthy impeller at different speeds

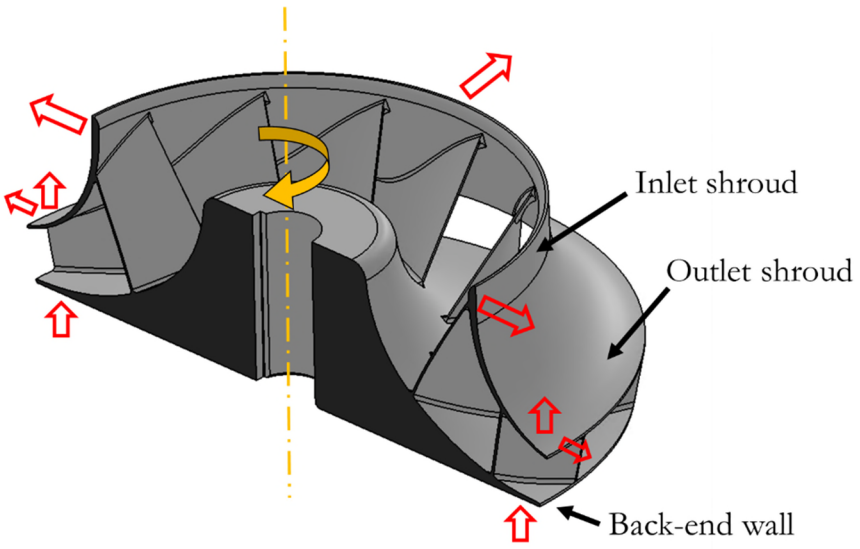


Figure 5. 11 Impeller movement diagram as the rotor speed increases

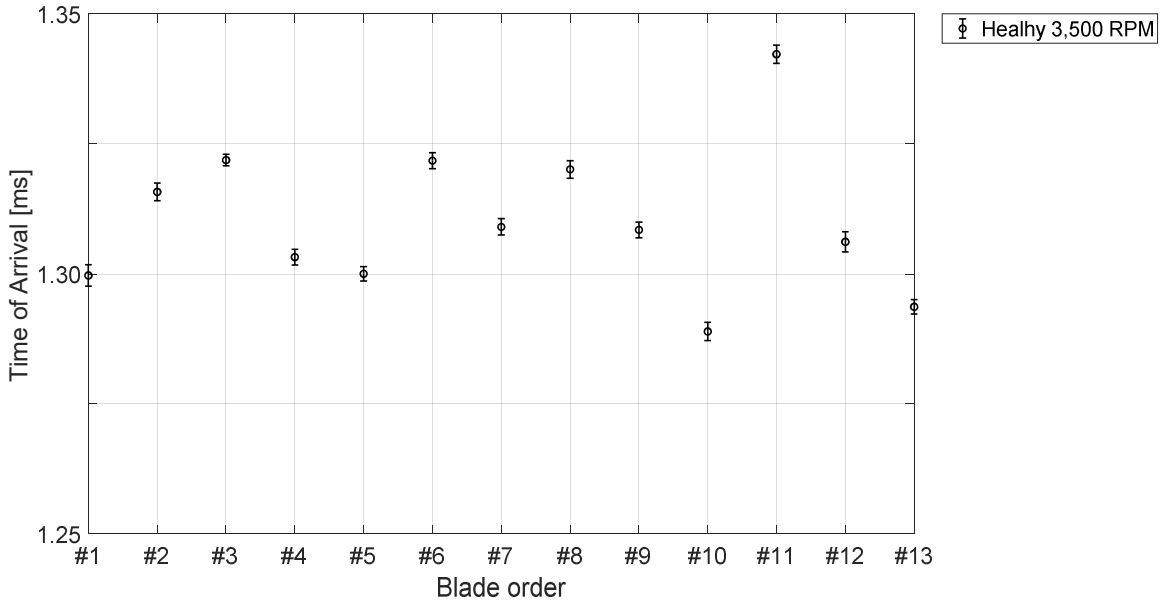


Figure 5. 12 Inlet blade tip timing signal of the impeller with healthy blades, measured from the inlet blade sensor at a rotor speed of 3,500 RPM

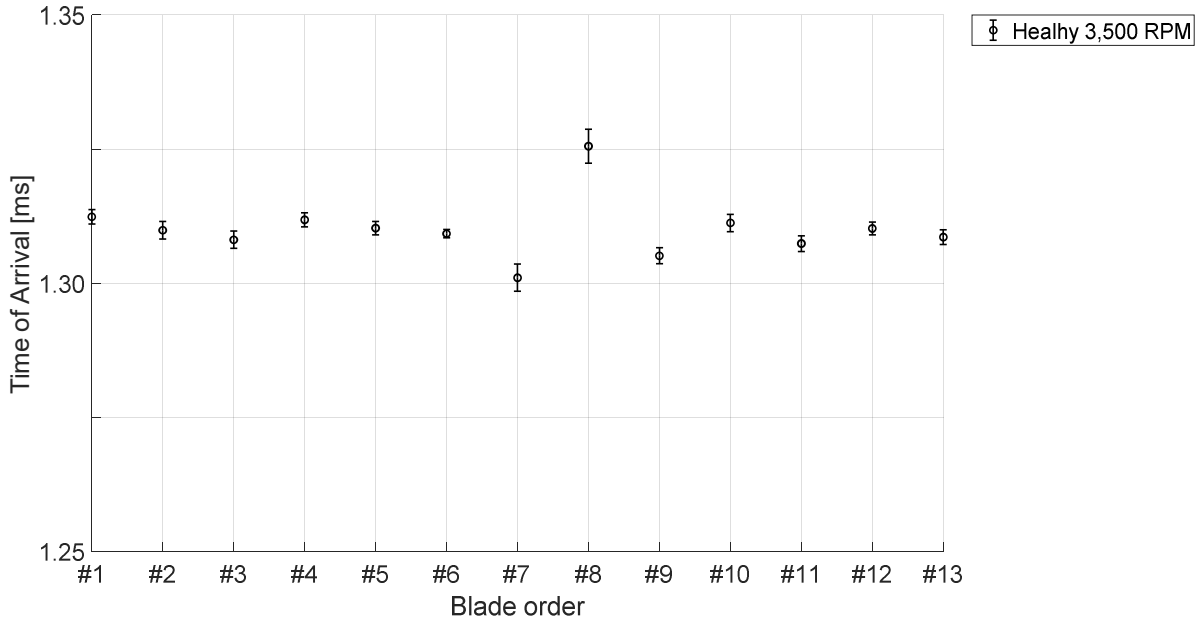


Figure 5. 13 Outlet blade tip timing signal of the impeller with healthy blades, measured from the outlet blade sensor at a rotor speed of 3,500 RPM

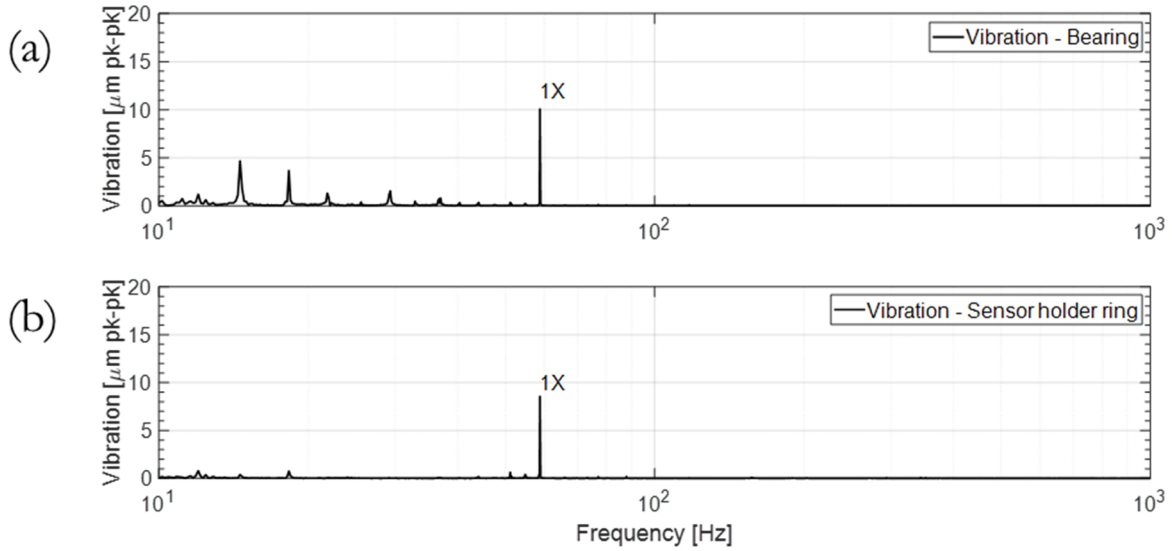


Figure 5. 14 The frequency spectra of the impeller with healthy blades system at 3,500 RPM (a) vibration of the bottom bearing; and (b) vibration of the sensor holder ring

5.3 Impeller with a cracked blade – the preliminary experiment

As stated in the chapter's introduction, the objective of the preliminary experiment was to assess the feasibility of using the shroud clearance measurement to detect a shrouded impeller's damaged blade, particularly crack propagation. This critical blade failure mode is not possible to detect with conventional measurement methods, such as a shaft displacement vibration measurement or casing vibration measurement using an accelerometer.

Notably, the first 3D-printed impeller was used in this preliminary experiment. This impeller was not tested in the healthy blade condition (without crack condition).

5.3.1. Crack detection experiment

The preliminary experiment was performed with the high-speed spinning facility described in Chapter 3. The scaled impeller was driven by an electrical motor to promote crack propagation, which requested a speed of up to 4,900 RPM. Three types of sensors, including a speed sensor, an inlet shroud sensor, and an inlet blade tip timing sensor were used in this experiment. Figure 5.15 shows the sensor installation.

A small V-shape notch was created as a starting point of the crack propagation on blade number 10. The maximum stress intensity concentrates at the notch tip of this V-shaped profile [94]. Consequently, the crack propagates from this tip location. The initial crack size was measured at 11 mm in length, as shown in Figure 5.16 (b).

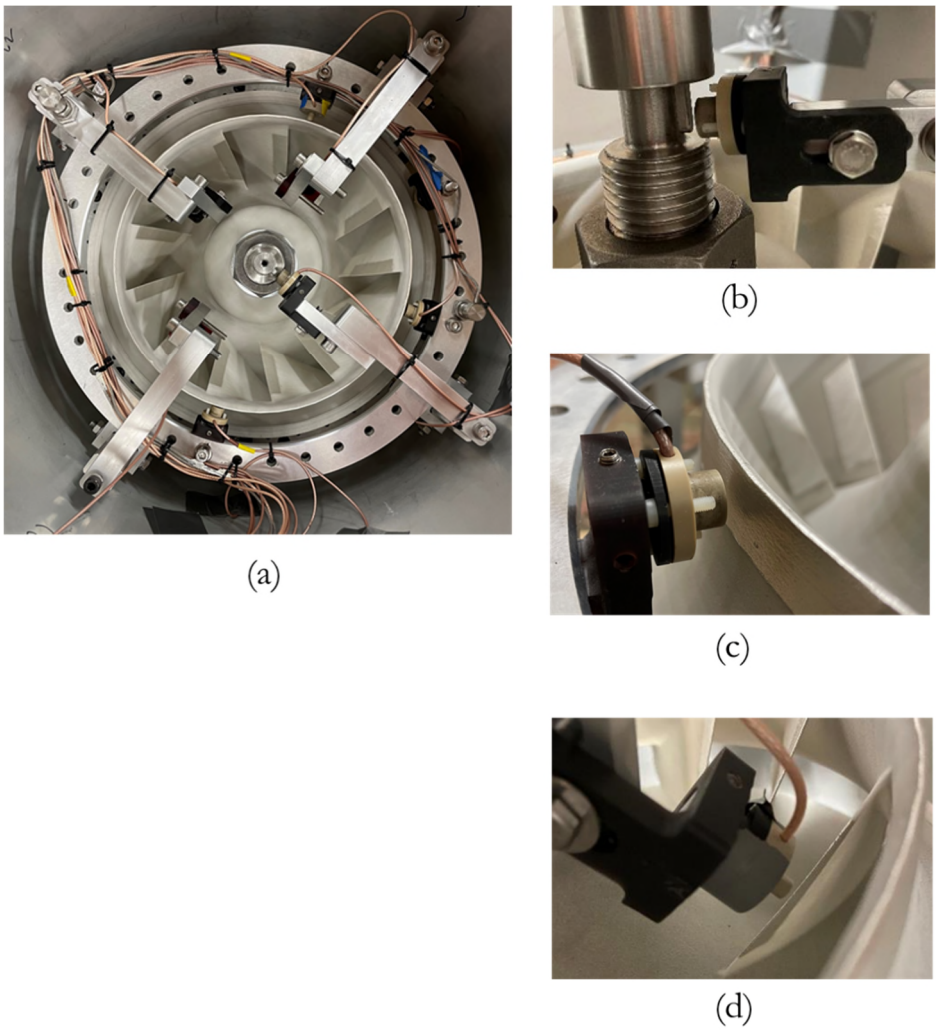


Figure 5. 15 The scaled impeller with sensor installation in the preliminary experiment (a) a shrouded impeller in the containment; (b) a 1/rev (speed) sensor; (c) a clearance sensor on the inlet shroud; and (d) a BTT sensor on the inlet blades

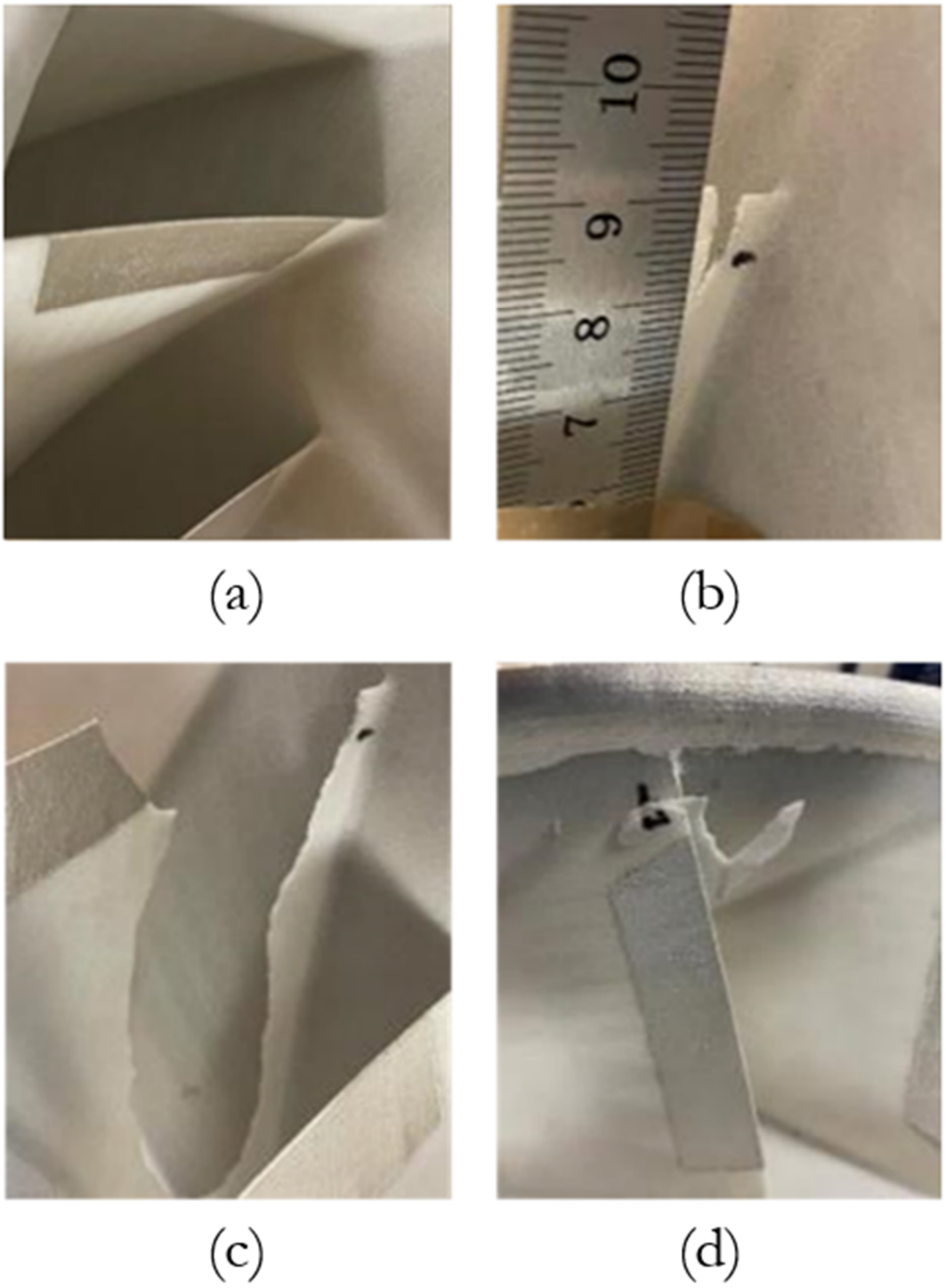


Figure 5. 16 Blade conditions (a) a healthy blade; (b) an initial 11-mm crack on blade number 10; (c) the broken blade number 10; and (d) a piece of the blade fragment stuck on blade number 7

This preliminary experiment was divided into five runs with increasing rotor speed in stages from 3,100 RPM to 4,900 RPM, as shown in Figure 5.17. The speed of the impeller was precisely controlled by a variable speed drive unit (VSD) connected to the electrical motor. Notably, the crack propagation was not achieved by the impeller centrifugal force only, even at 4,900 RPM. It was found, through various attempts to induce an unsteady flow and vortices in the impeller blades, that turning the vacuum pumps off let the air circulate inside the containment. The interaction between the air circulation and the rotor blades accelerated the crack growth. This failure mechanism was different from that observed in industrial impellers, possibly due to the difference between the fluid interacting force and the impeller strength. A thermometer was placed inside the containment to monitor the air temperature during the experiments. The air temperature was limited to 30 degrees for each run.

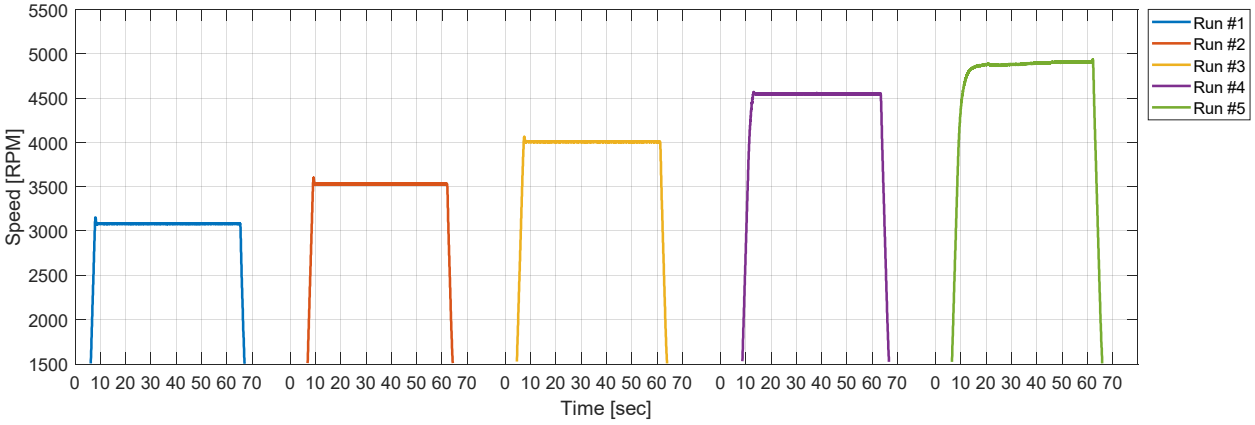


Figure 5. 17 The rotor speed during the five runs

The rotor operating speed of the first and the second run was set at 3,000 and 3,500 RPM, respectively. The inlet shroud clearance signals in Figures 5.18 and 5.19 showed no significant difference, particularly in the shroud area connected to the

cracked blade. In addition, the same magnitude of the clearance signals at 1,500 RPM from start-up to coast-down indicated that the impeller had no permanent deformation. These two pieces of evidence implied that there was no crack growth in the first and second runs.

From the third to the fifth run, the 11-mm crack initiation was stimulated by increasing the rotor speed to 4,000 RPM, 4,500 RPM, and 4,900 RPM, respectively. The polar plots in Figures 5.20, 5.21, and 5.22 show the increase of clearance signals with the rotor speed. However, the clearance signals at 1,500 RPM between the start-up to the coast-down periods are different, especially after the rotor was operated at 4,500 RPM and 4,900 RPM. This phenomenon was not observed in the previous runs with lower rotor speed, indicating a permanent deformation of the rotor shroud.

The change of the clearance signals during the five runs was compared at the same operating speed of 3,000 RPM to eliminate the rotor deflection caused by the change of the centrifugal forces. Figure 5.23 shows that the clearance signal increased significantly at the location between blade numbers 10 and 11 when the crack propagated.

The absence of rotor blades was confirmed with the tip timing and impeller inspection results. Figures 5.24 and 5.25 show the tip timing results from the fifth run. The tip timing of blade number 10 disappeared at 19.96 sec, while the tip timing of blade number 11 doubled. The lost tip timing means there was no sign of blade number 10 passing the blade tip timing sensor during that period. The blade passing

signals confirmed that blade 10 was lost between 19.947 to 19.96 sec, as shown in Figure 5.26. Figure 5.27 (a) shows the broken blade of blade number 10. The sawtooth pattern in Figure 5.27 (b) indicated the fatigue-crack propagation caused by cyclic load [22].

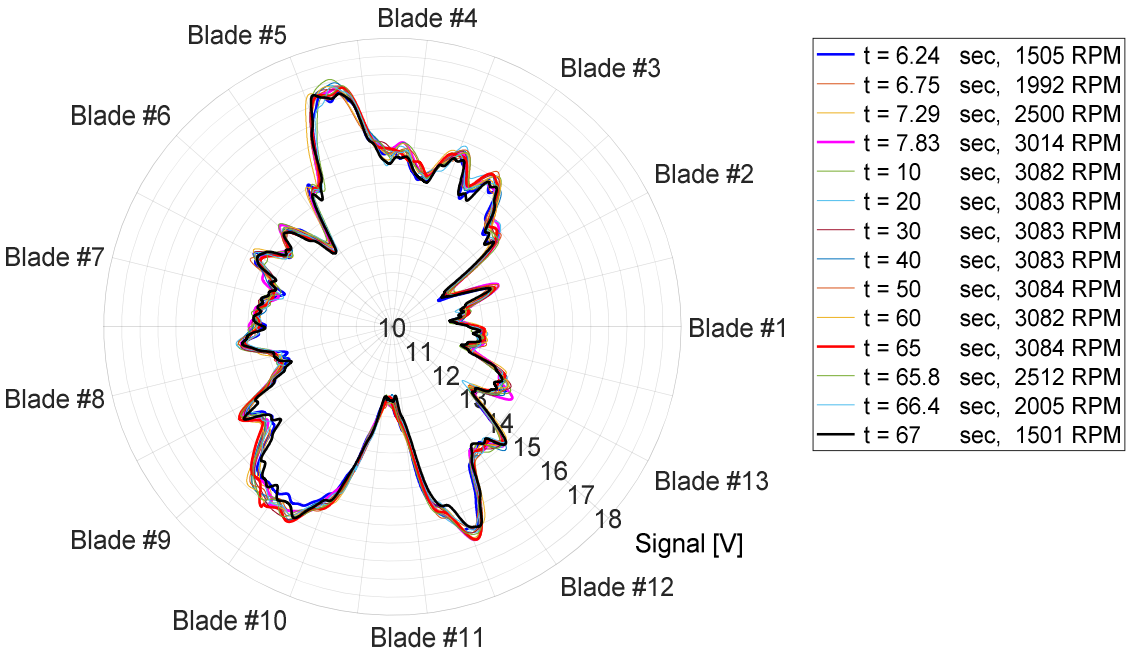


Figure 5. 18 Inlet shroud clearance signal of the impeller with the initial 11-mm crack on blade number 10 during the 1st run

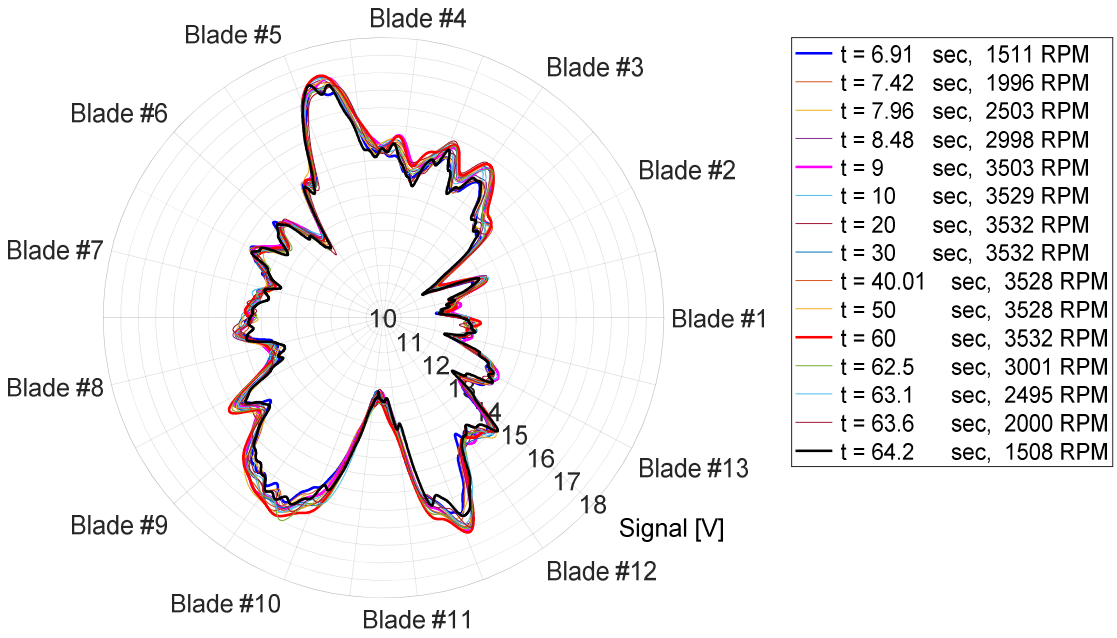


Figure 5. 19 Inlet shroud clearance signal of the impeller with the initial 11-mm crack on blade number 10 during the 2nd run.

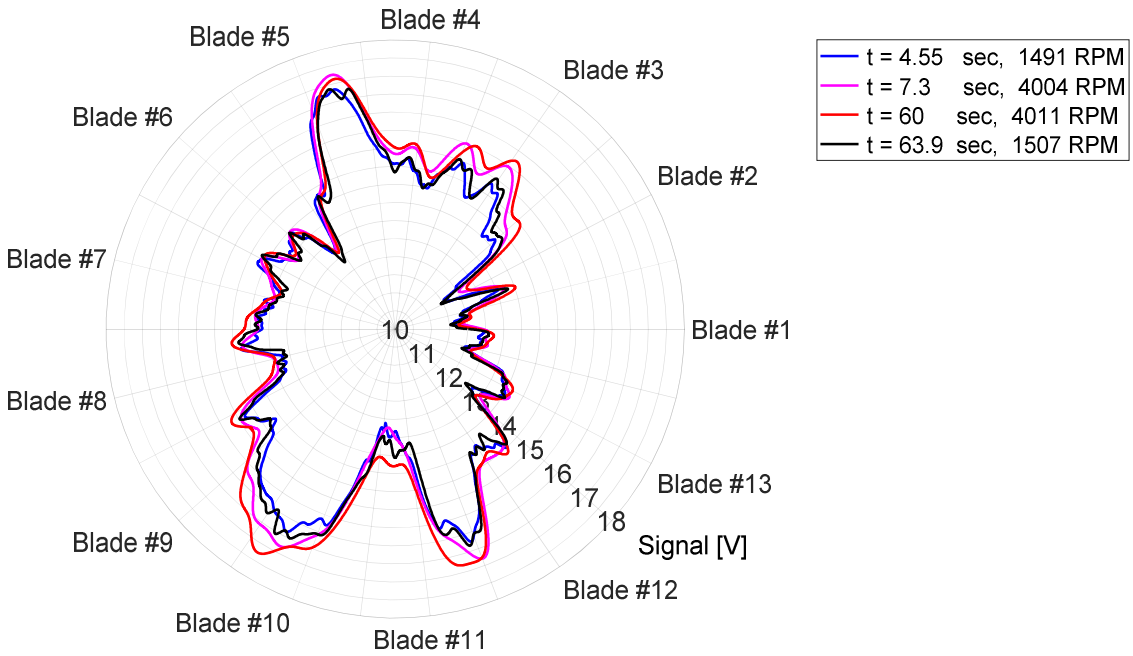


Figure 5. 20 Inlet shroud clearance signal of the impeller with the initial 11-mm crack on blade number 10 during the 3rd run

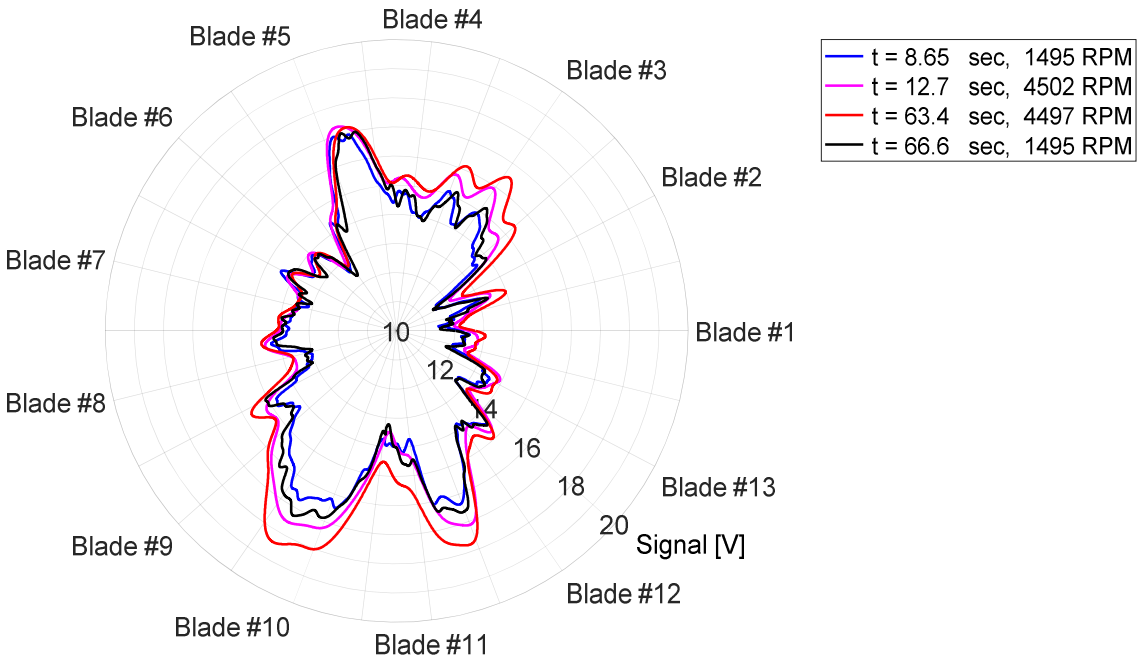


Figure 5. 21 Inlet shroud clearance signal of the impeller with the initial 11-mm crack on blade number 10 during the 4th run

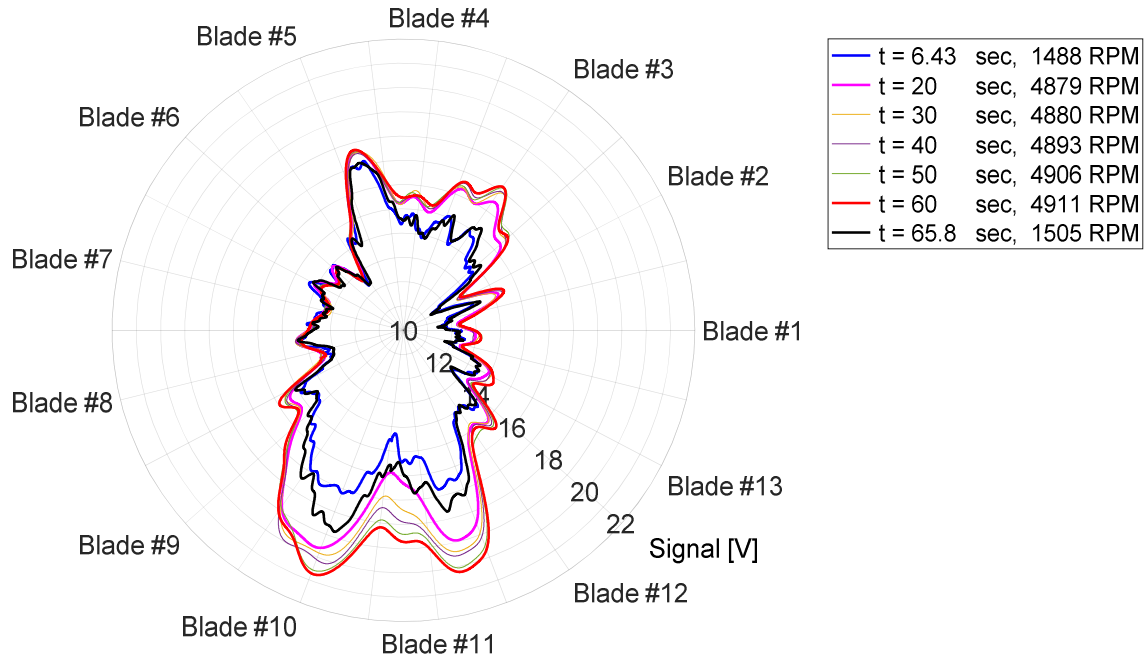


Figure 5. 22 Inlet shroud clearance signal of the impeller with the initial 11-mm crack on blade number 10 during the 5th run

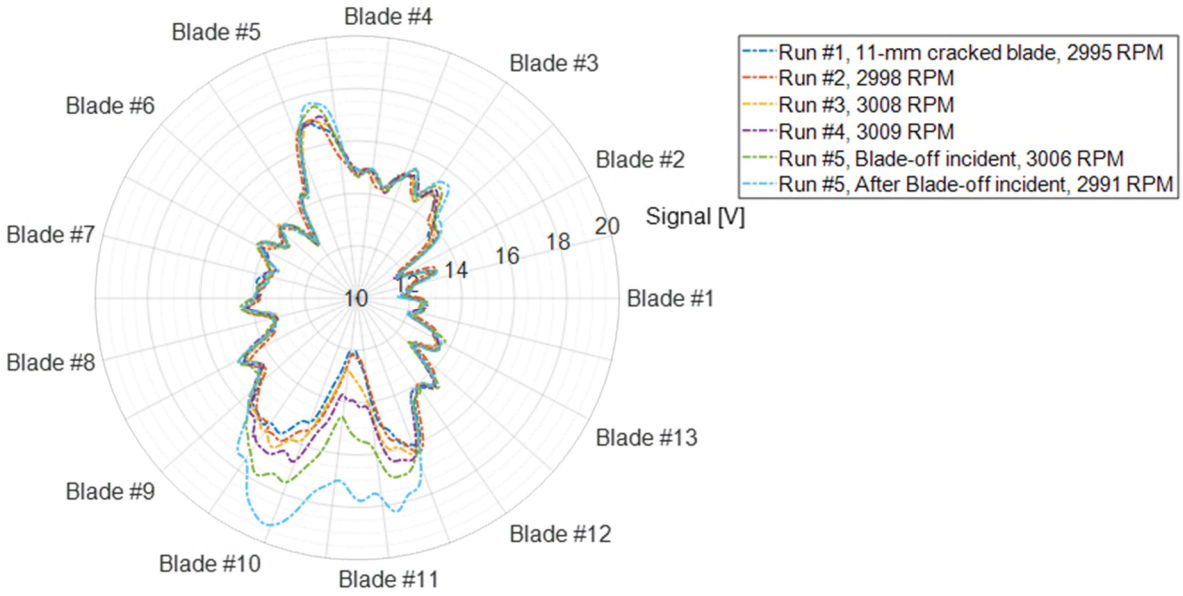


Figure 5. 23 Comparison of the inlet shroud clearance signals of the impeller with the initial 11-mm crack on blade number 10 between the five runs at the same speed of 3,000 RPM

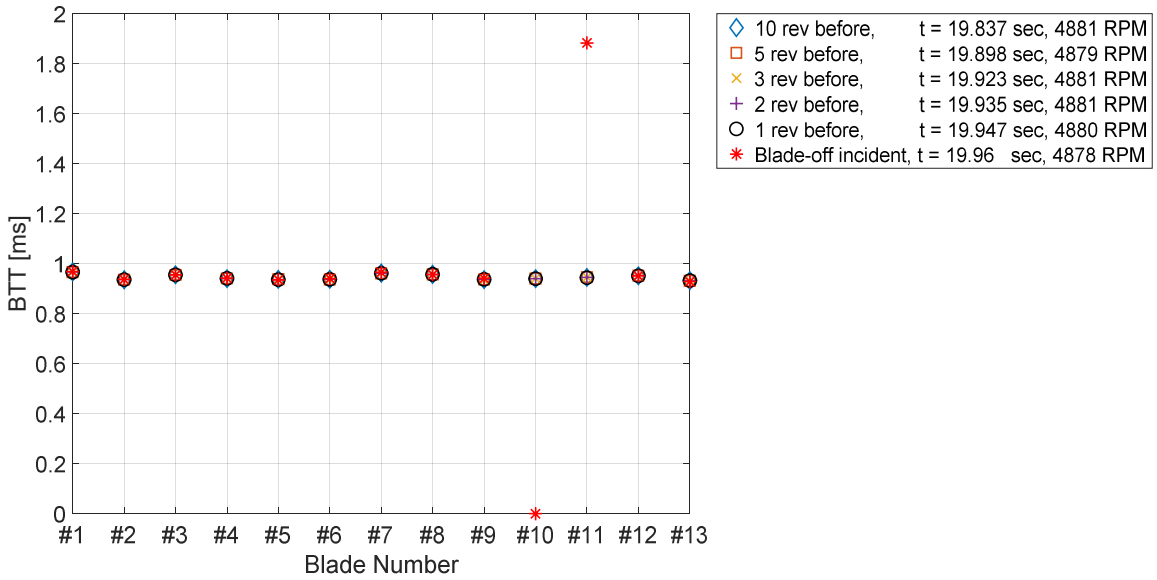


Figure 5. 24 Tip timing before and at the blade-off incident from the 5th run

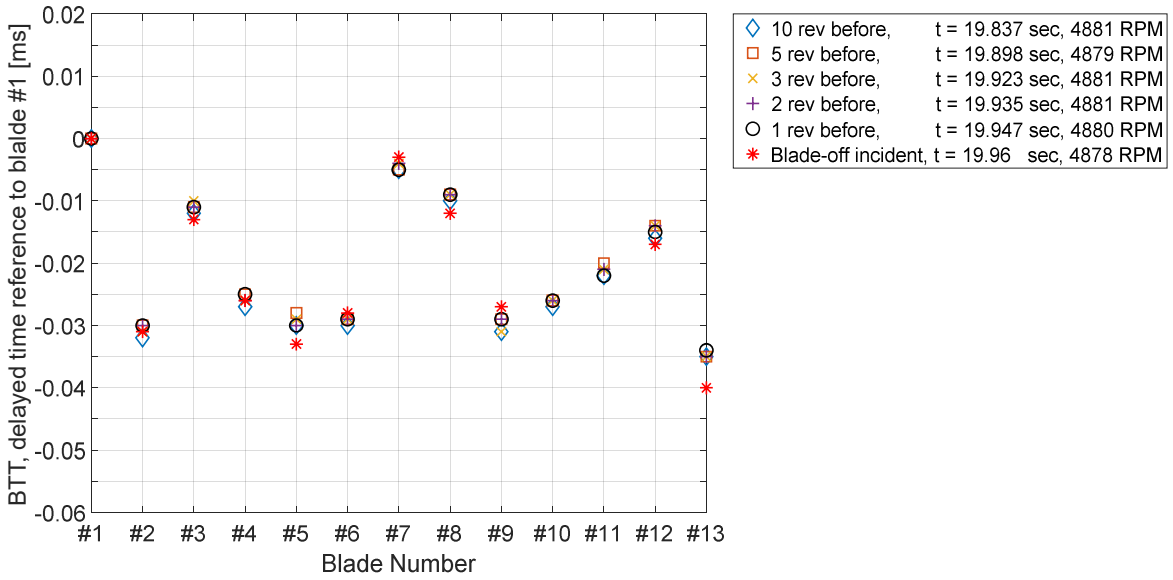


Figure 5. 25 Tip timing before and at the blade-off incident from the 5th run (magnified)

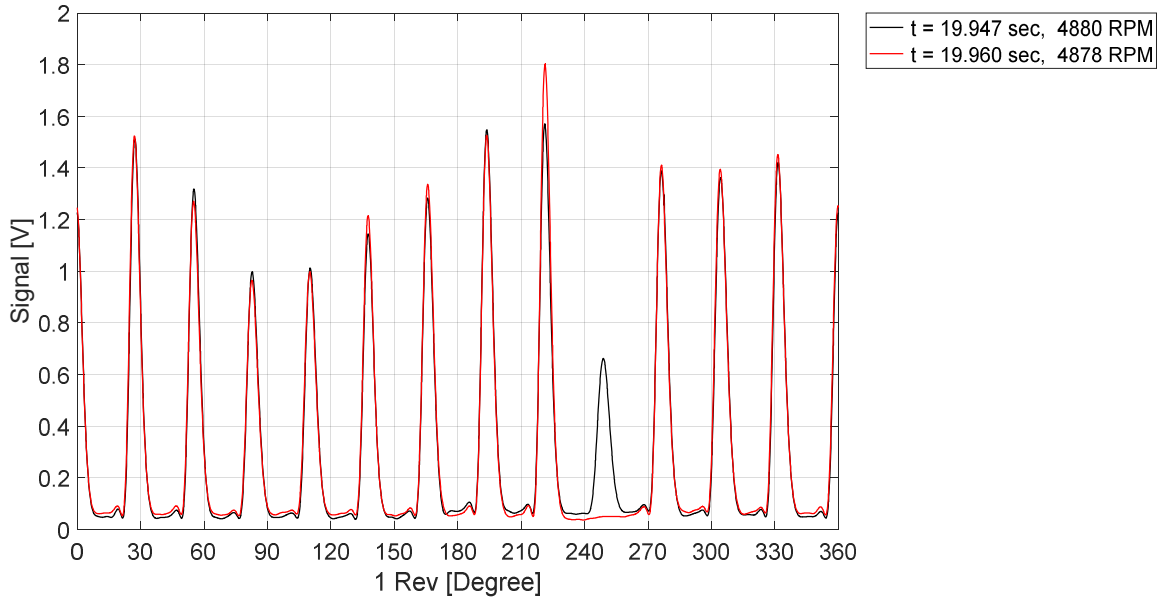


Figure 5. 26 Blade passing signals before and after the blade-off incident from the 5th run

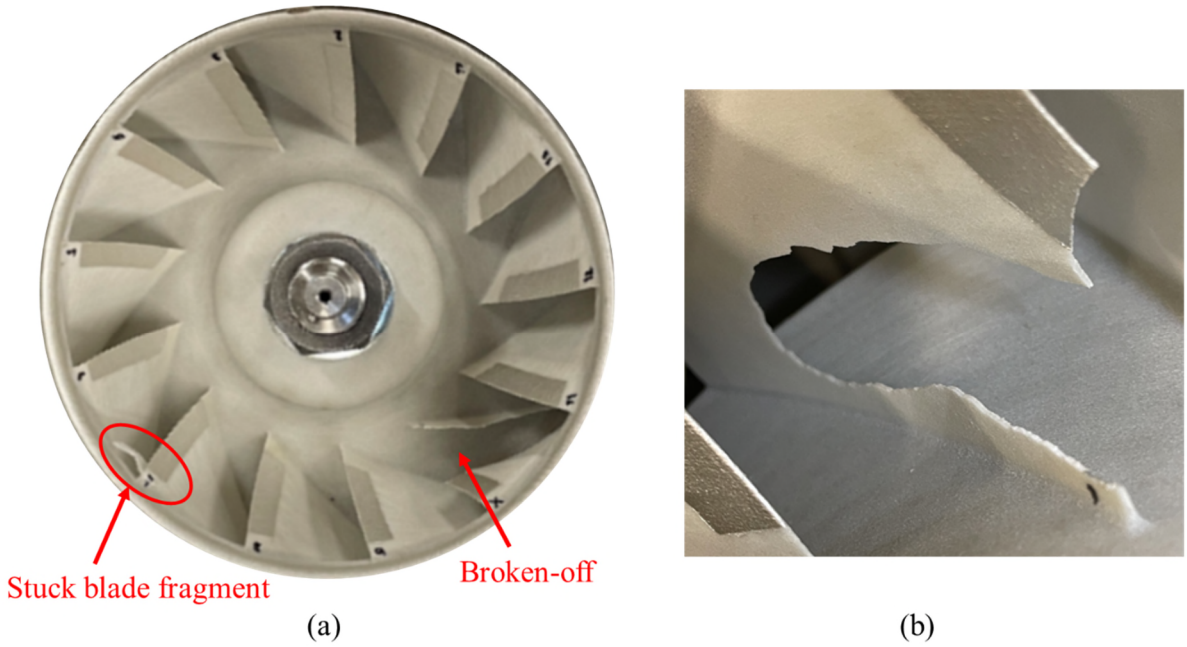


Figure 5. 27 The damaged impeller (a) the location of the broken blade and the stuck blade fragment; and (b) the sawtooth pattern on the broken-off blade

5.3.2. Stuck blade fragment incident

In addition to the blade-off incident on blade number 10, the impeller inspection after the experiment revealed that a piece of the broken blade had hit and was stuck with blade number 7. If this piece of the broken blade finds its way through the blades and impacts the impeller in the next stage, this may define as Foreign Object Debris (FOD) [17]. Figures 5.16 (d) and 5.27 (a) show the size of the stuck blade fragment and impact location on the shrouded impeller.

The clearance signal was investigated to identify this impact event. The clearance signals from the fifth run in Figure 5.28 indicate that the impact on the shroud area connected to blade number 7 occurred at 19.96 sec – the same period as the blade-off incident. It is worth noting that the clearance signal suddenly decreased at the

impact time before returning close to the same value. This finding indicated the possibility of impact detection of the blade fragment on a rotor blade with the outer shroud clearance measurement.

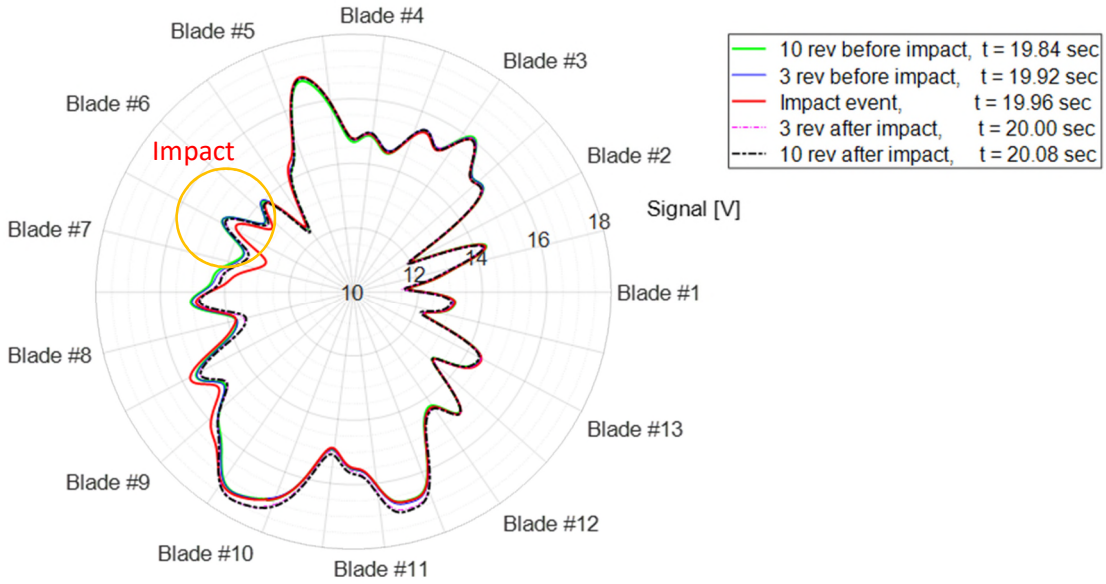


Figure 5. 28 Inlet shroud clearance signal during the impact at blade number 7

5.3.3. Discussion for the preliminary experiment in crack detection

The results from the preliminary experiment confirmed the feasibility of detecting shrouded impeller blade damage by using shroud/casing clearance measurement. It was possible to detect the impeller blade crack propagation and even the stuck blade fragment incident with the change in the clearance signals from an eddy current sensor mounted on the outside of a shrouded impeller. However, the relationship between the change in clearance and the crack length was still unknown because the crack continued to grow during the experiment and blade inspection can be done at the end of each experiment stage. Therefore, the main experiment with the second impeller (identical design and fabrication) was planned to fulfil this gap.

In the main experiment, the impeller runout and eddy current sensor calibration were conducted with the second identical impeller to convert the eddy current signal to the absolute clearance. These processes and results are described in Chapter 3.

5.4 Impeller with a cracked blade – the main experiment

The objective of this main experiment was to determine the characteristics of the impeller shroud deflection in terms of magnitude and location on various blade conditions. Thus, an artificial crack was created on blade number 4 using the same method as the preliminary experiment: a V-shape notch at the blade leading edge near the hub of the impeller. This artificial crack was created following the crack propagation path in the preliminary experiment. However, this blade crack detection experiment was divided into five runs, each with a different blade crack length. The crack length varied from 4 mm to 20 mm in five steps to simulate each crack propagation stage. Figure 5.29 shows the healthy impeller blade and a cracked blade with various crack lengths. Notably, the impeller used in this experiment was the same impeller that was used in section 5.2 the impeller with healthy blades experiment.

In this experiment, the vacuum condition was controlled at an absolute pressure of 49.2 kPa to keep in line with the previous experimental condition, where the interaction of fluid passing through the impeller was limited. The rotor speed was controlled at 3,500 RPM to prevent crack propagation between each experimental stage.

The results from both the preliminary experiment and the impeller with the healthy blade experiment indicated that the inlet shroud position was the optimal location because it has a good response to the impeller blade condition. Besides, the shroud deflection at this location aligned with the sensor axial direction, making the clearance measurement straightforward. Therefore, these blade crack detection experiments were based primarily on clearance signals from the eddy current sensor at the inlet shroud.

Figure 5.30 compares the clearance signal of the impeller with a healthy blade with the impeller with a cracked blade at the same rotor speed of 3,500 RPM. It can be seen that with the clearance signal alone, it was quite challenging to distinguish the difference in the shroud impeller blade conditions.

However, the differences in blade conditions can be noticeable with the plot of relative signals. These relative signals in Figure 5.31 were calculated in reference to the clearance signal from the healthy impeller experiment at the same speed of 3,500 RPM. Therefore, the effect of changing centrifugal force to the shroud expansion was cancelled.

The experimental results confirmed that the change of relative clearance signals related to the crack propagation stages, as shown in Figure 5.31. Specifically, when the crack length exceeded 7 millimetres, the shroud clearance signal increased at two locations: at blade number 4 (corresponding with the cracked blade) and between blade number 10 and number 11. However, the increase was more prominent at the blade number 4 location, as evident in a crack length of 20 millimetres. In the same

way as the healthy experiment, increasing the clearance signal means the shroud is deflected closer to the clearance sensor.

The absolute clearance of each blade condition was computed using the calibration curves obtained in session 3.6.1. After that, the absolute clearances were deducted by the absolute clearance of the healthy impeller at 200 RPM in order to determine the relative clearance (Δ Clearance). The comparison of the relative clearances between various impeller blade conditions at the rotor speed of 3,500 RPM is shown in Figure 5.32. As the crack length increased, the shroud/sensor clearance decrease at the cracked blade number 4 became noticeable in the polar plots.

The relative shroud deflections with reference to the healthy impeller at the same speed of 3,500 RPM are shown in Figure 5.33. The shroud deflection increased in two opposite locations: at the cracked blade number 4 and on its opposite side between blade number 10 to 11. Nonetheless, when the crack was longer than 15 millimetres, the rise of shroud deflection was more significant at blade number 4.

The relation between the crack length and the change of shroud deflection is shown in Figure 5.34. It can be seen that the crack should be at least 7 millimetres in order to alter the shroud deflection significantly. The linear relation was readily apparent when the crack was greater than 5 millimetres. Thus, the crack length on a cracked blade could be predicted with the change of shroud deflection.

The linear relationship between the inlet shroud deflection and the crack length agreed with the study of Hou (2006) [47]. His study proposed the mechanisms of

cracked-induced mistuning in a blade-disk system using a simplified lumped-mass model. The study results indicated that the crack reduced local blade stiffness. In this case, the cracked blade connected the shroud and the hub. Thus, the reduced blade stiffness led to an increase in shroud deflection at the blade connecting location.

Based on the uncertainty of clearance measurement of ±8.8 μm., it can be deduced that the proposed technique could detect a cracked blade with a crack length of at least 15 millimetres. With this crack size, the shroud deflected around 18 μm at the cracked blade location. The calculation of clearance measurement uncertainty is detailed in session 3.6.2.

The crack on the impeller blade can also be detected with the conventional blade tip timing measurement. The blade arrival times and the relative blade arrival time with reference to blade number 1 are shown in Figures 5.35 and 5.36, respectively. When considered with uncertainty bars, the minimum crack size detected by the blade tip timing measurement was 15 mm in length. The arrival times depended on the crack size. Crack growth led to a reduction in the arrival time. However, installing a blade tip timing sensor in front of the blade leading edge is impractical because the sensor would impede the gas flow.

Furthermore, the vibration measurements using accelerometers cannot detect the differences in blade conditions since the cracked blade was still attached to the impeller (no mass loss with a split part) and therefore had less effect on the change of rotor mass distribution. The comparison of vibrational spectra between the

healthy blade impeller and the impeller with a 20-millimetre cracked blade at a rotor speed of 3,500 RPM is shown in Figure 5.37.

In brief, the artificial crack was created on blade number 4 to determine the behaviour of the impeller shroud in terms of the change in clearance. The artificial crack was varied from 4 to 20 millimetres. The increase in shroud deflection was significant as the crack exceeded 15 millimetres. The linear relation between the crack length and the relative shroud deflection was reported.

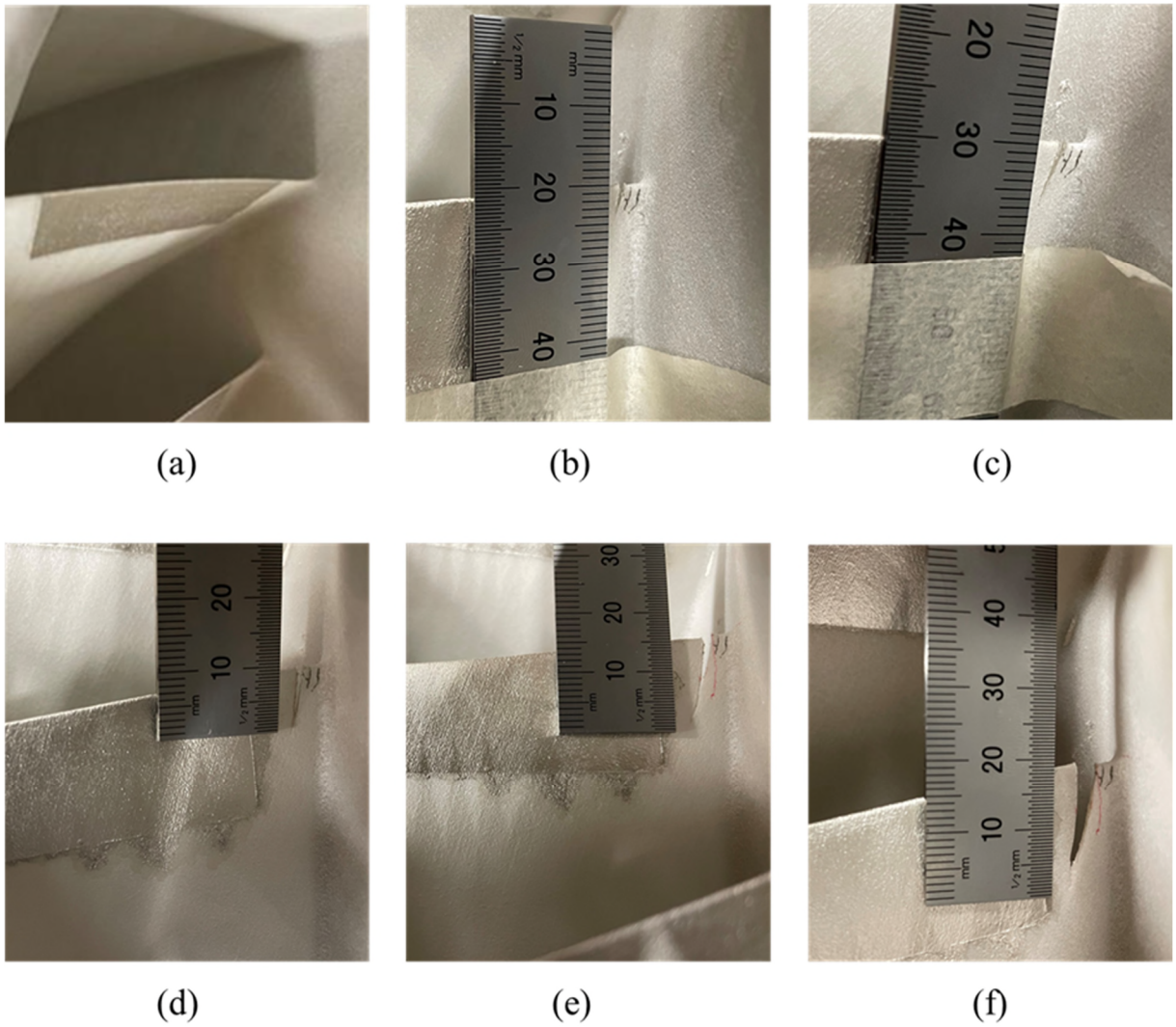


Figure 5. 29 Impeller blade conditions (a) a healthy blade; (b) a 4-mm cracked blade; (c) a 7-mm cracked blade; (d) a 10-mm cracked blade; (e) a 15-mm cracked blade; and (f) a 20-mm cracked blade

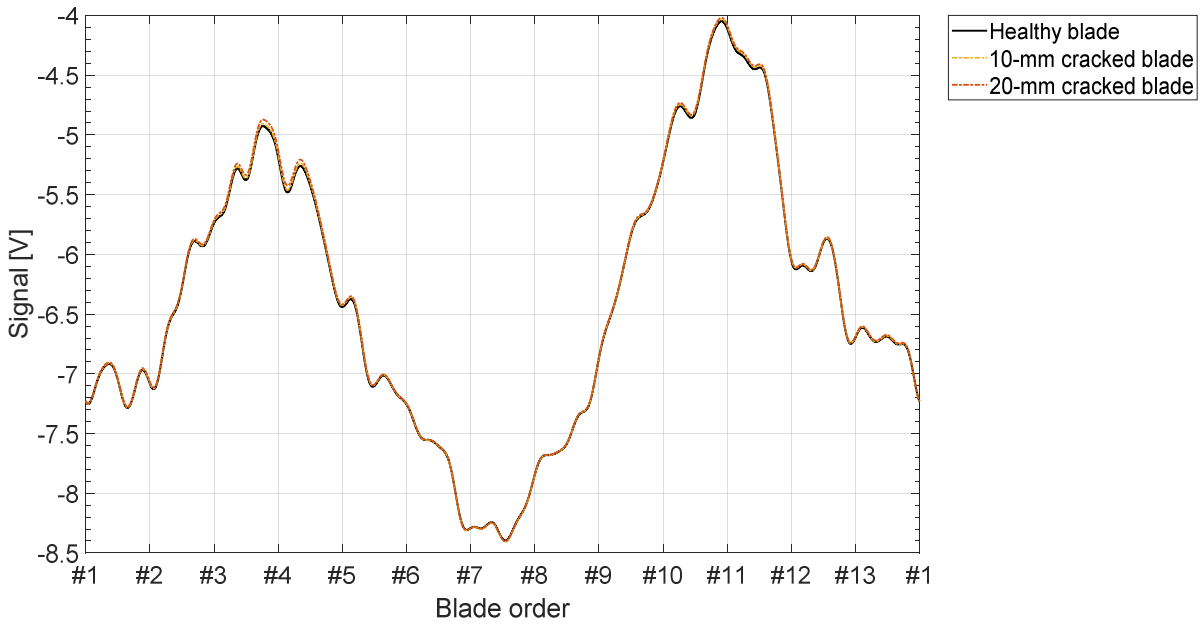


Figure 5. 30 Inlet shroud clearance signals of the healthy impeller compared with the impeller with a cracked blade at a rotor speed of 3,500 RPM

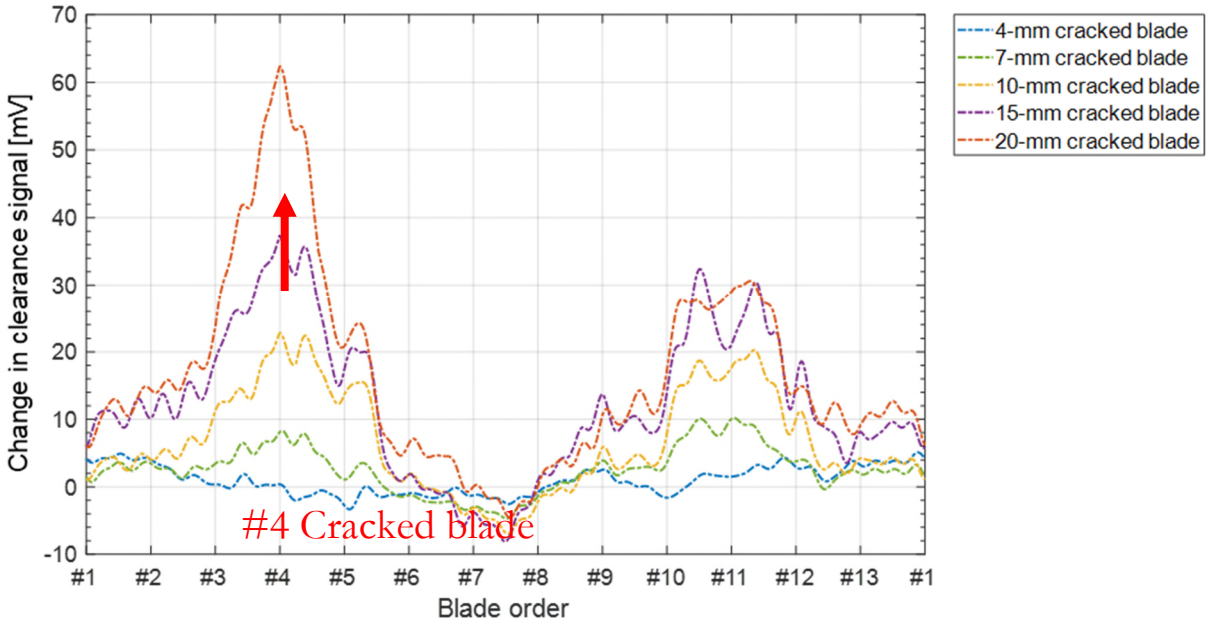


Figure 5. 31 The differences in clearance signals with reference to the signal of the impeller with healthy blades at a rotor speed of 3,500 RPM

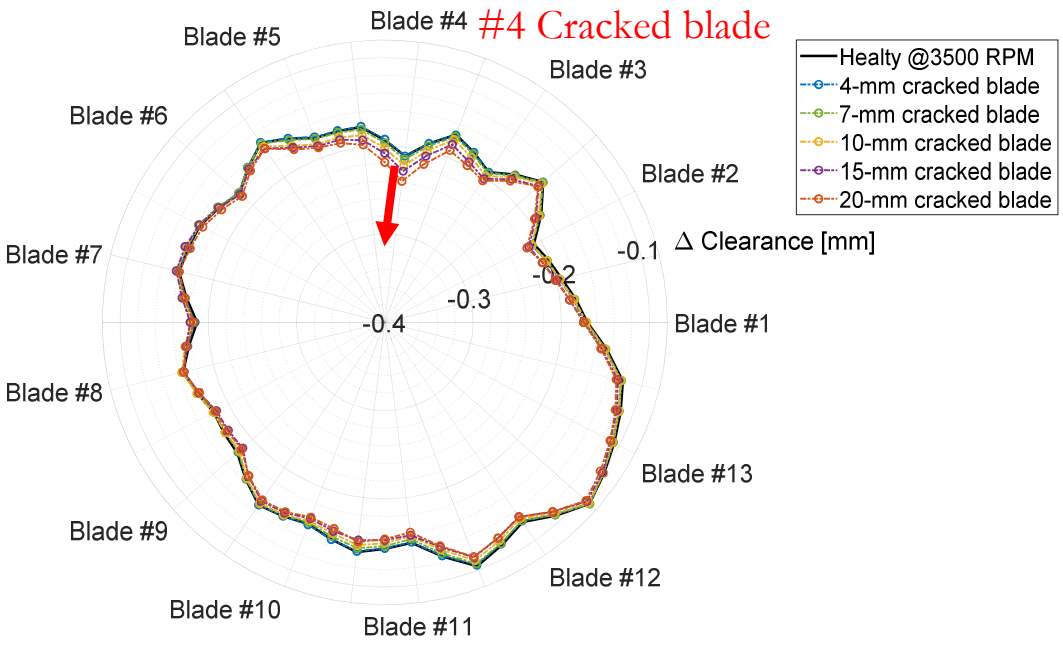


Figure 5. 32 The change of the inlet shroud clearance at different impeller blade conditions at 3,500 RPM with reference to the impeller with healthy blade condition at 200 RPM

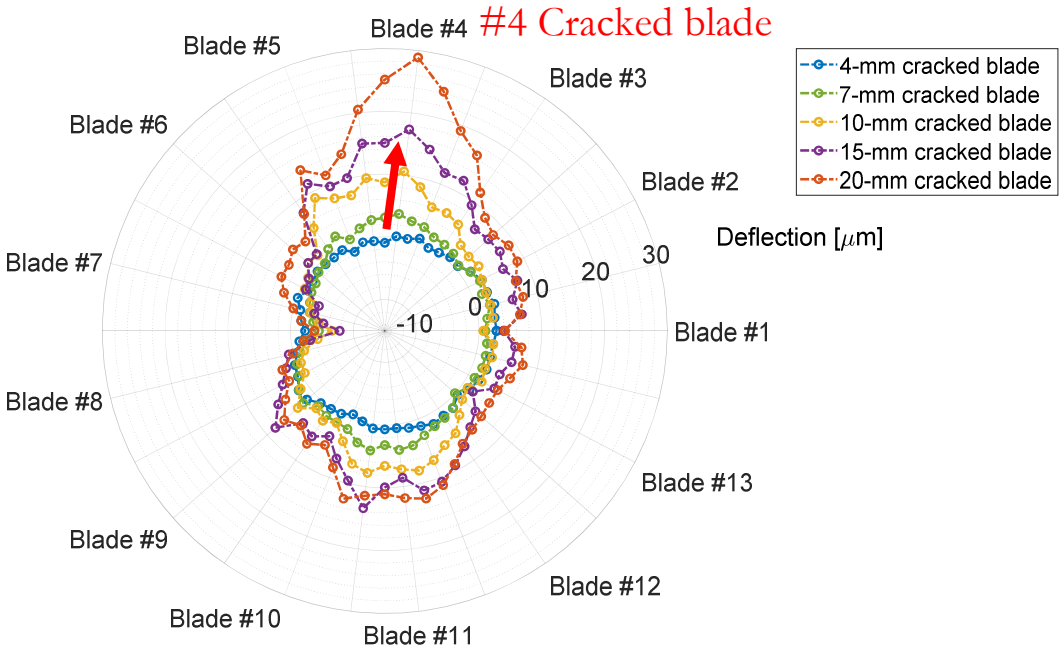


Figure 5. 33 The polar plot of the change of the inlet shroud clearance at different impeller blade conditions with reference to the impeller with healthy blade condition at the same speed of 3,500 RPM

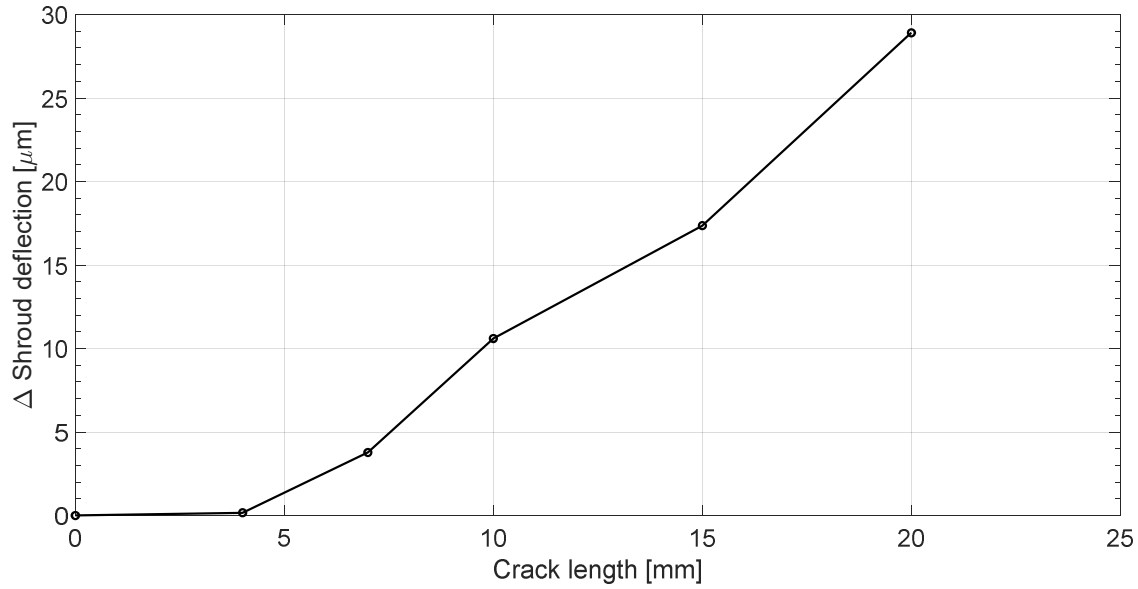


Figure 5. 34 The relation between the crack length and the change in shroud deflection at the inlet shroud position at 3,500 RPM

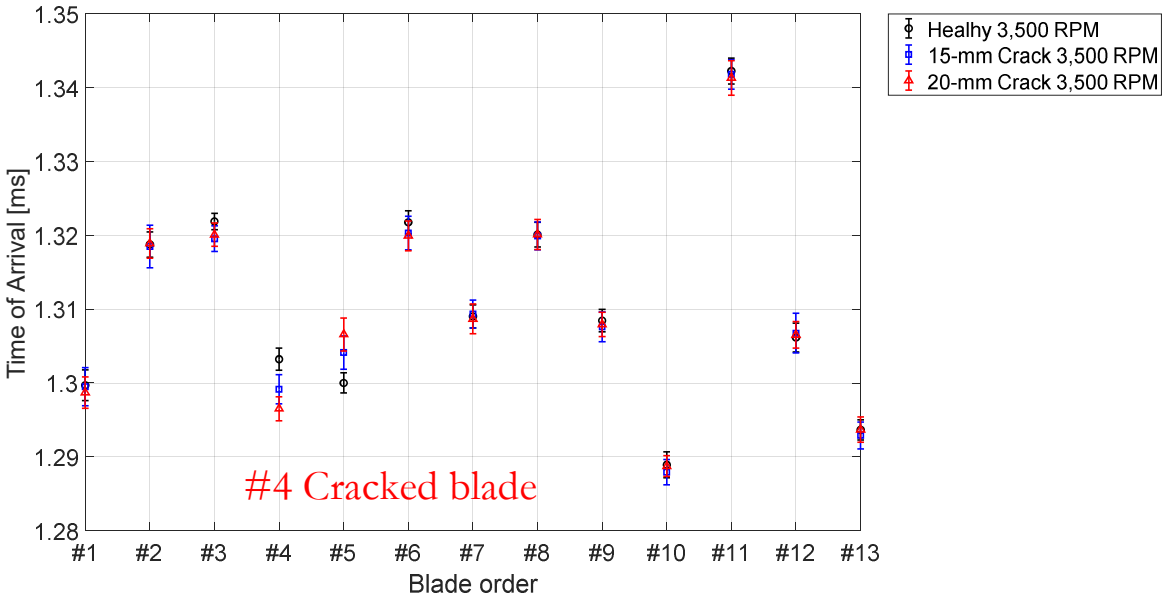


Figure 5. 35 Comparison of blade arrival times among the different blade conditions, including a healthy blade, a 15-mm cracked blade, and a 20-mm cracked blade at a rotor speed of 3,500 RPM

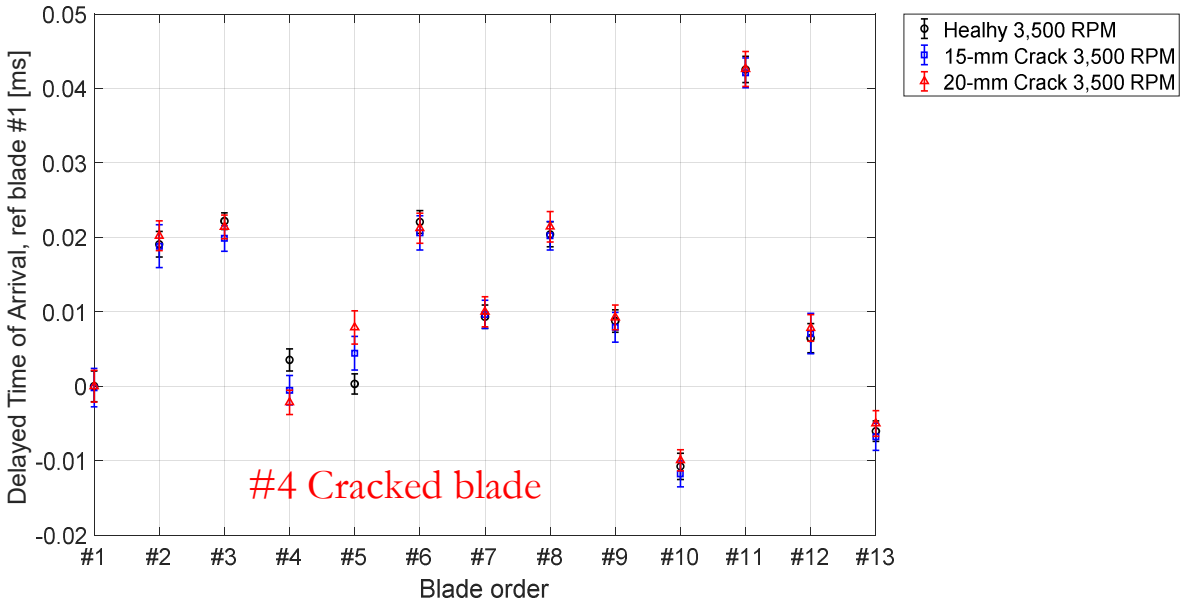


Figure 5. 36 Comparison of the delayed arrival times among the different blade conditions, including a healthy blade, a 10-mm cracked blade, and a 20-mm cracked blade with reference to blade number 1 at a rotor speed of 3,500 RPM

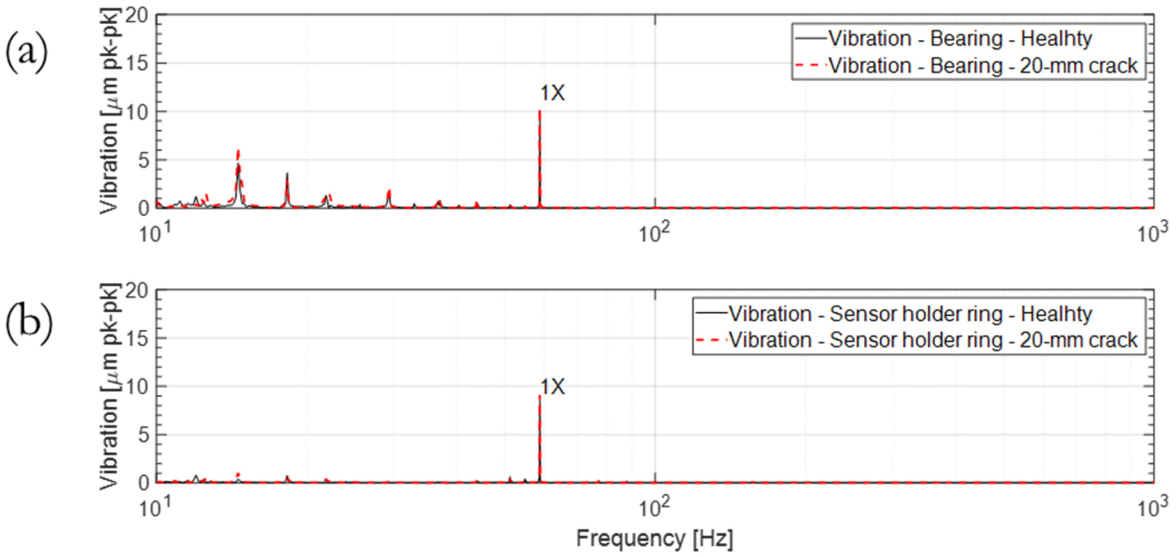


Figure 5. 37 Comparison of the frequency spectra impeller with a 20-mm cracked blade system at 3,500 RPM (a) vibrational spectra of the bottom bearing; and (b) vibrational spectra of the sensor holder ring

initial cracked blade to detect crack propagation on the shrouded impeller. The experimental results confirmed that the clearance measurement using eddy current sensors mounted on the outside of a shrouded impeller was able to detect the crack propagation on a shrouded impeller's blade without affecting the gas flow path through the impeller. In addition, the stuck blade fragment incident can also be detected using the proposed clearance measurement method.

5.5 Chapter conclusion

In this chapter, the blade health monitoring experiments were conducted. The experiments were divided into two conditions: the impeller with healthy blades and the impeller with a cracked blade. The

The experimental results from the impeller with the healthy blade experiment provided the baseline case for impeller deformation caused by the effect of the centrifugal force. The deflection magnitude depended on the rotational speed and location. These results were used as a basis for the cracked blade experiments.

Results from the preliminary crack blade experiment confirmed that the clearance measurement using eddy current sensors mounted on the outside of a shrouded impeller was able to detect the crack propagation on a shrouded impeller's blade without affecting the gas flow path through the impeller. In addition, the stuck blade fragment incident can also be detected using the proposed clearance measurement method.

Another two research objectives were achieved in the main crack blade experiment. In this main experiment, the crack length was varied from 4 to 20 millimetres. The clearance signal from the eddy current sensor at the inlet shroud location established the linear relationship between the crack length and the characteristics of the shroud deflection. In addition, when combined with the clearance measurement uncertainty from Chapter 3, the minimum detectable crack for the scaled 3D-printed plastic impeller using in the experiment was around 15 millimetres. This result indicated the crack stage that can be detected early with the proposed system.

Chapter 6

Numerical Studies of Blade Crack Detection

6.1 Introduction

Numerical studies of blade crack detection aimed to create a simulation model to predict the deformations of the scaled impeller with different blade conditions. The experimental results in Chapter 5 were used to validate the simulation model. Subsequently, the simulation model was adjusted in parametric studies to determine the characteristics of shroud deflections for various impeller designs, including blade numbers, blade thickness and shroud thickness. In addition, the effect of different impeller materials on the shroud deflection was also investigated.

6.2 Static structural analysis

In these numerical studies, the Finite Element Analysis (FEA) of the scaled impeller with and without a crack blade was conducted using the Static Structural module in ANSYS®. The solutions in terms of displacement $\{x\}$ was obtained by solving the linear matrix Hooke's law equation [95]:

$$[K]\{x\} = \{F\} \quad (6.1)$$

where $[K]$ and $\{F\}$ were stiffness and applied force matrices, respectively.

The linear static structural analysis is based on the assumptions that a material has linear elastic behaviour (constant stiffness) and the force is statically applied.

6.3 Simulation models

6.3.1 Simulation models and boundary conditions

A 3-dimensional simulation model in Figure 6.1 (a) was used to simulate the deflection of the scaled impeller in various blade conditions. This simulation model was based on the CAD file created for the impeller manufacturing process (3D printed). Notably, the shrouded impeller was modelled as a perfect round geometry which may not accurately capture the shape of the unstressed test impeller. Nonetheless, a reasonable match has been obtained. Figure 6.1 (b) illustrates the mesh of the model. The finer mesh was specified at the impeller blades, which were critical components of the shrouded impeller. The mechanical properties of the fibre-reinforce polymer are shown in Table 6.1. These mechanical properties were obtained from the 3D printing manufacturer's material data sheet. This may be a potential source of differences between the model results and the experimental data.

These simulations neglected the fluid interaction with the shrouded impeller. This criterion conformed with the experimental studies in Chapter 5, which were conducted under vacuum conditions at an absolute pressure of 49.2 kPa. Thus, the boundary conditions in these simulations were only varying rotating velocity in the

clockwise direction, the standard earth gravity in the impeller axial direction, and the fixed support at the impeller shaft hole. Figure 6.1 (c) shows the assigned boundary conditions.

To simulate a crack on an impeller blade, the actual crack path in the experimental studies was mapped into the CAD model using a 3D scan. This crack path was divided into sixteen equal sections to simulate the steps of the crack propagation. The red arrow in Figure 6.1 (d) indicates the crack path on the simulation models. Frictionless contact was assigned between the crack surfaces. This frictionless contact allows the separation and transition of bodies in the normal and tangential directions, respectively. However, penetration between bodies is not permitted by this setup [96].

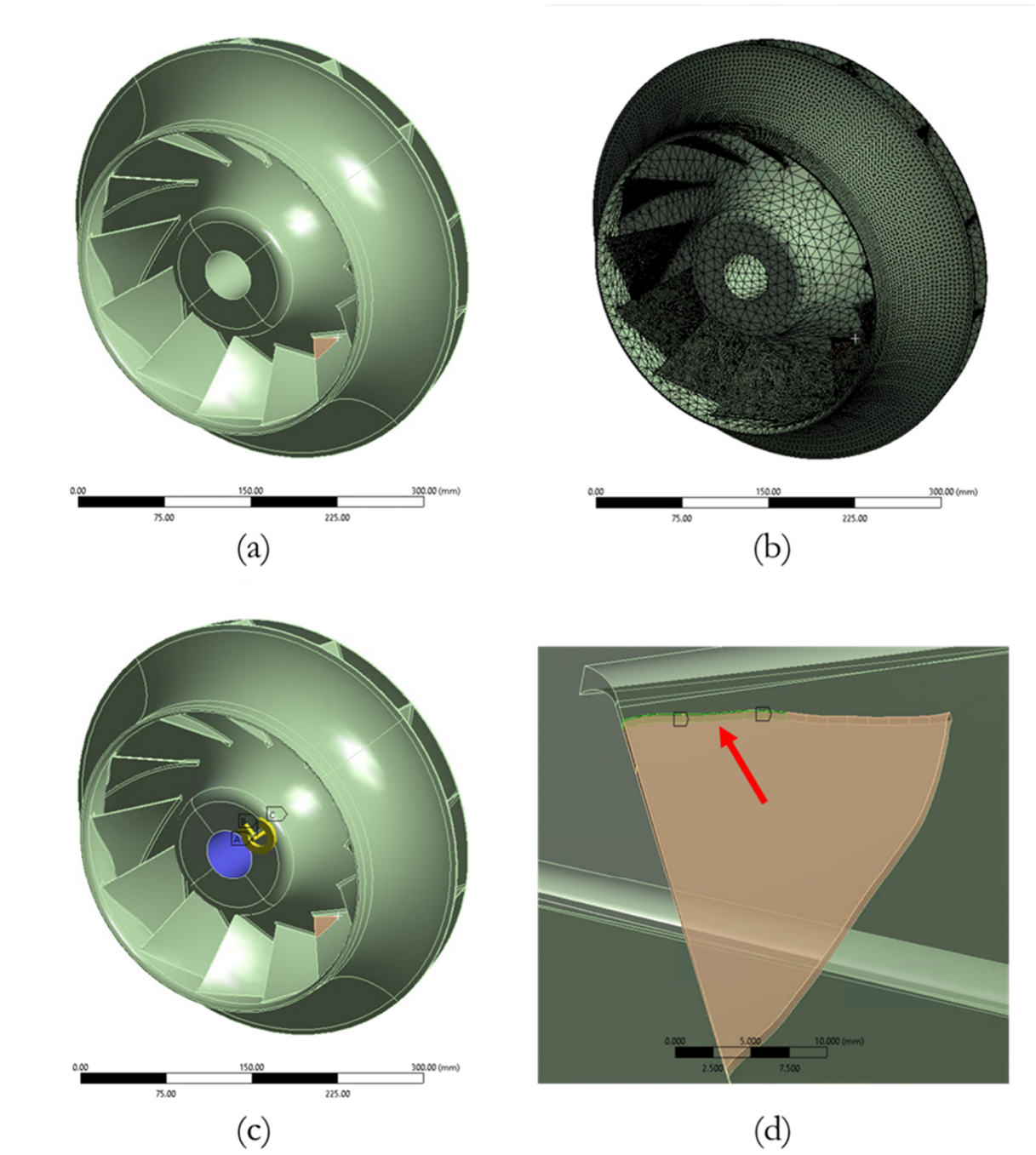


Figure 6. 1 Finite element simulation model (a) the scaled impeller with a cracked blade; (b) mesh of the simulation model; (c) the applied boundary conditions; and (d) the crack path

Table 6. 1 Mechanical properties of the material used in simulations

Mechanical properties	Fibre-reinforce polymer
Density [kg/m^3]	1,620
Modulus of elasticity [kPa]	3,300
Passion's ratio	0.39

6.3.2 Mesh sizing

In FEA studies, algebraic equations of discretised elements are solved to obtain a predicted solution. The accuracy of the predicted solution partly depends on the number of elements used in a simulation model. However, an excessive number of elements consumes computational resources and calculation time. Thus, the mesh sizing was performed to obtain the optimal balance between the number of elements and the processing time without compromising the accuracy of the simulation results.

The mesh sizing was conducted with the simulation model of the scaled impeller with a 21.5-mm cracked blade, as shown in Figure 6.1. The rotating velocity related to the impeller rotational speed of 4,000 RPM in the clockwise direction and the fixed support at the impeller shaft hole were set as boundary conditions. The tetrahedral elements had minimum element sizes ranging from 0.5 to 5 mm. The number of elements and nodes increase as the element size decreases. At a minimal element size of 0.5 mm, the simulation models had around 7.03 x 10^5 elements and 6.89 x 10^5 nodes.

The predicted maximum and minimum shroud deflection converge as the number of elements increases, as shown in Figure 6.2. Consequently, the minimum element size of 0.5 mm with 7.03 x 10^5 elements was specified in these FEA studies due to the optimal balance between the predicted results and the simulation time of around 40 minutes per simulation case.

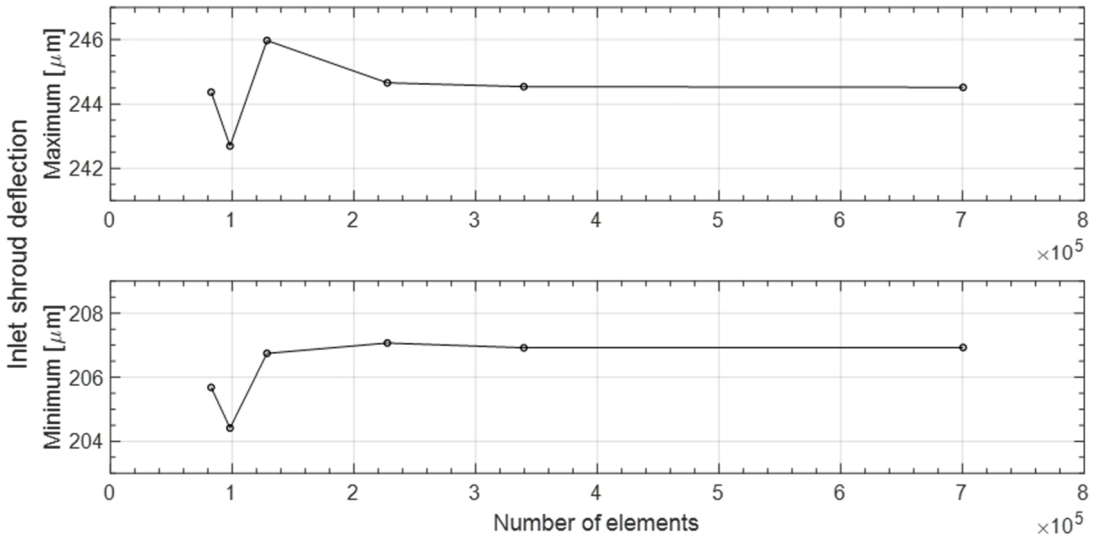


Figure 6. 2 The maximum and minimum inlet shroud deflection against the number of elements

6.4 FEA of the scaled impeller

6.4.1 FEA of the scaled impeller with healthy blades

The deflections of the scaled impeller with healthy blades were predicted using the simulation model in Figure 6.1. The impeller rotational speed between 1,000 to 4,000 RPM was assigned as a boundary condition for the Static Structural analysis.

The healthy impeller simulation results predicted that the outlet shroud and the impeller blades were the components with significant total deflections. In contrast, there was less total deflection at the impeller hub. Figures 6.3 (a) and (b) illustrate the total deflection of the healthy impeller at the speed of 3,500 RPM in the front and the back impeller sides, respectively.

Figure 6.3 (c) depicts only the blade total deflection. It can be seen that the maximum deflection occurred at the mid-span of the blade. This blade deflection corresponded with the first mode of blade vibration.

The Static Structural analysis also provided the predicted stress distribution. The maximum stress occurred at the blade leading edge near the hub side, as shown in Figure 6.3 (d). This maximum stress location was the location of the initial crack in the experimental studies.

The predicted relationship between the maximum stress at this location and the impeller speed is shown in Figure 6.4. The predicted relationship indicated that the maximum stress would be over the ultimate tensile strength of the impeller at the speed of 4,000 RPM. These simulation results explained why there was no crack

propagation in the experimental studies in Chapter 5, which limited the impeller speed to 3,500 RPM.

The predicted deflections from various locations based on the measurement locations in the experimental studies are shown in Figure 6.5. The coordinate system for identifying deflection direction is shown at the centre of each plot. Obviously, the maximum deflections were observed at the blade-connecting regions for both shroud and back-end wall.

The healthy impeller simulation model was validated with the experimental results from Chapter 5. The polar plot in Figure 6.6 compares the radial inlet shroud deflections of the healthy impeller between the experimental and simulation results at various speeds. The correspondence was observed in most locations, except between blade numbers 11 and 13. This difference may relate to the quality of the 3D-printed impeller using the experiments, which might not be perfect as the simulation model.

The quadratic relationship between the radial inlet shroud deflection and the speed of the impeller is shown in Figure 6.7. The deflection increased with increasing speed. However, this increase in shroud deflection did not ideally follow the effect of the centrifugal force as speed increased because the shroud stiffness was involved.

The relationship between the averaged axial shroud deflection and the speed of the impeller is shown in Figure 6.8. The decreased deflection means that the impeller

moved to the hub side as the speed increased. However, this axial deflection was slight and uniform, so it did not affect the inlet shroud measurement in the radial direction. Similarly, the radial inlet shroud measurement was less affected by the change in the shroud twist angle. Figure 6.9 shows the relationship between the shroud twist angle and impeller speed. Notably, the shroud twist angle was measured in the counter-clockwise direction, opposite to the direction of rotation.

Apart from the inlet shroud deflection, the predicted deflection of the back-end wall was also compared with the experimental results. The consistency between the two results is shown in Figure 6.10. The increased deflection as speed in Figure 6.11 indicated that the impeller back-end wall moved upward. In other words, the clearance between the back-end wall and a clearance sensor underneath was increased with impeller speed.

Furthermore, the comparison of the axial outlet shroud deflections between the simulation and the experimental results is shown in Figure 6.12. In this location, the increase in deflection means that the shroud bent forward to the inlet side – the clearance between the shroud/sensor decreased.

As the impeller speed increased, the disparity between the predicted and the experimental results became more apparent. This difference is because the impeller at the outlet shroud location exhibited axial and radial deflections. These deflections increased with the impeller speed, as shown in Figure 6.13. As the shroud expanded, the clearance measurement location was shifted closer to the shroud in the radial direction. This shift in measurement location causes the measured deflections to be

greater than predicted. The comparison of the axial outlet shroud deflections between the experimental results and the simulation results, taking into account the effect of the radial deflection, is shown in Figure 6.14.

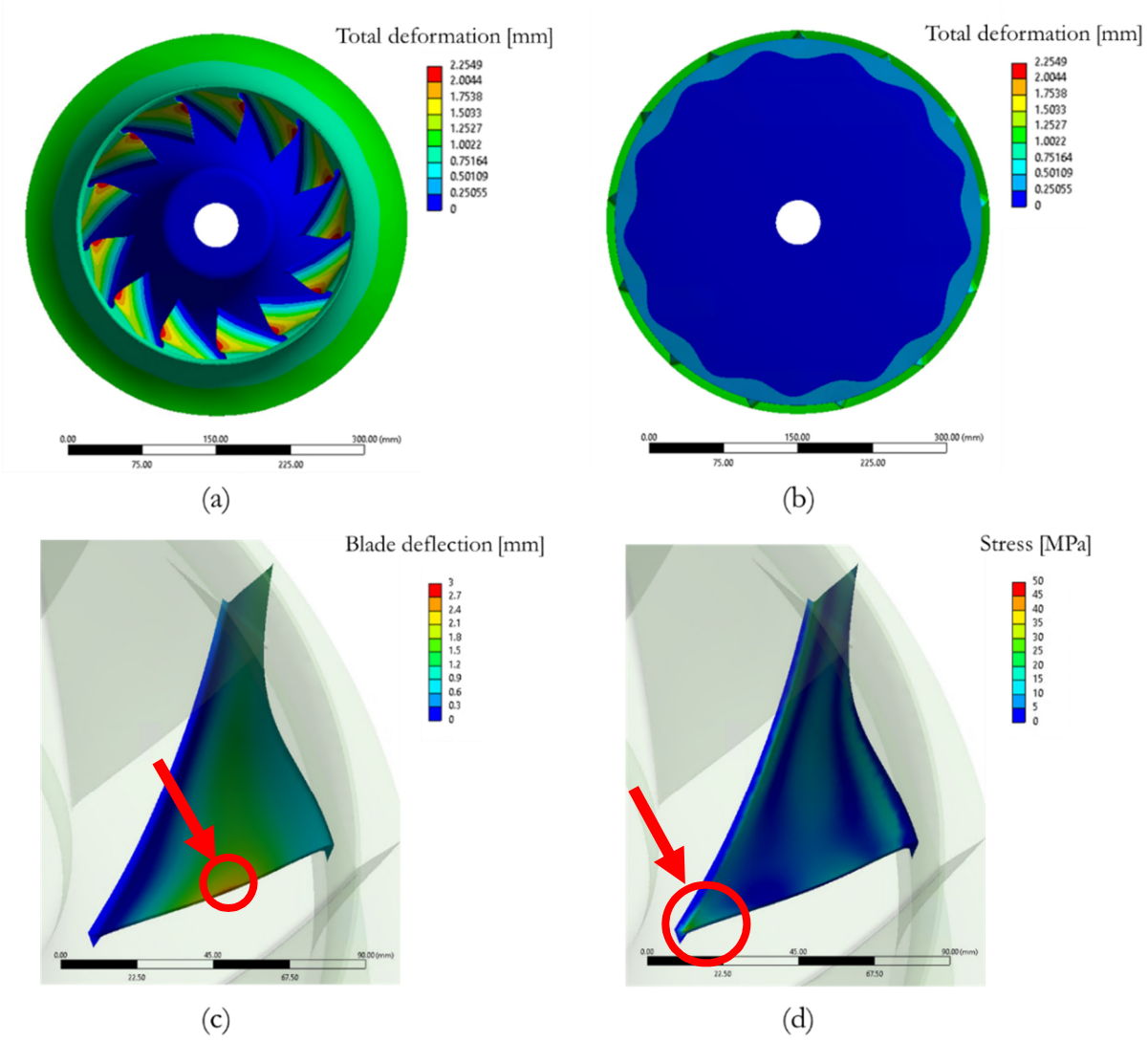


Figure 6. 3 Simulation results of the healthy impeller at the rotating speed of 3,500 RPM (a) total deflection at the front view; (b) total deflection at the back view; (c) blade total deflection; and (d) blade stress distribution

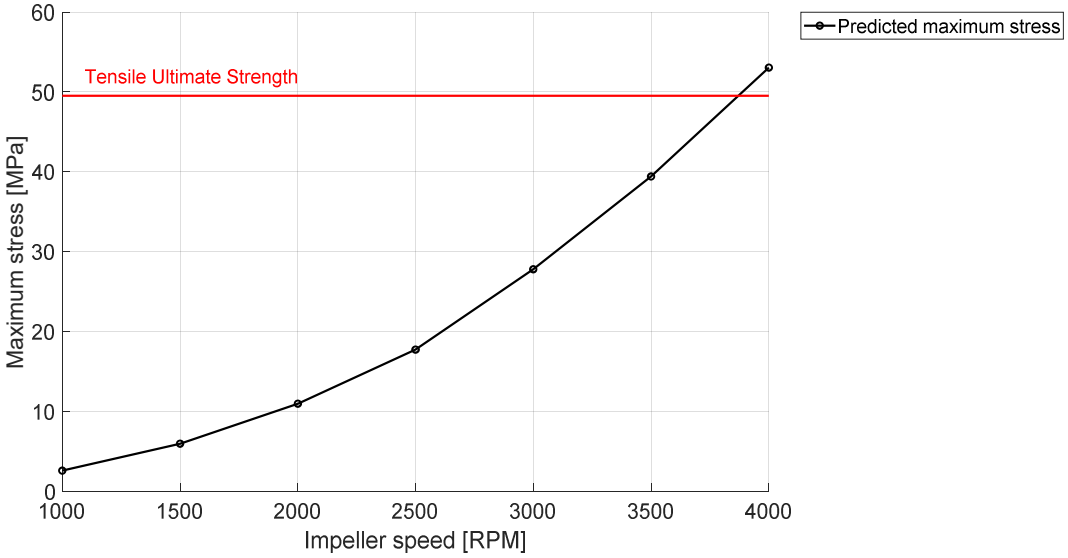


Figure 6. 4 The predicted relationship between the maximum stress and the impeller speed

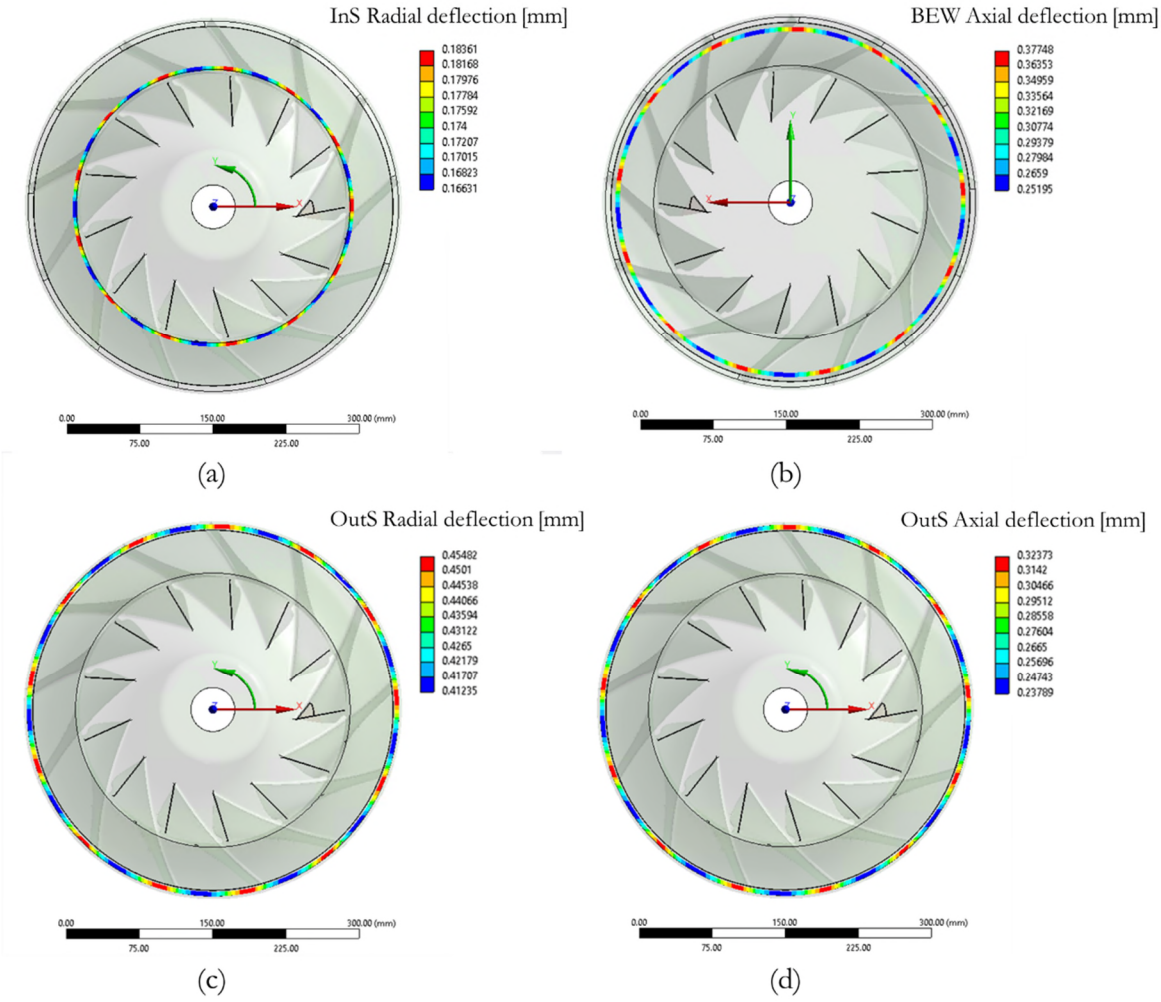


Figure 6. 5 The predicted deflections (a) inlet shroud, radial; (b) back-end wall, axial; (c) Outlet shroud, radial; and (d) Outlet shroud, axial

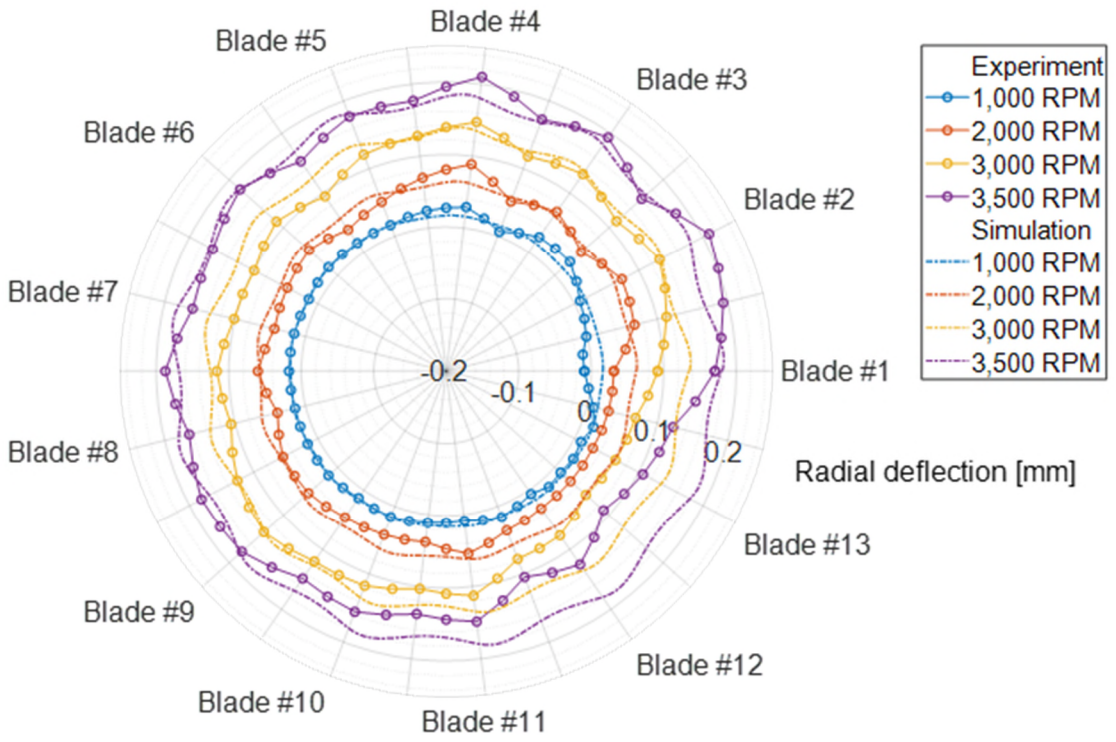


Figure 6. 6 Comparison of the radial inlet shroud deflections of the healthy impeller between the experimental and the simulation results in a polar plot

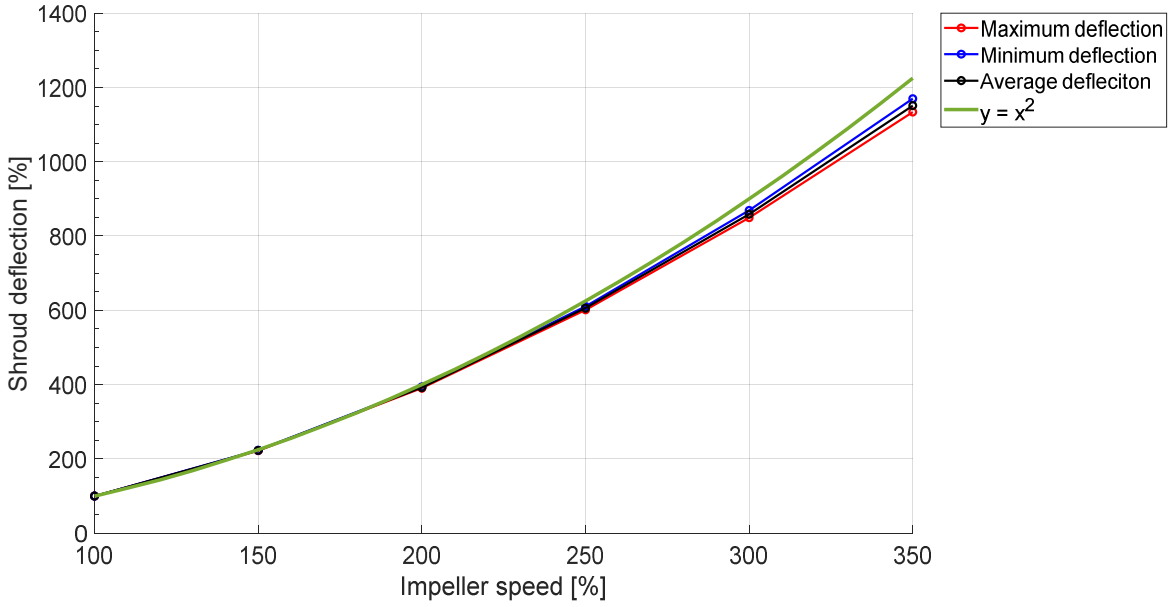


Figure 6. 7 The relationship between the radial inlet shroud deflection and the rotating speed of the impeller

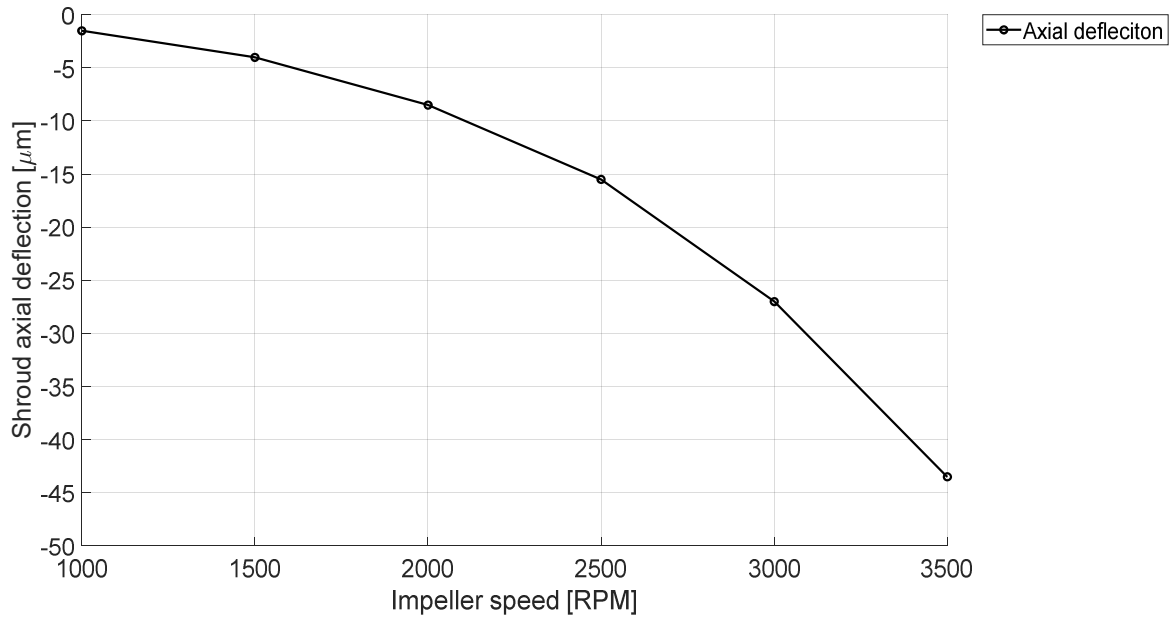


Figure 6. 8 The relationship between the axial shroud deflection and the speed of the impeller

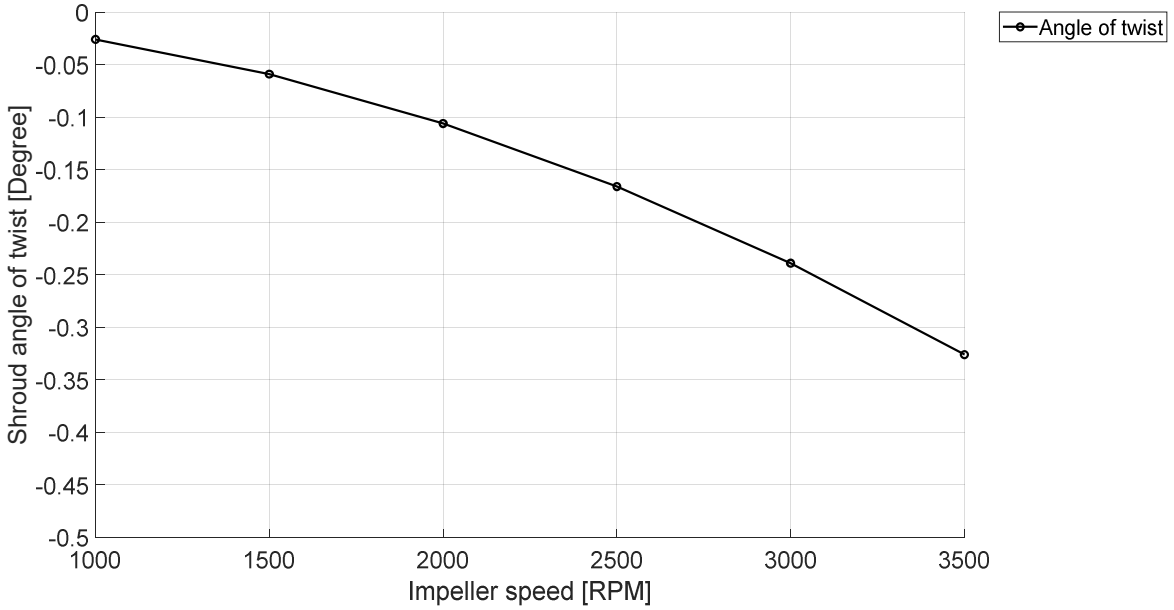


Figure 6. 9 The relationship between the shroud twist angle (CCW) and the speed of the impeller

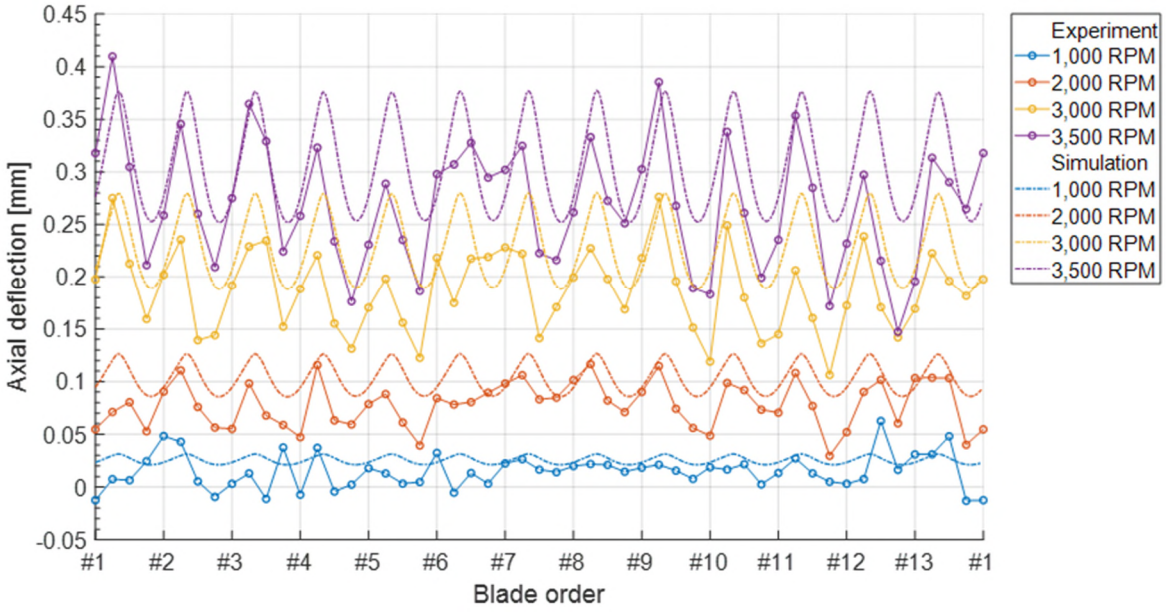


Figure 6. 10 Comparison of the axial back-end wall deflections of the healthy impeller between the experimental results and the simulation results

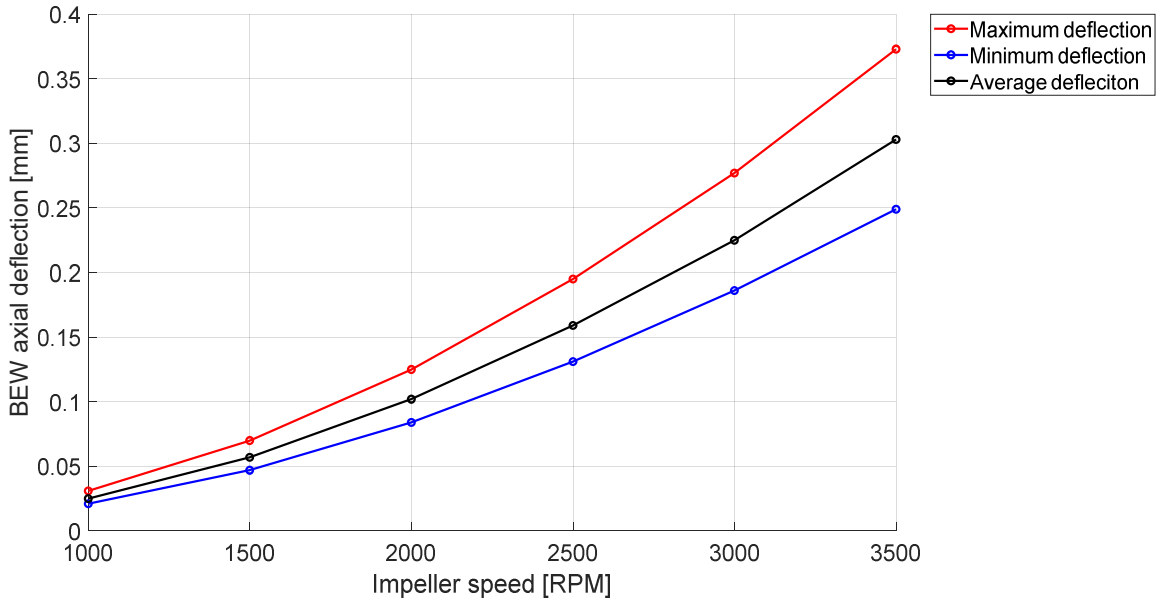


Figure 6. 11 The relationship between the axial back-end wall deflection and the speed of the impeller

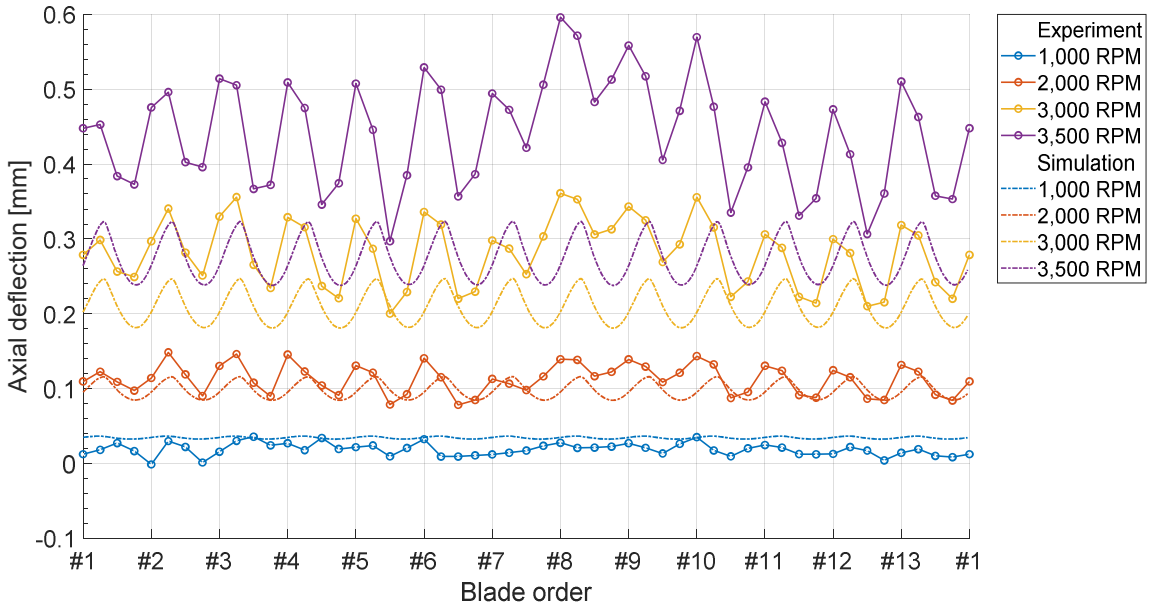


Figure 6. 12 Comparison of the axial outlet shroud deflections of the healthy impeller between the experimental results and the simulation results

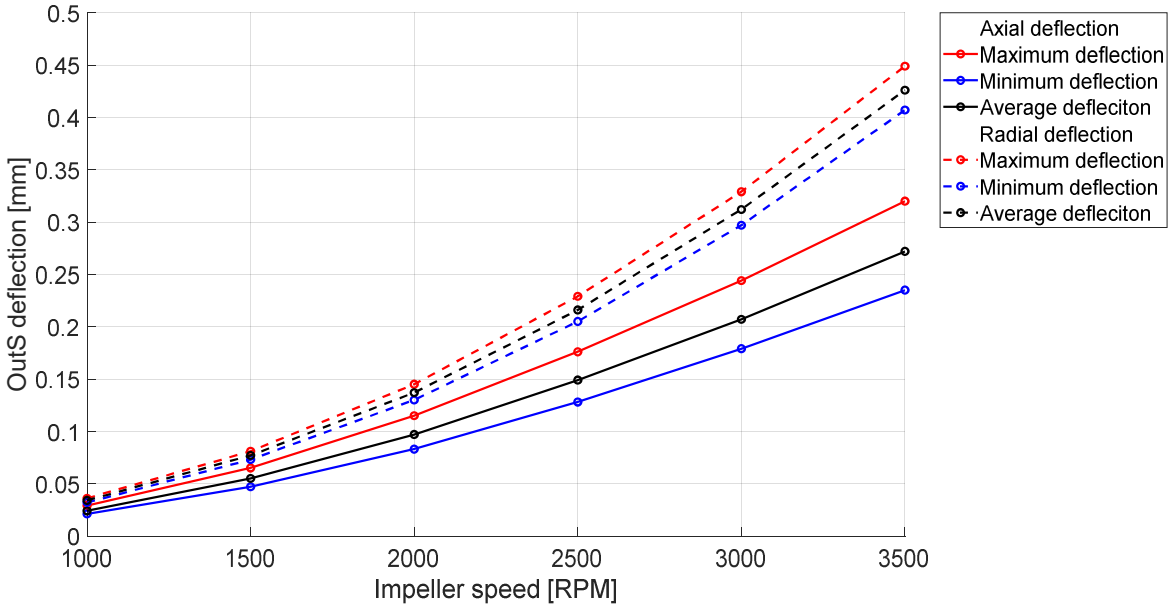


Figure 6. 13 The relationship between the outlet shroud deflections and the speed of the impeller

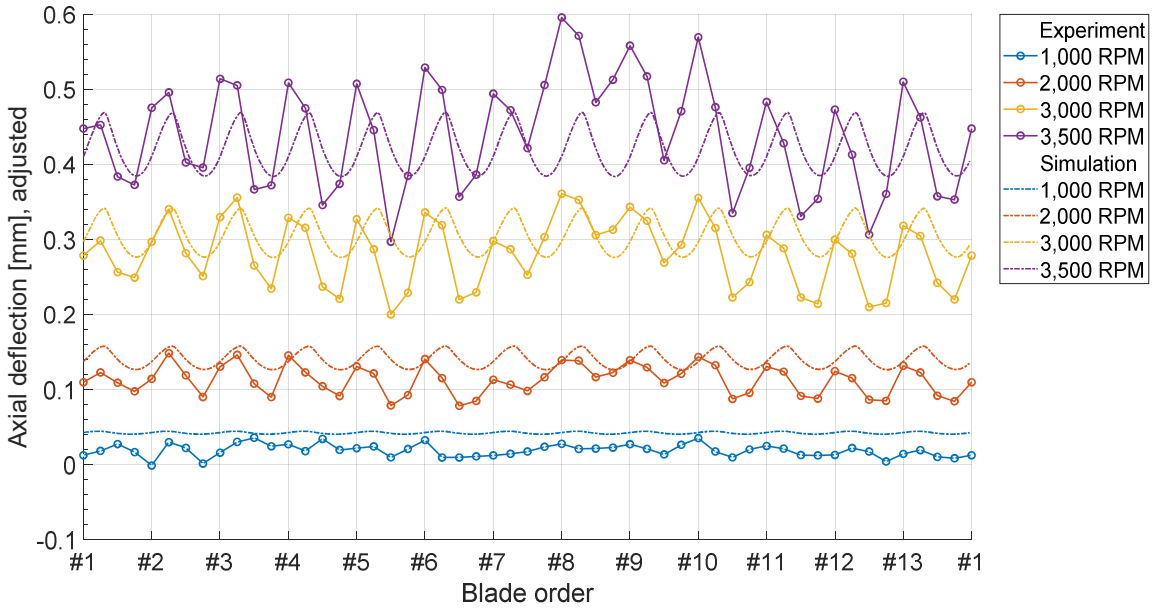


Figure 6. 14 Comparison of the axial outlet shroud deflections of the healthy impeller between the experimental results and the simulation results after accounting for the effect of radial deflection

6.4.2 FEA of the scaled impeller with a cracked blade

In this section, the simulation model presented in Figure 6.1 was utilised to predict the change in the inlet shroud deflections of a scaled impeller with various crack conditions. The cracked blade was specified as blade number 4, which corresponded to the cracked blade in the experimental studies given in Chapter 5. Similar to the experimental studies, the impeller rotational speed of 3,500 RPM was assigned as a boundary condition.

Figure 6.15 depicts the deflections of a cracked blade with 4-mm, 7-mm, 15-mm, and 20-mm crack conditions. The magnitude of the deflection increased as the crack propagated, with the maximum deflection occurring at the mid-span of the blade leading edge.

In the same way as the healthy impeller simulation, the crack blade experimental results were used to validate the cracked blade simulation model. Figure 6.16 shows the comparison of the radial inlet shroud deflection between the experimental and predicted results. The consistency between simulation and experimental results can be observed in the cracked and adjacent blade areas. However, the difference was noticeable on the opposite side of the cracked blade between blade numbers 9 to 13.

This difference may be due to two reasons. First, as mentioned in the case of the healthy impeller simulation that the quality of the scaled impeller manufacturing process – 3D-printing process – may cause the built propeller not to be as round as in the simulation model. One of the pieces of evidence was the significant runout of the scaled impeller, as described in section 3.3.2 Runout measurements.

The second reason might be related to the uncertainty of clearance measurement. It can be seen that the difference in deflection was in the range of around 10 μm or less, while the uncertainty of clearance measurement was reported as 7 μm. However, this reason might not be as robust as the previous one.

Figure 6.17 compares the predicted and experimental relations of the crack length and the change in the inlet shroud deflection at 3,500 RPM. The cracked blade simulation model provided predicted results comparable to those from the experimental studies. Thus, this simulation model was used in parametric studies with the healthy blade simulation model to determine how the impeller design parameters affect the inlet shroud deflection.

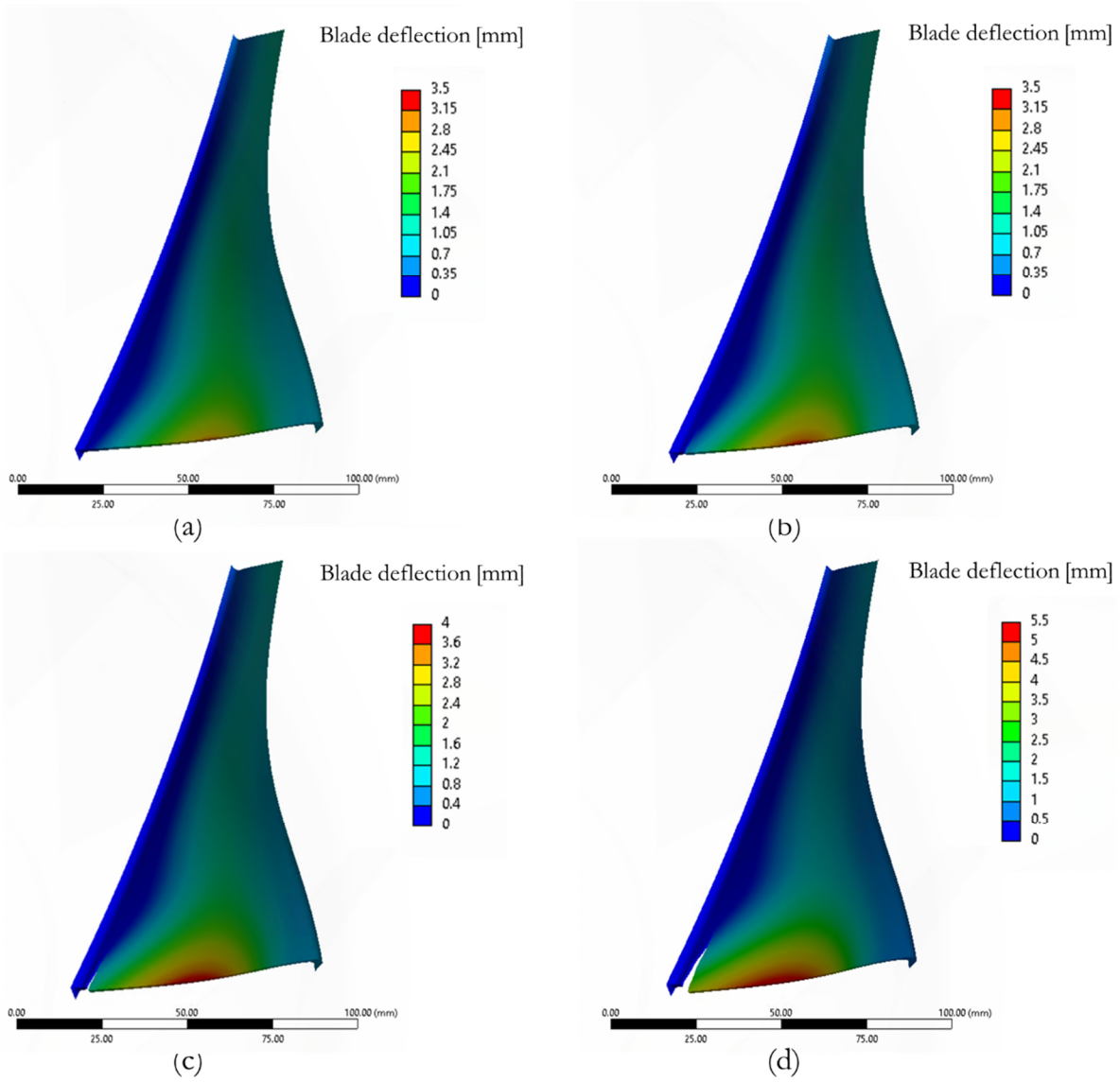


Figure 6. 15 Deflections of a cracked blade of the scaled impeller (a) 4-mm crack; (b) 7-mm crack; (c) 10-mm crack; and (d) 20-mm crack

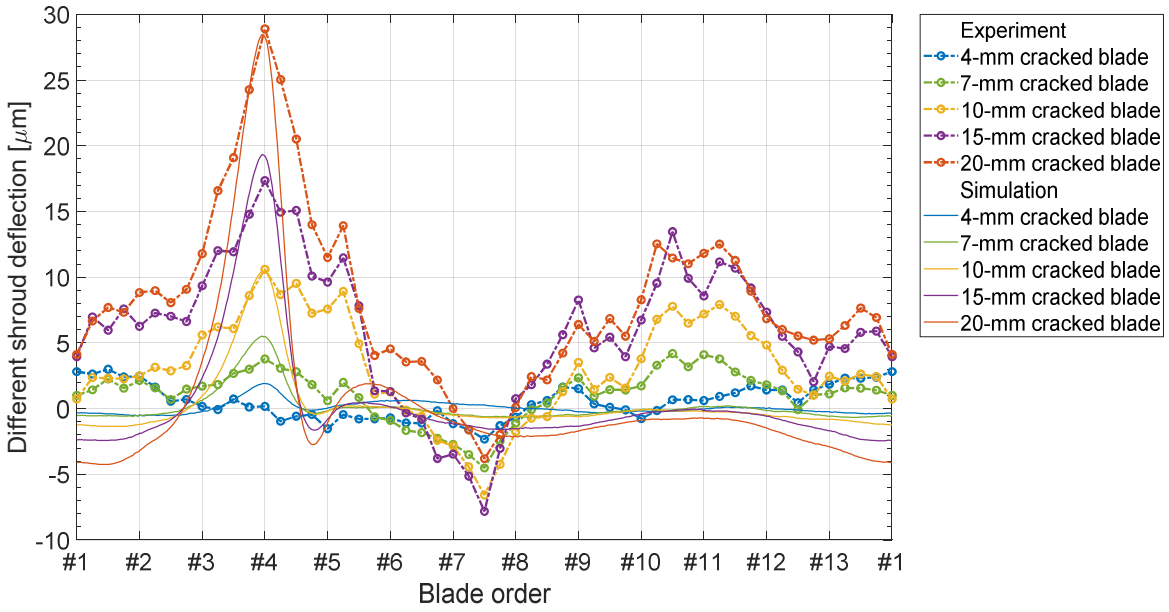


Figure 6. 16 Comparison of the radial deflections of the impeller with a cracked blade between the experimental results and the simulation results at 3,500 RPM

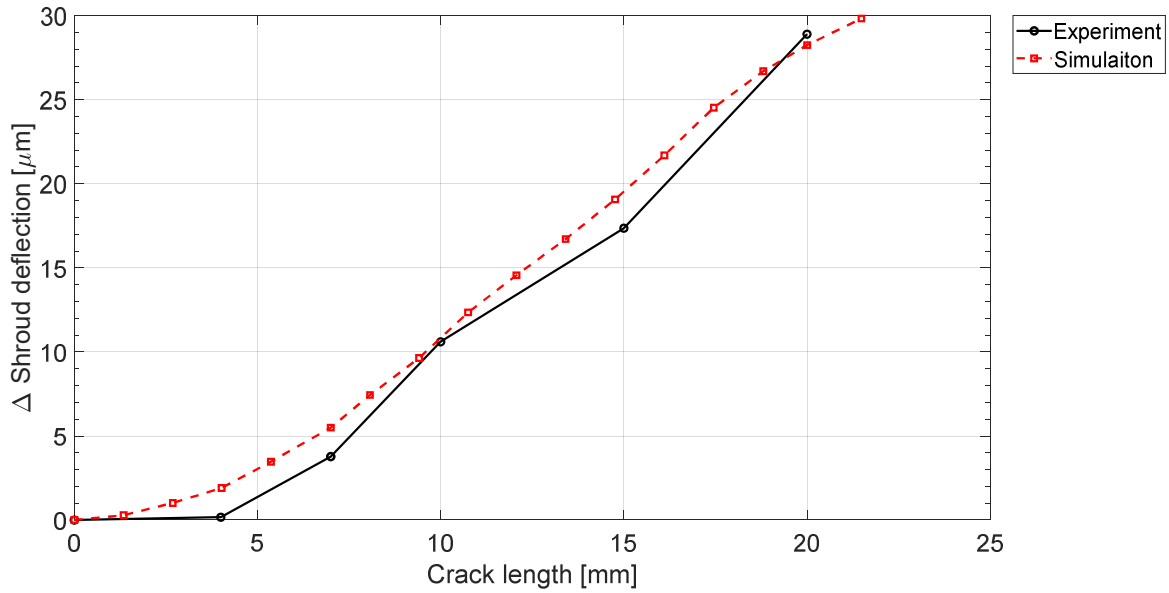


Figure 6. 17 The predicted relationship between the crack length and the change in the inlet shroud deflection at 3,500 RPM, compared with the experimental results

6.5 Effect of impeller design parameters on the inlet shroud deflection

The objective of the parametric studies was to determine the influence of each impeller design parameter on the deflection of the scaled impeller. The validated simulation model in the previous section was used as the baseline in these parametric studies with a fixed rotating speed of 3,500 RPM. Table 6.2 shows the seven impeller design parameters used in these parametric studies, such as the blade thickness, number of blades, and shroud thickness. Each parameter was adjusted separately, while the others remained at their default values. The range and limit of each parameter were arbitrarily determined. However, the general concept was to set the range between 50 to 200 percent of the baseline with at least four values of each parameter. The studies focused on the inlet shroud deflection, the optimal measurement location for detecting a cracked blade. The comparison was made in three cases: the healthy impeller, the impeller with a 10-mm cracked blade, and the impeller with a 20-mm cracked blade. Notably, these parametric studies were conducted solely through numerical studies; these predicted results presented in this section should be validated through experimental studies by varying the impeller design according to the list of parameters.

Table 6. 2 The list of parameters in the parametric studies

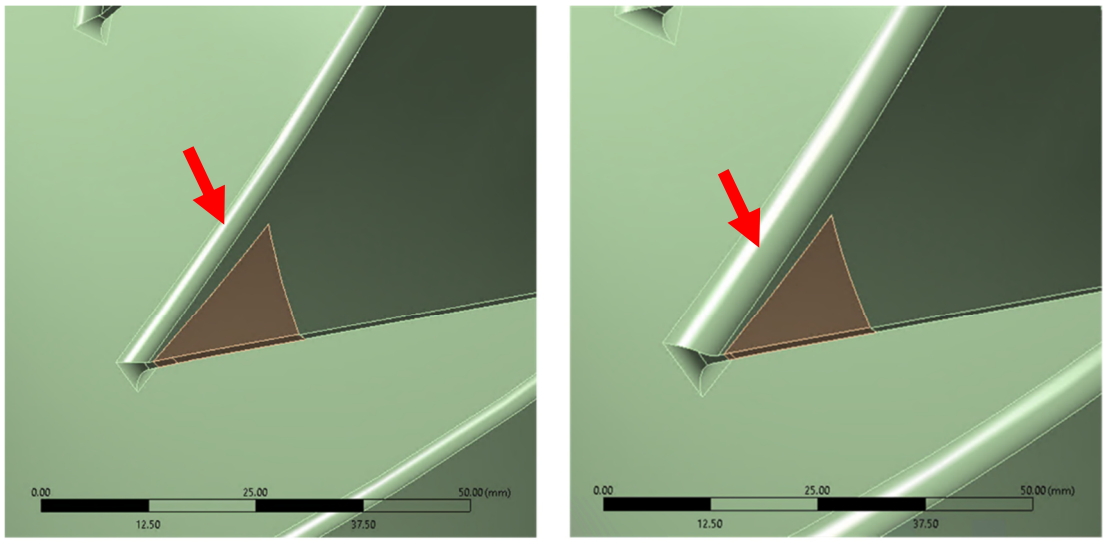
No.	Parameter	Range	Baseline
1.	Fillet radius [mm]	1 to 4	2
2.	Blade thickness [mm]	1 to 2.5	1
3.	Shroud thickness [mm]	4.46 to 17.83	4.46
4.	Back-end wall thickness [mm]	2 to 5	2
5.	Number of blades	9 to 17	13
6.	Size of impeller [%]	90 to 110	380 mm diameter
7.	Materials	6 different materials	Fibre-reinforce polymer

6.5.1 Effect of the fillet radius on the inlet shroud deflection

Fillets in the simulation model represented the fillet weld that was used to join blades with the hub and the shroud in the impeller manufacturing process [97]. The weld fillet radius depended on the welding parameters.

In these simulations, the fillet radius was varied from 1 mm to 4 mm to determine the effect of the fillet radius on the inlet shroud deflection. Figure 6.18 shows the CAD models of impellers with a 2-mm fillet radius (baseline case) and a 4-mm fillet radius.

The simulation results predicted similar inlet shroud deflections in both the cases of the healthy impellers and the impeller with a cracked blade, as shown in Figures 6.19 and 6.20, respectively. Hence, the fillet radii had a minimal effect on the change of the inlet shroud deflection.



(a) (b)

Figure 6. 18 CAD model of impellers with different fillet sizes (a) 2-mm fillet radius (baseline case); and (b) 4-mm fillet radius

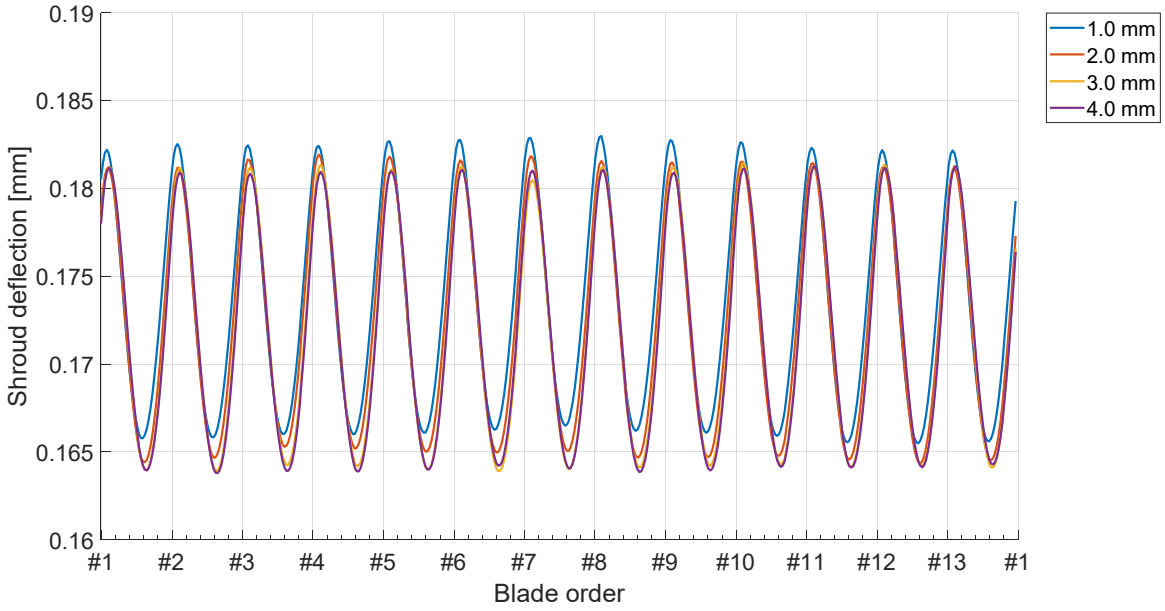


Figure 6. 19 The inlet shroud deflections of the healthy impellers at different fillet sizes

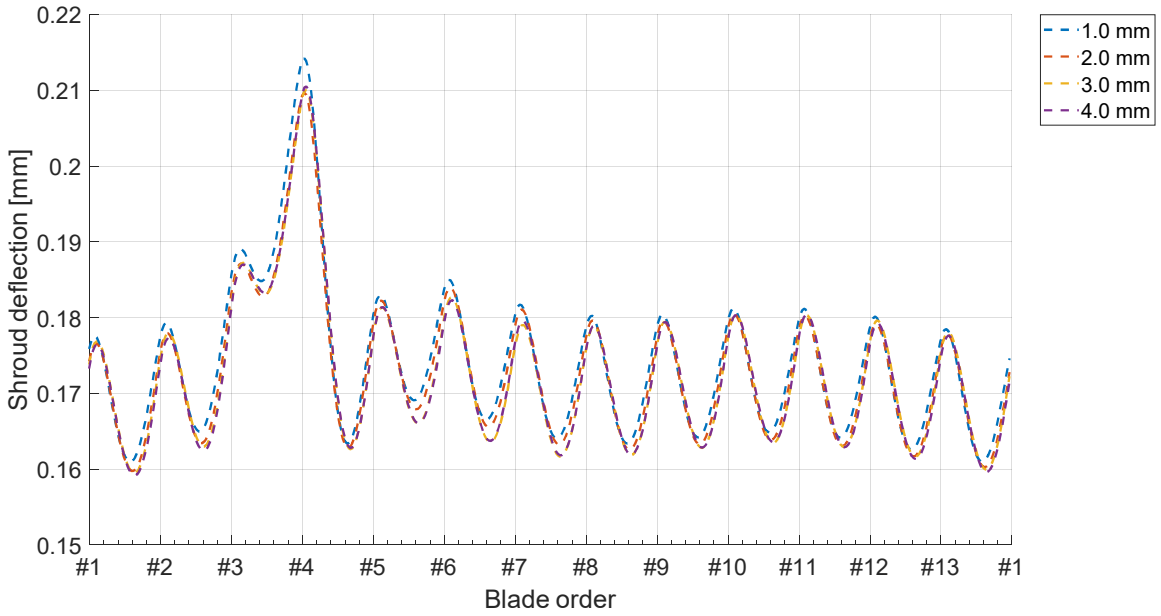


Figure 6. 20 The inlet shroud deflections of an impeller with a 20-mm cracked blade at different fillet sizes

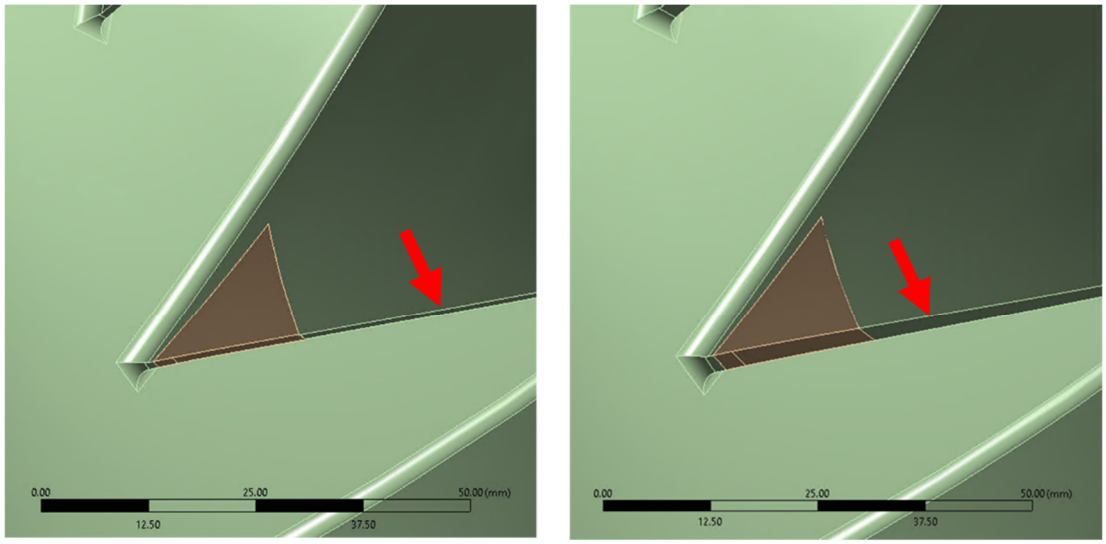
6.5.2 Effect of the blade thickness on the inlet shroud deflection

Blade thickness was the second parameter in these studies. The blade thickness was related to the mass and stiffness of the blade that connected the hub/shroud. In these simulations, the blade thicknesses was varied in the range of 1 to 2.25 mm. Figure 6.21 illustrates the CAD models of the impellers with 1-mm (baseline case) and 2.5-mm blade thicknesses.

In the case of the healthy impeller, the increase in the blade thickness led to an increase in the inlet shroud deflection, as shown in Figure 6.22. A significant increase occurred at the blade/shroud connecting area in particular. This increase in deflection indicates that the increase in mass resulting from the thicker blade had a more significant impact than the increase in stiffness. Figure 6.23 shows the

relationship between the change of the shroud deflection and the blade thickness at the healthy blade condition.

In addition, the effect of increased blade thickness was determined in the case of a cracked blade. Figure 6.24 shows the comparison of the changes of the inlet shroud deflection of an impeller with a 20-mm cracked blade at different blade thicknesses. Due to the increased deflection, detecting a cracked blade was more effortless in the case of the thicker blade.



(a) (b)

Figure 6. 21 CAD model of impellers with different blade thicknesses (a) 1-mm blade thickness (baseline case); and (b) 2.5-mm blade thickness

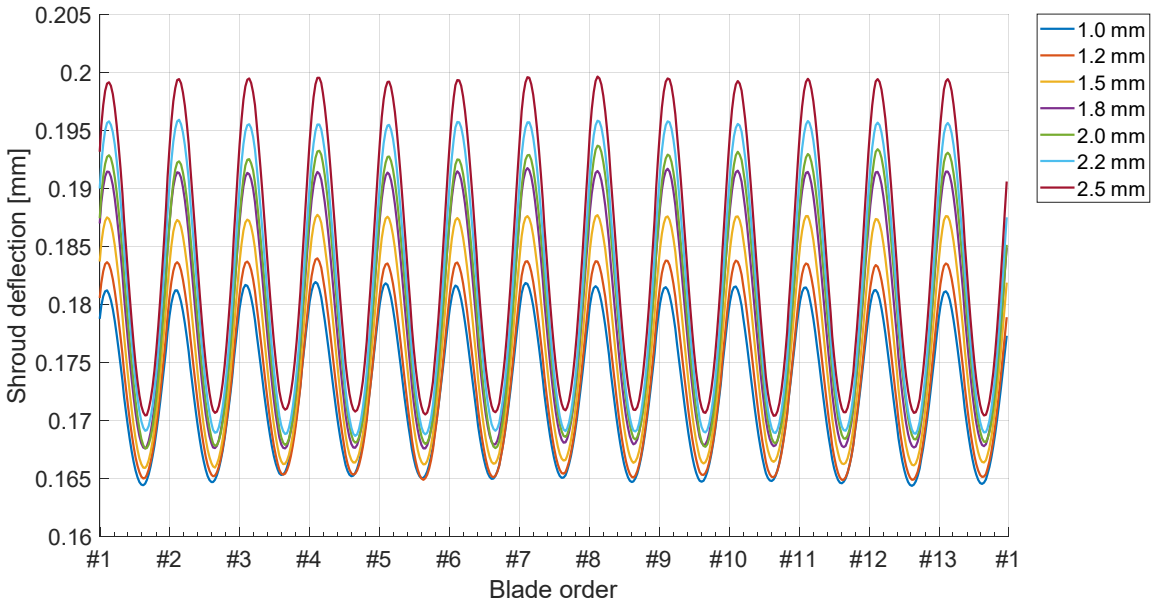


Figure 6. 22 The inlet shroud deflections of the healthy impellers at different blade thicknesses

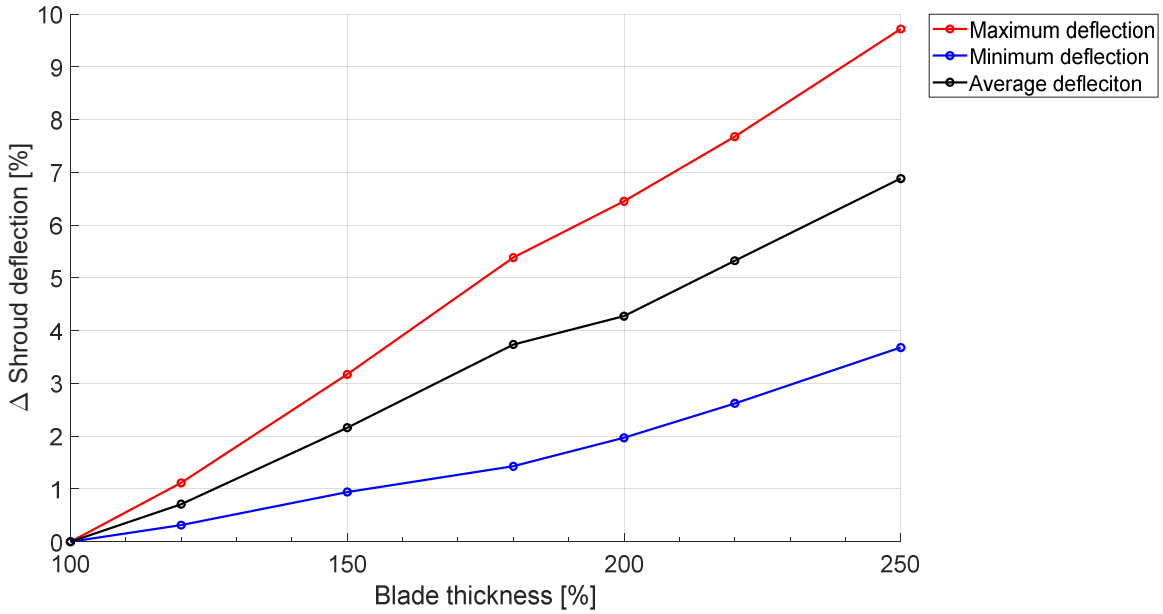


Figure 6. 23 The relationship between the change of the shroud deflection and the blade thickness of the healthy impeller

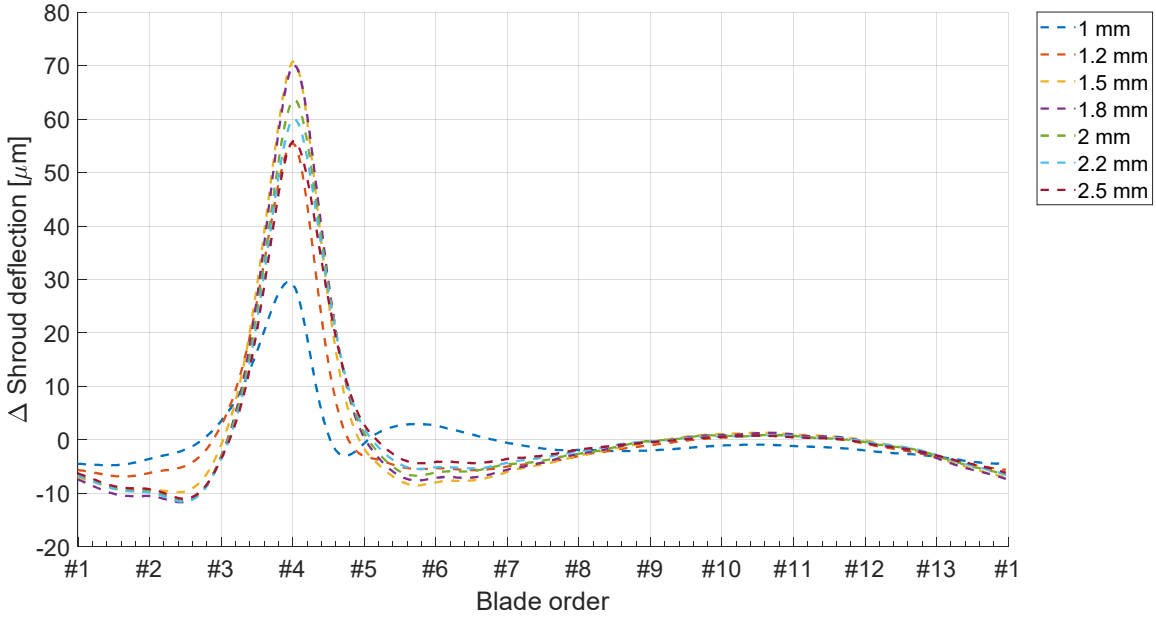


Figure 6. 24 Comparison of the change in the inlet shroud deflection of an impeller with a 20-mm cracked blade at different blade thicknesses

6.5.3 Effect of the shroud thickness on the inlet shroud deflection

The impact of the change in shroud thickness on deflection was examined by varying the shroud thickness in four steps from 4.46 mm (baseline) to 17.83 mm. CAD models of the impellers with 4.46-mm (baseline case) and 17.83-mm shroud thicknesses are shown in Figures 6.25 (a) and (b), respectively.

Figure 6.26 shows the inlet shroud deflections of the healthy impeller with various shroud thicknesses. In each case, the maximum and minimum deflections occurred at the blade/shroud connected location and the mid-span between two adjacent blades, respectively. The increased shroud thickness led to a reduction in the difference between the two locations. The reason was that the shroud stiffness increased as its thickness increased.

While the maximum and minimum deflection of the inlet shroud depended on the thickness of the shroud, the mean deflection depended on the mass and stiffness of the shroud. However, this relation was not directly proportional. In the case of the thin shroud (4.46 mm thickness), the mean deflection was highest due to the stiffness of the shroud being lowest compared to the other simulation cases. In contrast, the mean deflection of the shroud with a thickness of 17.83 mm was not the lowest because the increasing mass of the shroud increased the centrifugal force acting on the impeller. Moreover, when comparing cases with shroud thicknesses of 8.95 mm and 13.37 mm, the mean deflections of both cases were comparable. This indicates that the increases in stiffness and mass in these two cases were proportional.

In addition, the inlet shroud deflections of the cracked blade impeller at varying shroud thicknesses are depicted in Figure 6.27. It can be seen that the maximum shroud deflection at the cracked blade location reduced for the thicker impeller shroud. The relationship between the change of the maximum shroud deflection and the shroud thickness at two different blade conditions is illustrated in Figure 6.28. The thicker shroud makes it more difficult to detect a cracked blade the difference in shroud deflection is diminished.

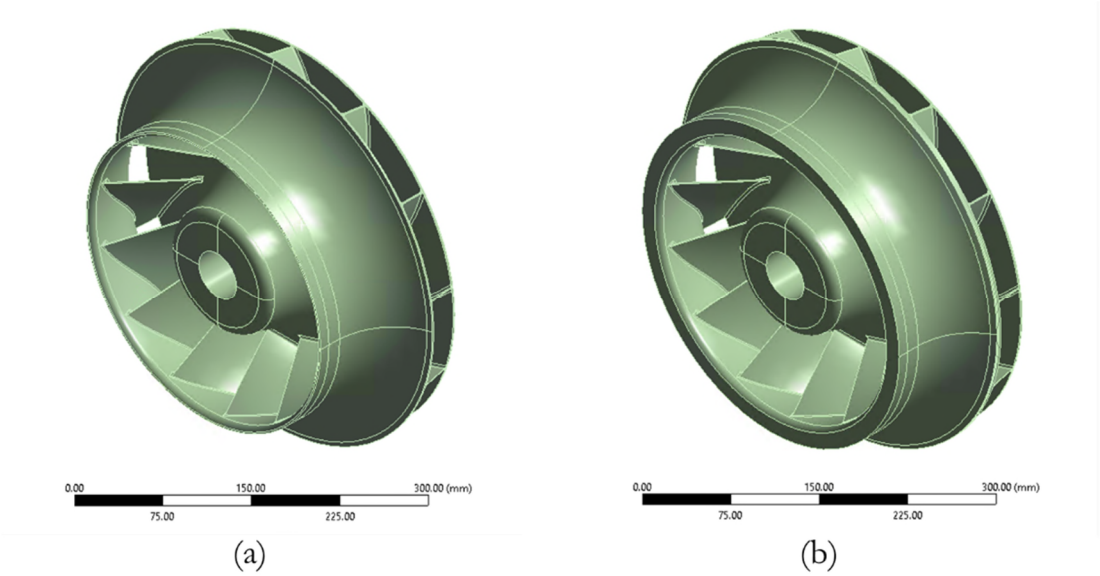


Figure 6. 25 CAD model of impellers with different shroud thicknesses (a) 4.46-mm shroud thickness (baseline case); and (b) 17.83-mm shroud thickness

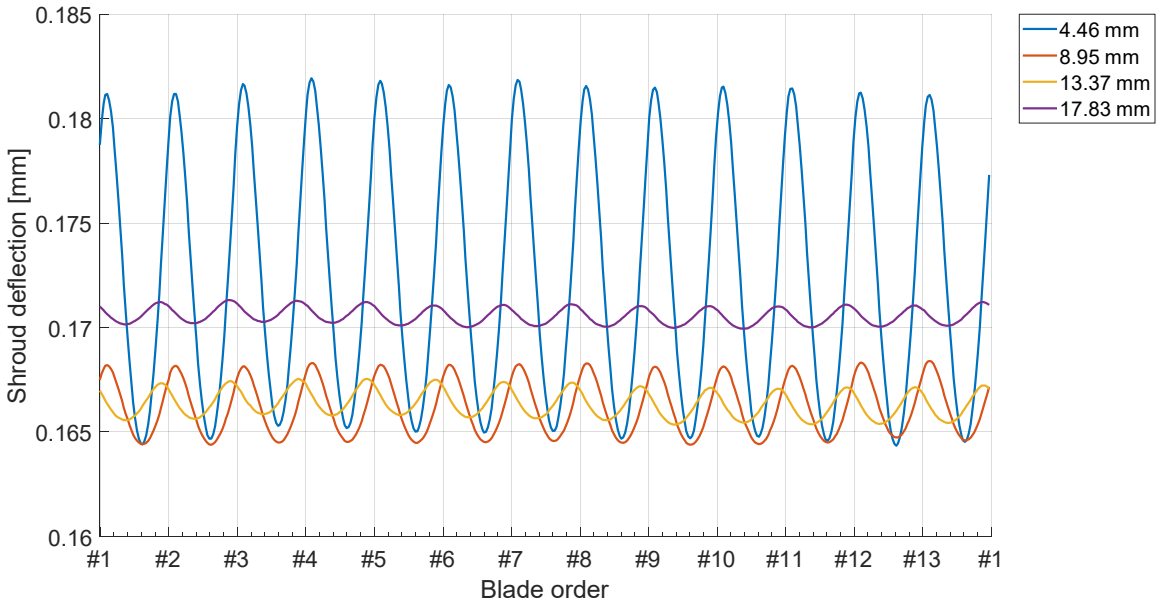


Figure 6. 26 The inlet shroud deflections of the healthy impeller at different shroud thicknesses

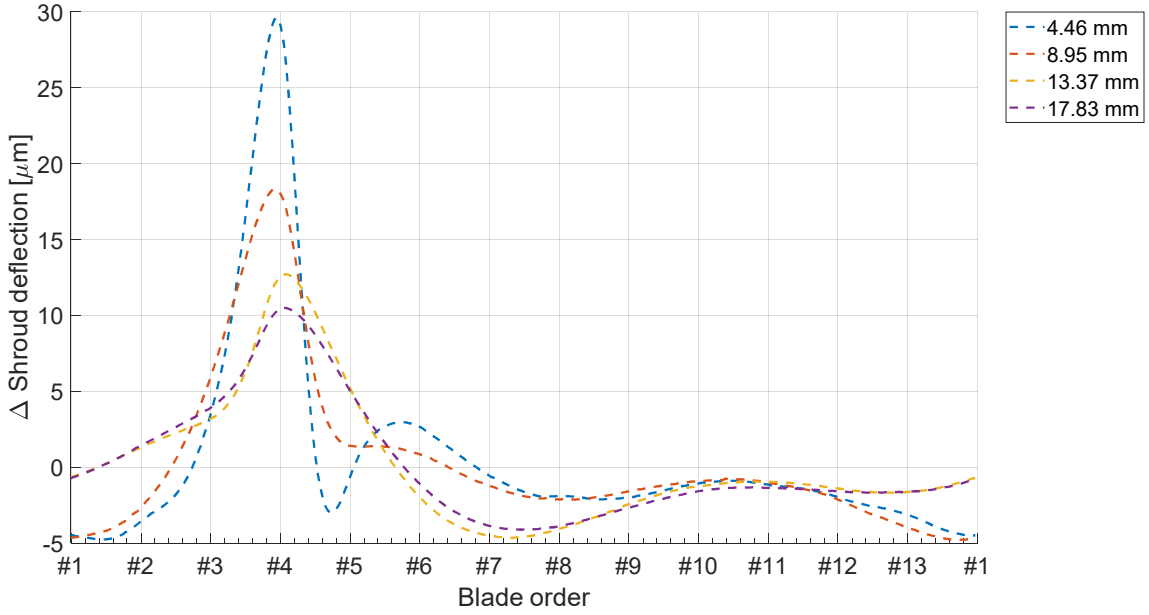


Figure 6. 27 Comparison of the changes of the inlet shroud deflection of an impeller with a 20-mm cracked blade at different shroud thicknesses

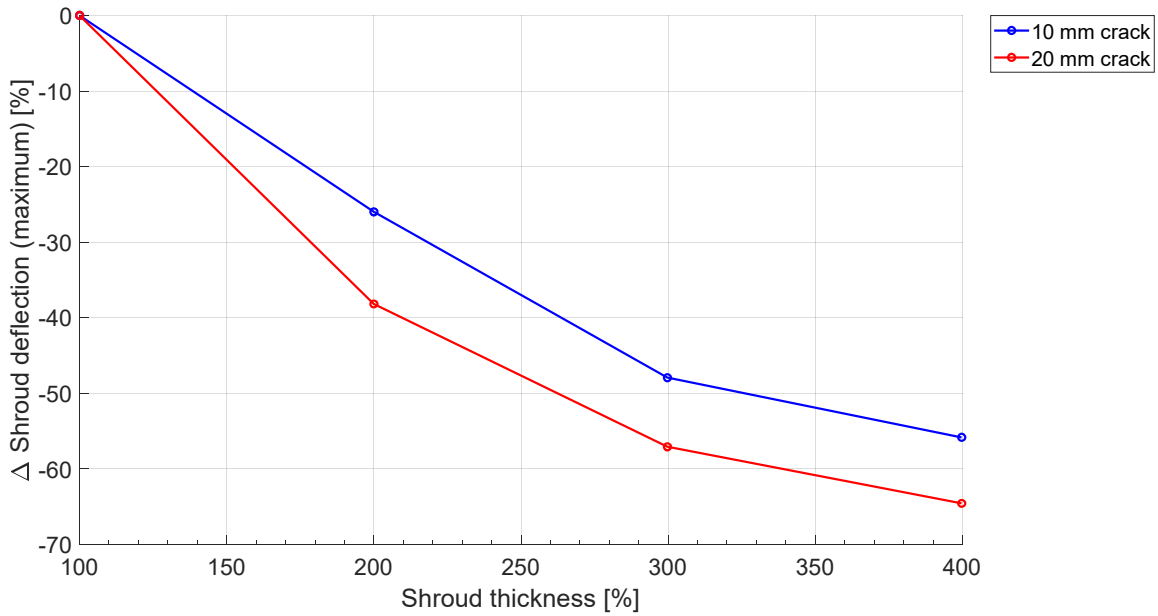


Figure 6. 28 The relationship between the change of the maximum shroud deflection and the shroud thickness at two different blade conditions

6.5.4 Effect of the back-end wall thickness on the inlet shroud deflection

In these simulations, the thickness of the back-end wall was varied from 2 mm to 5 mm to determine the impact on the inlet shroud deflection. Figure 6.29 depicts the CAD models of impellers with a 2-mm (baseline case) and 5-mm back-end wall.

Figures 6.30 and 6.31 show the inlet shroud deflections in the case of the healthy impeller blade and the comparison of the changes of the inlet shroud deflection of the impeller with a 20-mm cracked blade, respectively. As anticipated, the increase of the back-end wall thickness had minimal effect on the change in the inlet shroud deflection in both cases. The reason was that the back-end wall was a rigid component attached to the impeller's rotating shaft. Based on the simplified dynamic model for a bladed disk system proposed by He et al. (2021) [49], the back-end wall acted as a foundation in the model.

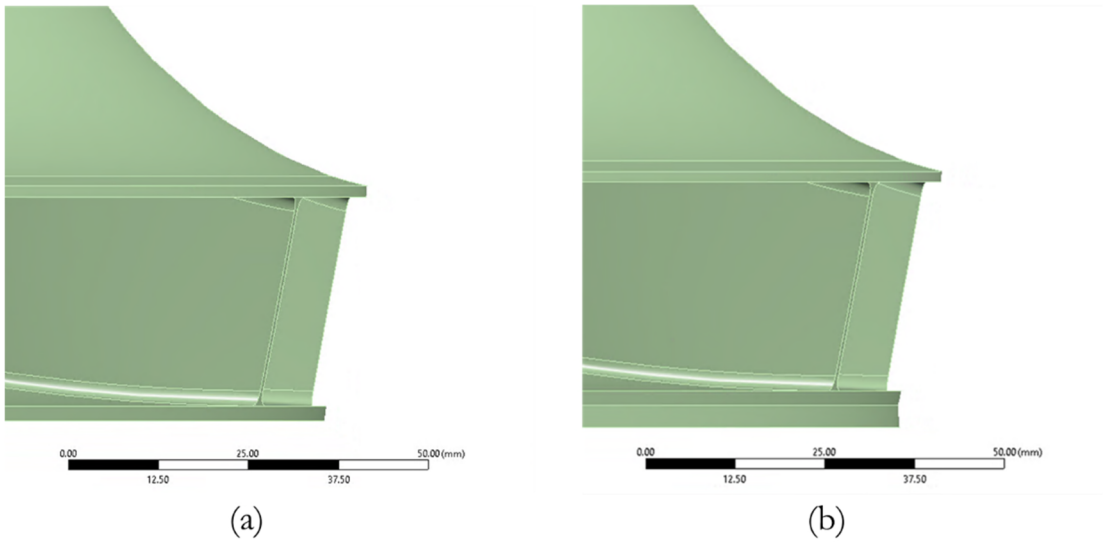


Figure 6. 29 CAD model of impellers with different back-end wall thickness (a) 2-mm shroud thickness (baseline case); and (b) 5-mm shroud thickness

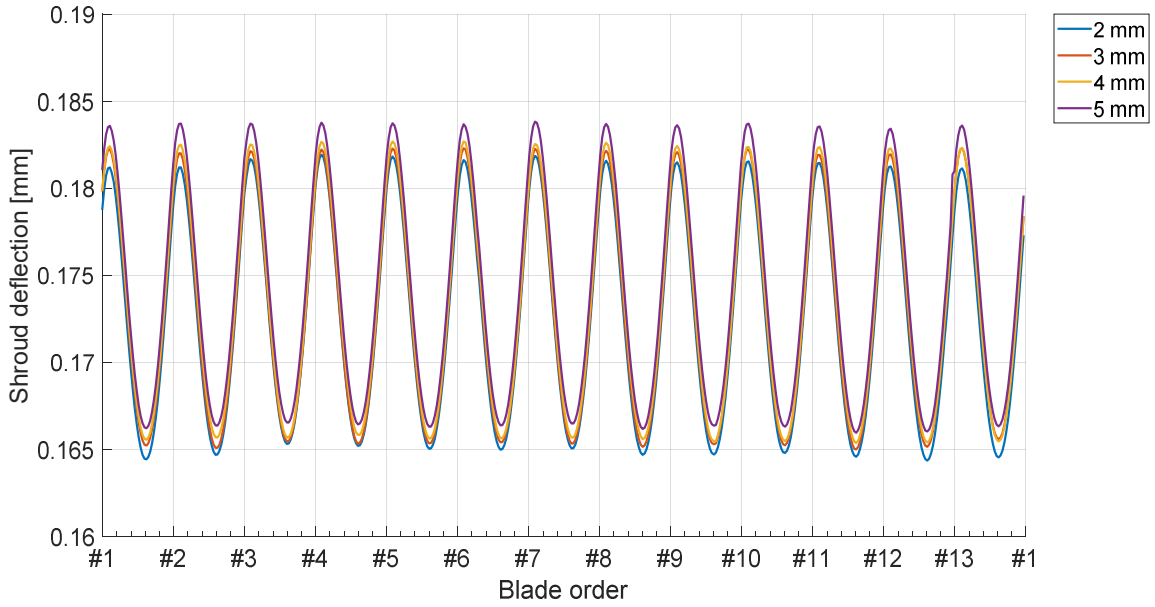


Figure 6. 30 The inlet shroud deflections of the healthy impellers at different back-end wall thicknesses

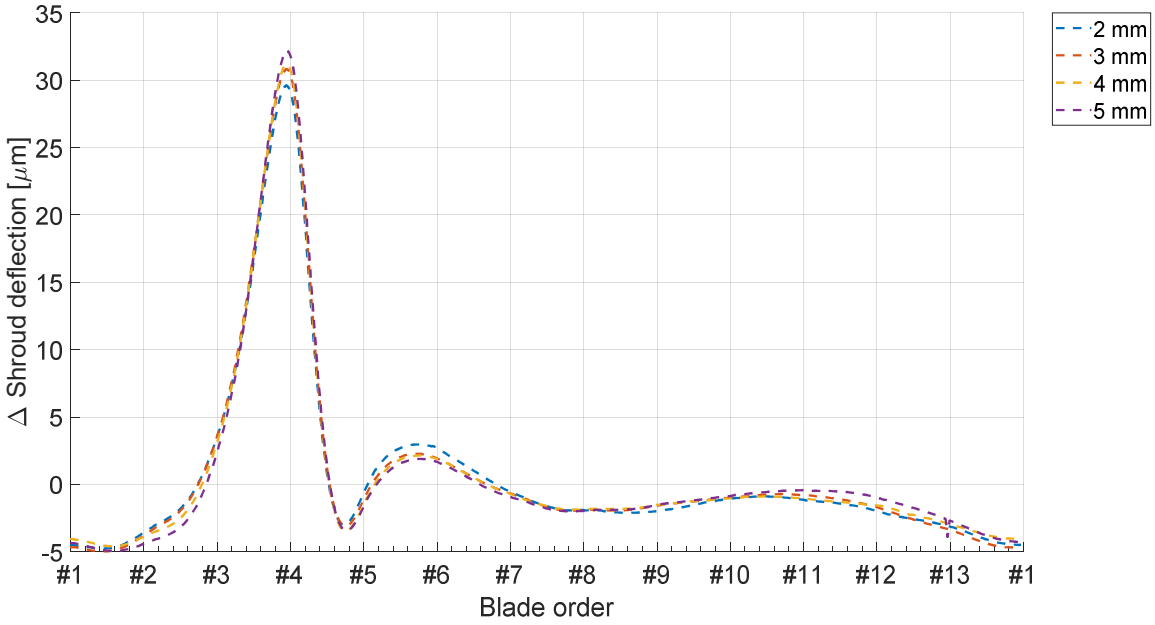


Figure 6. 31 Comparison of the changes of the inlet shroud deflection of an impeller with a 20-mm cracked blade at different back-end wall thicknesses

6.5.5 Effect of the number of blades on the inlet shroud deflection

In this section, the scaled impeller models with different numbers of blades from 13 to 17 were used to predict the effect of the number of blades on the inlet shroud deflection. Figure 6.32 shows the CAD models of a 13-blade impeller (baseline case) and a 17-blade impeller.

The inlet shroud deflections of the impellers with different numbers of blades in various blade conditions are shown in Figure 6.34. The crack was applied to blade number 3 for each simulation case. Notably, the plots were synced at the position of cracked blade number 3. It can be seen that the number of blades did not affect the pattern of the inlet shroud deflection. In the case of a healthy impeller, the maximum shroud deflection was reduced due to the additional blades added stiffness to the system. On the other hand, the increase in the number of blades reduced the pitch between two adjacent blades, and therefore the local shroud stiffness increased. The result was an increase in the minimum inlet shroud deflection at the mid-span. Figure 6.33 shows the relationship between the change of the shroud deflection and the number of blades for the healthy blade condition.

However, the simulation results indicated that the number of blades slightly impacted crack detection, as shown in Figure 6.35. The reason was that a crack only reduced the stiffness of that blade, not affecting the stiffness of an adjacent blade.

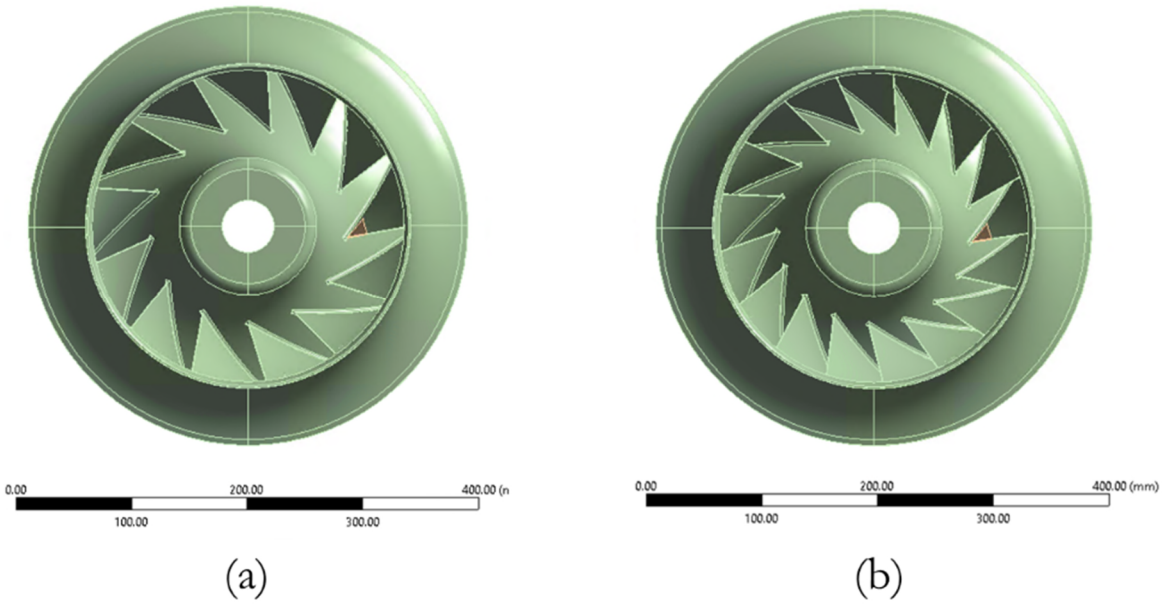


Figure 6. 32 CAD model of impellers with different numbers of blades (a) 13-blade impeller (baseline case); and (b) 17-blade impeller

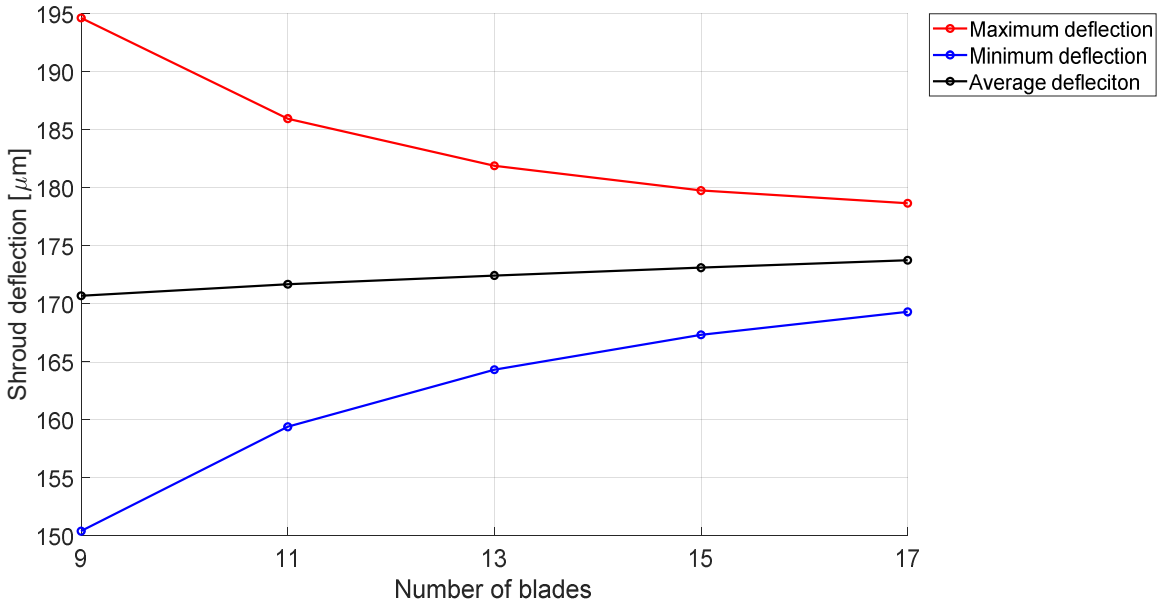


Figure 6. 33 The relationship between the change of the shroud deflection and the number of blades for the healthy blade condition

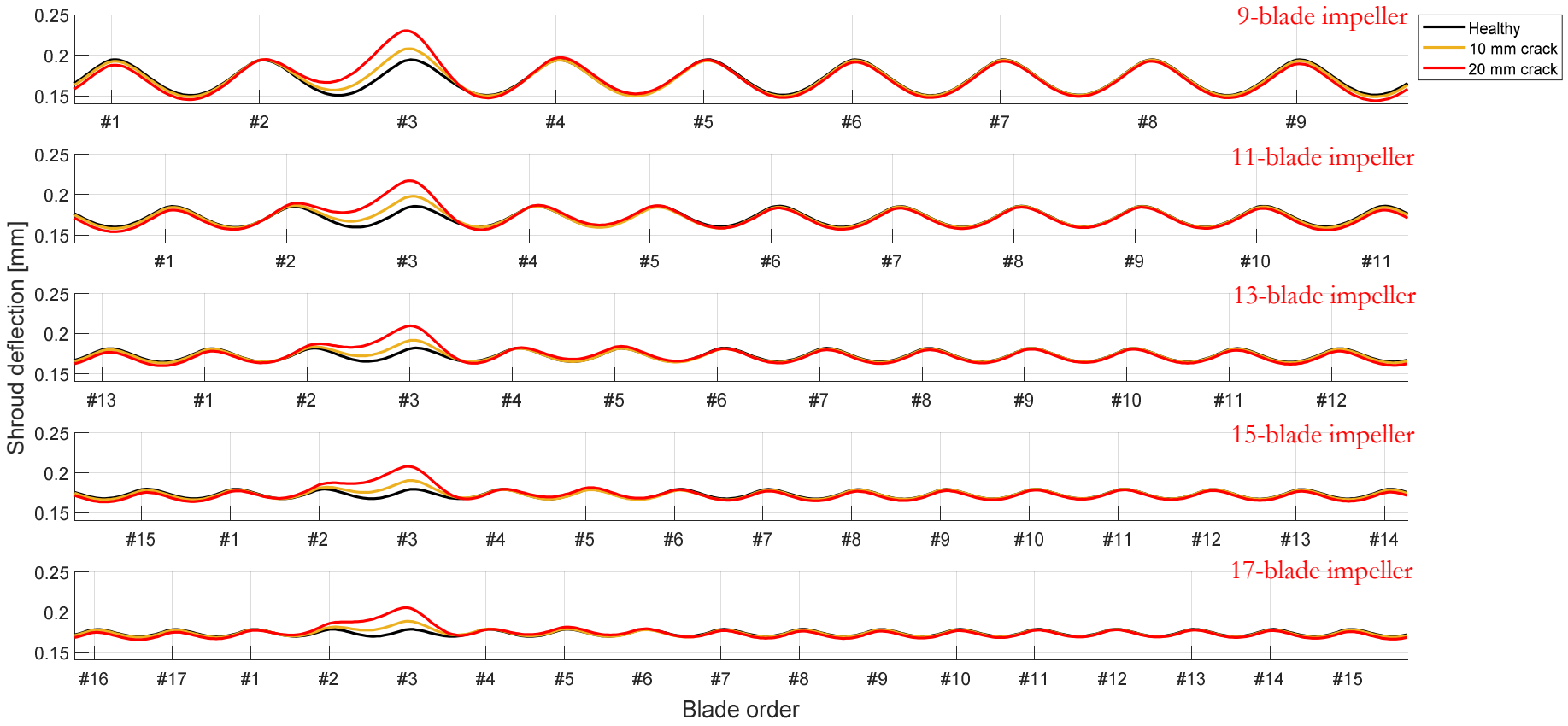


Figure 6. 34 The inlet shroud deflections of impellers with different numbers of blades in three blade conditions including healthy blade, 10-mm cracked blade, and 20-mm cracked blade

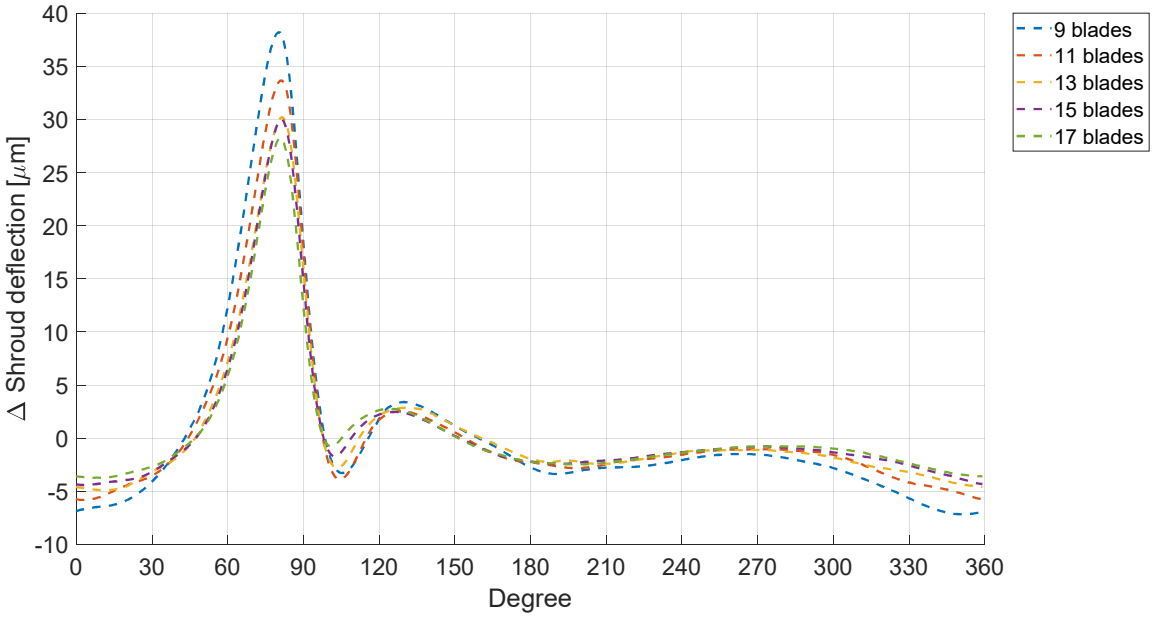


Figure 6. 35 Comparison of the changes of the inlet shroud deflection of an impeller with a 20-mm cracked blade for different numbers of blades

6.5.6 Effect of the impeller size on the inlet shroud deflection

In this parametric study, the scaled impeller size was varied between 90% and 110% of the based model in Figure 6.1 to determine its effect on the inlet shroud deflection.

The healthy impeller simulation results revealed that the change in impeller size was proportional to the inlet shroud deflection. The linear relationship between the change of the shroud deflection and the healthy impeller size is shown in Figure 6.36.

Figure 6.37 compares the changes in the inlet shroud deflection of an impeller with a 20-mm cracked blade at different impeller sizes. It can be seen that the pattern of the inlet shroud deflection was changed depending on the impeller size. As the

impeller size increased, the peak of the cracked blade reduced. However, there was an increase in deflection at the following blades.

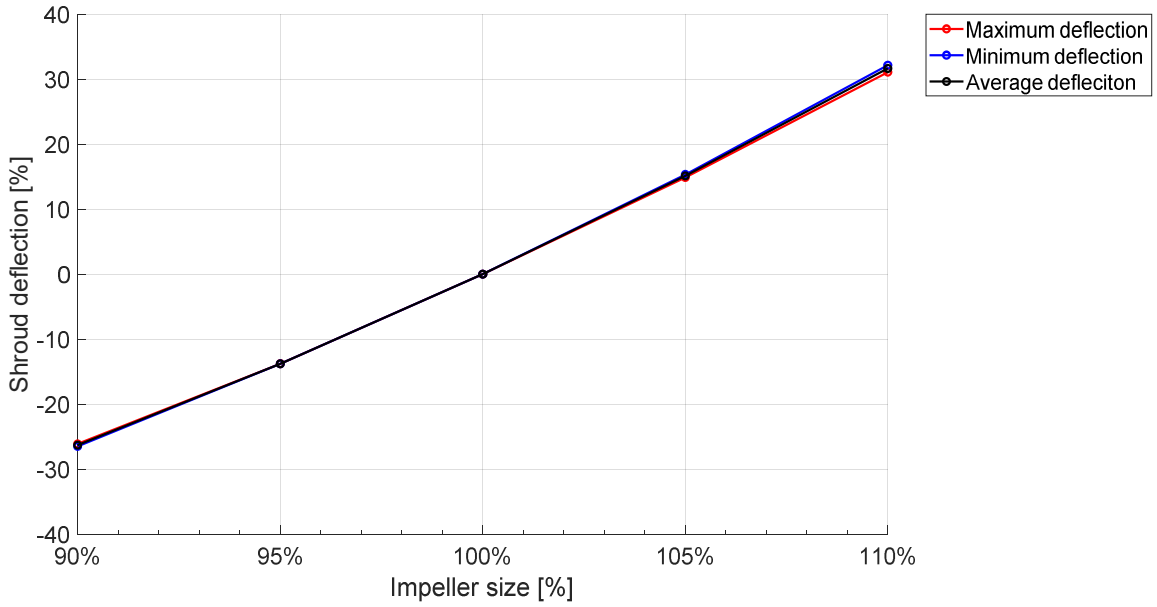


Figure 6. 36 The relationship between the change of the shroud deflection and the size of the healthy impeller

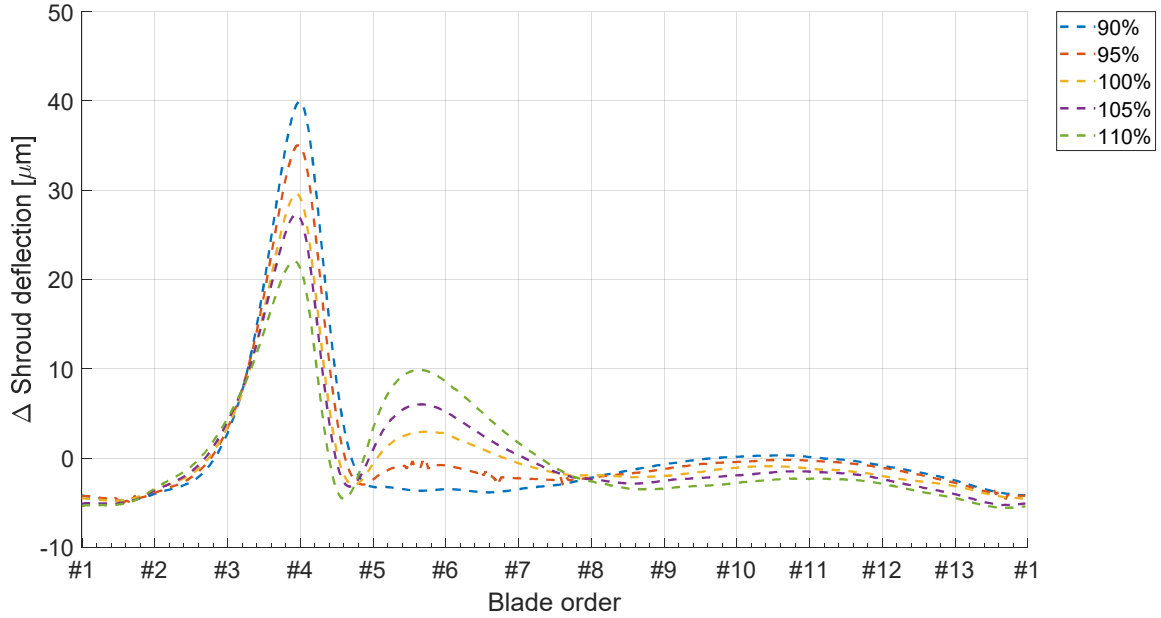


Figure 6. 37 Comparison of the changes in the inlet shroud deflection of an impeller with a 20-mm cracked blade at different impeller sizes

6.5.7 Effect of the impeller material on the inlet shroud deflection

In this parametric study, different impeller materials, such as Stainless steel and Titanium alloy, were assigned to the base impeller model in Figure 6.1. The objective was to determine the effect on the inlet shroud deflection for healthy and cracked blade conditions. The mechanical properties of the materials are shown in Table 6.3.

Figure 6.38 shows the inlet shroud deflections of the healthy impellers with various materials. The simulation results predicted that the copper impeller had the highest deflection, whereas the carbon steel impeller had the lowest deflection. In detail, the carbon steel, aluminium alloy, magnesium alloy, and stainless steel impellers had comparable deflection. In which the ratio of density to the modulus of elasticity was nearly equivalent for all four impellers.

Further investigation found that the inlet shroud deflection was proportional to the ratio of density to the modulus of elasticity of the impeller material. Figure 6.39 illustrates this linear relationship.

In the case of the impeller with a cracked blade, changing the impeller material also affected the magnitude of the inlet shroud deflection. Figure 6.40 compares the deflections of a 20-mm cracked blade impellers made from various materials.

Figure 6.41 shows the linear relationship between the change of the maximum shroud deflection and a ratio of density to the modulus of elasticity at two different cracked blade conditions. A similar relationship was also observed in these cases.

This linear relationship could be explained using the simplified dynamic model for a bladed disk system. In the simplified dynamic model, the deflection x is defined as

$$x = F/k \tag{6.2}$$

where F is the centrifugal force

$$F = m\omega^2 r = \rho V \omega^2 r, \tag{6.3}$$

and k the stiffness of the bladed disk system

$$k = \frac{EA}{L}. \tag{6.4}$$

Substitute equations 6.3 and 6.4 into equation 6.2

$$x = \frac{\rho V \omega^2 r}{EA/L}. \tag{6.5}$$

In this case, the impeller geometry is conserved with a fixed rotational speed condition. Therefore

$$x \propto \frac{\rho}{E}. \tag{6.6}$$

Thus, the deflection is proportional to the ratio of density to the modulus of elasticity.

In addition, the dimensional analysis was conducted to investigate the discovered relationship. The functional relationship in terms of nondimensional groups

$$\Pi_1 = f(\Pi_2, \Pi_3, \Pi_4, \Pi_5) \tag{6.7}$$

is

$$\frac{x}{\omega}\sqrt{\frac{\rho}{E}} = f(\omega^3\sqrt{\left(\frac{\rho}{E}\right)^3}, \frac{r}{\omega}\sqrt{\frac{\rho}{E}}, \frac{\rho\omega^2 A}{E}, \frac{L}{\omega}\sqrt{\frac{\rho}{E}}). \tag{6.8}$$

At fixed rotational speed and impeller geometries, the functional relationship (equation 6.8) can be rewritten as

$$x = h(\frac{\rho}{E}). \quad (6.9)$$

which corresponded with the relationship between the deflection and the ratio of density to the modulus of elasticity in equation 6.6. Thus, at fixed rotational speed and impeller geometry, the shroud deflection is the function of the ratio of density and the elasticity of the impeller material. Notably, a calculation detail for the dimensional analysis is presented in Appendix.

Notably, even the simulation result in Figure 6.41 shows the change of the maximum deflection of 10-mm cracked blade metal impellers. The detection of this crack size of the 380-mm diameter metal impellers may be impractical due to the small changes in shroud deflection.

Table 6. 3 The mechanical properties of materials used in the parametric studies

Material	**Density [kg/m^3]**	**Modulus of elasticity [MPa]**	**Density/ Modulus of elasticity**
Carbon steel, AISI4340	7,850	205,000	0.038
Aluminium alloy	2,770	71,000	0.039
Magnesium alloy	1,800	45,000	0.040
Stainless steel	7,750	193,000	0.040
Titanium alloy	4,620	96,000	0.048
Copper alloy	8,300	110,000	0.075

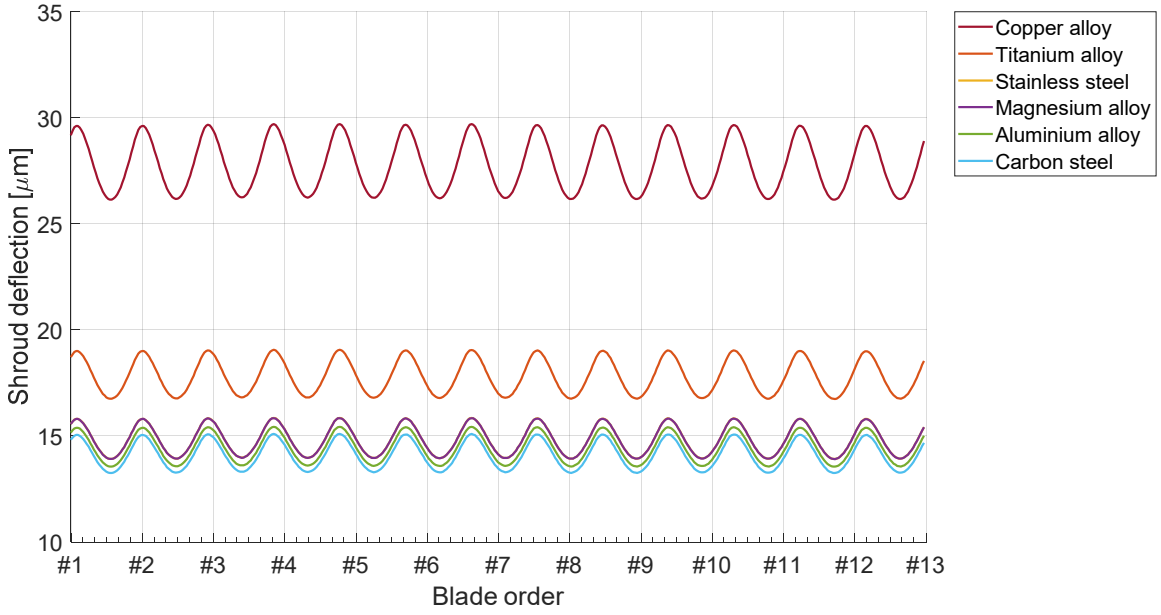


Figure 6. 38 The inlet shroud deflections of the healthy impellers at different materials

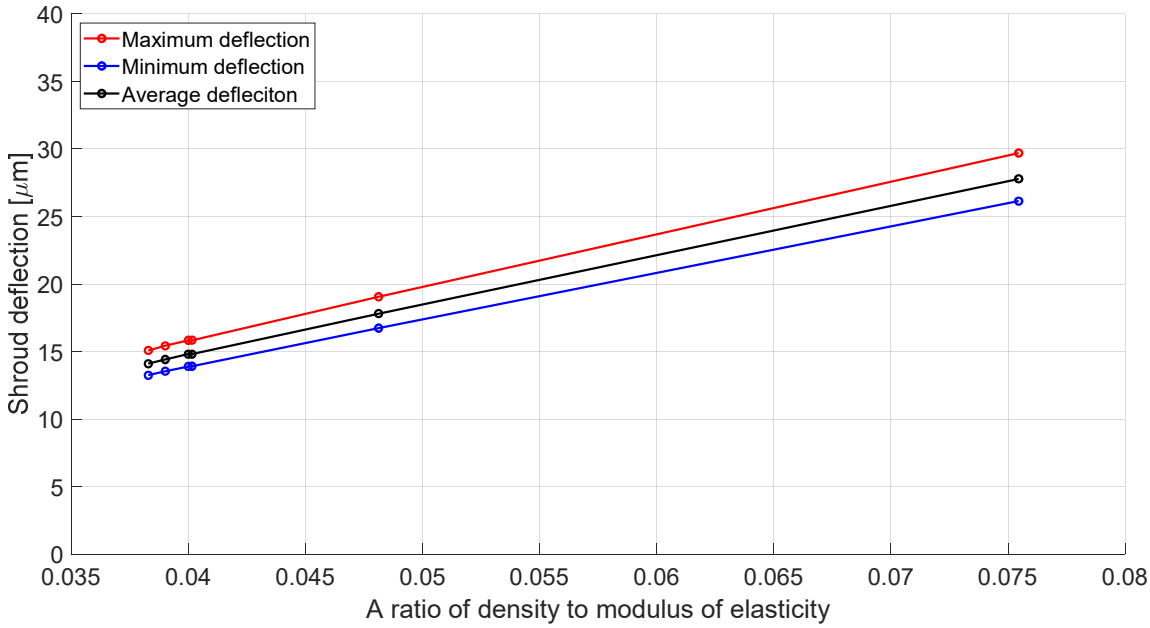


Figure 6. 39 The relationship between the shroud deflection of a healthy impeller and the ratio of density to the modulus of elasticity of the impeller material

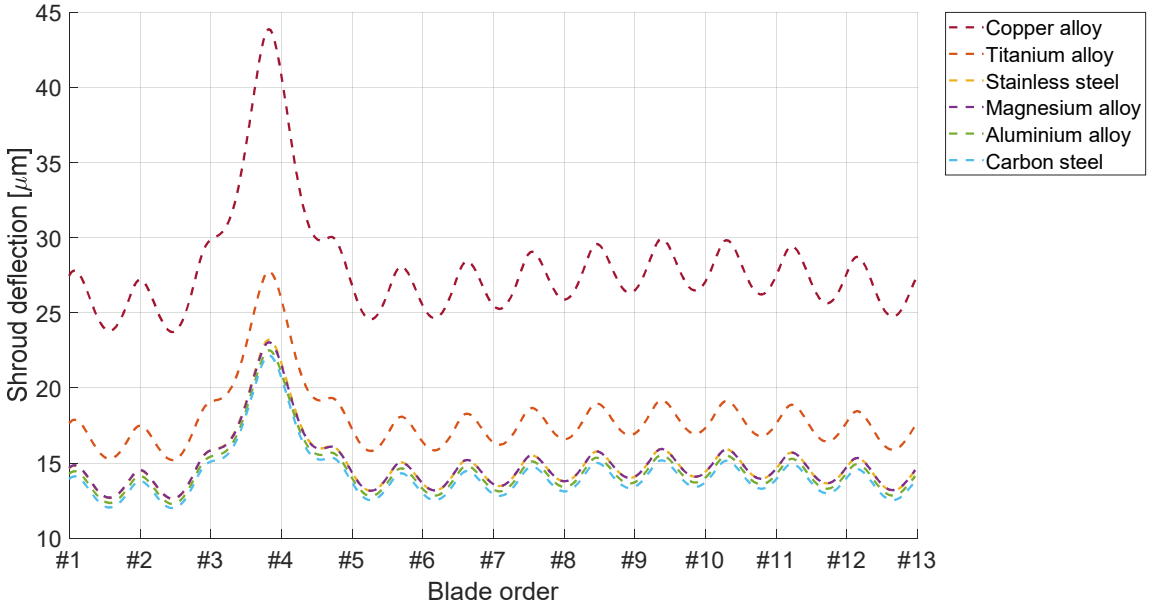


Figure 6. 40 The inlet shroud deflections of an impeller with a 20-mm cracked blade for different impeller materials

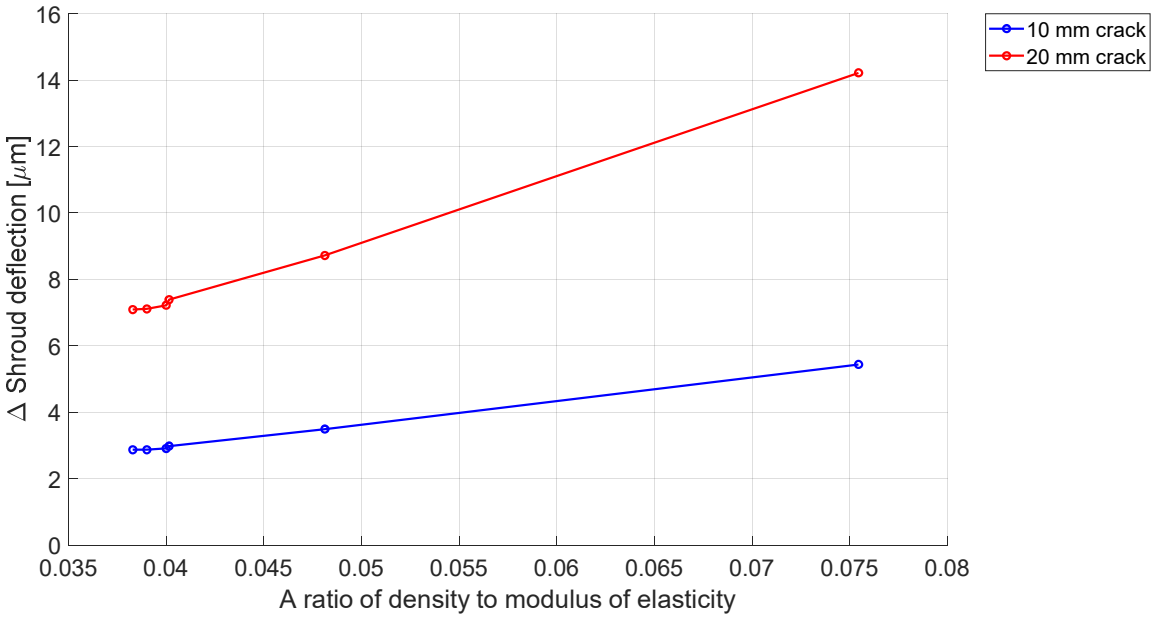


Figure 6. 41 The relationship between the change of the maximum shroud deflection and a ratio of density to the modulus of elasticity at two different blade conditions

6.6 Chapter conclusion

In this chapter, the Finite Element Analysis (FEA) of the scaled impeller was conducted. The simulation model was validated using the experimental results from Chapter 5. The validation was performed in both cases: the healthy impeller case and the impeller with a cracked blade case. The consistency between the simulation and experimental results was observed — especially the relationship between the crack length and the change in the inlet shroud deflection.

Subsequently, the simulation model was used as a basis for the parametric studies. The intention was to determine the effect of impeller design parameters on the change of the deflection of the inlet shroud. Seven impeller design parameters were investigated in the parametric studies, including the fillet radius, the blade thickness, the shroud thickness, the back-end wall thickness, the number of blades, the impeller size, and the impeller material.

The results from the parametric studies indicated that, for the same size impeller, blade thickness and shroud thickness were the most influential parameters in the change of the inlet shroud deflection. In contrast, the fillet radius and the back-end wall thickness had less effect on the change of the inlet shroud deflection. The information from these studies gave the guideline for estimating the inlet shroud deflection for shrouded impeller designs.

In addition, the parametric studies disclosed the relationship between the maximum inlet shroud deflection and the impeller material in terms of a ratio between density

to the modulus of elasticity. This relationship was observed for both healthy blade and cracked blade impellers.

Chapter 7

Proposed Blade Crack Detection System

7.1 Introduction

The objective of this chapter is to propose a blade crack detection system for a full-scaled shrouded impeller. This proposed system was based on the predicted results from the numerical studies and experimental results detailed in the previous section. The numerical studies combined Computational Fluid Dynamics (CFD) and Static Structural Analysis to predict the inlet shroud deflection of the full-scaled impeller in various blade conditions.

7.2 Passing fluid interaction

The computational fluid dynamics (CFD) analysis has been widely applied and validated for turbomachinery flow simulations [100, 101, 102]. The pressure and velocity fields within the flow domain are obtained in this analysis by solving the Navier-Stokes equations.

The computational fluid dynamics (CFD) analysis is a part of the one-direction fluid-structural interaction (FSI) simulation. The one-direction FSI simulation means that the force from the passing fluid is transferred to the structural model as an external load causing deformations. However, the results of solid deformation are not transferred back to the fluid domain as the changing of the fluid geometry domain [98]. In this research, this simulation technique was chosen since the fluid interaction was anticipated to be minimal, hence conserving simulation resources.

Hence, the objective of this CFD analysis was to determine the fluid force acting on the full-scaled impeller during operation, specifically the pressure and suction surfaces of the blades. The CFD simulation result in terms of pressure distribution was used as a boundary condition in the following static structural simulation to predict the deflection of the shroud in various blade conditions. The CFD analysis used a commercial CFD simulation module "CFX" which is compatible with the Static Structural model in ANSYS®. Figure 7.1 shows the simulation diagram.

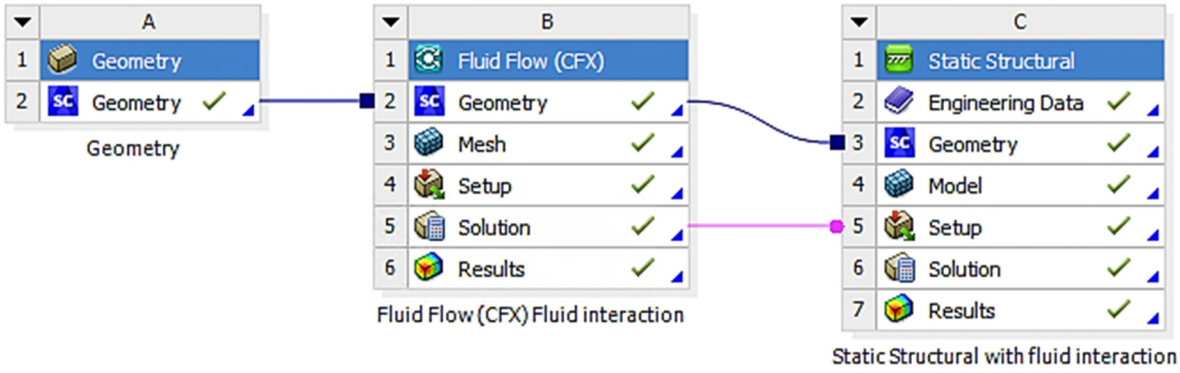


Figure 7. 1 Simulation diagram

7.2.1 CFD Simulation model

The CFD analysis was performed on the whole-body simulation model. The flow domain in this study is shown as the red boundary in Figure 7.2 (a). Due to the limit in acquiring geometries, including the inlet guide vanes and the return passage, the CFD analysis was started from the inlet of the shrouded impeller through the discharge channel. The leakage flows between the shroud/casing, and the back-end wall/casing were also neglected in this study due to the small clearance of around 6 mm.

Figure 7.2 (b) shows the CAD model of the flow domain and the shrouded impeller, which was used in the following step: the Static Structural analysis. The mesh of the fluid domain is shown in Figure 7.2 (c). The five-layer inflation mesh with a smooth transition was applied to all boundaries except the inlet and outlet to account for the effect of boundary layers within the flow domains. The mesh independency study is described in section 7.2.3.

Steady-state analysis with the Shear Stress Transport (SST) turbulence model was selected for this study since the CFD analysis was aimed at estimating the averaged pressure distribution on the impeller surfaces. The uniform total pressure and temperature were assigned as the inlet boundary conditions. The uniform static pressure was assigned as the outlet boundary condition. Figure 7.2 (d) shows the inlet and outlet domains. The set-up values of boundary conditions were presented at operating point number 4 in Table 7.3.

To simulate the effect of the rotating impeller, the fluid domains were separated into two frame types: the rotating frame domain and the static frame domain. The rotating frame domain consisted of fluid domains attached to the rotating parts, including the shroud, the hub and the impeller blades. This rotating frame domain was assigned a rotational speed equivalent to 5,800 RPM (the normal operating condition of the machine). Whereas the static frame domains, such as the inlet, the outlet and the outlet channel, were modelled as a counter-rotating wall [99]. The no-slip condition (smooth wall) with adiabatic heat transfer was assigned as the boundary condition for both rotating and counter-rotating walls.

In this analysis, the thermodynamic state of the passing fluid, a cracked gas, was assigned as an ideal gas. The thermodynamic properties and the composition of the cracked gas are shown in Tables 7.1 and 7.2, respectively.

Table 7. 1 Thermodynamic properties of a cracked gas

Thermodynamic properties	Value
Molar mass [kg/kmol]	27.89
Specific heat capacity [J/(kg.K)] @ 25 C^{o}, 1 atm	1,795
The ratio of specific heats, $k = C_P/C_v$	1.199
The polytropic exponent index, n	1.254
Gas compressibility factor, Z_{avg}	0.9875
Gas molecular weight, MW [kg/kmol]	27.89
Polytropic efficiency, η	0.82

Table 7. 2 The composition of a cracked gas

Cracked gas composition	Mole percent [%]
Ethylene	30.5
Methane	24.5
Hydrogen	14.5
Propylene	9.3
Ethane	6.0
Stream	5.3
Other hydrocarbons	9.9

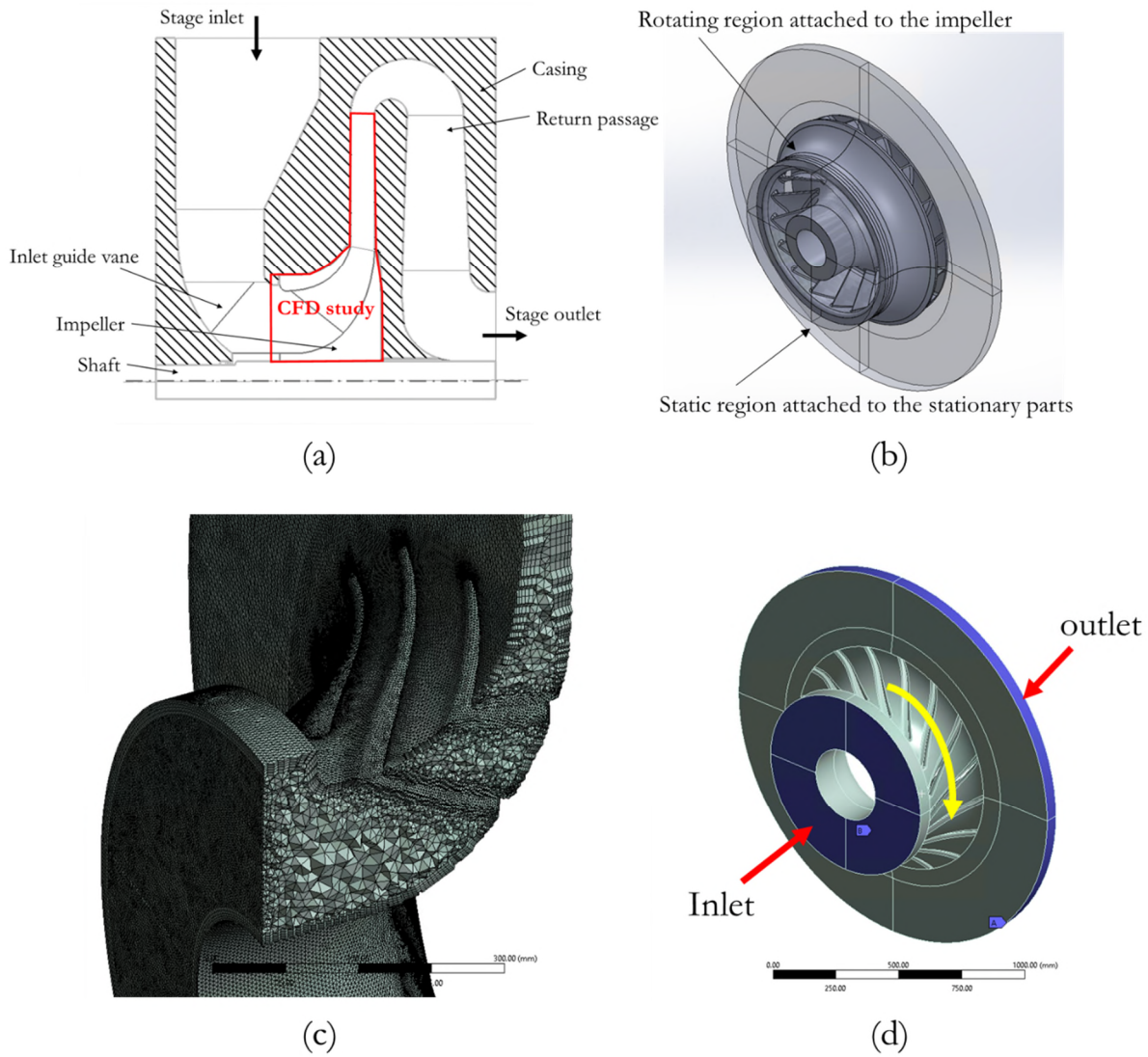


Figure 7. 2 CFD simulation model (a) computational domains in CFD studies; (b) simulation model, including a rotating region attached to the impeller and static region attached to the stationary parts; (c) mesh of the fluid domain; and (d) applied boundary conditions

7.2.2 Model validation

The CFD simulation model of a full-scaled impeller was validated by comparing simulation results with a petrochemical plant operating data. The parameters of interest were the inlet volume flow rate and the polytropic head. These two parameters were the plant's production control parameters. The polytropic head of a compressor is defined by equation 2.7 in section 2.2.1 Dynamic similarity of centrifugal compressors.

In the model validation, the total inlet pressure, the total inlet temperature, and static outlet pressure were varied following the machine operating data points in Table 7.3 to predict the mass flow rates through the impeller. Then the inlet volumes for each operating point were calculated from the predicted mass flow rates.

Figure 7.3 shows the correspondence between the predicted inlet volume flow rate from CFD simulations and the machine operating data. The calculated inlet volume flow rates were slightly higher than the actual operating data. The uniform inlet assumption might cause these differences. However, the difference was less than 5%; this implied that the CFD simulation model was sufficiently accurate.

Table 7. 3 Compressor operating data

Operating point	Polytropic head [m]	Inlet volume flow rate [m^3/s]	Inlet total pressure [bar]	Inlet total temperature [ºC]	Outlet static pressure [bar]
1	2430.9	26.95	2.77	43.7	4.02
2	2395.8	30.31	2.78	42.7	4.00
3	2181.9	33.16	2.77	41.4	3.91
4	1778.1	34.24	2.84	40.9	3.85
5	1541.8	34.93	2.79	40.5	3.68

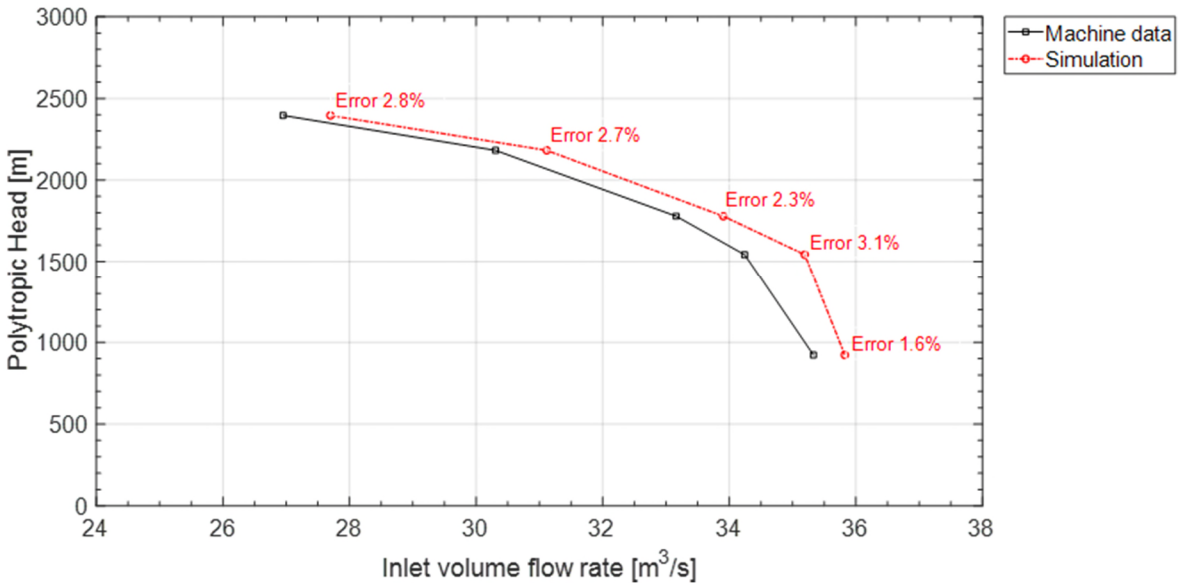


Figure 7. 3 Comparison between the predicted polytropic head and the machine data

7.2.3 Mesh sizing

The mesh sizing was performed to determine a converged solution with respect to the number of elements used in the simulation model. The simulation model in Figure 7.2 with six mesh densities was used in this mesh independency study.

The model was set up as described in section 7.2.1. The averaged mass flow rate and the averaged discharge temperature were chosen as target parameters to determine a solution convergence. The convergence of target parameters as the number of elements increased is shown in Figure 7.4. Consequently, the model with 1.22 x 10^7 elements was specified.

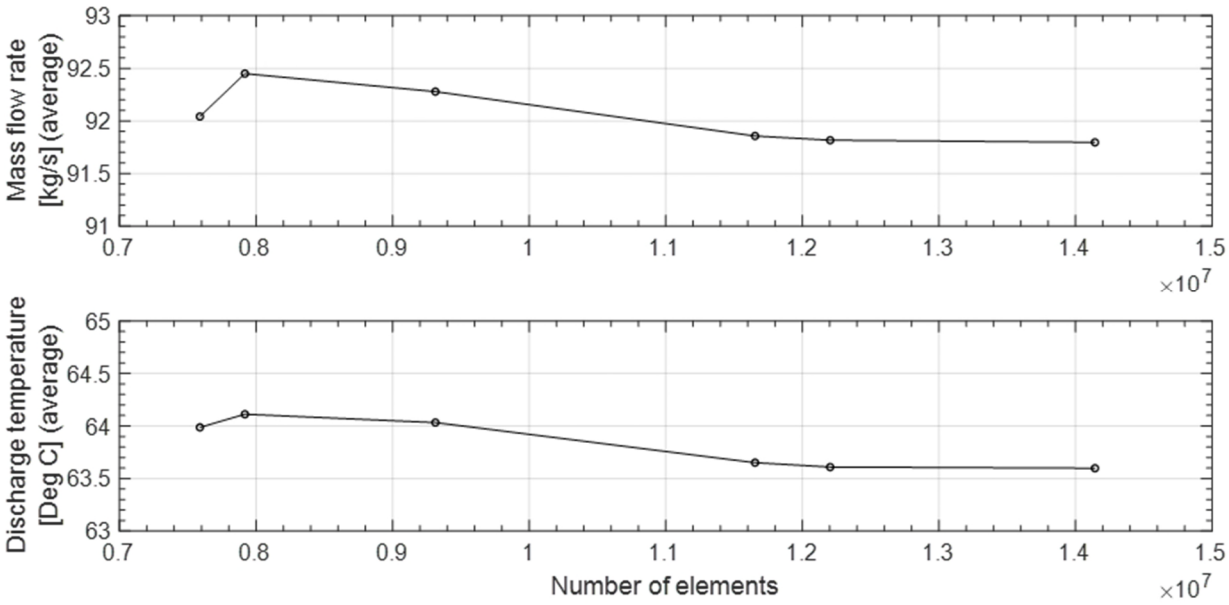


Figure 7. 4 Averaged mass flow rate and the averaged discharge temperature against the number of elements

7.2.4 CFD simulation results

Figure 7.5 (a) shows a sectional view of the pressure distribution at 50% span. As expected, the pressure side had slightly higher pressure than the suction side. It can be seen that pressure was built up along the streamwise direction from 2.7 to 3.55 bar. The relatively low compression ratio of around 1.3 was typical for a single-stage centrifugal compressor [62].

The Mach number distribution at 50% span is shown in Figure 7.5 (b). The Mach number increases along the streamwise direction from 0.4 to 0.6. The higher Mach number occurred near the outlet on the suction side of a blade, which has lower pressure as anticipated.

The blade pressure distributions on the pressure and suction sides are shown in Figure 7.6 (a) and (b), respectively. Along the length of the blade, the pressures on both sides increased from the leading edge to the trailing edge. In the same way, the pressure acting on the shroud and hub surfaces raised at the impeller outlet, as shown in Figure 7.6 (c) and (d), respectively..

The pressure distributions on the pressure side and suction side along the streamwise direction at various spans are shown in Figure 7.7. Similar pressure distributions were observed across various spans. In addition, the pressure fluctuations occurred upstream, where the flow encountered the leading edge of a blade. These pressure fluctuations were particularly intense at the shroud side.

Finally, the pressure difference was calculated to determine the net fluid pressure acting on a blade. The pressure difference of around 0.5 bar was shown in Figure 7.8. The lower pressure difference indicated that the passing fluid was likely to have less effect on blade deflection. Hence, to prove this assumption, the pressure distribution results were assigned as a passing fluid pressure boundary condition in the following static structural analysis.

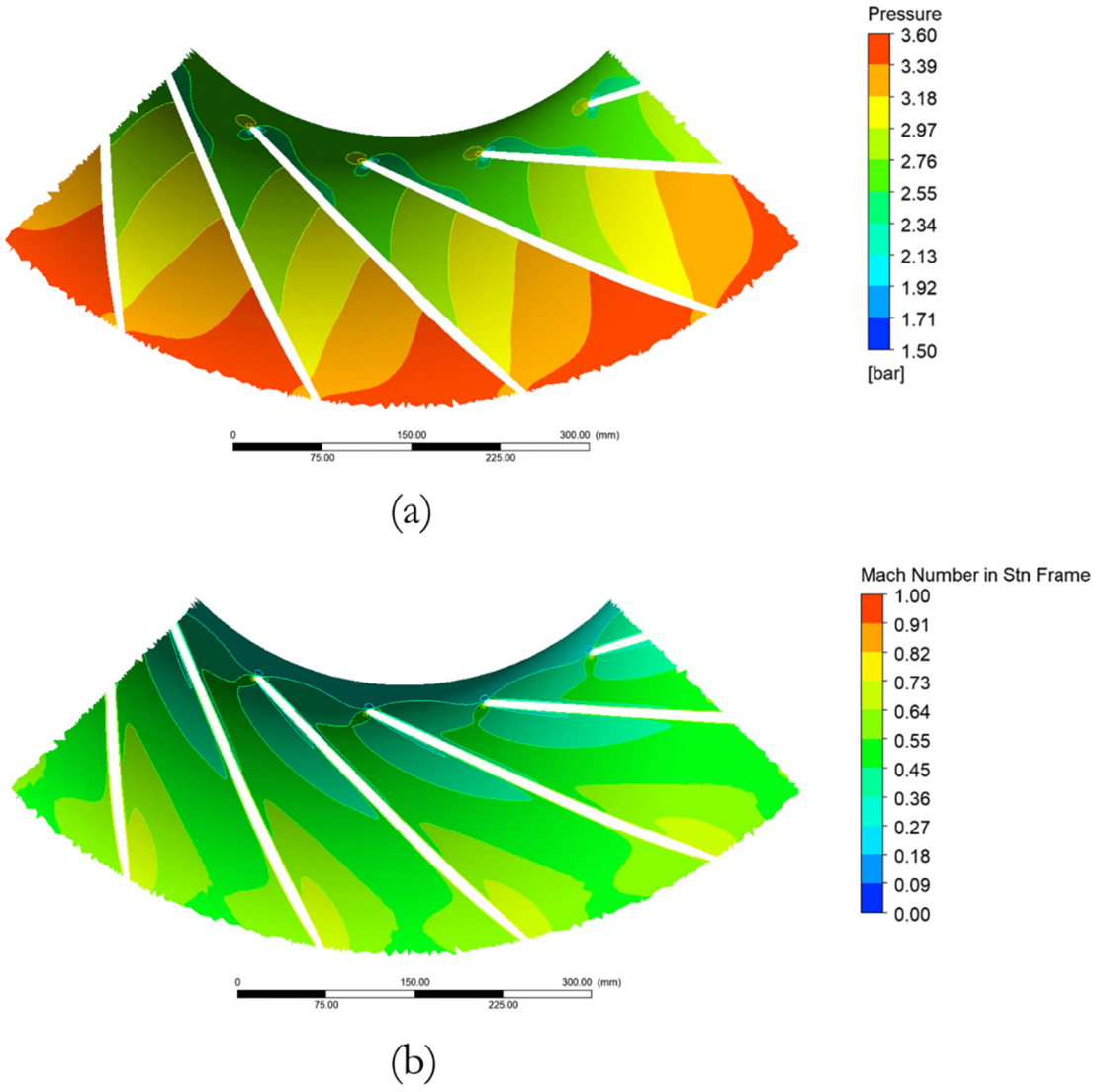


Figure 7. 5 Contours of pressure and Mach number at a 50% span (a) the pressure distribution; and (b) the Mach number distribution

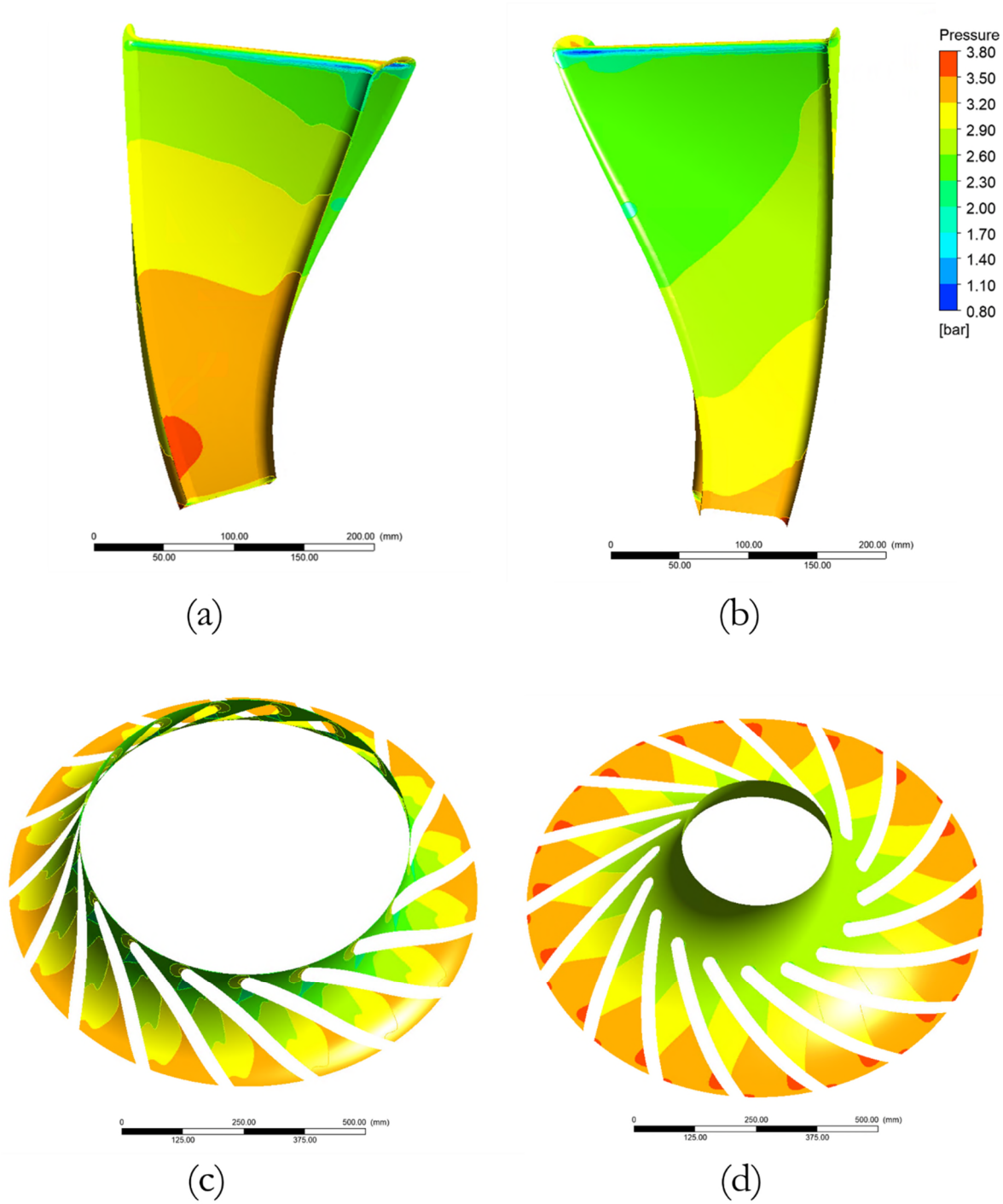


Figure 7. 6 Pressure distribution contours (a) at the pressure side of a blade; (b) at the suction side of a blade; (c) at the inside surface of the shroud; and (d) at the inside surface of the hub

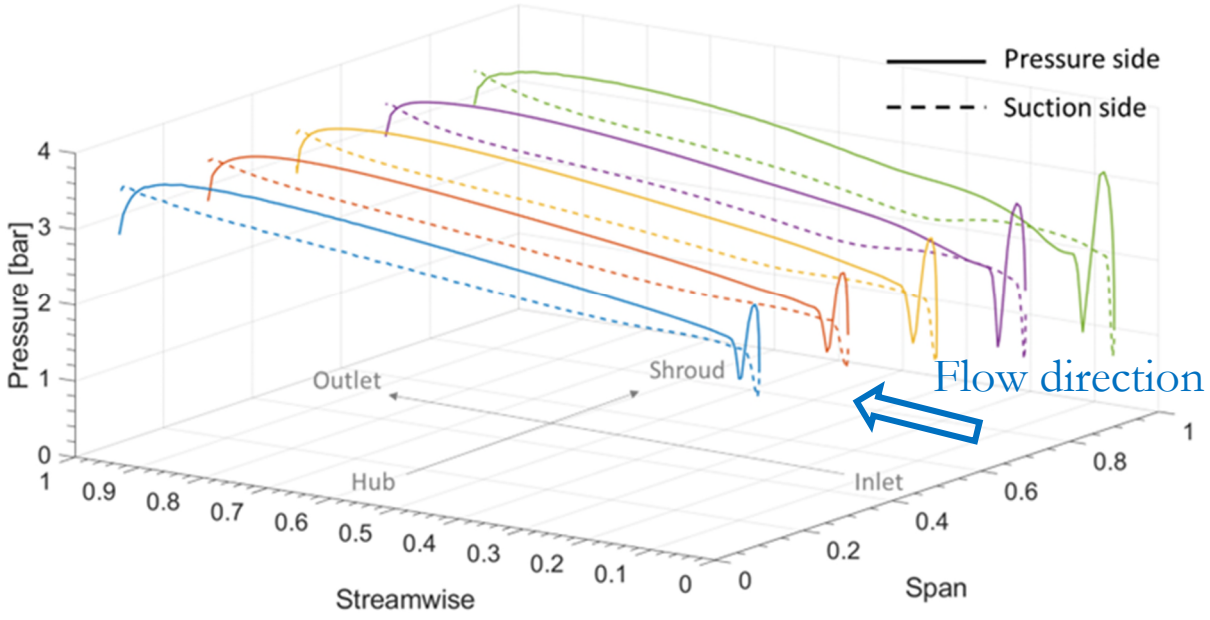


Figure 7. 7 The pressure distributions on the pressure side and suction side along the streamwise direction at various spans

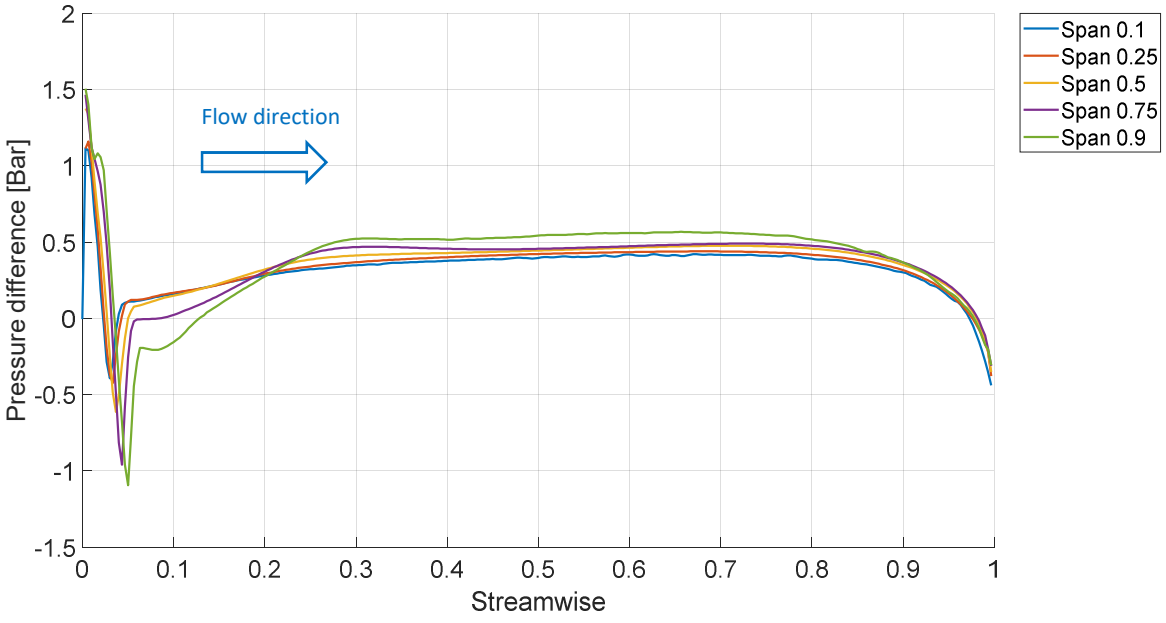


Figure 7. 8 The pressure difference acting on the blade between the pressure side and the suction side

7.3 Static structural analysis of the full-scaled impeller

In this study, the shroud deflections of an actual impeller in various blade conditions were predicted using the Static Structural module in ANSYS®. This FEA software was the same one used in the scaled impeller in Chapter 7.

7.3.1 Simulation models

The FEA simulation model of the actual impeller was built from a 3D scan of a compressor shrouded impeller installed in an ethylene plant. The damaged shrouded impeller with cracked blades, and a CAD model are shown in Figures 7.9 (a) and 7.10 (a), respectively. The impeller blades, which are essential parts, were designated to have a finer mesh than the rest of the impeller. This mesh set-up was similar to the simulation model of the scaled impeller. Figure 7.10 (b) shows the mesh of the simulation model.

The boundary conditions assigned in these simulations include the fluid interacting pressure from CFD analysis, the seal pressure at the inlet shroud location, the fixed rotating velocity equivalent to 5,800 RPM in the clockwise direction, and the fixed support at the impeller shaft hole. The assigned boundary conditions were shown in Figure 7.10 (c).

The cracked blade of the simulation model was based on the actual blade damage of the shrouded impeller in Figure 7.9 (c). Figure 7.10 (d) shows the crack path of the simulation model. To simulate the stages of crack propagation, this crack path

was divided into sixteen equal segments. The crack surfaces were assigned frictionless contacts, allowing body separation and transition but not penetration.

The actual impeller was made out of carbon steel AISI43440 with a blazing process. Thus, the mechanical properties of carbon steel given in Table 7.4 were used for the simulation model.

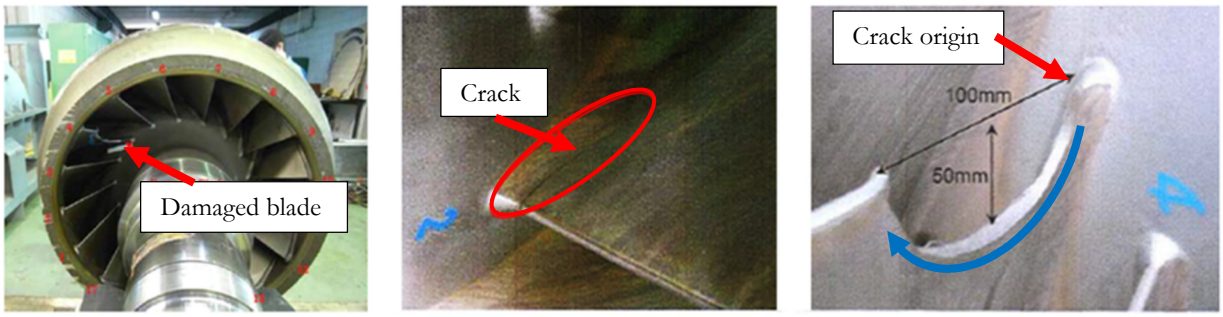


Figure 7. 9 A shrouded impeller with damaged blades (a) the location of a damaged blade; (b) a cracked impeller blade; and (c) the size of the damaged blade of a 50 mm radius, the blue arrow indicates the crack path

Table 7. 4 Mechanical properties of the actual impeller

Mechanical properties	**Carbon steel**
Density [kg/m^3]	7,850
Modulus of elasticity [MPa]	205,000
Passion ratio	0.29

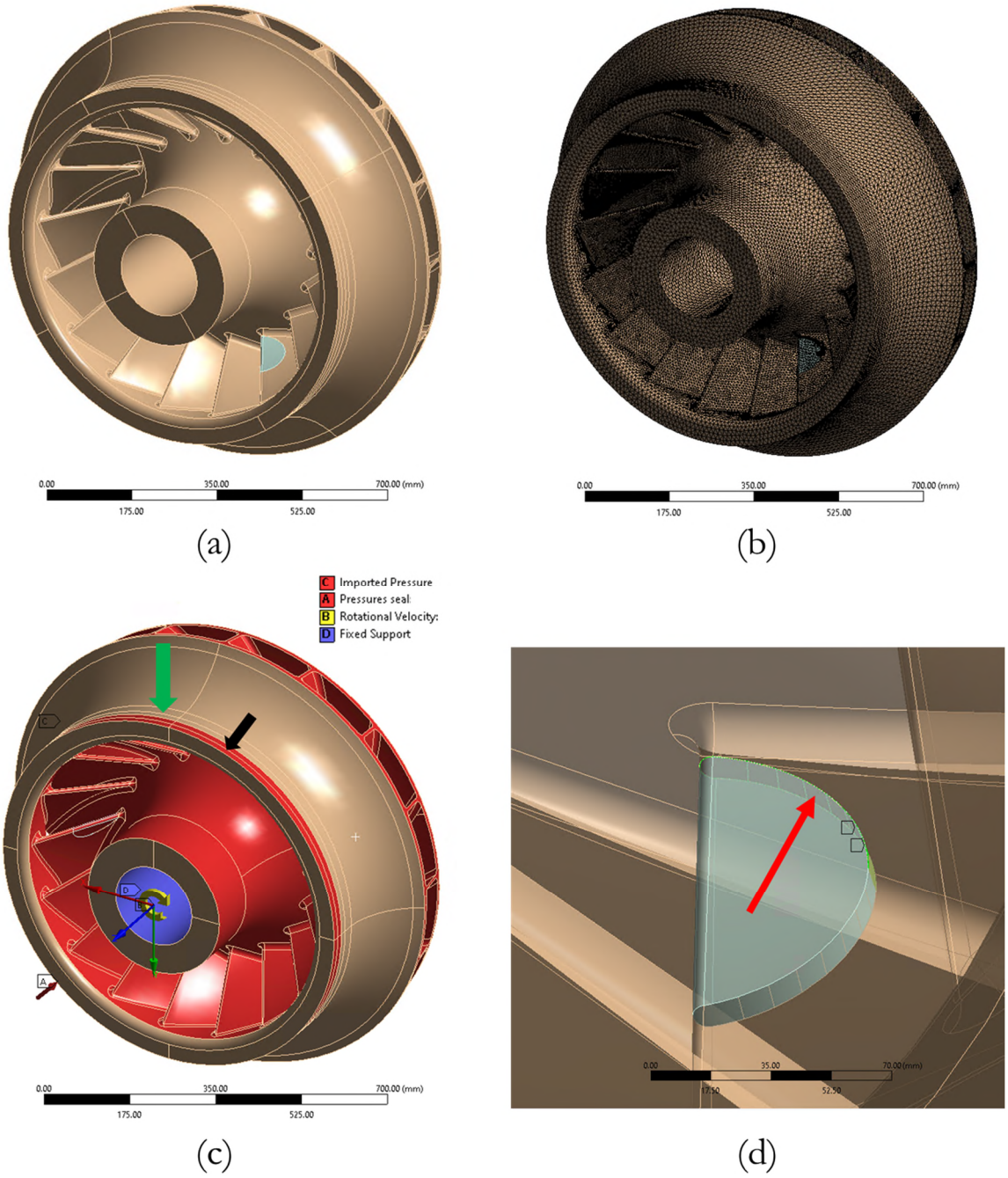


Figure 7. 10 Finite element simulation model (a) the scaled impeller with a cracked blade; (b) mesh of the simulation model, the green arrow indicates the inlet shroud location (clearance measurement location); (c) the applied boundary conditions; and (d) the crack path

7.3.2 Mesh sizing

In the same way as the mesh sizing of the scaled impeller simulation model, the model simulation in Figure 7.11 was used to identify the number of elements that generated a mesh independence solution. The boundary conditions were assigned as described in section 7.3.1. The crack was set at 50% of the crack path.

In this mesh sizing, the size of the tetrahedral elements was varied in seven different values. The maximum and minimum inlet shroud deflections were selected as target parameters. Figure 7.12 illustrates the convergence of the target parameters as the number increased. Therefore, a simulation model with 6.52 x 10^5 elements was specified for the FEA studies.

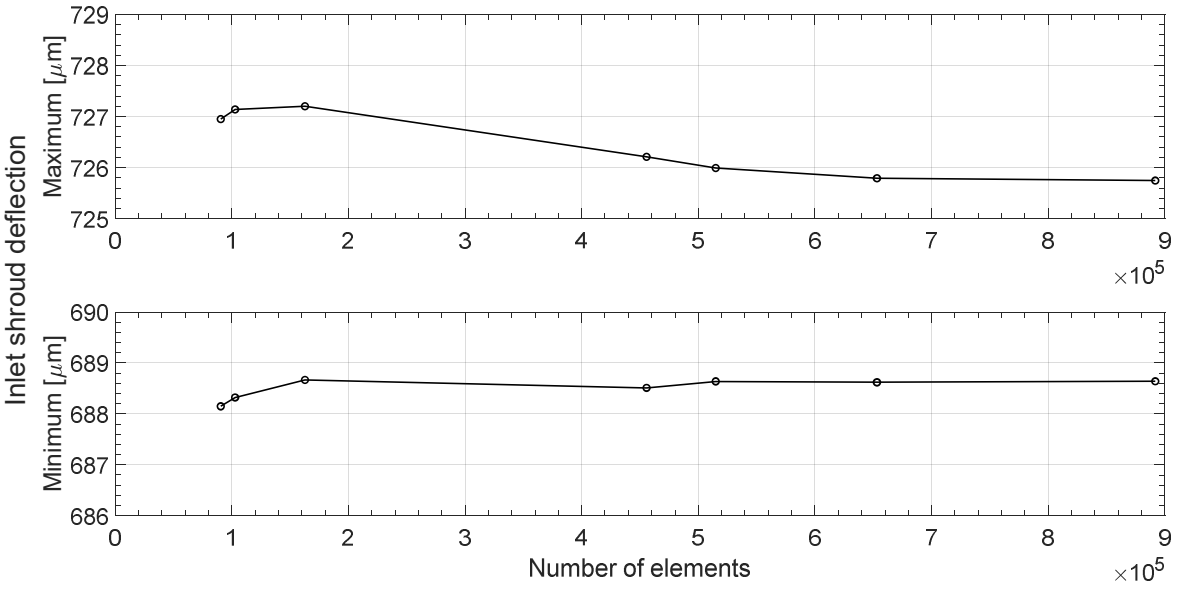


Figure 7. 11 The maximum and minimum inlet shroud deflection against the number of elements

7.4 FEA of the actual impeller

7.4.1 Effect of the passing fluid

In this simulation, the effect of passing fluid on the deflection of the inlet shroud impeller was determined. The CFD simulation result in terms of fluid pressure distribution was assigned as the additional boundary condition. The comparisons were made in the two cases: the healthy impeller and the impeller with a 50% cracked blade.

Figure 7.12 compares the simulation cases with and without pressure boundary conditions. In the case of the healthy blades, the inlet shroud deflection increased when the pressure boundary condition was applied. This increase in shroud deflection was caused by the fluid pressure acting on the impeller inner surfaces being higher than the outside surface. The result was the shroud expansion. However, the increases were less than 5 μm. This increase in shroud deflection also occurred in the case of the impeller with a cracked blade.

The change in deflection was the difference between the shroud deflection of the impeller with a cracked blade case and the impeller with a healthy case. Figure 7.13 shows the fluid boundary condition effect on the deflection change. The predicted results indicated that the fluid boundary condition did not affect the change in shroud deflection.

Two reasons might be the causes of the similarity in the change of defection. First, the pressure boundary condition acted evenly along the circumference of the

impeller. Secondly, these simulations did not account for the effect of the transient pressure fluctuations. For these reasons, the shroud evenly expanded in the radial direction.

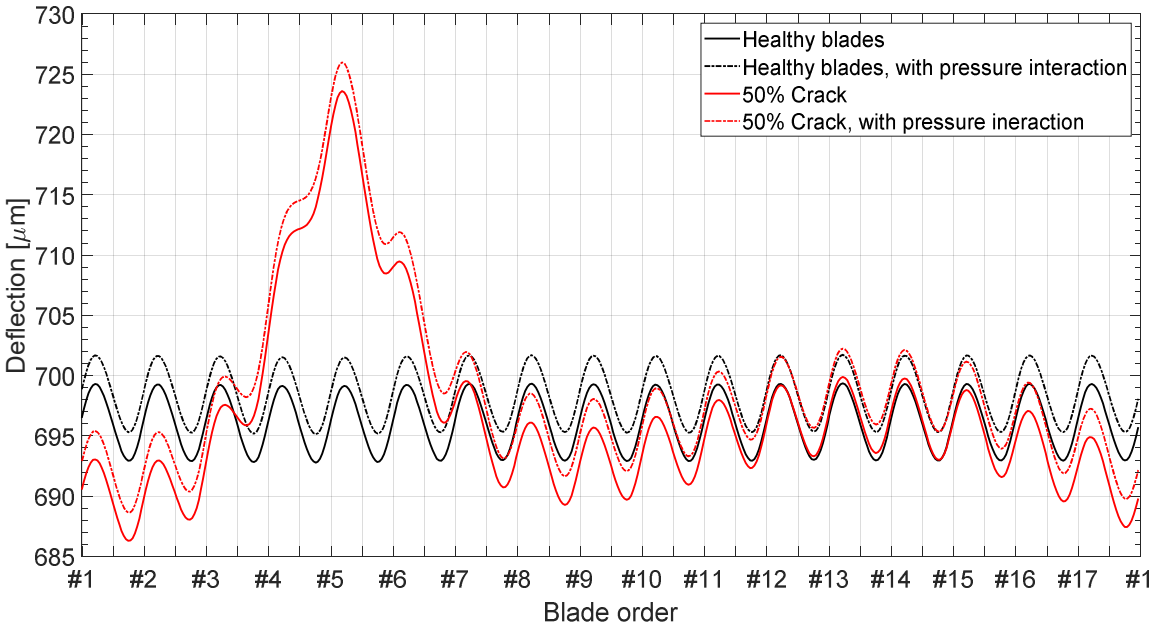


Figure 7. 12 The effect of the passing fluid pressure boundary condition on the inlet shroud deflections

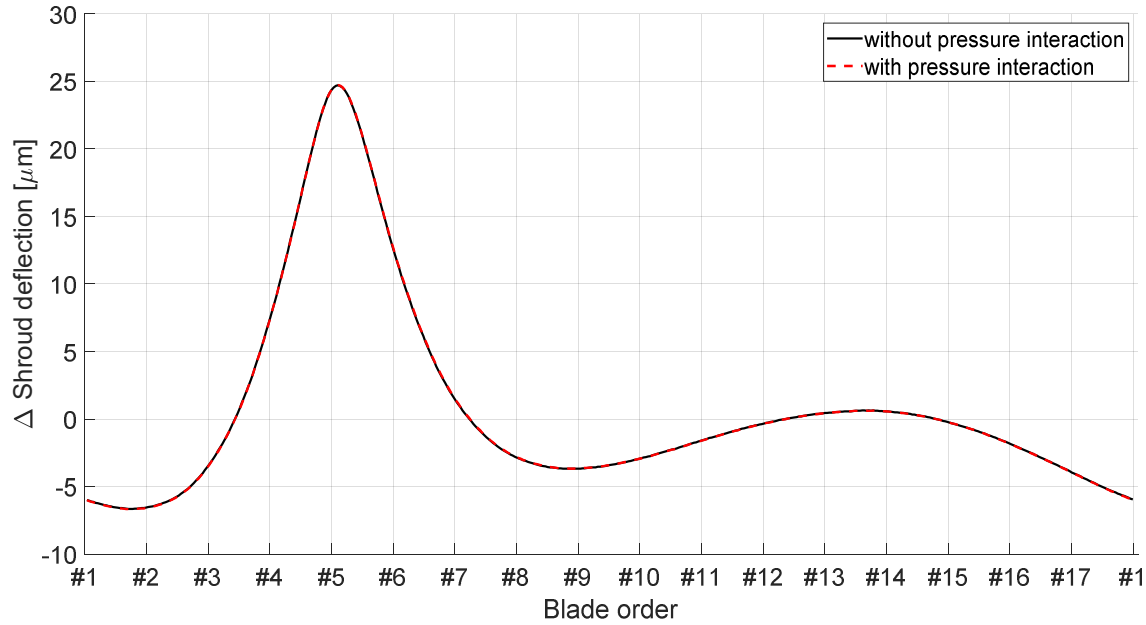


Figure 7. 13 The effect of the passing fluid pressure on the change of the inlet shroud deflection between healthy and 50% cracked blade conditions

7.4.2 Effect of a dry gas seal

In a centrifugal compressor for a petrochemical process, a dry gas seal has been typically used to provide shaft sealing and sealing between the inlet shroud/casing. A dry gas seal consists of a rotating ring and a stationary ring. The rotating ring is attached to the rotating component of the compressor, such as a shaft or an impeller inlet shroud. On the other hand, the stationary ring is connected to a spring attached to the compressor casing. During service, the dry gas seal works by generating a film gas between the grooves of the rotating ring and the stationary ring [103]. This function requires a steady flow of a supplied clean seal gas, for example, Nitrogen. Generally, the supplied gas pressure is 5 to 15 psi higher than the sealing pressure [104].

This study modelled the dry gas seal as a uniform pressure boundary over the seal contact location. The range of operating gas seal pressure was between 2.9 to 3.3 Bar [105]. Thus, the uniform pressure of 3.1 Bar was assigned normal to the sealing surface. This assigned boundary condition was based on the assumption that the fluid-dynamic force acting on the rotating component was uniform. The location of the assigned boundary condition is indicated by the black arrow in Figure 7.10 (c). The effect of the dry gas seal on the inlet shroud deflection was determined by comparing the results from two simulation cases: the healthy impeller and the impeller with a 50% cracked blade.

Figure 7.14 shows the simulation results. In both simulation cases, the seal pressure boundary condition had a negative effect on the shroud deflection. This decrease in

deflection was because the gas seal pressure acted in the opposite direction of the shroud deflection. However, the gas seal pressure has less effect on changing the shroud deflection.

Note that when applied with the passing fluid pressure boundary condition, the results were an increase in the shroud deflections. This increase was because the force from the pressure of the passing fluid inside the impeller was higher than the force from the pressure of the dry gas seal.

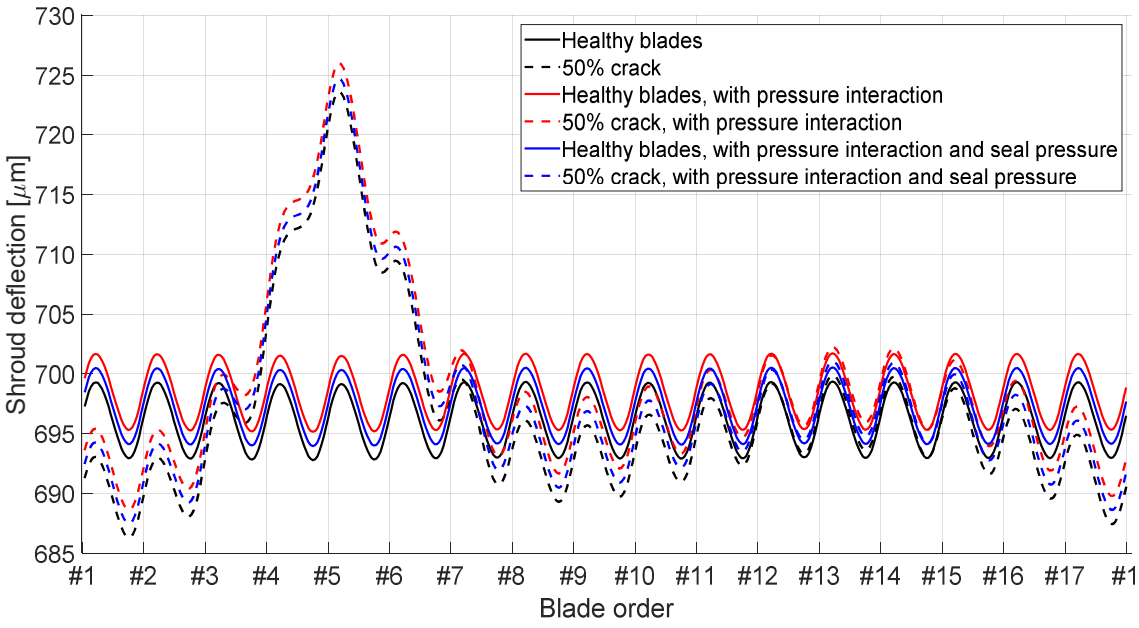


Figure 7. 14 The effect of the seal pressure boundary condition on the inlet shroud deflections

7.4.3 FEA of the impeller with healthy blades

The full-scaled impeller model in Figure 7.10 was used in the Finite Element Analysis (FEA) to determine the inlet shroud deflection of the impeller with healthy blades. The simulation results served as a baseline for comparison with the impeller with a cracked blade.

For the simulation to be as accurate as possible, the fluid pressure distribution and seal pressure at the inlet shroud were assigned as boundary conditions. The impeller rotational speed was fixed at 5,800 RPM.

The modal analysis was conducted to investigate the mode shapes of the full-scaled shrouded impeller with the assigned boundary conditions, including the rotational speed and pressure loads (passing fluid pressure distribution and seal pressure). Figure 7.15 shows the impeller's four different mode shapes, including the 1-ND mode, the impeller twist mode, and the first and second blade modes. As expected, the natural frequencies of the blade modes were higher than the impeller modes. The effect of pressure loading on the impeller's natural frequencies is shown in Figure 7.16. It can be observed that the pressure loads had less effect on the change of the impeller's natural frequencies because the magnitude of pressure distribution on the impeller's surfaces was low and acting on both sides of the blades. Consequently, the impeller's stiffness, which corresponded to its natural frequencies, remained nearly unchanged.

The results from the static structural analysis predicted that the maximum deflection occurred at the outlet shroud and the impeller blade mid-span. In contrast, the impeller hub had less total deflection as a result of its increased rigidity. Figures 7.17 (a) and (b) show the total deflection of the healthy impeller in the front and the back sides, respectively.

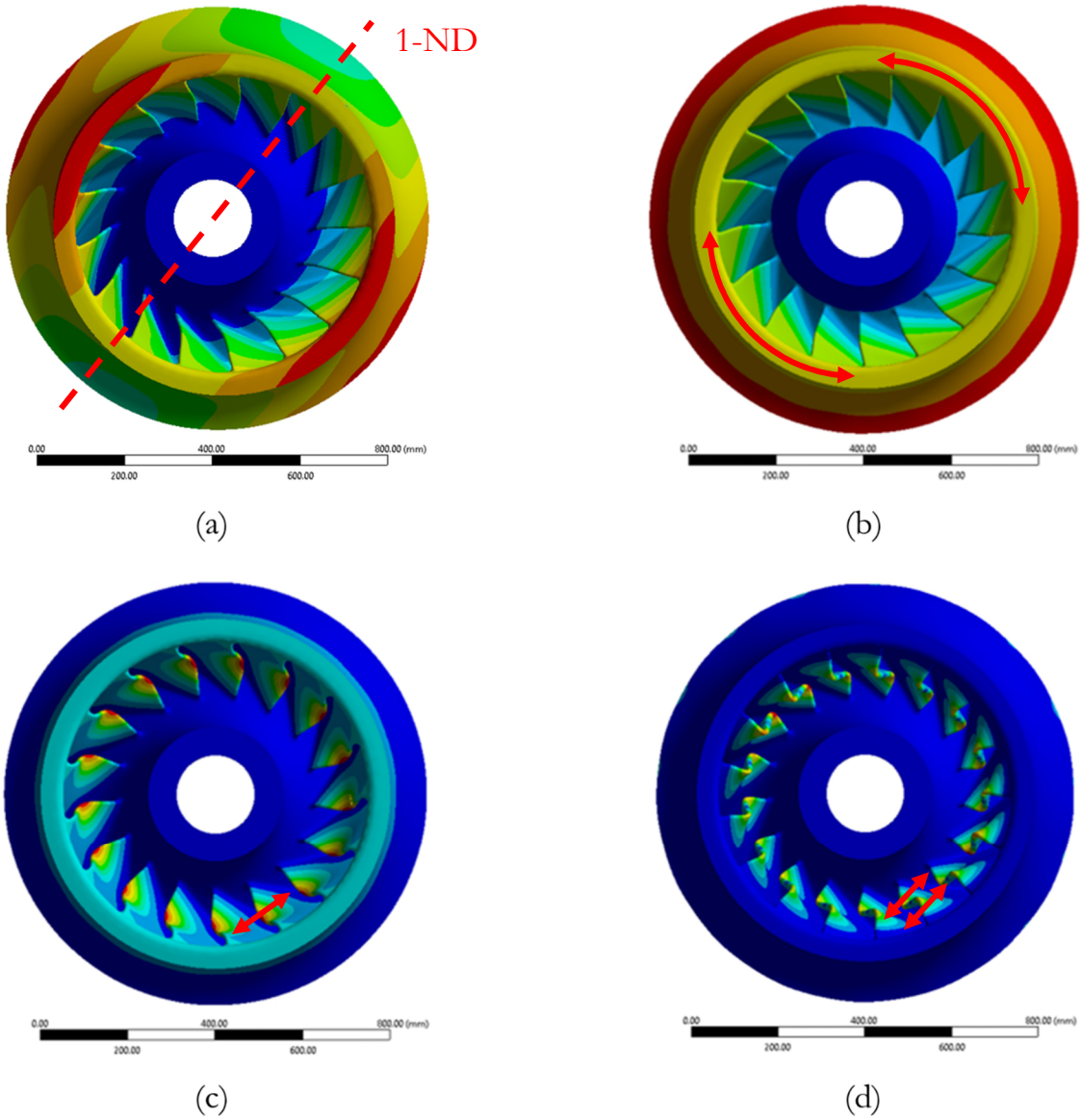


Figure 7. 15 Comparison between the whole impeller vibration modes and blade vibration modes, red arrows indicate the movement direction (a) the impeller one-nodal diameter mode at 553 Hz; (b) the impeller twist mode at 582 Hz; (c) the 1st blade mode at 2,443 Hz; and (d) the 2nd blade mode at 5,172 Hz

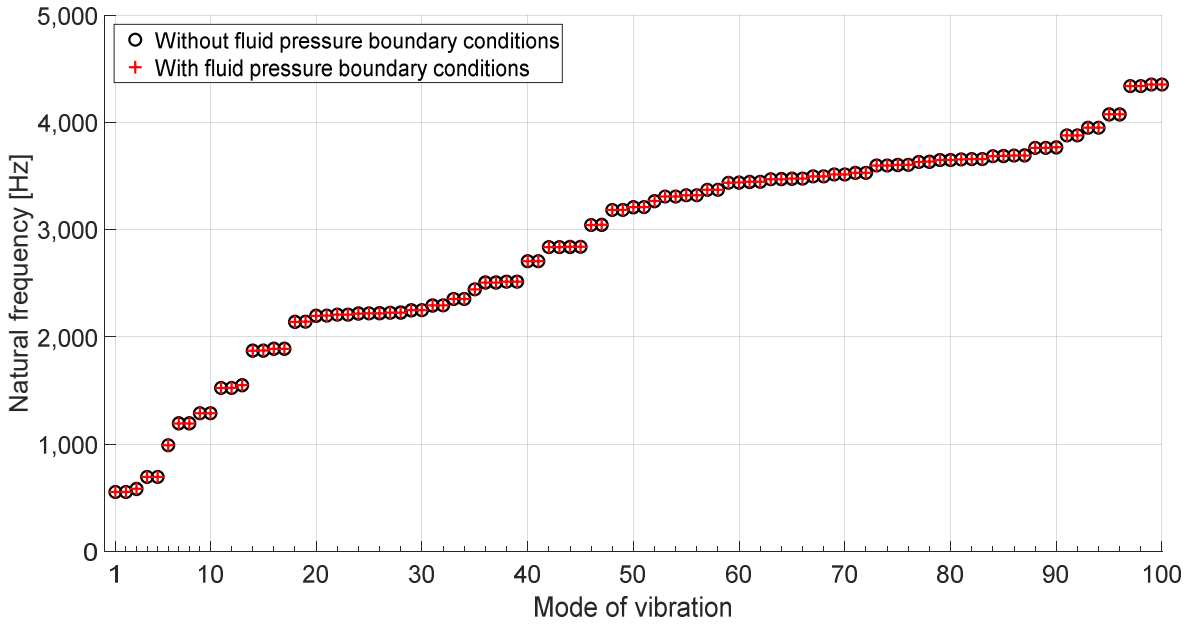


Figure 7. 15 Effect of applying fluid pressure boundary conditions, including passing fluid pressure distribution and seal pressure, on the natural frequencies of the actual impeller

Figure 7.17 (c) shows the predicted total deflection at a blade. The maximum deflection was observed in the blade/shroud interference region close to the outlet. This maximum area differed from the scaled impeller maximum deflection area, which appeared at the mid-span of the blade leading edge. However, the first mode deflection still appeared in that area in this simulation case.

The predicted blade stress distribution is shown in Figure 7.17 (d). The maximum stress occurred along the blade/hub connecting area. At the blade leading edge, the maximum stress location was close to the initial crack location of the actual case.

The comparison of the deflection magnitude in various locations on the full-scaled impeller is shown in Figure 7.18. Among the other locations, the inlet shroud location behind the location of the dry seal had the highest deflection of around 0.7

mm in the radial direction, with less fluctuation. This location was used to determine a blade condition in the following section.

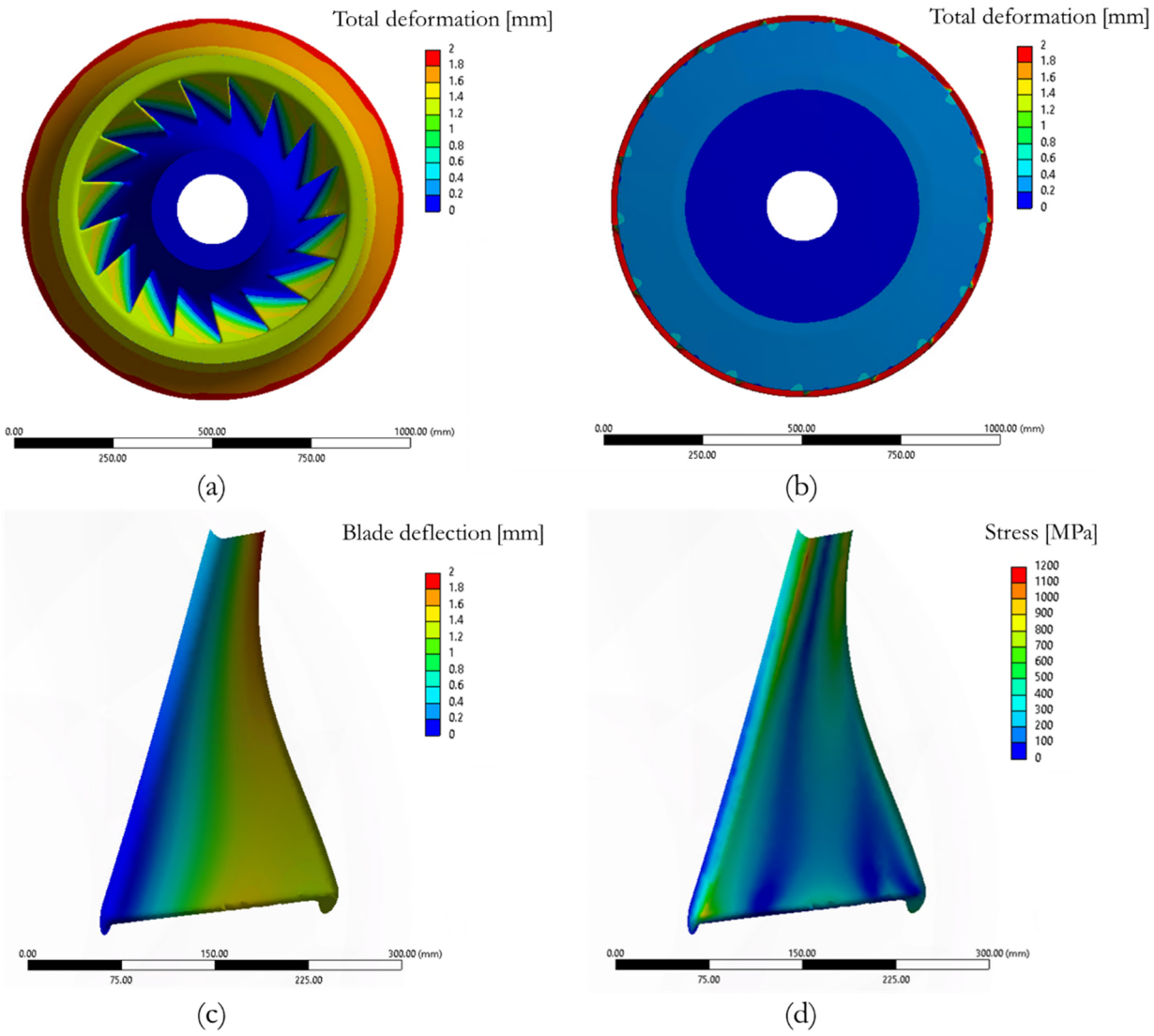


Figure 7. 17 Simulation results of the healthy impeller (a) total deflection at the front view; (b) total deflection at the back view; (c) blade total deflection; and (d) blade stress distribution

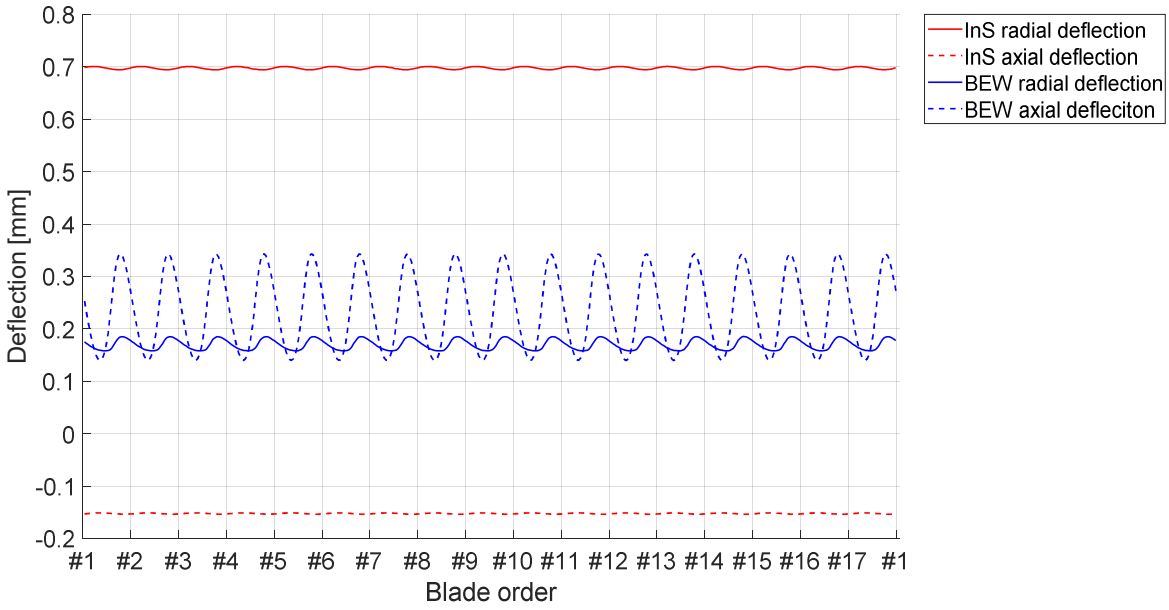


Figure 7. 18 Deflections of the actual impeller with healthy blades

7.4.4 FEA of the impeller with a cracked blade

The change in the inlet shroud deflections of a full-scaled impeller in various crack conditions was predicted through the Static Structural analysis module in ANSYS® as well as the scaled impeller in Chapter 6. The cracked blade was specified as blade number 5.

In the same way as the healthy impeller simulation, the passing fluid pressure, the dry gas seal pressure, and the fixed rotating velocity equivalent to 5,800 RPM were assigned as the boundary conditions in these simulations.

Note that the assigned passing fluid pressure boundary condition was calculated from the healthy impeller condition. This means that when applied to the cracked blade condition, the interrupted flow that occurred at the cracked blade was

neglected. However, this assigned boundary condition should still be valid due to the slight pressure difference between the two sides of around 0.5 bar.

Figure 7.19 shows the deflections of a cracked blade in four crack conditions, including 12.5%, 25%, 50% and 75% crack. As the crack propagated, the deflection magnitude increased while the location of maximum deflection changed from the mid-span of the blade leading edge to the initial crack location.

When the crack propagated less than 50%, the maximum blade deflection was around 3 mm. This slight deflection indicated that the cracked blade had relatively less effect on the change of the unbalanced force of the impeller (the total impeller mass was still the same).

The change of the inlet shroud deflection can be divided into three regions based on the state of the crack propagation. Figure 7.20 shows that in the first region, the peak of the inlet shroud deflection increased as the crack propagated. This region covered from the initial crack to the 37.5% crack. It can be observed that the rate of increase in deflection decreased as the crack propagated. The decrease might depend on the curved crack path. The further crack propagated, the increase in the crack area reduced. This increase in crack area was related to the decreased stiffness of the cracked blade that connected the hub and the shroud. Figure 7.21 shows the change of inlet shroud deflection in the first region.

The second region was characterised by the decrease of the peak of the inlet shroud deflection. In this simulation, this region covered the crack propagation from 37.5%

to 93.75% crack, where the cracked blade was close to breaking off. In addition to the decrease in the deflection peak, the rising of the subsequent blade deflection was observed. This change in the inlet shroud deflection is shown in Figure 7.22.

The last region was the case of the missing part of a blade or blade loss. In this region, the peak of the inlet shroud deflection shifted to the subsequent blade (blade number 6 in this simulation). The red dotted line indicates the inlet shroud deflection in case of a blade loss in Figure 7.22.

The predicted relationship between the crack length (%) and the change in the inlet shroud deflection is shown in Figure 7.23. The linear relation can be observed at the early stage of the crack detection, which was the detection target of the proposed system. Note that this linear relation was consistent with the experimental results from the scaled impeller.

The uncertainty of the clearance measurement system used in the experimental studies was used as a criterion to determine the minimum detectable crack for this full-scale impeller. Based on the calibration result described in Chapter 3, the uncertainty of the clearance measurement was ±9 μm. Consequently, the early stage of a cracked blade at a 20% crack which produced the inlet shroud deflection of around 20 μm could be detected with the proposed clearance measurement system.

Figure 7.24 shows the polar plot of the change of the peak of the inlet shroud deflection in various blade conditions. During the early stage of crack propagation (the first region), the peak location shown by the angle was relatively constant along

the blade/shroud connecting location. After that, the peak shifted towards the adjacent front blade number 4.

The back-end wall axial deflections at different blade conditions is presented in Figure 7.25. It can be seen that the cracked blade had less affected on the deflection in this impeller location. The changes in deflection appear to be less than 10 um with likely to be within the clearance measurement uncertainty. Thus, this measurement location is not suitable for impeller crack detection. However, installing a clearance sensor in this location still provides the benefit of detecting the entire axial movement of the impeller during machine operation.

In addition, during the crack propagation, the simulation model predicted similar results of the back-end wall deflection. Therefore, the clearance measurement in this location should be used to detect the movement of the impeller for reference.

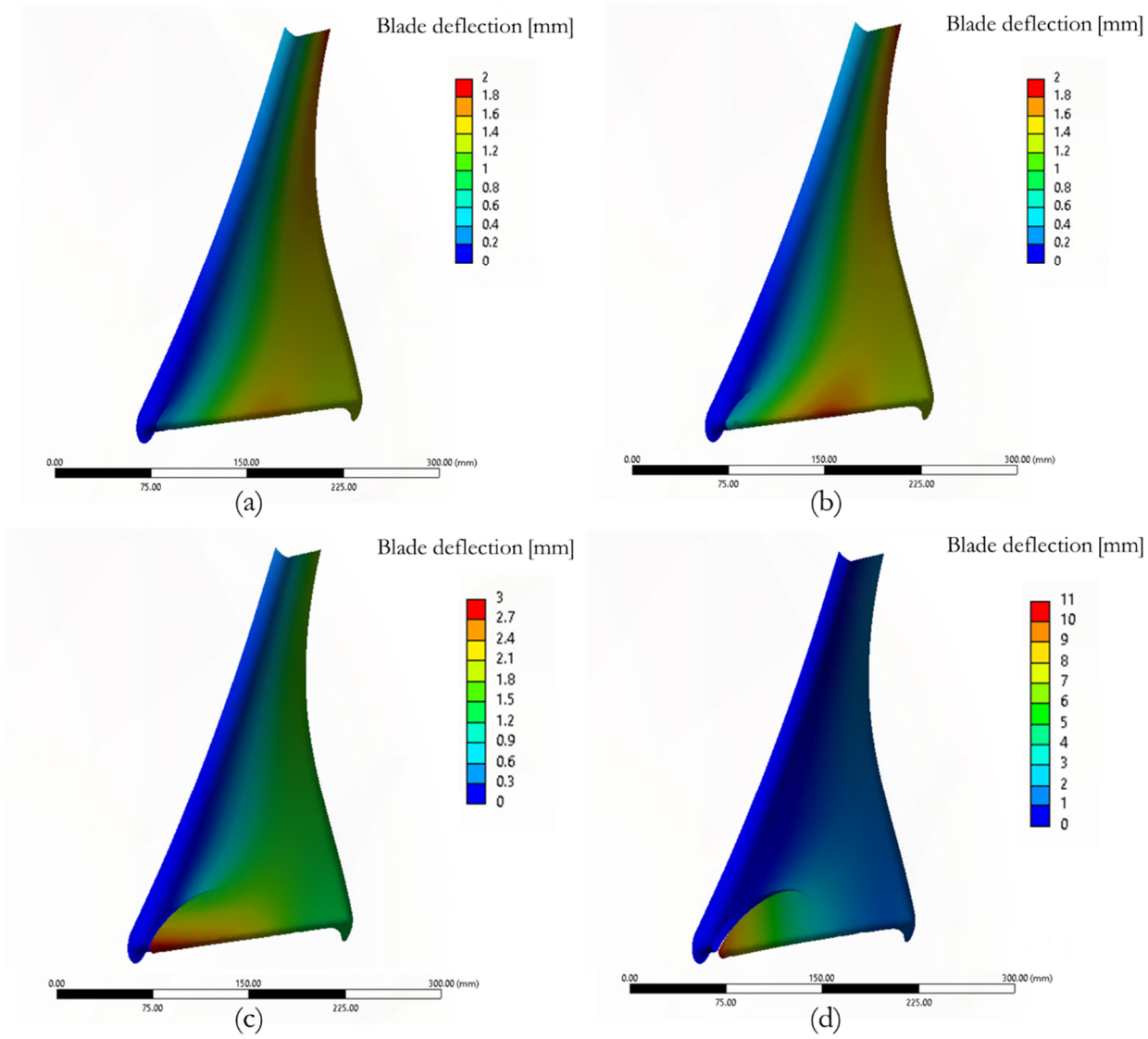


Figure 7. 19 Deflections of a cracked blade of the full-scaled impeller (a) 12.5% crack; (b) 25% crack; (c) 50% crack; and (d) 75% crack

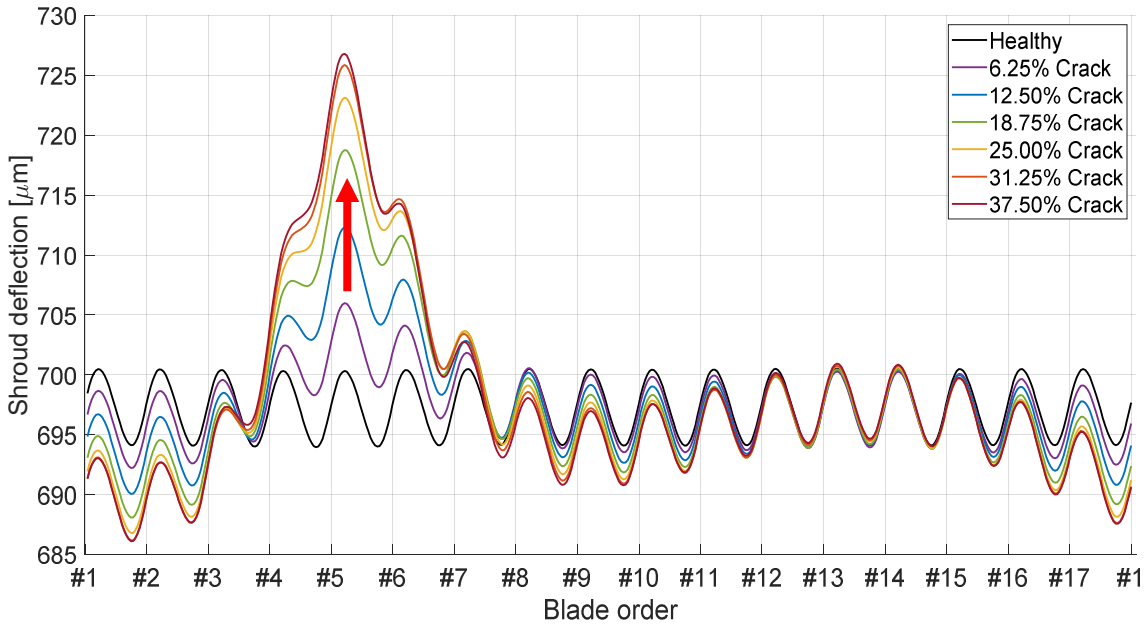


Figure 7. 20 The inlet shroud deflection of the full-scaled impeller in various conditions (healthy to 37.5% crack)

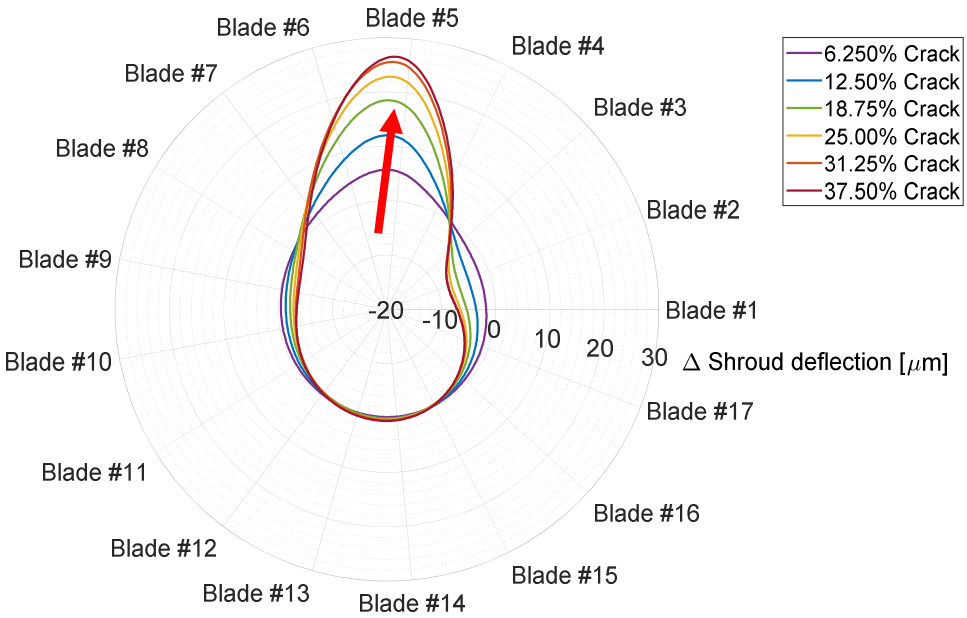


Figure 7. 21 Polar plot of the change of the inlet shroud deflection in the first region: 6.25% crack to 37.5% crack

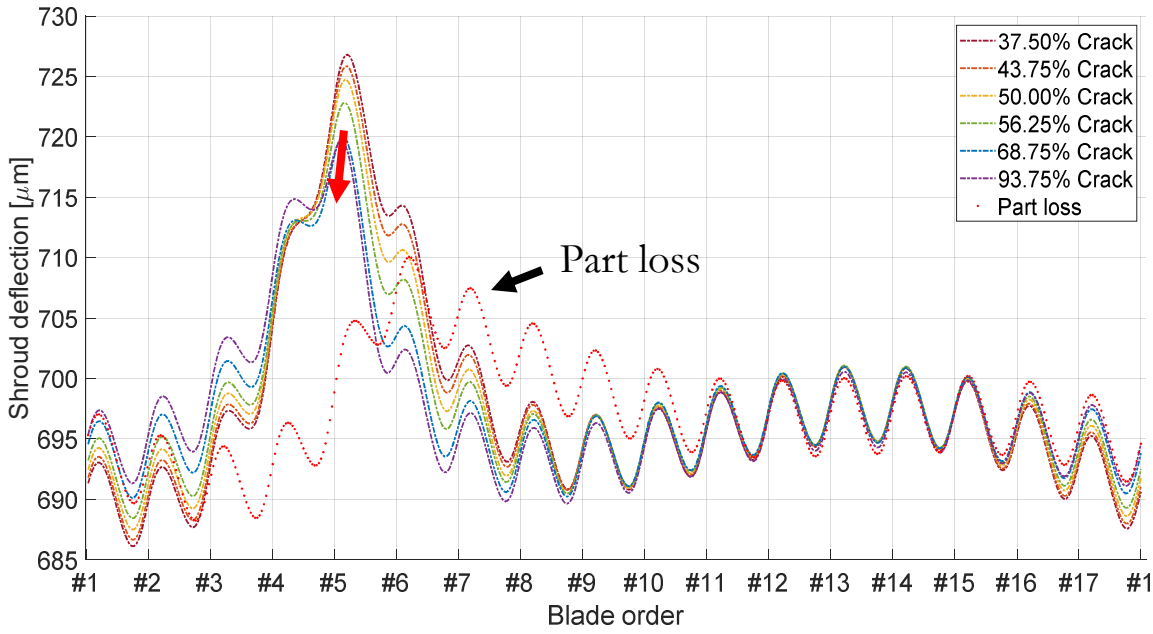


Figure 7. 22 The inlet shroud deflection of the full-scaled impeller in various conditions (37.5% crack to part loss)

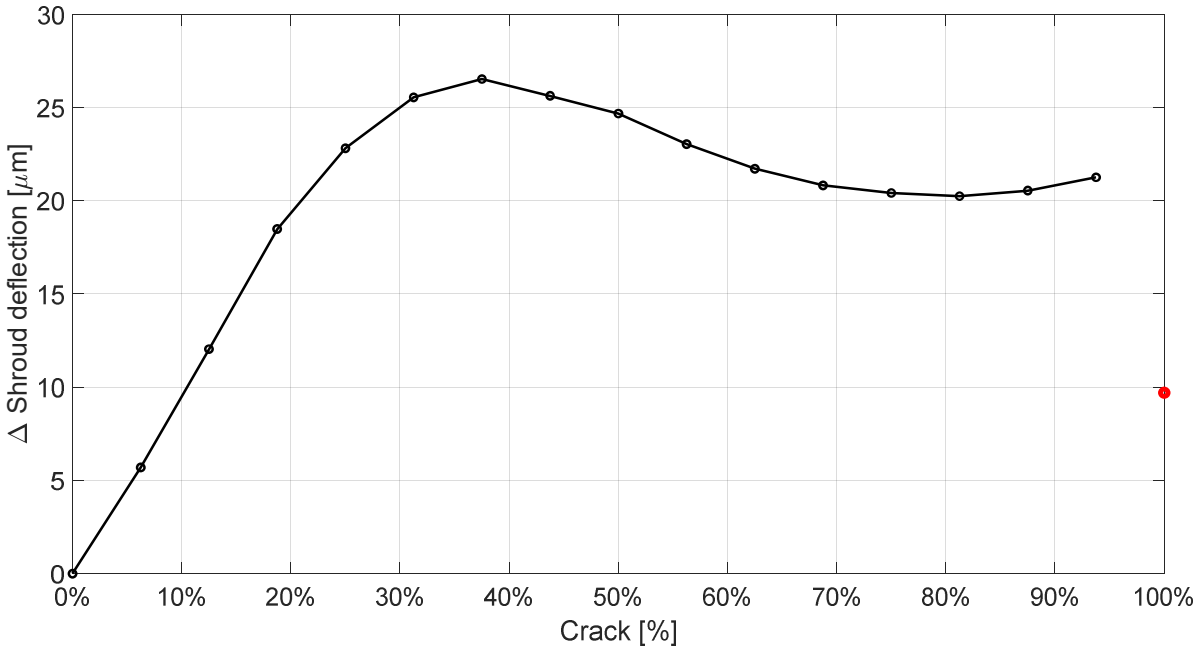


Figure 7. 23 The predicted relation between the crack length (%) and the change in the peak of the inlet shroud deflection

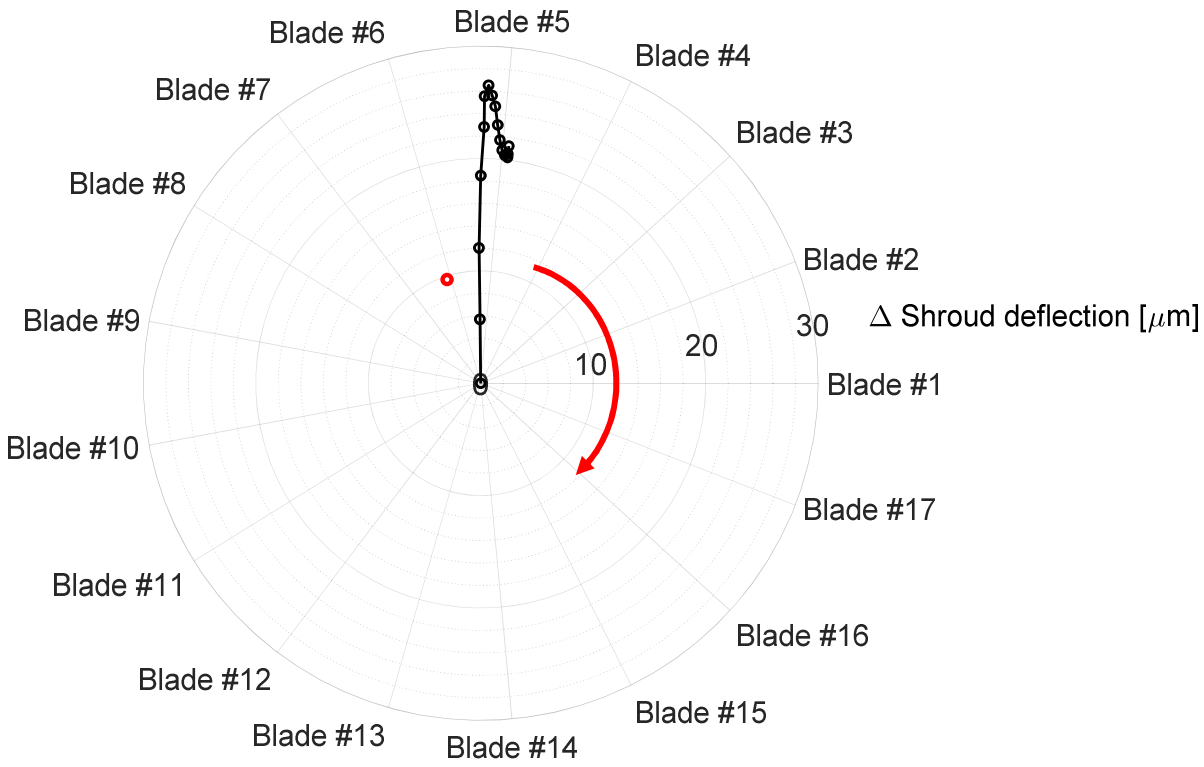


Figure 7. 24 Polar plot of the predicted relation between the crack length (%) and the change in the peak of the inlet shroud deflection, the red arrow shows the direction of rotation

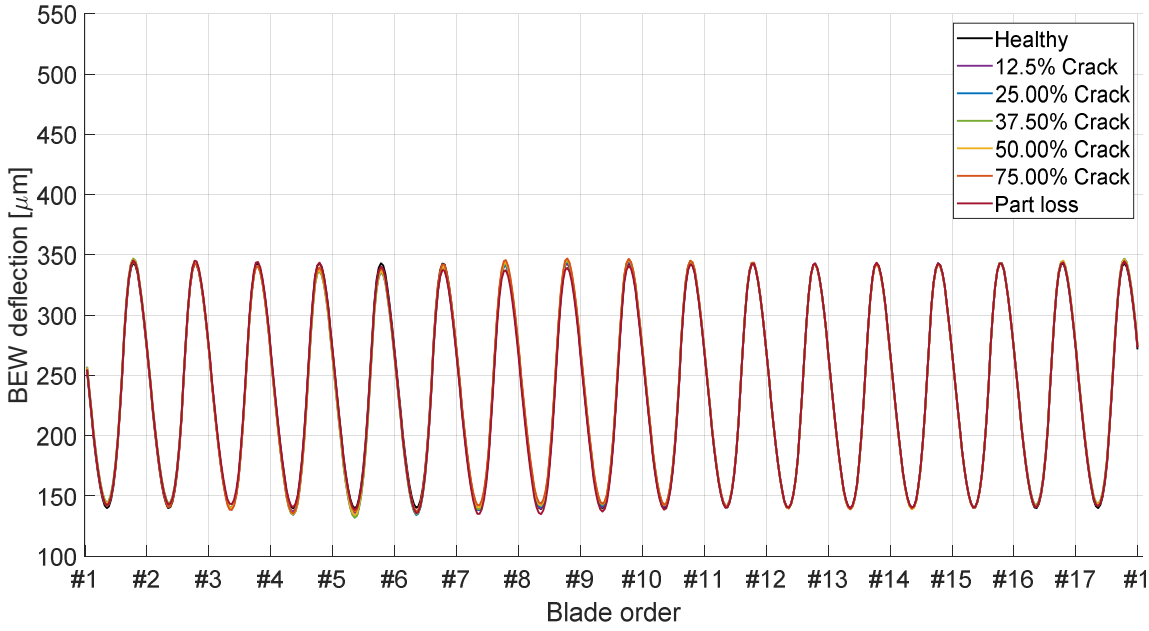


Figure 7. 25 The back-end wall axial deflections at different blade conditions

7.5 The proposed blade crack detection system

This section provides the guidelines for designing a crack blade detection system for a shrouded impeller with clearance measurement.

Starting with the type of sensor, an eddy current sensor that is immune to contamination and accurate to micron level is appropriate for this clearance measurement application. As opposed to a capacitance sensor that is susceptible to the effects of ionised particles such as oil, dust, and rub particles, this sensor is impervious to the effects of such particles.

The electromagnetic simulation should be used for sensor design and optimisation, as shown in Chapter 4. The range of measurement is the main criterion for sensor design regarding sensor coil diameter. The rule of thumb for a sensor with a circular coil design, the range of measurement is half of the sensor coil diameter [6]. In the case of 7 mm clearance between the target/casing, for example, the minimum size of 14 mm sensor diameter is required.

Notably, an eddy current sensor with a circular coil design (commercial sensor) is recommended for clearance measurement for the actual impeller because the shrouded impeller has a large radius compared to the sensor diameter. Thus, using the unique rectangular sensor design is not beneficial for the actual impeller, in contrast with the testing impeller, which needs a rectangular sensor for better accuracy. In addition, using a commercial sensor has benefits in sensor installation

and calibration. Unlike when using a rectangular sensor, in which the sensor needs to be aligned.

Eddy current sensors should select sensors that operate linearly within the operating range of an industrial compressor, which is approximately 80 – 90 ^{o}C. In designing a measurement system, it is necessary to account for temperature drift compensation [113]. API Standard 670 Machine Protection Systems should be used as a guideline [16].

The proposed sensor location for a crack detection system is shown in Figure 7.26. The clearance sensor should be installed behind a dry gas seal at the inlet shroud location. Based on these studies, this location was the optimal sensor location for detecting crack propagation.

In addition to the inlet shroud location, the impeller's back-end wall is another position where the sensor should be installed, as shown in Figure 7.26. This back-end wall sensor location is coincident with the model results in Figure 7.25. The clearance data from this location is utilised to monitor the axial movement of the impeller.

Regarding the number of sensors, at least two sensors are required for each measurement location to track the impeller movement. The two sensors should align perpendicular to each other. By using the combined data, the impeller movement can be compensated to calculate the relative deflection.

The sensor landing areas should be prepared by adapting the API Standard 670 Machine Protection Systems [16]. The standard gives the guideline that the combined electrical and mechanical runout of the sensor landing area should not exceed 6 μm. However, the control of runout of 6 μm may be impractical in the case of a large impeller. Consequently, the recommendation is to measure the runout as a reference point during the sensor installation process. Note that less runout makes clearance calibration and measurement easier.

In terms of the monitoring system, an online continuous monitoring system is required to distinguish the stage of crack propagation. Monitoring should commence on the first day that a machine is in service. Consequently, the blade condition can be determined by monitoring the change in the pattern of the inlet shroud deflection compared with the record data from the healthy blade condition at the same speed. The change in clearance may need to be detected by automated post-processing. In addition, the predicted clearance from a validated simulation model may also be a guideline for predicting the condition of impeller blades.

Note that the proposed crack detection system should be combined with a Machine Monitoring System (MMS), such as a radial shaft vibration measurement for detecting the change of unbalanced forces. The crack detection system is intended to provide a warning of the impeller blade condition in advance before the machine will shut down by the protection function from its MMS. In the case of petrochemicals or refineries, this insight information will help in maintenance planning, production process adjustment, and supply chain management. Notably,

the production process planning is the main benefit of installing this blade health monitoring system. In the case of an emergency shutdown of the ethylene plant in Thailand in 2009 (detailed in section 1.1 Background), if this system were installed in advance, the saving from process adjustment and preparation would be around £2 million.

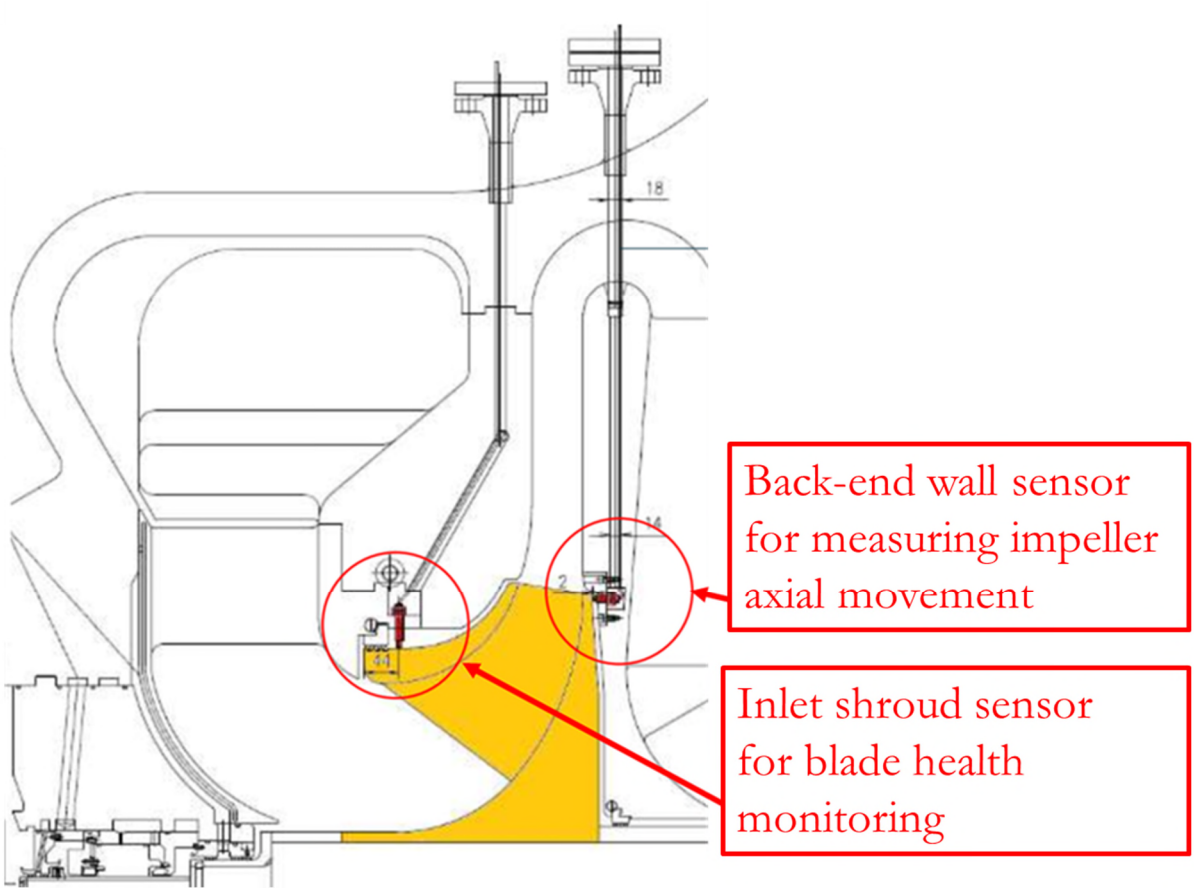


Figure 7. 26 The proposed locations for clearance sensor installations and the inlet shroud, and the back-end wall locations

7.6 Chapter conclusion

In this chapter, the inlet shroud deflections of the full-scaled shrouded impeller in various blade conditions were predicted using the FEA simulation models. The effect of passing fluid and a dry gas seal in terms of pressure acting on the impeller components were assigned as boundary conditions. A crack from an actual incident was used to simulate the path of crack propagation. The predicted results indicated that detecting a cracked blade in the early stage was possible using the inlet shroud/casing clearance measurement. Based on the clearance measurement system used in the experimental studies with an uncertainty of ± 9 μm, the proposed detection system could detect the early stage of a cracked blade from around a 20% crack. Lastly, the guideline for designing a blade crack detection system for an actual impeller was proposed.

Chapter 8

Conclusion

8.1 Overall conclusions

The key achievement of this thesis is to propose a novel blade health monitoring solution for shrouded impellers. The proposed monitoring solution is based on the principle that the condition of the blades can be correlated to the impeller shroud deflection. The shroud deflection can be related to the clearance between the shroud and the sensor installed through the static casing. Thus, the condition of the blade is able to be determined. The feasibility of a proposed solution was investigated and evaluated through a combination of experimental, numerical (FEA and CFD), and theoretical studies. An intensive literature review indicates that this clearance measurement solution is a novel approach for monitoring the blade condition of a shrouded impeller, and has not previously been attempted, researched, patented, commercialised, or published in the open literature.

As the part of the experimental studies, a new high-speed spinning rig was designed and fabricated for testing a scaled impeller. This scaled impeller was 3D-printed

based on the shape of an actual impeller. Its characteristics, including the runout, the residual unbalance, and the blade resonant frequencies were measured for reference purposes.

Eddy current sensors were utilised to perform the clearance measurements due to their acceptable accuracy and potential to be applied in contaminated environments of an actual machine. The calibrated eddy current sensors with an uncertainty of ±9 μm were installed in various locations, including the inlet shroud, the outlet shroud, and the back-end wall. Electrically conductive paint was applied to these impeller target measurement locations in order to be detectable by the eddy current sensors.

The experimental studies were performed with the scaled impeller in two conditions: the impeller with healthy blades and the impeller with an initial cracked blade. The results of the preliminary blade crack detection experiment confirmed that the clearance measurement using eddy current sensors mounted on the outside of a shrouded impeller enables the detection of the impeller deflection, blade defect, crack propagation, and even a stuck blade fragment incident without affecting the gas flow path through the impeller.

With regards to the healthy impeller, impeller deformation was caused by the effect of the centrifugal force. The magnitude of the impeller deflection was dependent on the rotational speed and location.

The experimental investigation of the impeller with a 4-mm to 20-mm cracked blade revealed three critical findings. First, the inlet shroud was the optimal location for

the shrouded impeller blade condition monitoring with clearance measurement. Secondly, the clearance signal at this location determined the linear relationship between the crack length and the characteristics of the shroud deflection. This linear relationship indicated that the simplified lumped-mass model was acceptable to explain the mechanisms of the crack-induced mistuning in a blade-disk system. The reduced blade stiffness caused by crack propagation led to an increase in the shroud deflection in areas where blades were connected. Finally, when the clearance measurement uncertainty was accounted for, the smallest detectable crack measured approximately 15 millimetres for the scaled impellers used in these studies, suggesting that the blade crack stage can be detected early with the proposed system.

For the numerical studies, Finite Element Analysis (FEA) was performed on the scaled impeller. Experimental results were used to validate the simulation model for both the healthy and cracked blades. Consistency was established between the simulation and the experimental results. Particularly, the linear relationship between the crack length and the change in the inlet shroud deflection was evaluated.

Subsequently, the influence of various impeller designs on the impeller shroud deflection was determined in the parametric studies using the validated simulation model as a basis. Seven impeller design parameters were studied, including the fillet radius, the blade thickness, the shroud thickness, the back-end wall thickness, the number of blades, the impeller size, and the impeller material. The findings of the parametric analysis suggested that, for a given impeller size, blade thickness and shroud thickness had the most significant impact on the change in the inlet shroud

deflection. In contrast, the fillet radius and back-end wall thickness had relatively less impact. In addition, the relationship between the maximum inlet shroud deflection and the impeller material in terms of the ratio of density to the modulus of elasticity was discovered in the parametric studies. This relationship was evaluated for both cases, healthy and cracked blade impellers. These findings provided the guidelines for predicting the inlet shroud deflection for shrouded impeller designs.

The inlet shroud deflection of the full-scaled impeller in various blade conditions was also determined using the FEA simulation models. The effect of passing fluid and a dry gas seal in terms of surface pressure distribution were accounted for the boundary conditions. The predicted results indicated that detecting a cracked blade in the early stage of around 20% crack length was possible for this impeller using the proposed inlet shroud/casing clearance measurement. The guidelines for designing an industrial blade crack detection system for a shrouded impeller are also presented.

The findings of these studies have an impact on both the academic and industrial communities. For the academic community, it paves the way for future research on the relationship between shroud impeller deflection and blade condition, and also the effect of impeller design on the behaviour of a shrouded impeller. Original Equipment Manufacturers (OEMs) could benefit from future research results by gaining an understanding of the failure mechanisms, which could ultimately inform impeller design.

On the other hand, this research initiates the development of an industrial blade health monitoring system for shrouded impellers, which primarily benefits production planning. Referring to a 2009 emergency shutdown of an ethylene plant in Thailand, the potential savings could approach £2 million.

8.2 Recommendations for future works

While the proposed method can be considered novel for the reasons discussed above, there remain issues that should be considered prior to designing and implementing an industrial blade condition monitoring system for a shrouded impeller. The recommendations for future work are listed as follows.

First, a transient CFD study with complete inlet and outlet compressor geometries should be performed to determine the stress fluctuation due to the unsteady external excitation force acting on the shrouded impeller blades. Thus, the blade vibration response is able to be determined using the predicted stress fluctuation combined with the blade's natural frequency from the FEA study. The blade vibration response indicates the potential for blade fatigue damage. Therefore, the fluid-induced blade fatigue problem may be solved by changing the design and number of inlet guide vanes.

Secondly, the fracture mechanics of the crack propagation should be studied in terms of applied stress, crack size and part geometry to determine the stress intensity factor for characterising the stress field near the crack tip. This stress intensity factor is a crucial parameter for predicting the crack propagation path and crack growth

rate. When combined with the characteristics of the shroud deflection, this information permits the estimation of the remaining life before a blade ruptures.

Thirdly, experimental studies should be conducted to validate the predicted results from the parametric studies. Specifically, the blade and shroud thicknesses were the most influential parameters in the change in inlet shroud deflection. Additionally, the observation of the relationship between the maximum inlet shroud deflection and the impeller material in terms of a ratio between density to the modulus of elasticity should also be confirmed by experimental results.

Finally, experimental studies with an actual impeller should be conducted to establish any possible relationship between the characteristics of the shroud deflection and the blade condition, the knowledge and experience in the sensor design and installation, and the machine electrical noise level. Once this knowledge is gained from experimental studies, a fully optimised design of the blade health monitoring solution for shrouded impellers using clearance measurements can be made available.

Appendix

Dimensional analysis

The purpose of the dimensional analysis was to investigate the relationship between the shroud deflection and the ratio of density and modulus of elasticity. The steps of dimensional analysis were adapted from the example provided by Robert et al. (2004) [110].

Recall the relationship between shroud deflection and the ratio of density and modulus of elasticity (Equation 6.5),

$$x = \frac{\rho V \omega^2 r}{EA/L}. \tag{6.5}$$

Given:

$$x = f(\rho, V, \omega, r, E, A, L) \tag{A.1}$$

Step 1: List the dimensional parameters.

x ρ V ω r E A L $n = 8$ dimensional parameters

Step 2: Choose M, L, and t as primary dimensions.

Step 3: List the dimensions of parameters in terms of primary dimensions.

x	ρ	V	ω	r	E	A	L	
L	$\frac{M}{L^3}$	L^3	$\frac{1}{T}$	L	$\frac{M}{Lt^2}$	L^2	L	$r = 3$ primary dimension

Step 4: Choose ρ, ω, and E as repeating parameters.

$m = r = 3$ repeating parameters

Step 5: The number of dimensionless groups is equal to $n - m = 5$. Thus, the functional relationship is

$$\Pi_1 = f(\Pi_2, \Pi_3, \Pi_4, \Pi_5). \tag{A.2}$$

Solve for dimensionless group Π_1.

$$\Pi_1 = \rho^a \omega^b E^c x$$

$$\left(\frac{M}{L^3}\right)^a \left(\frac{1}{t}\right)^b \left(\frac{M}{Lt^2}\right)^c (L) = M^0 L^0 t^0$$

$$\left.\begin{array}{ll} M & 0 = a + C \\ L & 0 = -3a - c + 1 \\ t & 0 = -b - 2c \end{array}\right\} \begin{array}{c} a = 1/2 \\ b = -1 \\ c = -1/2 \end{array}$$

Therefore,

$$\Pi_1 = \rho^{1/2} \omega^{-1} E^{-1/2} x = \frac{x}{\omega}\sqrt{\frac{\rho}{E}}. \tag{A.3}$$

Solve for dimensionless group Π_2.

$$\Pi_2 = \rho^d \omega^e E^f V$$

$$\left(\frac{M}{L^3}\right)^d \left(\frac{1}{t}\right)^e \left(\frac{M}{Lt^2}\right)^f (L^3) = M^0 L^0 t^0$$

$$\left.\begin{array}{ll} M & 0 = d + f \\ L & 0 = -3d - f + 3 \\ t & 0 = -e - 2f \end{array}\right\} \begin{array}{c} d = 3/2 \\ e = 3 \\ f = -3/2 \end{array}$$

Therefore,

$$\Pi_2 = \rho^{3/2} \omega^3 E^{-3/2} x = \omega^3 \sqrt{\left(\frac{\rho}{E}\right)^3}. \tag{A.4}$$

Solve for dimensionless group Π_3.

$$\Pi_3 = \rho^g \omega^h E^i r$$

$$\left(\frac{M}{L^3}\right)^g \left(\frac{1}{t}\right)^h \left(\frac{M}{Lt^2}\right)^i (L) = M^0 L^0 t^0$$

$$\left.\begin{array}{ll} M & 0 = g + i \\ L & 0 = -3g - i + 1 \\ t & 0 = -h - 2i \end{array}\right\} \begin{array}{l} g = 1/2 \\ h = -1 \\ i = -1/2 \end{array}$$

Therefore,

$$\Pi_3 = \rho^{1/2}\omega^{-1}E^{-1/2}r = \frac{r}{\omega}\sqrt{\frac{\rho}{E}}\,. \tag{A.5}$$

Solve for dimensionless group Π_4.

$$\Pi_4 = \rho^j \omega^k E^l A$$

$$\left(\frac{M}{L^3}\right)^j \left(\frac{1}{t}\right)^k \left(\frac{M}{Lt^2}\right)^l (L^2) = M^0 L^0 t^0$$

$$\left.\begin{array}{ll} M & 0 = j + l \\ L & 0 = -3j - l + 2 \\ t & 0 = -k - 2l \end{array}\right\} \begin{array}{l} j = 1 \\ k = 2 \\ l = -1 \end{array}$$

Therefore,

$$\Pi_4 = \rho^1\omega^2E^{-1}A = \frac{\rho\omega^2 A}{E}. \tag{A.6}$$

Solve for dimensionless group 5.

$$\Pi_5 = \rho^m \omega^n E^p L$$

$$\left(\frac{M}{L^3}\right)^m \left(\frac{1}{t}\right)^n \left(\frac{M}{Lt^2}\right)^p (L) = M^0 L^0 t^0$$

$$\left.\begin{array}{ll} M & 0 = m + p \\ L & 0 = -3m - p + 1 \\ t & 0 = -n - 2p \end{array}\right\} \begin{array}{l} m = 1/2 \\ n = -1 \\ p = -1/2 \end{array}$$

Therefore,

$$\Pi_5 = \rho^{1/2}\omega^{-1}E^{-1/2}L = \frac{L}{\omega}\sqrt{\frac{\rho}{E}}. \tag{A.7}$$

Substitute equations A.3 to A.7 into equation A.1. Finally, the functional relationship can be written as

$$\frac{x}{\omega}\sqrt{\frac{\rho}{E}} = f(\omega^3\sqrt{\left(\frac{\rho}{E}\right)^3}, \frac{r}{\omega}\sqrt{\frac{\rho}{E}}, \frac{\rho\omega^2 A}{E}, \frac{L}{\omega}\sqrt{\frac{\rho}{E}}). \tag{A.8}$$

At fixed rotational speed and impeller geometries, ω, V, A, and L become constants. Therefore, the functional relationship (A.8) can be rewritten as

$$x = g(\frac{\rho}{E}, \sqrt{\frac{\rho}{E}}) \quad \text{(A.9)}$$

or

$$x = h(\frac{\rho}{E}). \quad \text{(A.10)}$$

Therefore, shroud deflection (x) is the function of the ratio of density (ρ) and the elasticity (E) of the impeller material at fixed rotational speed and impeller geometry.

References

[1] Boyce, M. P., 1993, "Principle of Operation and Performance Estimation of Centrifugal Compressors". *Proceedings of the twenty-second turbomachinery symposium*, Dallas, Texas, USA.

[2] Mevissen, F. and Meo M., 2019, "A Review of NDT/Structural Health Monitoring Techniques for Hot Gas Components in Gas Turbines". *Sensors*, 19(3).

[3] Sridhar, V. and Chana, K. S., 2017, "Tip-clearance Measurements on an Engine High Pressure Turbine Using an Eddy Current Sensor". *Proceedings of ASME Turbo Expo 2017*, Charlotte, USA.

[4] Garcia, I., Beloki, J., Zubia, J., Durana, G. and Aldabaldetreku, G., 2013, "Turbine-blade Tip Clearance and Tip Timing Measurements Using an Optical Fiber Bundle Sensor". *Proceedings of SPIE - The International Society for Optical Engineering*, in Optical Measurement Systems for Industrial Inspection VIII.

[5] Sheard, A. G., 2011, "Blade by Blade Tip Clearance Measurement". *International Journal of Rotating Machinery*, 2011, 1-13.

[6] Chana, K. S., 2007, "Tip Timing and Tip Clearance Problems in Turbomachines". Von Karman Institute, Belgium.

[7] Chana, K. S., Cardwell, D. N., and Russhard, P., 2008, "Eddy Current Sensors for the Measurement of Rotor Blade Tip Timing Sensor

Development and Engine Testing". *In Proceedings of the ASME Turbo Expo 2008: Power for Land, Sea and Air,* no. GT2008-50791, Berlin, Germany.

[8] Chana, K. S., Sridhar, V., and Singh, D., 2016, "The Use of Eddy Current Sensors for the Measurement of Rotor Blade Tip Timing: Development of a New Method Based on Integration". *In Proceedings of the ASME Turbo Expo 2016: Power for Land, Sea and Air*, no. GT2016-57368, Seoul, South Korea

[9] Heath, S. and Imregun, M., 1996, "An Improved Single-parameter Tip-timing Method for Turbomachinery Blade Vibration Measurements Using Optical Laser Probes". *International Journal of Mechanical Sciences*, 38(10), 1047-1058.

[10] Li, H., Zhang, X. and Xu, F., 2013, "Experimental Investigation on Centrifugal Compressor Blade Crack Classification Using the Squared Envelope Spectrum", *Sensor*, 13(9), 12548 – 12563.

[11] Zhang, M., Liu, Y., Wang, W., Wang, P. and Li, J., 2016, "The Fatigue of Impellers and Blades", *Engineering Failure Analysis*, 62, 208 – 231.

[12] Wang, S., Zi, Y., Li, B., Zhang, C. and He, Z., 2014, "Reduced-order Modeling for Mistuned Centrifugal Impellers with Crack Damages", *Journal of Sound and Vibration*, 333(25), 6979 – 6995.

[13] Jinlong, W., Yangyang, Y., Jing, Y., Jingsi, W., Fengming, D. and Yuxing, Y., 2020, "Fatigue Evaluation of FV520B-I Shrouded Impeller Blade with Fatigue Crack Based on FEA and Fracture Mechanics". *Engineering Failure Analysis*, 115, 104663.

[14] Wang, L., Sui, T., 2015, "Fatigue Life Prediction of an Impeller Based on Fracture Mechanics", *In Proceeding of the 2015 International Conference on Modeling, Simulation and Applied Mathematics*, Phuket, Thailand.

[15] Harada, H., 1985, "Performance Characteristics of Shrouded and Unshrouded Impellers of a Centrifugal Compressor", *Journal of Engineering for Gas Turbines and Power*, ASME, 107(2), 528 – 533.

[16] API Standard 670, 2000, "Machinery Protection Systems" – American Petroleum Institute.

[17] Cardwell, D. N., Chana, K. S. and Gilboy, M. T., 2010, "The Development and Testing of a Gas Turbine Engine Foreign Object Damage (FOD) Detection System", *In Proceeding Series of Turbo Expo: Power for Land, Sea and Air,* Glasgow, Scotland, UK.

[18] Iwata, T., Saeki, K., Shiga, T., Baba, Y., and Kameyama, Y., 2017, "Experimental Evaluation of Mechanical Reliability of the Impeller Blade for Large Integrally Graded Compressor", *In Proceeding of 46th Turbomachinery & 33rd Pump Symposia*, Houston, Texas, USA.

[19] Harvey, S. and Eng, P., 2017, "Centrifugal Compressors in Ethylene Plants", *Chem Eng. Prog.,* 133, 28 – 32.

[20] Van den Braembussche, R., 2019, *Design and Analysis of Centrifugal Compressors*, John Wiley & Sons.

[21] Johnson, J. A., Ablin, D. W. and Ernst, G. A., 2019, *Efficient Petrochemical Processes: Technology, Design and Operation*, John Wiley & Sons.

[22] Liu, D., and Pons, D.J., 2018, "Crack Propagation Mechanisms for Creep Fatigue: A Consolidated Explanation of Fundamental Behaviours from Initiation to Failure". *Metals*, 8(8), 623.

[23] Bertini, L., Neri, P., Santus, C., Guglielmo, A. and Mariotti, G., 2014, "Analytical investigation of the SAFE diagram for bladed wheels, numerical and experimental validation". *Journal of Sound and Vibration*, 333(19), 4771-4788.

[24] Dickmann, H.P., Secall Wimmel, T., Szwedowicz, J., Filsinger, D. and Roduner, C.H., 2006. "Unsteady flow in a turbocharger centrifugal compressor: three-dimensional computational fluid dynamics simulation and numerical and experimental analysis of impeller blade vibration", 455 – 465.

[25] Higashio, A., Yamashita, H. and Ota, M., 2010, "Dynamic Stress Measurement of Centrifugal Compressor Impeller and Study for Strength Criteria Based on Correlation by Unsteady CFD". *In Proceedings of the 39th Turbomachinery Symposium*. Texas A&M University. Turbomachinery Laboratories.

[26] Lüdtke, K.H., 2004, *Process centrifugal compressors: basics, function, operation, design, application*. Springer Science & Business Media.

[27] "*Depth of Penetration and Current Density*'. NDT Resource center, from https://www.ndeed.org/EducationResources/CommunityCollege/EddyCurrents/Physics/depthcurrentdensity.htm.

[28] Welsby, S.D. and Hitz, T., 1997, "True position measurement with eddy current technology', *Sensors-the Journal of Applied Sensing Technology*, 14(11), 30-41.

[29] Tian, G.Y., Zhao, Z.X. and Baines, R.W., 1998, "The research of inhomogeneity in eddy current sensors". *Sensors and Actuators A: physical*, 69(2), 148-151.

[30] Roach, S.D., 1998, "Designing and building an eddy current position sensor", *Sensors-the Journal of Applied Sensing Technology*, 15(9), 56-74.

[31] Terman, F.E., 1943, *Radio engineers' handbook*. 1st end, McGraw-Hill Book Company.

[32] Wheeler, H.A., 1928, "Simple inductance formulas for radio coils", *In Proceedings of the institute of Radio Engineers*, 16(10), 1398-1400.

[33] Chana, K. S., 2017, *Reactance Measurement*, WO 2017/125721 A1.

[34] Iwata, T., Baba, Y., Saeki, K., Kameyama, Y. and Shiga, T., 2017. "Experimental Evaluation of Mechanical Reliability of the Impeller Blade for Large Integrally Geared Compressors", *In Proceedings of the 46th Turbomachinery Symposium*. Turbomachinery Laboratory, Texas A&M Engineering Experiment Station.

[35] Diamond, D.H. and Heyns, P.S., 2018, "A Novel Method for The Design of Proximity Sensor Configuration for Rotor Blade Tip Timing". *Journal of Vibration and Acoustics*, 140(6).

[36] Du Toit, R.G., Diamond, D.H. and Heyns, P.H., 2019, "A Stochastic Hybrid Blade Tip Timing Approach for the Identification and

Classification of Turbomachine Blade Damage". *Mechanical Systems and Signal Processing*, 121, 389 – 411.

[37] Wilde, J. and Lai, Y., 2003, "Design optimization of an eddy current sensor using the finite-elements method". *Microelectronics Reliability*, 43(3), 345-349.

[38] Jamia, N., Friswell, M.I., El-Borgi, S. and Rajendran, P., 2019, "Modelling and experimental validation of active and passive eddy current sensors for blade tip timing". *Sensors and Actuators A: Physical*, 285, 98-110.

[39] Kono, M., Taura, T., Sunaga, H., Kimura, K., Suzuki, T., Morimura, M., Okano, H., Iwasaki, M., Takuno, H., Suzuki, M. and Kobayashi, H., 2006, November. "A high precision AC Wheatstone bridge strain gauge", *In 2006 IEEJ International Analog VLSI Workshop*, Hangzhou, China.

[40] Rigosi, G., Battiato, G. and Berruti, T.M., 2017, "Synchronous Vibration Parameters Identification by Tip Timing Measurements". *Mechanics Research Communications*, 79, 7-14.

[41] Zhou, Y., Song, Y., Xing, T., Wang, Y., Zhang, Q., Shao, L., Du, F. and Ding, S., 2021, "Parametric Modeling Method for Integrated Design and Manufacturing of Radial Compressor Impeller", *The International Journal of Advanced Manufacturing Technology*, 112(3), 1007-1021.

[42] Cumpsty, N.A., 1989, *Compressor aerodynamics*. Longman Scientific & Technical.

[43] Brun, K. and Kurz, R. eds., 2018, *Compression Machinery for Oil and Gas*, Gulf Professional Publishing. Chapter 3, 32.

[44] Hanachi, H., Alavi, E., Liu, J., Banerjee, A., Koul, A. and Liang, M., 2012, June, "Bladed Disk Crack Detection Through Advanced Analysis of Blade Time of Arrival Signal". *In 2012 IEEE Conference on Prognostics and Health Management*, IEEE, 1-4.

[45] Sato, T., Oh, J.M. and Engeda, A., 2005, "Experimental and Numerical Investigation of the Flow in a Vaneless Diffuser of a Centrifugal Compressor Stage. Part 1: Experimental Investigation", *In Proceedings of the Institution of Mechanical Engineers, Part C: Journal of Mechanical Engineering Science*, 219(10), 1053-1059.

[46] Dalbert, P., Ribi, B., Kmeci, T. and Casey, M.V., 1999, "Radial Compressor Design for Industrial Compressors", *In Proceedings of the Institution of Mechanical Engineers, Part C: Journal of Mechanical Engineering Science*, 213(1), .71-83.

[47] Hou, J., 2006, "Cracking-induced Mistuning in Bladed Disks. *AIAA journal*, 44(11), 2542-2546.

[48] Xu, H., Chen, Z., Yang, Y., Tao, L. and Chen, X., 2017, "Effects of Crack on Vibration Characteristics of Mistuned Rotated Blades", *Shock and Vibration*, 2017.

[49] He, C., Antoni, J., Daga, A.P., Li, H., Chu, N., Lu, S. and Li, Z., 2020, "An Improved Key-phase-free Blade Tip-timing Technique for Nonstationary Test Conditions and Its Application on Large-scale Centrifugal Compressor Blades", *IEEE Transactions on Instrumentation and Measurement*, 70, 1-16.

[50] Kuang, J.H. and Huang, B.W., 1999, Mode localization of a cracked blade disk.

[51] Liang, Z., Xiang, L., Wei, X., Chen, S., Liu, J. and Hao, Z., 2021, "Numerical Study on the Flow Characteristics of Centrifugal Compressor Impeller with Crack Damage", *Advances in Mechanical Engineering*, 13(7), 16878140211034622.

[52] Wei, S.T., and Pierre, C., 1988, "Localisation Phenomena in Mistuned Assemblies with Cyclic Symmetry Part 1: Free Vibrations," *Journal of Vibration, Acoustics, Stress, and Reliability in Design*, 110, 429–438.

[53] Wei, S.T., and Pierre, C., 1988, "Localisation Phenomena in Mistuned Assemblies with Cyclic Symmetry Part 2: Forced Vibrations," *Journal of Vibration, Acoustics, Stress, and Reliability in Design*, 110, 439–449.

[54] Wang, L. and Sui, T., 2015, "Fatigue Life Prediction of an Impeller Based on Fracture Mechanics", *In 2015 International Conference on Modeling, Simulation and Applied Mathematics* (15-19). Atlantis Press.

[55] Heath, S. and Imregun, M., 1998, "A Survey of Blade Tip-timing Measurement Techniques for Turbomachinery Vibration". *Journal of Engineering for Gas Turbines and Power-Transactions of the ASME*, 120(4), 784-791.

[56] White, N.M., Laney, S.J. and Zorzi, C., 2011, "RCFA for Recurring Impeller Failures in a 4.7 mtpa LNG Train Propane Compressor", *In Proceedings of the 40th Turbomachinery Symposium*. Texas A&M University. Turbomachinery Laboratories.

[57] Zablotsky, I.Ye., and Korostelev, Yu.A., 1970, "Measurement of Resonance Vibrations of Turbine Blades with the ELURA Device," *Energomashinostroneniye*, 2(2), 36–39.

[58] Xu, C. and Amano, R.S., 2012, "Empirical design considerations for industrial centrifugal compressors", *International Journal of Rotating Machinery, 2012*.

[59] Yu, B., Ke, H., Shen, E. and Zhang, T., 2020, "A Review of Blade Tip Clearance–measuring Technologies for Gas Turbine Engines", *Measurement and Control*, 53(3-4), 339-357.

[60] Casey, M. and Robinson, C., 2021, *Radial Flow Turbocompressors*, Cambridge University Press. Chapter 9, 284 – 285.

[61] Brun, K. and Kurz, R. eds., 2018, *Compression Machinery for Oil and Gas*, Gulf Professional Publishing, Chapter 3, 37.

[62] Mokhatab, S., Poe, W.A. and Mak, J.Y., 2018, *Handbook of natural gas transmission and processing: principles and practices*. Gulf professional publishing, Chapter 14, 433 – 461.

[63] Lettieri, C., Baltadjiev, N., Casey, M. and Spakovszky, Z., 2014, "Low-flow-coefficient Centrifugal Compressor Design for Supercritical CO2", *Journal of Turbomachinery*, 136(8), 081008.

[64] Dimitriadis, G., Carrington, I.B., Wright, J.R. and Cooper, J.E., 2002, "Blade-tip Timing Measurement of Synchronous Vibrations of Rotating Bladed Assemblies". Mechanical Systems and Signal Processing, 16(4), 599-622.

[65] Lerche, A.H., Moore, J.J., White, N.M. and Hardin, J., 2012, June, "Dynamic stress prediction in centrifugal compressor blades using fluid structure interaction". *In Turbo Expo: Power for Land, Sea, and Air*, 44724, 191-200, American Society of Mechanical Engineers.

[66] Melcher, K.J. and Kypuros, J.A., 2003, December, "Toward a Fast-response Active Turbine Tip Clearance Control", *In 16th International Symposium on Airbreathing Engines* (No. E-14185).

[67] Steinetz, B., Lattime, S., Taylor, S., DeCastro, J., Oswald, J. and Melcher, K., 2005, "Preliminary Evaluation of an Active Clearance Control System Concept", *In 41st AIAA/ASME/SAE/ASEE Joint Propulsion Conference and Exhibit*, 3989.

[68] Geisheimer, J., Billington, S. and Burgess, D., 2004, "A microwave blade tip clearance sensor for active clearance control applications", *In 40th AIAA/ASME/SAE/ASEE Joint Propulsion Conference and Exhibit*, 3720.

[69] Free, G.M., 1977, "Eddy Current Nondestructive Testing", *Gaithersburg*, Md, 3-4 Nov. 1977, 1981.

[70] Steve, K., 2017, *Shrouded or Open Impellers for Compressor Chillers – That is the Question*, viewed 20th May 2022, <https://www.conceptsnrec.com/blog/shrouded-or-open-impellers-for-compressor-chillers-that-is-the-question>.

[71] Casey, M.V. and Marty, F., 1986, *Centrifugal compressors-performance at design and off-design*, Institute of Refrigeration at the Institute of Marine Engineers, London, UK.

[72] Janicki, G., Pezouvanis A., Mason, B. and Ebrahimi, M.K., 2014, "Turbine Blade Vibration Measurement Methods for Turbocharges". *American Journal of Sensor Technology*, 2(2), 13-19.

[73] Cave, M. and Ji, M., 2017, June, "Impeller Manufacturing: Design for Machining", *In Turbo Expo: Power for Land, Sea, and Air*, 50800, p. V02CT44A027, American Society of Mechanical Engineers.

[74] Witoś, M., 2013, "High Sensitive Methods for Health Monitoring of Compressor Blades and Fatigue Detection. *The Scientific World Journal, 2013*.

[75] Madhavan, S., Jain, R., Sujatha, C. and Sekhar, A.S., 2014, "Vibration Based Damage Detection of Rotor Blades in a Gas Turbine Engine", *Engineering Failure Analysis*, 46, 26-39.

[76] Zeng, J., Chen, K., Ma, H., Duan, T. and Wen, B., 2019, "Vibration response analysis of a cracked rotating compressor blade during run-up process", *Mechanical Systems and Signal Processing*, 118, 568-583.

[77] Wang, S., Zi, Y., Wan, Z., Li, B. and He, Z., 2015, "Effects of multiple cracks on the forced response of centrifugal impellers", *Mechanical Systems and Signal Processing*, 60, 326-343.

[78] Kowshik, C.K.P., Tsugita, D., Takeyama, Y. and Ohta, Y., 2012, June, "Rotating Instability in a Centrifugal Blower with Shrouded Impeller", *In Turbo Expo: Power for Land, Sea, and Air*, 44694 685-694, American Society of Mechanical Engineers.

[79] Zhang, J., Duanm, F., Niu, G., Jiang, J. and Li, J., 2017, "A Blade Tip Timing Method Based on a Microwave Sensor". Sensors, 17(5).

[80] Innospection, *Eddy Current Theory*, viewed 24th April 2022, from <https://www.yumpu.com/en/document/read/23422660/eddy-current-theory-innospection>.

[81] Battiato, G., Firrone, C.M. and Berruti, T.M., 2017, "Forced Response of Rotating Bladed Disks: Blade Tip-Timing Measurements", *Mechanical Systems and Signal Processing*, 85, 912-926.

[82] Smith, J.H. and Dodd, C.V., 1973, "Optimization of Eddy-current Measurements of Coil-to-conductor Spacing (No. CONF-731014-1). Oak Ridge National Lab., Tenn.(USA).

[83] Dodd, C. V. and Deeds, W. E., 1968, 'Analysis Solutions to Eddy-Current Probe-Coil Problem'. *Journal of Applied Physics* 39, 2829-2838.

[84] Hajian, N.T. and Blitz, J., 1986, "Prediction of Impedance Components for Eddy-current Probe Coils for Standardisation". *NDT International,* 19(5), 333-339.

[85] Oaten, S.R. and Blitz, J., 1992, "Impedance Analysis for Air-cored Cylindrical Eddy Current Coils Scanning the Surfaces of Deflection-free Conductors". *Nondestructive Testing and Evaluation*, 6, 323-335.

[86] Palmer, S. and Lord, W., 1997, *Electrical and Magnetic Methods of Non-destructive Testing* (2nd edn). Springer Science + Business Media Dordrecht.

[87] Fladung, W. A., 1997, "Windows used for impact testing". *In Proceedings-SPIE The International Society for Optical Engineering*, SPIE INTERNATIONAL SOCIETY FOR OPTICAL, 1662-1666.

[88] Chana, K. S, 2009, *Eddy Current Sensor*, CA2688645A1.

[89] Foiles, W. C. and Allaire, P. E., 2006, September, "Single Plane and Multi-Plane Rotor Balancing Using Only Amplitude. *In International Conference on Rotor Dynamics*, 7, 25-28.

[90] COMSOL, 2021, *Single-turn and Multi-turn Coil Domains in 3D*, viewed on <https://www.comsol.jp/forum/thread/attachment/95136/3D_Coils_43a-17070.pdf>.

[91] COMSOL, 2018, *AC/DC Module User's Guilde, 5.4,* viewed on <https://doc.comsol.com/5.4/doc/com.comsol.help.acdc/ACDCModuleUsersGuide.pdf>.

[92] Frei, W., (2013) '*Computational Electromagnetics Modeling, Which Module to Use?*'. from https://uk.comsol.com/blogs/computational-electromagnetics-modeling-which-module-to-use/.

[93] Chana, K.S. and Cardwell D.N., 2008, "The Use of Eddy Current Sensor Based Blade Tip Timing for FOD Detection". *Proceedings of the ASME Turbo Expo 2008: Power for Land, Sea and Air*, 2, 169-178.

[94] Zhang, L., Zhao, S. and Wang, Z., 2014, " Investigation on the Crack Initiation of V-shaped Notch Tip in Precision Cropping", *Advances in Materials Science and Engineering*, 2014.

[95] ANSYS, Inc., 2009, Static Structural Analysis, viewed on 10th March 2022, <http://mguler.etu.edu.tr/WB-Mech_120_Ch04_Static.pdf>.

[96] Ozgun, 2021, Ansys Contact Types and Explanations, viewed on 12th April 2020, <https://www.mechead.com/contact-types-and-behaviours-in-ansys>.

[97] Boddenberg, K., 1986, "On the Manufacture of Impellers for Turbocompressors", *In Proceedings of the 15th Turbomachinery Symposium.* Texas A&M University. Turbomachinery Laboratories.

[98] Ezkurra Mayor, M., Esnaola, J.A., Martinez-Agirre, M., Lertxundi, U. and Etxeberria, U., 2018, "Analysis of One-way and Two-way FSI Approaches to Characterise the Flow Regime and the Mechanical Behaviour during Closing Manoeuvring Operation of a Butterfly Valve".

[99] ANSYS, Inc., 2021, *Ansys CFX Reference Guide*, viewed on 15th March 2022, <https://dl.cfdexperts.net/cfd_resources/Ansys_Documentation/CFX/Ansys_CFX_Reference_Guide.pdf>.

[100] Mortazavi, F., 2018. *CFD-Based Impeller and Seal Rotordynamic Forces* (Doctoral dissertation).

[101] Dewar, B., Tiainen, J., Jaatinen-Värri, A., Creamer, M., Dotcheva, M., Radulovic, J. and Buick, J.M., 2019, "CFD Modelling of a Centrifugal Compressor with Experimental Validation Through Radial Diffuser Static Pressure Measurement", *International Journal of Rotating Machinery*, 2019.

[102] Khalafallah, M.G., Saleh, H.S., Ali, S.M. and Abdelkhalek, H.M., 2021. "CFD Investigation of Flow Through a Centrifugal Compressor Diffuser with Splitter Blades", *Journal of Engineering and Applied Science*, 68(1), 1-23.

[103] Leong, C. and Goyal, S., 2015, "Process-Design Considerations for a Compressor Dry-Gas Seal-System Interface", *Oil and Gas Facilities*, 4(06), 72-76.

[104] Ross, S.L. and Gresh, M.T., 2003, "Compressor Seals for Hydrogen Recycle Service", *Sealing Technology*, 2003(5), 5-8, Compressor seals for hydrogen recycle service.

[105] API Standard 617, 2002, "Axial and Centrifugal Compressors and Expander-compressors for Petroleum, Chemical and Gas Industry Services". – American Petroleum Institute.

[106] Hanachi, H., Liu, J., Banerjee, A., Koul, A., Liang, M. and Alavi, E., 2012, "Bladed Disc Crack Diagnostics Using Blade Passage Signals". *Measurement Science and Technology*, 23(12).

[107] Peter M.F., Srinvas, M.V., Albers, R.J., DeLeonardo, G.W., 2005, *Method and System for Active Tip Clearance Control in Turbines*. US 2005/0149274 A1.

[108] Lattime, S.B. and Steinetz, B.M., 2002, "Turbine Engine Clearance Control Systems: Current Practices and Future Directions". *Proceedings of the 38th AIAA/ASME/SAE/ASEE Joint Propulsion Conference & Exhibit*, Indianapolis, Indiana, USA.

[109] Kai, P., Ding, F., Fan, Y., Qiang, F. and Yong, L., 2013, "Active Generalized Predictive Control of Turbine Tip Clearance for Aero-engines". *Chinese Journal of Aeronautics*, 26(5), 1147-1155.

[110] Robert, W.F., Alan, T.M., and Philip, J.P., 2004, *Introduction to Fluid Mechanics*, John Wiley & Sons.

[111] Monitran, Ltd., 1986, *Eddy Current Probes and Drivers*, viewed on 24th May 2023, <https://www.monitran.com/products/eddy-current-probes-and-drivers>.

[112] Czichos, H., 2018, *Measurement, Testing and Sensor Technology*, Springer.

[113] He, P., Ma, Y., and Chen, H., 2018, "Temperature Drift Compensation of Eddy Current Sensor under High Temperature Environment"., *In ICEMEE 2018 Conference, 38, 04005*.